

AD-A142 620

SUMMARY OF SAR (SYNTHETIC APERTURE RADAR) OCEAN WAVE  
DATA ARCHIVED AT ERI..(U) ENVIRONMENTAL RESEARCH INST  
OF MICHIGAN ANN ARBOR RADAR DIV U D LYDEN MAY 84

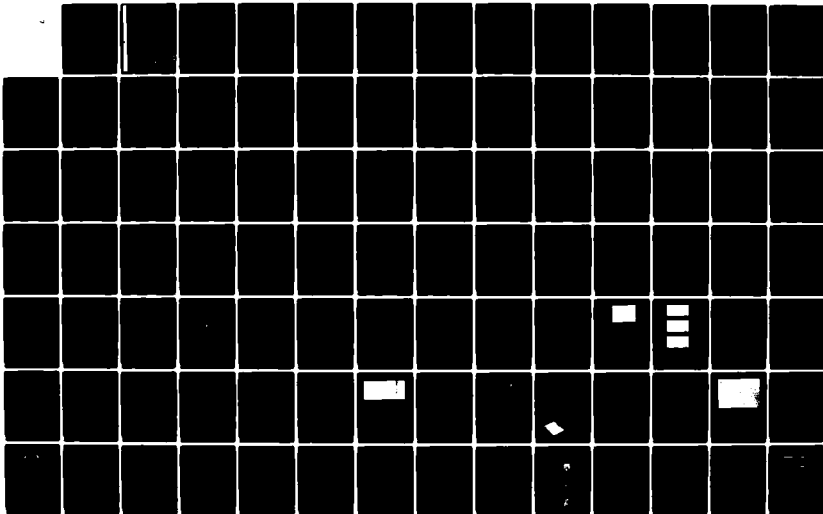
1/2

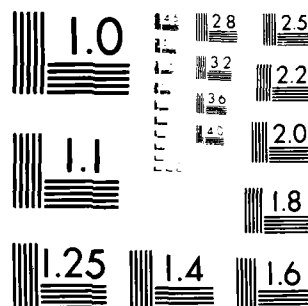
UNCLASSIFIED

ERIM-155900-17-T N00014-81-C-0692

F/G 20/4

NI





MICROCOPY RESOLUTION TEST CHART  
NATIONAL BUREAU OF STANDARDS-1963-A

155900-17-T

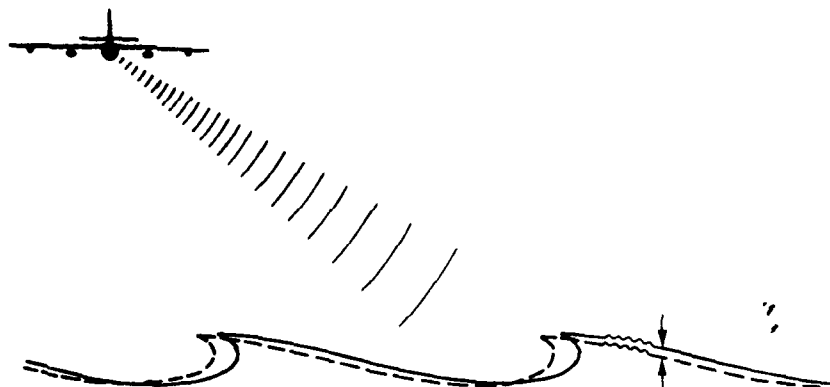
DTIC FILE COPY AD-A142 620

Topic Report

# SUMMARY OF SAR OCEAN WAVE DATA ARCHIVED AT ERIM

J.D. LYDEN  
Radar Division

MAY 1984



Ocean Sciences Division  
Office of Naval Research  
Arlington, VA 22217

Contract No. N00014-81-C-0692  
Technical Monitor: Mr. Hans Dolezalek

ENVIRONMENTAL  
**RESEARCH INSTITUTE OF MICHIGAN**  
BOX 8618 • ANN ARBOR • MICHIGAN 48107

This document has been approved  
for public release and sale; its  
distribution is unlimited.

DTIC  
SELECTED  
JUN 29 1984  
A

84 00 00 107

Unclassified

SECURITY CLASSIFICATION OF THIS PAGE (When Data Entered)

REPORT DOCUMENTATION PAGE		READ INSTRUCTIONS BEFORE COMPLETING FORM
1 REPORT NUMBER	2 GOVT ACCESSION NO <b>AD-A242 610</b>	3 RECIPIENT'S CATALOG NUMBER
4 TITLE (and Subtitle) SUMMARY OF SAR OCEAN WAVE DATA ARCHIVED AT ERIM		5 TYPE OF REPORT & PERIOD COVERED Topic Report Oct. 1982 - April 1984
7 AUTHOR(s) J.D. Lyden		6 PERFORMING ORG REPORT NUMBER 155900-17-T
9 PERFORMING ORGANIZATION NAME AND ADDRESS Environmental Research Institute of Michigan Radar Division; P.O. Box 8618 Ann Arbor, Michigan 48107		8 CONTRACT OR GRANT NUMBER (s) N00014-81-C-0692
11 CONTROLLING OFFICE NAME AND ADDRESS Ocean Sciences Division Office of Naval Research Arlington, Virginia 22217		10 PROGRAM ELEMENT PROJECT TASK AREA & WORK UNIT NUMBERS
14 MONITORING AGENCY NAME AND ADDRESS (if different from Controlling Office)		12 REPORT DATE May 1984
		13 NUMBER OF PAGES x plus 120
		15 SECURITY CLASS (of this report) Unclassified
16 DISTRIBUTION STATEMENT (of this Report)  Approved for public release; distribution unlimited.		15a DECLASSIFICATION/DOWNGRADING SCHEDULE
17 DISTRIBUTION STATEMENT (of the abstract entered in Block 20, if different from Report)		
18 SUPPLEMENTARY NOTES  The technical monitor for this work was Mr. Hans Dolezalek.		
19 KEY WORDS (Continue on reverse side if necessary and identify by block number) Synthetic Aperture Radar      Data Summary Ocean Waves      Remote Sensing Imaging Models		
20 ABSTRACT (Continue on reverse side if necessary and identify by block number)  Synthetic aperture radar (SAR) ocean wave imagery processed, analyzed, and archived at The Environmental Research Institute of Michigan (ERIM), is summarized. This summary includes a review of the SAR systems used to collect ocean wave imagery, as well as a brief review of the experiments where SAR ocean wave data was collected. The imagery from these experiments was manually examined to qualitatively rate the detectability (continued)		

Unclassified

SECURITY CLASSIFICATION OF THIS PAGE (When Data Entered)

20. ABSTRACT (continued)

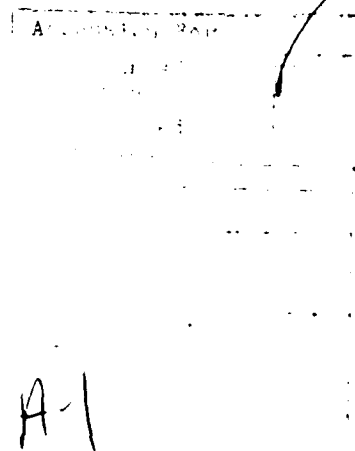
of waves in each pass. This information is summarized in table form, along with the SAR operating parameters and environmental conditions for each of the experiments. The data summarized in this report can be used in evaluating current and future SAR ocean wave imaging models.

Unclassified

SECURITY CLASSIFICATION OF THIS PAGE (When Data Entered)

## ABSTRACT

Synthetic aperture radar (SAR) ocean wave imagery processed, analyzed, and archived at the Environmental Research Institute of Michigan (ERIM) is summarized. This summary includes a review of the SAR systems used to collect ocean wave imagery, as well as a brief review of the experiments where SAR ocean wave data was collected. The imagery from these experiments was manually examined to qualitatively rate the detectability of waves in each pass. This information is summarized in table form, along with the SAR operating parameters and environmental conditions for each of the experiments. The data summarized in this report can be used in evaluating current and future SAR ocean wave imaging models.



## PREFACE AND ACKNOWLEDGEMENTS

The work described in this report was conducted by the Radar Science Laboratory of the Radar Division of the Environmental Research Institute of Michigan (ERIM) and was supported by the Office of Naval Research (ONR) Contract No. N-00014-81-0692. The ONR technical monitor was Mr. Hans Dolezalek. The author would like to thank Dr. Guy A. Meadows of the University of Michigan, and Drs. David R. Lyzenga and Robert A. Shuchman of ERIM for reviewing this report

## TABLE OF CONTENTS

ABSTRACT . . . . .	iii
PREFACE AND ACKNOWLEDGEMENTS . . . . .	v
LIST OF TABLES . . . . .	ix
1. INTRODUCTION . . . . .	1
2. SAR BACKGROUND . . . . .	3
2.1 Synthetic Aperture Radar	
2.1.1 ERIM X-L SAR	
2.1.2 APD-10 SAR	
2.1.3 Seasat SAR	
3. DATA SUMMARY . . . . .	9
3.1 Summary Procedure	
3.1.1 Marineland	
3.1.2 Lake Michigan 1977	
3.1.3 JASIN	
3.1.4 GOASEX	
3.1.5 Lake Michigan 1978	
3.1.6 MARSEN	
3.1.7 Other Experiments	
3.2 Statistical Summary	
4. CONCLUSIONS AND RECOMMENDATIONS . . . . .	41
REFERENCES . . . . .	43
APPENDIX . . . . .	47



## LIST OF TABLES

1. Nominal Operating Parameters for the ERIM X- and L-Band SAR System . . . . .	5
2. Nominal APD-10 SAR System Parameters (Mode 1) . . . . .	7
3. Nominal Operating Parameters of Seasat-A Synthetic Aperture Radar System . . . . .	8
4. Example Summary of Seasat SAR Operating Parameters and Environmental Conditions During the 1978 JASIN Experiment . . . . .	11
5. Summary of SAR Ocean Wave Experiments . . . . .	12
6. Summary of ERIM X-L SAR Operating Parameters and Environmental Conditions for 3 December 1975 . . . . .	14
7. Summary of ERIM X-L SAR Operating Parameters and Environmental Conditions for 4 December 1975 . . . . .	15
8. Summary of ERIM X-L SAR Operating Parameters and Environmental Conditions for 10 December 1975 . . . . .	16
9. Summary of ERIM X-L SAR Operating Parameters and Environmental Conditions for 14 December 1975 . . . . .	17
10. Summary of ERIM X-L SAR Operating Parameters and Environmental Conditions for 15 December 1975 . . . . .	18
11. Summary of ERIM X-L SAR Operating Parameters and Environmental Conditions for 6 October 1977 . . . . .	20
12. Summary of Seasat SAR Operating Parameters and Environmental Conditions During the 1978 JASIN Experiment . . . . .	22
13. Summary of Seasat SAR Operating Parameters and Environmental Conditions During the 1978 GOASEX Experiment . . . . .	24
14. Summary of ERIM X-L SAR Operating Parameters and Environmental Conditions for 22 September 1978 . . . . .	25
15. Summary of ERIM X-L SAR Operating Parameters and Environmental Conditions for 23 September 1978 . . . . .	26
16. Summary of ERIM X-L SAR Operating Parameters and Environmental Conditions for 25 September 1978 . . . . .	27

LIST OF TABLES  
(concluded)

17.	Summary of ERIM X-L SAR Operating Parameters and Environmental Conditions for 26 September 1978 . . . . .	28
18.	Summary of ERIM X-L SAR Operating Parameters and Environmental Conditions for 18 October 1978 . . . . .	30
19.	Summary of APD-10 SAR Operating Parameters and Environmental Conditions for 25 September 1979 (Line 8) . . . . .	32
20.	Summary of APD-10 SAR Operating Parameters and Environmental Conditions for 27 September 1979 (Line 12) . . . . .	33
21.	Summary of APD-10 SAR Operating Parameters and Environmental Conditions for 27 September 1979 (Line 13) . . . . .	34
22.	Summary of APD-10 SAR Operating Parameters and Environmental Conditions for 28 September 1979 (Line 10) . . . . .	35
23.	Summary of APD-10 SAR Operating Parameters and Environmental Conditions for 28 September 1979 (Line 7) . . . . .	36
24.	Summary of APD-10 SAR Operating Parameters and Environmental Conditions for 28 September 1979 (Line 6) . . . . .	38
A1.	Papers in Appendix . . . . .	48

## SUMMARY OF SAR OCEAN WAVE DATA ARCHIVED AT ERIM

1  
INTRODUCTION

Over the past nine years, scientists from the Environmental Research Institute of Michigan (ERIM) have explored the utility of synthetic aperture radar (SAR) for oceanographic applications. The major emphasis of this work has been in evaluating the ability of SAR to detect and accurately measure ocean surface gravity waves. ERIM's research activities in this area have included, but were not limited to: experiment planning, data collection, data processing, and the development of analysis techniques. The purpose of this report is to summarize the SAR ocean wave imagery from these past experiments which was processed, analyzed, and is presently archived at ERIM.

There is considerable debate among the radio oceanography community on the imaging mechanism for "wave-like" patterns on SAR imagery of the ocean surface (Alpers, et al., 1981; Plant, 1983; Hasselmann, et al., 1983). Three principal SAR imaging mechanisms have been proposed for gravity waves. These include: tilt modulation, hydrodynamic modulation, and velocity bunching. Tilt modulation is due to the change in the local incidence angle induced by the slopes of the surface waves. Hydrodynamic modulation is due to the hydrodynamic interaction between the short Bragg scattering waves and the longer gravity waves, which results in a nonuniform distribution of short waves with respect to the longer gravity waves. Velocity bunching is a consequence of the mis-mapping of scatterers with non-zero radial velocities, which is peculiar to the SAR as a range-Doppler imaging device.

Much of the past work in developing a SAR imaging mechanism for ocean surface waves has been solely theoretical (Alpers and Rufenach, 1979; Hasselmann, et al., 1983). These studies have presented elaborate mathematical descriptions of the SAR imaging process, but did

not include any supporting experimental data. The experimental observations presented in this report provide a basis by which the various imaging theories can be evaluated.

Presented in the following sections are descriptions of the various experiments where SAR imagery of ocean waves was collected. Included in this discussion will be a review of basic SAR theory and a description of the SAR systems used to collect wave data. In addition, the detectability of waves on the imagery based on a manual interpretation is presented. Also included as an Appendix to this report are a series of reprints which describe the various SAR experiments in greater detail.

2  
SAR BACKGROUND

Presented in this section is a review of basic SAR theory and a description of the SAR systems used to collect the ocean wave imagery summarized in this study.

## 2.1 SYNTHETIC APERTURE RADAR

Synthetic aperture radar (SAR) is a side-looking coherent imaging radar that uses the motion of a moderately broad physical antenna beam to synthesize a very narrow beam, thus providing fine azimuthal (along-track) resolution (Brown and Porcello, 1969; Harger, 1970). Fine range resolution is obtained by transmitting short pulses or longer coded pulses which are compressed into equivalent short pulses; usually the coded pulse is a waveform linearly modulated in frequency. The received signals may be recorded optically or digitally. In the optical case, the phase history of a scattering point in the scene is recorded on photographic film as an anamorphic (astigmatic) Fresnel zone plate. The parameters of the zone plate are set in the azimuth direction by the Doppler frequencies produced by the relative motion between the sensor and the scatterer, and in the range direction by the structure of the transmitted pulses. The film image is a collection of superimposed zone plates representing the collection of point scatterers in the scene. This film is used by a coherent optical processor which focuses the anamorphic zone plates into the points which produced the microwave scatter of the scene (Kozma, et al., 1972). Digital techniques may also be used to both record and process the data. Digital processors typically use matched filtering techniques to compress the signal in range, while fast Fourier transform (FFT) techniques achieve the required azimuthal compression of the SAR Doppler history (Ausherman, 1980). Specially-designed digital processors have also been designed for

real-time processing of SAR data aboard the aircraft for display or transmission to a ground receiver via a digital downlink.

Three SAR systems were used to collect the ocean wave data presented in this study. These were: the ERIM four-channel X- and L-band system, the Goodyear-manufactured APD-10 X-band system, and the L-band system aboard Seasat. Each of these SARs is discussed in more detail below.

#### 2.1.1 ERIM X-L SAR

The ERIM X- and L-band (3.2 and 23.5 cm wavelengths, respectively) four-channel SAR system has been used numerous times to collect ocean wave imagery. For ocean wave data collection, the system operates in a four-channel, narrow swath mode. In four-channel operation, alternate X- and L-band pulses (chosen to be either horizontally or vertically polarized) are transmitted, and reflections of both polarizations received; thus, four channels of radar imagery are simultaneously obtained. Both polarizations of X-band are recorded on one film, both polarizations of L-band on another. Only like-polarized data collected by this system are summarized in this report. The slant range swath width for each channel is approximately 5.8 km. The nominal resolution for the system is approximately 3 m for both slant range and azimuth. The operating parameters for this SAR are given in Table 1. A more detailed description of this SAR system is given by Rawson, et al. (1975).

Up until 1978, this system was operated by ERIM from a C-46 aircraft which flew at a nominal velocity of 80 m/s. In 1978, it was installed in a Convair 580 aircraft owned by the Canada Centre for Remote Sensing (CCRS). This SAR system is now jointly owned by ERIM and CCRS and is collectively known as the SAR 580 system. In contrast to the C-46, the Convair 580 operates at a nominal velocity of 125 m/s.

TABLE 1  
NOMINAL OPERATING PARAMETERS FOR THE ERIM X- AND L-BAND SAR SYSTEM

	<u>X-Band</u>	<u>L-Band</u>
Transmitter Average Power	5 watts	25 watts
Nominal Vehicle Velocity	110 m/sec	110 m/sec
Antenna Gain	25 dB	16.5 dB
Polarization Isolation	23 dB	19 dB
Along-Track Beamwidth	1.1°	7°
Incident Angle	0°-60°	0°-60°
Recorded Swath Width	5790 m	5790 m
	Slant Range	Slant Range
Maximum Range	24 km	24 km
FM Rate	33.3 MHz/ $\mu$ sec	33.3 MHz/ $\mu$ sec
Pulse Width	3 sec	2 sec
Wavelength	0.032 m	0.235 m
Range Packing Factor (Q)	196,000	185,465
Azimuth Packing Factor (P)	14,947	41,478
Correlator Demagnification (M)	13.7	4.8
CRT Sweep Speed (on film)	765 m/sec	765 m/sec
PRF (transmitter)	3400 pps	3400 pps
PRF (receiver, per channel)	1700 pps	1700 pps
Azimuth Offset Frequency	100 Hz	0
Range Offset Frequency	0	67.7 MHz
Input Aspect Ratio	13.1 to 1	4.5 to 1
Output Aspect Ratio	1:1	1:1
Film Speed	5.15 mm/sec	1.86 mm/sec
Resolution	3 m Slant Range 3 m Azimuth	3 m Slant Range 3 m Azimuth
Laser Wavelength of ERIM SAR Processor	.633 $\times 10^{-6}$ m	.633 $\times 10^{-6}$ m

### 2.1.2 APD-10 SAR

Another SAR utilized by ERIM scientists to collect ocean wave imagery was the APD-10 system flown in an RF-4 jet. The APD-10 system is a high-resolution airborne side-looking SAR which operates at X-band (3.2 cm). The APD-10 has six modes of operation which provide a variety of standoff distances and also provide both fixed target imagery (FTI) or FTI along with moving target imagery (MTI). Imagery can be obtained on either side of the aircraft.

For the ocean wave imagery summarized in this report, Mode 1 was used in which FTI is recorded on 9.5-inch film in four channels. Each channel corresponds to a slant range swath width of 4.6 km with an additional 0.46 km overlap between adjacent channels. The nominal resolution of this system is approximately 3 m for both slant range and azimuth. The operating parameters for the APD-10 system in Mode 1 are given in Table 2.

### 2.1.3 SEASAT SAR

In addition to the above two aircraft systems, ocean wave imagery collected by the SAR on the Seasat satellite was used in this study. The SAR aboard Seasat was an L-band (23.5 cm) system which generated continuous radar imagery with a 100 km ground swath width and lengths of up to 4000 km. The nominal resolution of this system is 25 m for both ground range and azimuth.

The data received by the Seasat SAR was transmitted to any of several ground stations via a digital data link where it was stored on high density digital tape (HDDT). The HDDT could then be played back and recorded on film for optical processing (Kozma, et al., 1972), or transferred to a computer compatible tape (CCT) for digital processing (Wu, et al., 1981). The operating parameters for the Seasat SAR are given in Table 3. For a more detailed discussion on the Seasat SAR, the reader is referred to Jordan (1980).



TABLE 2  
NOMINAL APD-10 SAR SYSTEM PARAMETERS (MODE 1)

Vehicle Velocity	210 m/s
Along-Track Beamwidth	1.5°
Incident Angle	0-90°
Swath Width	18.5 km Slant Range (4-4.63 km sub-swaths)
Wavelength	0.032 m
Maximum Range	23.2 km
FM Rate	105 MHz/ $\mu$ sec
Pulse Width	0.95 $\mu$ sec
Polarization	HH
Resolution	3 m Slant Range 3 m Azimuth
Range Packing Factor	100,000
Azimuth Packing Factor	12,500
Correlation Demagnification	8:1

TABLE 3  
NOMINAL OPERATING PARAMETERS OF SEASAT-A  
SYNTHETIC APERTURE RADAR SYSTEM

Frequency	1274.8 MHz
Wavelength	23.5 cm (L-band)
Polarization	HH
Transmitted Bandwidth	19 MHz
Pulse Duration	33.8 $\mu$ sec
Pulse Time-Bandwidth Product	642
Transmitter RF Power	800 W Peak - 46 W Average
Transmitter Type	Solid-State Bipolar Transmitter
PRF	1647
Satellite Altitude	~800 km
Nominal Range (20°)	~850 km
Antenna Dimensions	10.7 x 2.16 m
Antenna Beamwidth, Elevation	6°
Antenna Pointing Angle	19-25° off nadir, right side
Surface Resolution	25 m x 25 m (4 look data)
Slant Range Resolution	8 m
Azimuth Resolution (one look)	6.25 m
Integration Time	0.5 to 2.5 sec depending on resolution
Image Swath Width	100 km
Image Length	250 to 4000 km
Sensor Power	60 W, nominal operation
Satellite Velocity	~7000 m/sec

### 3 DATA SUMMARY

In this section of the report, a detailed summary of the various SAR data sets is presented in table form. These summary tables should prove useful in evaluating current and future SAR ocean wave imaging models. In addition to the tables, a set of summary statistics is presented.

#### 3.1 SUMMARY PROCEDURE

The procedure used in producing the summary tables presented below consisted of examining flight logs and satellite ephemeris data to determine various flight and radar parameters including:

1. Aircraft pass or satellite revolution,
2. Aircraft or satellite heading,
3. Aircraft or satellite velocity,
4. Aircraft or satellite altitude,
5. Range distance to near edge of SAR coverage,
6. Radar wavelength,
7. Transmitted polarization, and
8. Received polarization.

In addition, available surface measurements were located including:

1. Significant wave height ( $H_{1/3}$ ),
2. Dominant wavelength,
4. Dominant wave direction,
4. Wind speed, and
5. Wind direction.

Finally, the SAR imagery from each pass or revolution was manually examined to determine whether waves were imaged. The detectability of waves at 20°, 40°, 60° and 80° incidence angle was also recorded.

An example summary of SAR data collected by Seasat during the JASIN Experiment is presented in Table 4 . The 0 and -0.0 values represent cases where the data did not exist for one reason or another. For example, the Seasat SAR only collected data from approximately 19 to 25° incidence angle. This is reflected in Table 4 by 0's in the last 3 columns. The detectability rating in the last 4 columns is a qualitative measure based on the author's experience. Comparison of these ratings with actual quantitative measures of wave detectability (available for a small subset of the data) showed close relative agreement.

Presented in chronological order below is a review of the various experiments during which SAR ocean wave imagery was collected. An overview of these experiments is presented in Table 5. Over 200 individual passes (revolutions) of SAR data were examined and are summarized below.

### 3.1.1 MARINELAND

A major collaborative oceanographic experiment was conducted offshore of Marineland, Florida, in December 1975. The primary objectives of this experiment were to determine whether the proposed Seasat SAR could detect waves, and to better understand the SAR imaging mechanism by measuring surface waves coincident with the SAR flights. In addition to the ERIM X-L SAR, the NASA JPL CV-990 L-band SAR also participated. More complete descriptions of the Marineland Experiment are given elsewhere (Shemdin, 1980; Shuchman, et al., 1977; Shemdin, et al., 1978; and McLeish, et al., 1980).

Multi-sided data collection patterns were flown by the ERIM X-L SAR on the 3rd, 4th, 10th, 14th, and 15th of December. During these flights, 69 passes of SAR data were collected. Except for the flights on the 4th and 10th, surface wind and wave measurements by a pitch-and-roll buoy were made coincident with SAR data collection.

TABLE 4  
EXAMPLE SUMMARY OF SEASAT SAR OPERATING PARAMETERS AND  
ENVIRONMENTAL CONDITIONS DURING THE 1978 JASIN EXPERIMENT

1	2	3	4	5	6	7	8	9	10	11	12	13	14	15	16	17	18	
547.	321.	7000.	2625000.	840000.	2	1	1	1	60	170	83.	3	60	15.	1	3	0	0
556.	216.	7000.	2625000.	840000.	2	1	1	1	50	151	100	3	00	30	1	2	0	0
590.	323.	7000.	2625000.	840000.	2	1	1	1	20	222	70	6	60	10	2	1	0	0
599.	215.	7000.	2625000.	840000.	2	1	1	1	10	71.	200	6	20	14	2	1	0	0
633.	323.	7000.	2625000.	840000.	2	1	1	1	10	89.	40	7	90	150	2	1	0	0
642.	214.	7000.	2625000.	840000.	2	1	1	2	70	169	20	10	90	160	2	1	0	0
714.	217.	7000.	2625000.	840000.	2	1	1	0	0	-0	-0	-0	0	-0	-0	1	2	0
719.	323.	7000.	2625000.	840000.	2	1	1	0	0	-0	-0	-0	0	-0	-0	1	2	0
757.	215.	7000.	2625000.	840000.	2	1	1	4	90	256.	60	-0	0	-0.	1	2	0	0
762.	324.	7000.	2625000.	840000.	2	1	1	5	50	210.	60	7	20	164	1	3	0	0
791.	325.	7000.	2625000.	840000.	2	1	1	3	10	151	50.	4	00	224.	1	3	0	0
834.	324.	7000.	2625000.	840000.	2	1	1	2	80	147.	115.	7	80	280.	1	2	0	0
958.	215.	7000.	2625000.	840000.	2	1	1	1	40	108.	174.	-0	0	-0.	1	2	0	0
1001.	219.	7000.	2625000.	840000.	2	1	1	2	30	63.	335.	10	70	120.	1	2	0	0
1006.	322.	7000.	2625000.	840000.	2	1	1	3	60	105.	289.	11	90	120.	2	1	0	0
1044.	220.	7000.	2625000.	840000.	2	1	1	5	70	244.	84.	-0	0	-0.	1	3	0	0
1049.	323.	7000.	2625000.	840000.	2	1	1	5	00	244.	84.	-0	0	-0.	1	3	0	0
1087.	221.	7000.	2625000.	840000.	2	1	1	0	0	-0.	-0.	-0	0	-0.	1	3	0	0
1	AIRCRAFT PASS OR SATELLITE REVOLUTION																	
2	AIRCRAFT OR SATELLITE HEADING (°TRUE)																	
3	AIRCRAFT OR SATELLITE VELOCITY (M/S)																	
4	AIRCRAFT OR SATELLITE ALTITUDE (FT ABOVE SEA LEVEL)																	
5	RANGE DISTANCE TO NEAR EDGE OF RADAR COVERAGE (M)																	
6	RADAR WAVELENGTH (1=X-BAND; 2=L-BAND)																	
7	TRANSMITTED POLARIZATION (1=HORIZONTAL; 2=VERTICAL)																	
8	RECEIVED POLARIZATION (1=HORIZONTAL; 2=VERTICAL)																	
9	SIGNIFICANT WAVE HEIGHT (M)																	
10	DOMINANT WAVELENGTH (M)																	
11	DOMINANT WAVE DIRECTION (°TRUE)																	
12	WIND SPEED (M/S)																	
13	WIND DIRECTION (°TRUE)																	
14	WAVES PRESENT IN IMAGERY? (0=NO DATA, 1=YES, 2=NO)																	
15	WAVE DETECTABILITY AT 20° INCIDENCE ANGLE (0=NO DATA, 1=NOT DETECTED, 2=DETECTED, 3=CLEARLY DETECTED)																	
16	WAVE DETECTABILITY AT 40° INCIDENCE ANGLE (0=NO DATA, 1=NOT DETECTED, 2=DETECTED, 3=CLEARLY DETECTED)																	
17	WAVE DETECTABILITY AT 60° INCIDENCE ANGLE (0=NO DATA, 1=NOT DETECTED, 2=DETECTED, 3=CLEARLY DETECTED)																	
18	WAVE DETECTABILITY AT 80° INCIDENCE ANGLE (0=NO DATA, 1=NOT DETECTED, 2=DETECTED, 3=CLEARLY DETECTED)																	

TABLE 5  
SUMMARY OF SAR OCEAN WAVE EXPERIMENTS

Name	Flight Date (s)	SAR System	Number of Passes or Overflights	Range of Conditions		
				H 1/3 (m)	$\lambda$ (m)	Wind (m/s)
Marineland	December 1975	ERIM X-L	69	1-1.56	80-131	1.5-5.5
Lake Michigan	6 October 1977	ERIM X-L	2	1.03	49	6.0
JASIN	August-September 1978	Seasat	18	1.1-5.7	63-256	3.0-11.9
GOASEX	September 1978	ERIM X-L	35	1.1-3.7	130-177	5.1-11.8
		Seasat	5	1.1-3.6	130-256	3.8-11.8
Lake Michigan	18 October 1978	ERIM X-L	2	0.95	54	8.7
MARSEN	September 1979	APD-10	39	1-1.2	35-100	3.5-11.8

A summary of the ERIM X- and L-band SAR operating parameters and environmental conditions are presented in Table 6 for 3 December 1975. In each of the 9 passes where X-band data was available, waves were imaged at some location within the swath. The L-band channel failed to image waves in 5 of the 10 passes where data was available. Included in these 5, were 4 passes in which vertically polarized signals were transmitted.

The ERIM X- and L-band SAR operating parameters and environmental conditions for 4 December 1975 are summarized in Table 7. Surface wind and wave measurements were not performed on this day. Waves were visible in all 10 X-band passes and in 9 of the 10 L-band passes. Waves were not detected for either wavelength at 60° incidence angle. In addition, waves at 20° incidence angle were only visible in 2 of the 10 L-band passes.

Presented in Table 8 is a summary of the ERIM X- and L-band SAR operating parameters for 10 December 1975. Surface wind and wave measurements are unavailable for this day. In each of the 13 passes studied, the X-band data imaged waves at some location within the swath. The L-band data contained wave images in only 5 of the 13 passes. The SAR imaging geometry and flight lines were identical to those on the 3rd and 4th.

The ERIM X- and L-band SAR operating parameters and environmental conditions for 14 December 1975 are summarized in Table 9. In each of the 16 X-band passes, waves were visible. In the 4 L-band passes which failed to produce wave imagery, the surface waves were traveling in the azimuth direction relative to the radar line-of-sight. X- and L-band digitally-processed directional spectra from the first 8 passes of this data set have been rigorously compared (Shuchman, et al., 1983). A copy of this article is included in the Appendix.

The data presented in Table 10 summarize the ERIM X- and L-band SAR operating parameters and environmental conditions for 15 December

TABLE 6  
SUMMARY OF ERIM X-L SAR OPERATING PARAMETERS AND  
ENVIRONMENTAL CONDITIONS FOR 3 DECEMBER 1975

	1	2	3	4	5	6	7	8	9	10	11	12	13	14	15	16	17	18
1	160	90	13250	4040	1 1 1	1 00	131	262	5 50 360	0	0	0	0	0	0	0	0	0
2	250	77	13250	4040	1 1 1	1 00	131	262	5 50 360	1	2	2	1	0	0	0	0	0
3	70	88	13250	4040	1 1 1	1 00	131	262	5 50 360	1	3	3	1	0	0	0	0	0
4	340	80	13250	4040	1 1 1	1 00	131	262	5 50 360	1	0	3	1	0	0	0	0	0
5	160	89	13250	4040	1 2 2	1 00	131	262	5 50 360	1	2	3	0	0	0	0	0	0
6	250	77	13250	4040	1 2 2	1 00	131	262	5 50 360	1	3	3	1	0	0	0	0	0
7	70	89	13250	4040	1 2 2	1 00	131	262	5 50 360	1	3	3	2	0	0	0	0	0
8	340	81	13250	4040	1 2 2	1 00	131	262	5 50 360	1	0	3	1	0	0	0	0	0
9	160	91	13250	4040	1 1 1	1 00	131	262	5 50 360	1	3	3	0	0	0	0	0	0
10	340	80	13250	4040	1 1 1	1 00	131	262	5 50 360	1	0	3	1	0	0	0	0	0
1	160	90	13250	4040	2 1 1	1 00	131	262	5 50 360	1	2	2	0	0	0	0	0	0
2	250	77	13250	4040	2 1 1	1 00	131	262	5 50 360	1	2	2	0	0	0	0	0	0
3	70	88	13250	4040	2 1 1	1 00	131	262	5 50 360	2	1	1	1	0	0	0	0	0
4	340	80	13250	4040	2 1 1	1 00	131	262	5 50 360	2	1	1	1	0	0	0	0	0
5	160	89	13250	4040	2 2 2	1 00	131	262	5 50 360	2	1	1	1	0	0	0	0	0
6	250	77	13250	4040	2 2 2	1 00	131	262	5 50 360	2	1	1	1	0	0	0	0	0
7	70	89	13250	4040	2 2 2	1 00	131	262	5 50 360	2	1	1	1	0	0	0	0	0
8	340	81	13250	4040	2 2 2	1 00	131	262	5 50 360	2	0	1	1	0	0	0	0	0
9	160	91	13250	4040	2 1 1	1 00	131	262	5 50 360	1	1	1	2	0	0	0	0	0
10	340	80	13250	4040	2 1 1	1 00	131	262	5 50 360	1	0	2	1	0	0	0	0	0

1. AIRCRAFT PASS OR SATELLITE REVOLUTION

2. AIRCRAFT OR SATELLITE HEADING (°TRUE)

3. AIRCRAFT OR SATELLITE VELOCITY (M/S)

4. AIRCRAFT OR SATELLITE ALTITUDE (FT ABOVE SEA LEVEL)

5. RANGE DISTANCE TO NEAR EDGE OF RADAR COVERAGE (M)

6. RADAR WAVELENGTH (1=X-BAND; 2=L-BAND)

7. TRANSMITTED POLARIZATION (1=HORIZONTAL; 2=VERTICAL)

8. RECEIVED POLARIZATION (1=HORIZONTAL; 2=VERTICAL)

9. SIGNIFICANT WAVE HEIGHT (M)

10. DOMINANT WAVELENGTH (M)

11. DOMINANT WAVE DIRECTION (°TRUE)

12. WIND SPEED (M/S)

13. WIND DIRECTION (°TRUE)

14. WAVES PRESENT IN IMAGERY? (0=NO DATA; 1=YES; 2=NO)

15. WAVE DETECTABILITY AT 20° INCIDENCE ANGLE (0=NO DATA; 1=NOT DETECTED; 2=DETECTED; 3=CLEARLY DETECTED)

16. WAVE DETECTABILITY AT 40° INCIDENCE ANGLE (0=NO DATA; 1=NOT DETECTED; 2=DETECTED; 3=CLEARLY DETECTED)

17. WAVE DETECTABILITY AT 60° INCIDENCE ANGLE (0=NO DATA; 1=NOT DETECTED; 2=DETECTED; 3=CLEARLY DETECTED)

18. WAVE DETECTABILITY AT 80° INCIDENCE ANGLE (0=NO DATA; 1=NOT DETECTED; 2=DETECTED; 3=CLEARLY DETECTED)



TABLE 7  
SUMMARY OF ERIM X-L SAR OPERATING PARAMETERS AND  
ENVIRONMENTAL CONDITIONS FOR 4 DECEMBER 1975

1	2	3	4	5	6	7	8	9	10	11	12	13	14	15	16	17	18
1.	70.	86.	12780.	3900.	1	1	1	-0.0	-0.	-0.	-0.0	-0.	1	3	3	1	0
2.	250.	85.	12780.	3900.	1	1	1	-0.0	-0.	-0.	-0.0	-0.	1	3	3	1	0
3.	70.	84.	12780.	3900.	1	1	1	-0.0	-0.	-0.	-0.0	-0.	1	3	3	1	0
4.	205.	88.	12780.	3900.	1	1	1	-0.0	-0.	-0.	-0.0	-0.	1	3	3	1	0
5.	340.	80.	12780.	3900.	1	1	1	-0.0	-0.	-0.	-0.0	-0.	1	0	3	1	0
6.	115.	91.	12780.	3900.	1	1	1	-0.0	-0.	-0.	-0.0	-0.	1	3	3	1	0
7.	250.	82.	12780.	3900.	1	1	1	-0.0	-0.	-0.	-0.0	-0.	1	3	3	1	0
8.	25.	85.	12780.	3900.	1	1	1	-0.0	-0.	-0.	-0.0	-0.	1	3	3	1	0
9.	160.	92.	12780.	3900.	1	1	1	-0.0	-0.	-0.	-0.0	-0.	1	3	3	1	0
10.	295.	85.	12780.	3900.	1	1	1	-0.0	-0.	-0.	-0.0	-0.	1	3	3	1	0
1.	70.	86.	12780.	3900.	2	1	1	-0.0	-0.	-0.	-0.0	-0.	2	1	1	1	0
2.	250.	85.	12780.	3900.	2	1	1	-0.0	-0.	-0.	-0.0	-0.	1	2	2	1	0
3.	70.	84.	12780.	3900.	2	1	1	-0.0	-0.	-0.	-0.0	-0.	1	1	2	1	0
4.	205.	88.	12780.	3900.	2	1	1	-0.0	-0.	-0.	-0.0	-0.	1	1	2	1	0
5.	340.	80.	12780.	3900.	2	1	1	-0.0	-0.	-0.	-0.0	-0.	1	0	2	1	0
6.	115.	91.	12780.	3900.	2	1	1	-0.0	-0.	-0.	-0.0	-0.	1	1	2	1	0
7.	250.	82.	12780.	3900.	2	1	1	-0.0	-0.	-0.	-0.0	-0.	1	2	2	1	0
8.	25.	85.	12780.	3900.	2	1	1	-0.0	-0.	-0.	-0.0	-0.	1	1	2	1	0
9.	160.	92.	12780.	3900.	2	1	1	-0.0	-0.	-0.	-0.0	-0.	1	1	2	1	0
10.	295.	85.	12780.	3900.	2	1	1	-0.0	-0.	-0.	-0.0	-0.	1	1	2	1	0

- 1 AIRCRAFT PASS OR SATELLITE REVOLUTION
- 2 AIRCRAFT OR SATELLITE HEADING (°TRUE)
- 3 AIRCRAFT OR SATELLITE VELOCITY (M/S)
- 4 AIRCRAFT OR SATELLITE ALTITUDE (FT ABOVE SEA LEVEL)
- 5 RANGE DISTANCE TO NEAR EDGE OF RADAR COVERAGE (M)
- 6 RADAR WAVELENGTH (1=X-BAND; 2=L-BAND)
- 7 TRANSMITTED POLARIZATION (1=HORIZONTAL; 2=VERTICAL)
- 8 RECEIVED POLARIZATION (1=HORIZONTAL; 2=VERTICAL)
- 9 SIGNIFICANT WAVE HEIGHT (M)
- 10 DOMINANT WAVELENGTH (M)
- 11 DOMINANT WAVE DIRECTION (°TRUE)
- 12 WIND SPEED (M/S)
- 13 WIND DIRECTION (°TRUE)
- 14 WAVES PRESENT IN IMAGERY? (0=NO DATA; 1=YES; 2=NO)
- 15 WAVE DETECTABILITY AT 20° INCIDENCE ANGLE (0=NO DATA; 1=NOT DETECTED; 2=DETECTED; 3=CLEARLY DETECTED)
- 16 WAVE DETECTABILITY AT 40° INCIDENCE ANGLE (0=NO DATA; 1=NOT DETECTED; 2=DETECTED; 3=CLEARLY DETECTED)
- 17 WAVE DETECTABILITY AT 60° INCIDENCE ANGLE (0=NO DATA; 1=NOT DETECTED; 2=DETECTED; 3=CLEARLY DETECTED)
- 18 WAVE DETECTABILITY AT 80° INCIDENCE ANGLE (0=NO DATA; 1=NOT DETECTED; 2=DETECTED; 3=CLEARLY DETECTED)

TABLE 8  
SUMMARY OF ERM X-L SAR OPERATING PARAMETERS AND  
ENVIRONMENTAL CONDITIONS FOR 10 DECEMBER 1975

1	2	3	4	5	6	7	8	9	10	11	12	13	14	15	16	17	18
3	70	102	13200	4020	1	1	1	-0	0	-0	-0	0	1	3	3	2	0
4	205	77	13200	4020	1	1	1	-0	0	-0	-0	0	1	3	3	2	0
5	340	69	13200	4020	1	1	1	-0	0	-0	-0	0	1	3	2	1	0
6	115	109	13200	4020	1	1	1	-0	0	-0	-0	0	1	2	3	2	0
7	250	69	13200	4020	1	1	1	-0	0	-0	-0	0	1	3	3	1	0
9	70	99	13200	4020	1	1	1	-0	0	-0	-0	0	1	2	3	1	0
10	205	89	13200	4020	1	1	1	-0	0	-0	-0	0	1	2	1	1	0
11	340	53	13200	4020	1	1	1	-0	0	-0	-0	0	1	0	2	1	0
12	115	117	13200	4020	1	1	1	-0	0	-0	-0	0	1	2	2	1	0
13	250	64	13200	4020	1	1	1	-0	0	-0	-0	0	1	2	3	1	0
14	25	65	13200	4020	1	1	1	-0	0	-0	-0	0	1	2	2	1	0
15	160	116	13200	4020	1	1	1	-0	0	-0	-0	0	1	1	2	0	0
16	295	50	13200	4020	1	1	1	-0	0	-0	-0	0	1	2	2	1	0
3	70	102	13200	4020	2	1	1	-0	0	-0	-0	0	1	2	2	1	0
4	205	77	13200	4020	2	1	1	-0	0	-0	-0	0	1	2	2	1	0
5	340	69	13200	4020	2	1	1	-0	0	-0	-0	0	2	1	1	1	0
6	115	109	13200	4020	2	1	1	-0	0	-0	-0	0	1	2	2	1	0
7	250	69	13200	4020	2	1	1	-0	0	-0	-0	0	1	2	2	1	0
9	70	99	13200	4020	2	1	1	-0	0	-0	-0	0	2	1	1	1	0
10	205	89	13200	4020	2	1	1	-0	0	-0	-0	0	2	1	1	1	0
11	340	53	13200	4020	2	1	1	-0	0	-0	-0	0	2	0	1	1	0
12	115	117	13200	4020	2	1	1	-0	0	-0	-0	0	2	1	1	1	0
13	250	64	13200	4020	2	1	1	-0	0	-0	-0	0	2	1	1	0	0
14	25	65	13200	4020	2	1	1	-0	0	-0	-0	0	2	1	1	1	0
15	160	116	13200	4020	2	1	1	-0	0	-0	-0	0	2	1	1	0	0
16	295	50	13200	4020	2	1	1	-0	0	-0	-0	0	2	1	1	0	0
1 AIRCRAFT PASS OR SATELLITE REVOLUTION																	
2 AIRCRAFT OR SATELLITE HEADING (°TRUE)																	
3 AIRCRAFT OR SATELLITE VELOCITY (M/S)																	
4 AIRCRAFT OR SATELLITE ALTITUDE (FT ABOVE SEA LEVEL)																	
5 RANGE DISTANCE TO NEAR EDGE OF RADAR COVERAGE (M)																	
6 RADAR WAVELENGTH (1=X BAND; 2=L-BAND)																	
7 TRANSMITTED POLARIZATION (1=HORIZONTAL; 2=VERTICAL)																	
8 RECEIVED POLARIZATION (1=HORIZONTAL; 2=VERTICAL)																	
9 SIGNIFICANT WAVE HEIGHT (M)																	
10 DOMINANT WAVELENGTH (M)																	
11 DOMINANT WAVE DIRECTION (°TRUE)																	
12 WIND SPEED (M/S)																	
13 WIND DIRECTION (°TRUE)																	
14 WAVES PRESENT IN IMAGERY? (0=NO DATA; 1=YES; 2=NO)																	
15 WAVE DETECTABILITY AT 20° INCIDENCE ANGLE (0=NO DATA; 1=NOT DETECTED; 2=DETECTED; 3=CLEARLY DETECTED)																	
16 WAVE DETECTABILITY AT 40° INCIDENCE ANGLE (0=NO DATA; 1=NOT DETECTED; 2=DETECTED; 3=CLEARLY DETECTED)																	
17 WAVE DETECTABILITY AT 60° INCIDENCE ANGLE (0=NO DATA; 1=NOT DETECTED; 2=DETECTED; 3=CLEARLY DETECTED)																	
18 WAVE DETECTABILITY AT 80° INCIDENCE ANGLE (0=NO DATA; 1=NOT DETECTED; 2=DETECTED; 3=CLEARLY DETECTED)																	

TABLE 9  
SUMMARY OF ERIM X-L SAR OPERATING PARAMETERS AND  
ENVIRONMENTAL CONDITIONS FOR 14 DECEMBER 1975

1	2	3	4	5	6	7	8	9	10	11	12	13	14	15	16	17	18
1.	70.	78.	13200	4020.	1	1	1	1.56	80.	256.	3.00	90.	1	3	3	1	0
2.	205.	83.	13200	4020.	1	1	1	1.56	80.	265.	3.00	90.	1	3	3	1	0
3.	340.	86.	13200	4020.	1	1	1	1.56	80.	265.	3.00	90.	1	0	3	1	0
4.	115.	76.	13200.	4020.	1	1	1	1.56	80.	265.	3.00	90.	1	3	3	1	0
5.	250.	86.	13200.	4020.	1	1	1	1.56	80.	265.	3.00	90.	1	3	3	1	0
6.	25.	81.	13200.	4020.	1	1	1	1.56	80.	265.	3.00	90.	1	3	3	1	0
7.	160.	81.	13200.	4020.	1	1	1	1.56	80.	265.	3.00	90.	1	3	3	0	0
8.	295.	89.	13200.	4020.	1	1	1	1.56	80.	265.	3.00	90.	1	3	3	1	0
9.	70.	77.	13200.	4020.	1	1	1	1.56	80.	265.	3.00	90.	1	3	3	1	0
10.	250.	87.	13200.	4020.	1	1	1	1.56	80.	265.	3.00	90.	1	3	3	2	0
11.	70.	80.	13200.	4020.	1	1	1	1.56	80.	265.	3.00	90.	1	3	3	1	0
12.	205.	87.	13200.	4020.	1	1	1	1.56	80.	265.	3.00	90.	1	3	3	1	0
13.	340.	89.	13200.	4020.	1	1	1	1.56	80.	265.	3.00	90.	1	0	3	1	0
14.	115.	82.	13200.	4020.	1	1	1	1.56	80.	265.	3.00	90.	1	3	3	1	0
15.	250.	87.	13200.	4020.	1	1	1	1.56	80.	265.	3.00	90.	1	3	3	1	0
16.	340.	87.	13200.	4020.	1	1	1	1.56	80.	265.	3.00	90.	1	0	3	1	0
1.	70.	78.	13200.	4020.	2	1	1	1.56	80.	265.	3.00	90.	1	1	2	2	0
2.	205.	83.	13200.	4020.	2	1	1	1.56	80.	265.	3.00	90.	1	1	3	3	0
3.	340.	86.	13200.	4020.	2	1	1	1.56	80.	265.	3.00	90.	1	0	3	3	0
4.	115.	76.	13200.	4020.	2	1	1	1.56	80.	265.	3.00	90.	2	1	1	1	1
5.	250.	86.	13200.	4020.	2	1	1	1.56	80.	265.	3.00	90.	1	2	2	1	0
6.	25.	81.	13200.	4020.	2	1	1	1.56	80.	265.	3.00	90.	1	3	3	0	0
7.	160.	81.	13200.	4020.	2	1	1	1.56	80.	265.	3.00	90.	1	1	3	0	0
8.	295.	89.	13200.	4020.	2	1	1	1.56	80.	265.	3.00	90.	2	1	3	2	0
9.	70.	77.	13200.	4020.	2	1	1	1.56	80.	265.	3.00	90.	2	1	3	2	0
10.	250.	87.	13200.	4020.	2	1	1	1.56	80.	265.	3.00	90.	1	2	3	2	0
11.	70.	80.	13200.	4020.	2	1	1	1.56	80.	265.	3.00	90.	2	1	1	1	0
12.	205.	87.	13200.	4020.	2	1	1	1.56	80.	265.	3.00	90.	1	2	2	1	0
13.	340.	89.	13200.	4020.	2	1	1	1.56	80.	265.	3.00	90.	1	0	3	2	0
14.	115.	82.	13200.	4020.	2	1	1	1.56	80.	265.	3.00	90.	2	1	1	1	0
15.	250.	87.	13200.	4020.	2	1	1	1.56	80.	265.	3.00	90.	1	2	2	1	0
16.	340.	87.	13200.	4020.	2	1	1	1.56	80.	265.	3.00	90.	1	0	3	2	0

- 1 AIRCRAFT PASS OR SATELLITE REVOLUTION
- 2 AIRCRAFT OR SATELLITE HEADING (°TRUE)
- 3 AIRCRAFT OR SATELLITE VELOCITY (M/S)
- 4 AIRCRAFT OR SATELLITE ALTITUDE (FT ABOVE SEA LEVEL)
- 5 RANGE DISTANCE TO NEAR EDGE OF RADAR COVERAGE (M)
- 6 RADAR WAVELENGTH (1=X-BAND; 2=L-BAND)
- 7 TRANSMITTED POLARIZATION (1=HORIZONTAL; 2=VERTICAL)
- 8 RECEIVED POLARIZATION (1=HORIZONTAL; 2=VERTICAL)
- 9 SIGNIFICANT WAVE HEIGHT (M)
- 10 DOMINANT WAVELENGTH (M)
- 11 DOMINANT WAVE DIRECTION (°TRUE)
- 12 WIND SPEED (M/S)
- 13 WIND DIRECTION (°TRUE)
- 14 WAVES PRESENT IN IMAGERY? (0=NO DATA, 1=YES, 2=NO)
- 15 WAVE DETECTABILITY AT 20° INCIDENCE ANGLE (0=NO DATA, 1=NOT DETECTED, 2=DETECTED, 3=CLEARLY DETECTED)
- 16 WAVE DETECTABILITY AT 40° INCIDENCE ANGLE (0=NO DATA, 1=NOT DETECTED, 2=DETECTED, 3=CLEARLY DETECTED)
- 17 WAVE DETECTABILITY AT 60° INCIDENCE ANGLE (0=NO DATA, 1=NOT DETECTED, 2=DETECTED, 3=CLEARLY DETECTED)
- 18 WAVE DETECTABILITY AT 80° INCIDENCE ANGLE (0=NO DATA, 1=NOT DETECTED, 2=DETECTED, 3=CLEARLY DETECTED)

TABLE 10  
SUMMARY OF ERM X-L SAR OPERATING PARAMETERS AND  
ENVIRONMENTAL CONDITIONS FOR 15 DECEMBER 1975

1	2	3	4	5	6	7	8	9	10	11	12	13	14	15	16	17	18	
1	70	90	13475	4110	1	1	1	1	30	131	272	1	50	90	1	2	1	0
2	205	75	13475	4110	1	1	1	1	30	131	272	1	50	90	1	3	3	1
3	340	84	13475	4110	1	1	1	1	30	131	272	1	50	90	1	0	3	1
4	115	86	13475	4110	1	1	1	1	30	131	272	1	50	90	1	3	3	2
5	250	75	13475	4110	1	1	1	1	30	131	272	1	50	90	1	3	3	1
6	25	90	13475	4110	1	1	1	1	30	131	272	1	50	90	1	3	3	1
7	160	84	13475	4110	1	1	1	1	30	131	272	1	50	90	1	2	3	0
8	295	80	13475	4110	1	1	1	1	30	131	272	1	50	90	1	3	3	1
9	70	92	13475	4110	1	1	1	1	30	131	272	1	50	90	1	3	3	1
10	205	77	13475	4110	1	1	1	1	30	131	272	1	50	90	1	3	3	2
11	340	85	13475	4110	1	1	1	1	30	131	272	1	50	90	1	3	3	2
12	115	88	13475	4110	1	1	1	1	30	131	272	1	50	90	1	3	3	2
13	250	76	13475	4110	1	1	1	1	30	131	272	1	50	90	1	3	3	1
14	250	77	13475	4110	1	1	1	1	30	131	272	1	50	90	1	3	3	2
15	70	92	13475	4110	1	1	1	1	30	131	272	1	50	90	1	2	3	1
16	340	81	13475	4110	1	1	1	1	30	131	272	1	50	90	1	0	2	1
17	160	81	13475	4110	1	2	2	1	30	131	272	1	50	90	1	2	2	0
1	70	90	13475	4110	2	1	1	1	30	131	272	1	50	90	1	2	2	0
2	205	75	13475	4110	2	1	1	1	30	131	272	1	50	90	1	2	2	0
3	340	84	13475	4110	2	1	1	1	30	131	272	1	50	90	1	0	3	2
4	115	86	13475	4110	2	1	1	1	30	131	272	1	50	90	1	1	2	1
5	250	75	13475	4110	2	1	1	1	30	131	272	1	50	90	1	2	2	1
6	25	90	13475	4110	2	1	1	1	30	131	272	1	50	90	1	2	2	0
7	160	84	13475	4110	2	1	1	1	30	131	272	1	50	90	1	1	2	0
8	295	80	13475	4110	2	1	1	1	30	131	272	1	50	90	1	2	2	1
9	70	92	13475	4110	2	1	1	1	30	131	272	1	50	90	1	2	3	0
10	205	77	13475	4110	2	1	1	1	30	131	272	1	50	90	1	2	3	3
11	340	85	13475	4110	2	1	1	1	30	131	272	1	50	90	1	2	3	3
12	115	88	13475	4110	2	1	1	1	30	131	272	1	50	90	1	2	3	2
13	250	76	13475	4110	2	1	1	1	30	131	272	1	50	90	1	3	3	2
14	250	77	13475	4110	2	1	1	1	30	131	272	1	50	90	1	3	3	2
15	70	92	13475	4110	2	1	1	1	30	131	272	1	50	90	1	2	2	1
16	340	81	13475	4110	2	1	1	1	30	131	272	1	50	90	1	0	0	0
1	70	90	13475	4110	2	1	1	1	30	131	272	1	50	90	1	0	0	0
1 AIRCRAFT PASS OR SATELLITE REVOLUTION																		
2 AIRCRAFT OR SATELLITE HEADING (TRUE)																		
3 AIRCRAFT OR SATELLITE VELOCITY (M/S)																		
4 AIRCRAFT OR SATELLITE ALTITUDE (FT ABOVE SEA LEVEL)																		
5 RANGE DISTANCE TO NEAR EDGE OF RADAR COVERAGE (M)																		
6 RADAR WAVELENGTH (1=X BAND, 2=L BAND)																		
7 TRANSMITTED POLARIZATION (1=HORIZONTAL, 2=VERTICAL)																		
8 RECEIVED POLARIZATION (1=HORIZONTAL, 2=VERTICAL)																		
9 SIGNIFICANT WAVE HEIGHT (M)																		
10 DOMINANT WAVELENGTH (M)																		
11 DOMINANT WAVE DIRECTION (TRUE)																		
12 WIND SPEED (M/S)																		
13 WIND DIRECTION (TRUE)																		
14 WAVE% PRESENT IN IMAGERY? (0=NO DATA, 1=YES, 2=NO)																		
15 WAVE DETECTABILITY AT 20° INCIDENCE ANGLE (0=NO DATA, 1=NOT DETECTED, 2=DETECTED, 3=CLEARLY DETECTED)																		
16 WAVE DETECTABILITY AT 40° INCIDENCE ANGLE (0=NO DATA, 1=NOT DETECTED, 2=DETECTED, 3=CLEARLY DETECTED)																		
17 WAVE DETECTABILITY AT 60° INCIDENCE ANGLE (0=NO DATA, 1=NOT DETECTED, 2=DETECTED, 3=CLEARLY DETECTED)																		
18 WAVE DETECTABILITY AT 80° INCIDENCE ANGLE (0=NO DATA, 1=NOT DETECTED, 2=DETECTED, 3=CLEARLY DETECTED)																		

1975. In each of the 17 X-band and the 14 available L-band passes, waves were visible. This is somewhat surprising when compared to the 14th data since the wave height was smaller and the wind speeds were less on the 15th. One possible explanation for the non-imaging of azimuth-travelling waves on the 14th, is the degradation of azimuth resolution due to orbital acceleration effects. The larger heights and shorter lengths of the waves on the 14th cause a greater degradation in azimuth resolution than for the lower amplitude, longer waves on the 15th. The SAR data collected on the 15th were analyzed in detail in a previous study (Shuchman and Shemdin, 1983). A reprint of this article is included in the Appendix.

### 3.1.2 LAKE MICHIGAN 1977

On 6 October 1977, the ERIM X- and L-band SAR system collected two passes of data during a flight over Lake Michigan between Muskegon, Michigan, and Milwaukee, Wisconsin. At the time of the flight, surface wind and wave measurements were made from a research tower and a waverider buoy operated by the National Oceanic and Atmospheric Administration's (NOAA's) Great Lakes Environmental Research Laboratory (GLERL).

A summary of the ERIM X- and L-band SAR operating parameters and environmental conditions is presented in Table 11 for 6 October 1977. In both passes, waves were visible on both the X- and L-band imagery. Due to the limited fetch of Lake Michigan, these waves were wind-generated rather than swell. In both passes, the waves were more detectable on the X-band imagery than the L-band imagery. A more detailed comparison between the SAR-derived and surface-measured wave spectra has been performed on this data and is reported by Schwab, et al. (1981). A reprint of this paper is included in the Appendix.

TABLE 11  
SUMMARY OF ERIM X-L SAR OPERATING PARAMETERS AND  
ENVIRONMENTAL CONDITIONS FOR 6 OCTOBER 1977

	1	2	3	4	5	6	7	8	9	10	11	12	13	14	15	16	17	18
1																		
2																		
3		270	80	8500	3300	1	1	1	1	03	49	150	6 00 330	1	0	3	3	0
4		90	97	9500	3900	1	2	2	1	03	49	150	6 00 330	1	0	3	3	0
3		270	80	8500	3300	2	1	1	1	03	49	150	6 00 330	1	0	2	2	0
4		90	97	9500	3900	2	2	2	1	03	49	150	6 00 330	1	0	2	3	0
1	AIRCRAFT PASS OR SATELLITE REVOLUTION																	
2	AIRCRAFT OR SATELLITE HEADING (°TRUE)																	
3	AIRCRAFT OR SATELLITE VELOCITY (M/S)																	
4	AIRCRAFT OR SATELLITE ALTITUDE (FT ABOVE SEA LEVEL)																	
5	RANGE DISTANCE TO NEAR EDGE OF RADAR COVERAGE (M)																	
6	RADAR WAVELENGTH (1=X-BAND; 2=L-BAND)																	
7	TRANSMITTED POLARIZATION (1=HORIZONTAL; 2=VERTICAL)																	
8	RECEIVED POLARIZATION (1=HORIZONTAL; 2=VERTICAL)																	
9	SIGNIFICANT WAVE HEIGHT (M)																	
10	DOMINANT WAVELENGTH (M)																	
11	DOMINANT WAVE DIRECTION (°TRUE)																	
12	WIND SPEED (M/S)																	
13	WIND DIRECTION (°TRUE)																	
14	WAVES PRESENT IN IMAGERY? (0=NO DATA; 1=YES; 2=NO)																	
15	WAVE DETECTABILITY AT 20° INCIDENCE ANGLE (0=NO DATA; 1=NOT DETECTED; 2=DETECTED; 3=CLEARLY DETECTED)																	
16	WAVE DETECTABILITY AT 40° INCIDENCE ANGLE (0=NO DATA; 1=NOT DETECTED; 2=DETECTED; 3=CLEARLY DETECTED)																	
17	WAVE DETECTABILITY AT 60° INCIDENCE ANGLE (0=NO DATA; 1=NOT DETECTED; 2=DETECTED; 3=CLEARLY DETECTED)																	
18	WAVE DETECTABILITY AT 80° INCIDENCE ANGLE (0=NO DATA; 1=NOT DETECTED; 2=DETECTED; 3=CLEARLY DETECTED)																	

### 3.1.3 JASIN

Seasat SAR images were obtained on 18 separate occasions over the North Atlantic in conjunction with the Joint Air-Sea Interaction (JASIN) Experiment during the late summer of 1978. Simultaneously with most of the Seasat overpasses, surface measurements including wave height, wavelength, wave direction, and wind speed and direction were performed by personnel aboard oceanographic research vessels and wave buoys deployed within the study area. More detailed descriptions of the JASIN Seasat Experiment are available (Allan and Guymer, 1980; Allan and Guymer, 1984).

The Seasat SAR operating parameters and environmental conditions for the 18 overpasses in the late summer of 1978 in support of the JASIN Experiment are summarized in Table 12. A wide range of environmental conditions were present during the 18 passes including: wave heights ranging from 1.1 to 5.7 meters, wavelengths from 63 to 256 meters, and wind speeds of 3.0 to 11.9 m/s. Of the 18 passes, waves were visible in 13. More detailed studies have been performed using this data set (Kasischke, 1980; Vesecky, et al., 1982). A reprint of the Vesecky, et al. paper is included in the Appendix.

### 3.1.4 GOASEX

The Gulf of Alaska Seasat Experiment (GOASEX) was conducted in September 1978 in the Northeast Pacific. This experiment provided surface wave measurements coincident with aircraft and satellite SAR imagery. Seasat L-band SAR imagery was collected during five overpasses of the test area. In addition, the ERIM X- and L-band SAR system collected data during multi-sided flight patterns on the 22nd, 23rd, 25th, and 26th of September. The total number of aircraft passes was 35. During the SAR data collection, surface wind and wave measurements were performed by pitch-and-roll and NOAA data buoys. A more detailed description of the GOASEX Experiment is given by Gonzalez, et al. (1979).

TABLE 12  
SUMMARY OF SEASAT SAR OPERATING PARAMETERS AND  
ENVIRONMENTAL CONDITIONS DURING THE 1978 JASIN EXPERIMENT

1	2	3	4	5	6	7	8	9	10	11	12	13	14	15	16	17	18
547.	321.	7000	2625000.	840000.	2	1	1	1.60	170.	83.	3.60	15.	1	3	0	0	0
556.	216	7000	2625000.	840000.	2	1	1	1.50	151.	100.	3.00	30.	1	2	0	0	0
590	323.	7000	2625000.	840000.	2	1	1	1.20	222.	70.	6.60	10.	2	1	0	0	0
599.	215	7000	2625000.	840000.	2	1	1	1.10	71.	200.	6.20	14.	2	1	0	0	0
633.	323	7000	2625000.	840000.	2	1	1	1.10	89.	40.	7.90	150.	2	1	0	0	0
642.	214	7000	2625000.	840000.	2	1	1	2.70	169.	20.	10.90	160.	2	1	0	0	0
714.	217	7000	2625000.	840000.	2	1	1	-0.0	-0.	-0.	-0.0	-0.	1	2	0	0	0
719.	323	7000	2625000.	840000.	2	1	1	-0.0	-0.	-0.	-0.0	-0.	1	2	0	0	0
757.	215.	7000	2625000.	840000.	2	1	1	4.90	256.	60.	-0.0	-0.	1	2	0	0	0
762.	324	7000	2625000.	840000.	2	1	1	5.50	210.	60.	7.20	164.	1	3	0	0	0
791.	325	7000	2625000.	840000.	2	1	1	3.10	151.	50.	4.00	224.	1	3	0	0	0
834.	324.	7000	2625000.	840000.	2	1	1	2.80	147.	115.	7.80	280.	1	2	0	0	0
958.	215	7000	2625000.	840000.	2	1	1	1.40	108.	174.	-0.0	-0.	1	2	0	0	0
1001.	219.	7000	2625000.	840000.	2	1	1	2.30	63.	335.	10.70	120.	1	2	0	0	0
1006.	322.	7000	2625000.	840000.	2	1	1	3.60	105.	289.	11.90	120.	2	1	0	0	0
1044.	220.	7000	2625000.	840000.	2	1	1	5.70	244.	84.	-0.0	-0.	1	3	0	0	0
1049.	323.	7000	2625000.	840000.	2	1	1	5.00	244.	84.	-0.0	-0.	1	3	0	0	0
1087.	221	7000	2625000.	840000.	2	1	1	-0.0	-0.	-0.	-0.0	-0.	1	3	0	0	0

- 1 AIRCRAFT PASS OR SATELLITE REVOLUTION
- 2 AIRCRAFT OR SATELLITE HEADING (°TRUE)
- 3 AIRCRAFT OR SATELLITE VELOCITY (M/S)
- 4 AIRCRAFT OR SATELLITE ALTITUDE (FT ABOVE SEA LEVEL)
- 5 RANGE DISTANCE TO NEAR EDGE OF RADAR COVERAGE (M)
- 6 RADAR WAVELENGTH (1=X-BAND; 2=L-BAND)
- 7 TRANSMITTED POLARIZATION (1=HORIZONTAL; 2=VERTICAL)
- 8 RECEIVED POLARIZATION (1=HORIZONTAL; 2=VERTICAL)
- 9 SIGNIFICANT WAVE HEIGHT (M)
- 10 DOMINANT WAVELENGTH (M)
- 11 DOMINANT WAVE DIRECTION (°TRUE)
- 12 WIND SPEED (M/S)
- 13 WIND DIRECTION (°TRUE)
- 14 WAVES PRESENT IN IMAGERY? (0=NO DATA, 1=YES, 2=NO)
- 15 WAVE DETECTABILITY AT 20° INCIDENCE ANGLE (0=NO DATA, 1=NOT DETECTED, 2=DETECTED, 3=CLEARLY DETECTED)
- 16 WAVE DETECTABILITY AT 40° INCIDENCE ANGLE (0=NO DATA, 1=NOT DETECTED, 2=DETECTED, 3=CLEARLY DETECTED)
- 17 WAVE DETECTABILITY AT 60° INCIDENCE ANGLE (0=NO DATA, 1=NOT DETECTED, 2=DETECTED, 3=CLEARLY DETECTED)
- 18 WAVE DETECTABILITY AT 80° INCIDENCE ANGLE (0=NO DATA, 1=NOT DETECTED, 2=DETECTED, 3=CLEARLY DETECTED)



Presented in Table 13 is a summary of the Seasat SAR operating parameters and environmental conditions for 5 overpasses in September 1978 in support of the GOASEX Experiment. Waves were imaged in 4 of the 5 passes. The one pass where waves were not imaged had a surface-measured significant wave height ( $H_{1/3}$ ) of only 1.1 meters.

The ERIM X- and L-band SAR operating parameters and environmental conditions for 22 September 1978 are presented in Table 14. Waves were clearly visible in each pass where data was available for both X- and L-band. Note that imagery for several passes was either lost or never processed. The signal films do exist for these passes so they could be processed into imagery in the future.

A summary of the ERIM X- and L-band SAR operating parameters and environmental conditions for 23 September 1978 is presented in Table 15. Waves were clearly visible in each pass where data was available for both X- and L-band. It is interesting to note that the L-band data appears equivalent to the X-band for this data set and that collected on the 22nd. This implies that under certain conditions, radar wavelength is not an important consideration for the detectability of waves.

The ERIM X- and L-band SAR operating parameters and environmental conditions for 25 September 1978 are summarized in Table 16. The image film from this flight could not be located at ERIM. However, as mentioned previously, the signal films do exist and could be processed into imagery in the future.

Presented in Table 17 is a summary of the ERIM X- and L-band SAR operating parameters and environmental conditions for 26 September 1978. Only 4 of the 9 passes were found and these all contained waves in both the X- and L-band imagery. It is interesting to note that the waves are not as detectable as on the 22nd or 23rd. This is most likely due to the lower wave heights or the different imaging geometries.

TABLE 13  
SUMMARY OF SEASAT SAR OPERATING PARAMETERS AND  
ENVIRONMENTAL CONDITIONS DURING THE 1978 GOASEX EXPERIMENT

1	2	3	4	5	6	7	8	9	10	11	12	13	14	15	16	17	18
1126	330	7000	2625000	840000	2	1	1	2	70	256	96	3.80	244	1	3	0	0
1169	330	7000	2625000	840000	2	1	1	3	60	256	110	11.80	295	1	3	0	0
1255	330	7000	2625000	840000	2	1	1	2	7	177	93	8.3	243	1	2	0	0
1269	330	7000	2625000	840000	2	1	1	2	50	151	93	5.10	90	1	2	0	0
1306	210	7000	2625000	840000	2	1	1	1	10	130	105	11.80	100	2	1	0	0

- 1 AIRCRAFT PASS OR SATELLITE REVOLUTION
- 2 AIRCRAFT OR SATELLITE HEADING (°TRUE)
- 3 AIRCRAFT OR SATELLITE VELOCITY (M/S)
- 4 AIRCRAFT OR SATELLITE ALTITUDE (FT ABOVE SEA LEVEL)
- 5 RANGE DISTANCE TO NEAR EDGE OF RADAR COVERAGE (M)
- 6 RADAR WAVELENGTH (1=X-BAND; 2=L-BAND)
- 7 TRANSMITTED POLARIZATION (1=HORIZONTAL; 2=VERTICAL)
- 8 RECEIVED POLARIZATION (1=HORIZONTAL; 2=VERTICAL)
- 9 SIGNIFICANT WAVE HEIGHT (M)
- 10 DOMINANT WAVELENGTH (M)
- 11 DOMINANT WAVE DIRECTION (°TRUE)
- 12 WIND SPEED (M/S)
- 13 WIND DIRECTION (°TRUE)
- 14 WAVES PRESENT IN IMAGERY? (0=NO DATA; 1=YES; 2=NO)
- 15 WAVE DETECTABILITY AT 20° INCIDENCE ANGLE (0=NO DATA; 1=NOT DETECTED; 2=DETECTED; 3=CLEARLY DETECTED)
- 16 WAVE DETECTABILITY AT 40° INCIDENCE ANGLE (0=NO DATA; 1=NOT DETECTED; 2=DETECTED; 3=CLEARLY DETECTED)
- 17 WAVE DETECTABILITY AT 60° INCIDENCE ANGLE (0=NO DATA; 1=NOT DETECTED; 2=DETECTED; 3=CLEARLY DETECTED)
- 18 WAVE DETECTABILITY AT 80° INCIDENCE ANGLE (0=NO DATA; 1=NOT DETECTED; 2=DETECTED; 3=CLEARLY DETECTED)

TABLE 14  
SUMMARY OF ERIM X-L SAR OPERATING PARAMETERS AND  
ENVIRONMENTAL CONDITIONS FOR 22 SEPTEMBER 1978

	1	2	3	4	5	6	7	8	9	10	11	12	13	14	15	16	17	18
1	270	112	22800	6950	1	1	1	2	70	177	93	8	30	243	1	3	3	0
2	260	123	22800	6950	1	1	1	2	70	177	93	8	30	243	1	3	3	0
3	332	138	22800	6950	1	1	1	2	70	177	93	8	30	243	1	3	3	0
4	62	150	22800	6950	1	1	1	2	70	177	93	8	30	243	1	3	3	0
5	152	142	22800	6950	1	1	1	2	70	177	93	8	30	243	1	3	3	0
6	242	122	22800	6950	1	1	1	2	70	177	93	8	30	243	1	3	3	0
7	332	129	22800	6950	1	2	2	2	70	177	93	8	30	243	1	3	3	0
8	88	158	22800	6950	1	1	1	2	70	177	93	8	30	243	0	0	0	0
9	185	114	22800	6950	1	1	1	2	70	177	93	8	30	243	0	0	0	0
1	270	112	22800	6950	2	1	1	2	70	177	93	8	30	243	1	3	3	0
2	260	123	22800	6950	2	1	1	2	70	177	93	8	30	243	1	3	3	0
3	332	138	22800	6950	2	1	1	2	70	177	93	8	30	243	1	3	3	0
4	62	150	22800	6950	2	1	1	2	70	177	93	8	30	243	0	0	0	0
5	152	142	22800	6950	2	1	1	2	70	177	93	8	30	243	1	3	3	0
6	242	122	22800	6950	2	1	1	2	70	177	93	8	30	243	1	3	3	0
7	332	129	22800	6950	2	2	2	2	70	177	93	8	30	243	0	0	0	0
8	88	158	22800	6950	2	1	1	2	70	177	93	8	30	243	0	0	0	0
9	185	114	22800	6950	2	1	1	2	70	177	93	8	30	243	0	0	0	0

- 1 AIRCRAFT PASS OR SATELLITE REVOLUTION
- 2 AIRCRAFT OR SATELLITE HEADING (TRUE)
- 3 AIRCRAFT OR SATELLITE VELOCITY (M/S)
- 4 AIRCRAFT OR SATELLITE ALTITUDE (FT ABOVE SEA LEVEL)
- 5 RANGE DISTANCE TO NEAR EDGE OF RADAR COVERAGE (M)
- 6 RADAR WAVELENGTH (1=X-BAND; 2=L-BAND)
- 7 TRANSMITTED POLARIZATION (1=HORIZONTAL; 2=VERTICAL)
- 8 RECEIVED POLARIZATION (1=HORIZONTAL; 2=VERTICAL)
- 9 SIGNIFICANT WAVE HEIGHT (M)
- 10 DOMINANT WAVELENGTH (M)
- 11 DOMINANT WAVE DIRECTION (TRUE)
- 12 WIND SPEED (M/S)
- 13 WIND DIRECTION (TRUE)
- 14 WAVES PRESENT IN IMAGERY? (O=NO DATA; 1=YES; 2=NO)
- 15 WAVE DETECTABILITY AT 20° INCIDENCE ANGLE (O=NO DATA; 1=NOT DETECTED; 2=DETECTED; 3=CLEARLY DETECTED)
- 16 WAVE DETECTABILITY AT 40° INCIDENCE ANGLE (O=NO DATA; 1=NOT DETECTED; 2=DETECTED; 3=CLEARLY DETECTED)
- 17 WAVE DETECTABILITY AT 60° INCIDENCE ANGLE (O=NO DATA; 1=NOT DETECTED; 2=DETECTED; 3=CLEARLY DETECTED)
- 18 WAVE DETECTABILITY AT 80° INCIDENCE ANGLE (O=NO DATA; 1=NOT DETECTED; 2=DETECTED; 3=CLEARLY DETECTED)

TABLE 15  
SUMMARY OF ERIM X-L SAR OPERATING PARAMETERS AND  
ENVIRONMENTAL CONDITIONS FOR 23 SEPTEMBER 1978

1	2	3	4	5	6	7	8	9	10	11	12	13	14	15	16	17	18
1	186.	129.	20000.	6095.	1	1	1	2.50	151.	93.	5.10	90.	0	0	0	0	0
2	283	111.	20000.	6095.	1	1	1	2.50	151.	93.	5.10	90.	1	3	3	0	0
3	333	133.	20000.	6095.	1	1	1	2.50	151.	93.	5.10	90.	1	3	3	0	0
4	62.	174.	20000.	6095.	1	1	1	2.50	151.	93.	5.10	90.	1	3	3	0	0
5	152	140.	20000.	6095.	1	1	1	2.50	151.	93.	5.10	90.	1	3	3	0	0
6	242.	105.	20000.	6095.	1	1	1	2.50	151.	93.	5.10	90.	1	3	3	0	0
7	332	133.	20000.	6095.	1	1	1	2.50	151.	93.	5.10	90.	1	3	3	0	0
8	242.	106.	20000.	6095.	1	1	1	2.50	151.	93.	5.10	90.	1	3	3	0	0
9	93.	171.	20000.	6095.	1	1	1	2.50	151.	93.	5.10	90.	1	3	3	0	0
1	186.	129.	20000.	6095.	2	1	1	2.50	151.	93.	5.10	90.	0	0	0	0	0
2	283	111.	20000.	6095.	2	1	1	2.50	151.	93.	5.10	90.	1	2	3	0	0
3	333	133.	20000.	6095.	2	1	1	2.50	151.	93.	5.10	90.	1	3	3	0	0
4	62.	174.	20000.	6095.	2	1	1	2.50	151.	93.	5.10	90.	1	3	3	0	0
5	152.	140.	20000.	6095.	2	1	1	2.50	151.	93.	5.10	90.	1	2	3	0	0
6	242.	105.	20000.	6095.	2	1	1	2.50	151.	93.	5.10	90.	1	3	3	0	0
7	332	133.	20000.	6095.	2	1	1	2.50	151.	93.	5.10	90.	1	3	3	0	0
8	242.	106.	20000.	6095.	2	1	1	2.50	151.	93.	5.10	90.	1	3	3	0	0
9	93.	171.	20000.	6095.	2	1	1	2.50	151.	93.	5.10	90.	1	3	3	0	0
1	AIRCRAFT PASS OR SATELLITE REVOLUTION																
2	AIRCRAFT OR SATELLITE HEADING (°TRUE)																
3	AIRCRAFT OR SATELLITE VELOCITY (M/S)																
4	AIRCRAFT OR SATELLITE ALTITUDE (FT ABOVE SEA LEVEL)																
5	RANGE DISTANCE TO NEAR EDGE OF RADAR COVERAGE (M)																
6	RADAR WAVELENGTH (1=X-BAND; 2=L-BAND)																
7	TRANSMITTED POLARIZATION (1=HORIZONTAL; 2=VERTICAL)																
8	RECEIVED POLARIZATION (1=HORIZONTAL; 2=VERTICAL)																
9	SIGNIFICANT WAVE HEIGHT (M)																
10	DOMINANT WAVELENGTH (M)																
11	DOMINANT WAVE DIRECTION (°TRUE)																
12	WIND SPEED (M/S)																
13	WIND DIRECTION (°TRUE)																
14	WAVES PRESENT IN IMAGERY? (0=NO DATA; 1=YES; 2=NO)																
15	WAVE DETECTABILITY AT 20° INCIDENCE ANGLE (0=NO DATA; 1=NOT DETECTED; 2=DETECTED; 3=CLEARLY DETECTED)																
16	WAVE DETECTABILITY AT 40° INCIDENCE ANGLE (0=NO DATA; 1=NOT DETECTED; 2=DETECTED; 3=CLEARLY DETECTED)																
17	WAVE DETECTABILITY AT 60° INCIDENCE ANGLE (0=NO DATA; 1=NOT DETECTED; 2=DETECTED; 3=CLEARLY DETECTED)																
18	WAVE DETECTABILITY AT 80° INCIDENCE ANGLE (0=NO DATA; 1=NOT DETECTED; 2=DETECTED; 3=CLEARLY DETECTED)																

TABLE 16  
SUMMARY OF ERM X-L SAR OPERATING PARAMETERS AND  
ENVIRONMENTAL CONDITIONS FOR 25 SEPTEMBER 1978

1	2	3	4	5	6	7	8	9	10	11	12	13	14	15	16	17	18
1	270	124	19000	5790	1	1	1	1	150	103	7	40	65	0	0	0	0
2	300	133	24500	5790	1	1	1	1	150	103	7	40	65	0	0	0	0
3	30	163	24500	5790	1	1	1	1	150	103	7	40	65	0	0	0	0
4	120	135	24500	5790	1	1	1	1	150	103	7	40	65	0	0	0	0
5	210	104	24500	5790	1	1	1	1	150	103	7	40	65	0	0	0	0
6	83	157	24500	5790	1	2	2	1	150	103	7	40	65	0	0	0	0
7	90	158	24500	5790	1	1	1	1	150	103	7	40	65	0	0	0	0
8	186	129	24500	5790	1	1	1	1	150	103	7	40	65	0	0	0	0
1	270	124	19000	5790	2	1	1	1	150	103	7	40	65	0	0	0	0
2	300	133	24500	5790	2	1	1	1	150	103	7	40	65	0	0	0	0
3	30	163	24500	5790	2	1	1	1	150	103	7	40	65	0	0	0	0
4	120	135	24500	5790	2	1	1	1	150	103	7	40	65	0	0	0	0
5	210	104	24500	5790	2	1	1	1	150	103	7	40	65	0	0	0	0
6	83	157	24500	5790	2	2	2	1	150	103	7	40	65	0	0	0	0
7	90	158	24500	5790	2	1	1	1	150	103	7	40	65	0	0	0	0
8	186	129	24500	5790	2	1	1	1	150	103	7	40	65	0	0	0	0

- 1 AIRCRAFT PASS OR SATELLITE REVOLUTION
- 2 AIRCRAFT OR SATELLITE HEADING (°TRUE)
- 3 AIRCRAFT OR SATELLITE VELOCITY (M/S)
- 4 AIRCRAFT OR SATELLITE ALTITUDE (FT ABOVE SEA LEVEL)
- 5 RANGE DISTANCE TO NEAR EDGE OF RADAR COVERAGE (M)
- 6 RADAR WAVELENGTH (1=X-BAND; 2=L-BAND)
- 7 TRANSMITTED POLARIZATION (1=HORIZONTAL; 2=VERTICAL)
- 8 RECEIVED POLARIZATION (1=HORIZONTAL; 2=VERTICAL)
- 9 SIGNIFICANT WAVE HEIGHT (M)
- 10 DOMINANT WAVELENGTH (M)
- 11 DOMINANT WAVE DIRECTION (°TRUE)
- 12 WIND SPEED (M/S)
- 13 WIND DIRECTION (°TRUE)
- 14 WAVES PRESENT IN IMAGERY? (0=NO DATA; 1=YES; 2=NO)
- 15 WAVE DETECTABILITY AT 20° INCIDENCE ANGLE (0=NO DATA; 1=NOT DETECTED; 2=DETECTED; 3=CLEARLY DETECTED)
- 16 WAVE DETECTABILITY AT 40° INCIDENCE ANGLE (0=NO DATA; 1=NOT DETECTED; 2=DETECTED; 3=CLEARLY DETECTED)
- 17 WAVE DETECTABILITY AT 60° INCIDENCE ANGLE (0=NO DATA; 1=NOT DETECTED; 2=DETECTED; 3=CLEARLY DETECTED)
- 18 WAVE DETECTABILITY AT 80° INCIDENCE ANGLE (0=NO DATA; 1=NOT DETECTED; 2=DETECTED; 3=CLEARLY DETECTED)

TABLE 17  
SUMMARY OF ERIM X-L SAR OPERATING PARAMETERS AND  
ENVIRONMENTAL CONDITIONS FOR 26 SEPTEMBER 1978

1	2	3	4	5	6	7	8	9	10	11	12	13	14	15	16	17	18
1	186	125	15500	9000	1	1	1	1.10	130	105	11.80	100	0	0	0	0	0
2	283	132	10000	5400	1	1	1	1.10	130	105	11.80	100	0	0	0	0	0
3	300	144	8000	3750	1	1	1	1.10	130	105	11.80	100	0	0	0	0	0
4	210	123	9000	4500	1	1	1	1.10	130	105	11.80	100	0	0	0	0	0
5	300	138	10000	5400	1	1	1	1.10	130	105	11.80	100	0	0	0	0	0
6	30	143	10000	5400	1	1	1	1.10	130	105	11.80	100	1	0	0	2	0
7	120	127	10000	5400	1	1	1	1.10	130	105	11.80	100	1	0	0	3	0
8	210	122	10000	5400	1	1	1	1.10	130	105	11.80	100	1	0	0	2	0
9	100	133	10000	5400	1	1	1	1.10	130	105	11.80	100	1	0	0	2	0
1	186	125	15500	9000	2	1	1	1.10	130	105	11.80	100	0	0	0	0	0
2	283	132	10000	5400	2	1	1	1.10	130	105	11.80	100	0	0	0	0	0
3	300	144	8000	3750	2	1	1	1.10	130	105	11.80	100	0	0	0	0	0
4	210	123	9000	4500	2	1	1	1.10	130	105	11.80	100	0	0	0	0	0
5	300	138	10000	5400	2	1	1	1.10	130	105	11.80	100	0	0	0	0	0
6	30	143	10000	5400	2	1	1	1.10	130	105	11.80	100	1	0	0	2	0
7	120	127	10000	5400	2	1	1	1.10	130	105	11.80	100	1	0	0	2	0
8	210	122	10000	5400	2	1	1	1.10	130	105	11.80	100	1	0	0	2	0
9	100	133	10000	5400	2	1	1	1.10	130	105	11.80	100	1	0	0	2	0

1 AIRCRAFT PASS OR SATELLITE REVOLUTION  
2 AIRCRAFT OR SATELLITE HEADING (°TRUE)  
3 AIRCRAFT OR SATELLITE VELOCITY (M/S)  
4 AIRCRAFT OR SATELLITE ALTITUDE (FT ABOVE SEA LEVEL)  
5 RANGE DISTANCE TO NEAR EDGE OF RADAR COVERAGE (M)  
6 RADAR WAVELENGTH (1=X-BAND; 2=L-BAND)  
7 TRANSMITTED POLARIZATION (1=HORIZONTAL; 2=VERTICAL)  
8 RECEIVED POLARIZATION (1=HORIZONTAL; 2=VERTICAL)  
9 SIGNIFICANT WAVE HEIGHT (M)  
10 DOMINANT WAVELENGTH (M)  
11 DOMINANT WAVE DIRECTION (°TRUE)  
12 WIND SPEED (M/S)  
13 WIND DIRECTION (°TRUE)  
14 WAVES PRESENT IN IMAGERY? (0=NO DATA; 1=YES; 2=NO)  
15 WAVE DETECTABILITY AT 20° INCIDENCE ANGLE (0=NO DATA; 1=NOT DETECTED; 2=DETECTED; 3=CLEARLY DETECTED)  
16 WAVE DETECTABILITY AT 40° INCIDENCE ANGLE (0=NO DATA; 1=NOT DETECTED; 2=DETECTED; 3=CLEARLY DETECTED)  
17 WAVE DETECTABILITY AT 60° INCIDENCE ANGLE (0=NO DATA; 1=NOT DETECTED; 2=DETECTED; 3=CLEARLY DETECTED)  
18 WAVE DETECTABILITY AT 80° INCIDENCE ANGLE (0=NO DATA; 1=NOT DETECTED; 2=DETECTED; 3=CLEARLY DETECTED)

The GOASEX data set represents the only example of coincident aircraft and spacecraft SAR coverage. Comparisons between the two platforms have been performed which indicate close agreement of the two sensors as described by Gonzalez, et al., 1981. A reprint of this article is included in the Appendix.

### 3.1.5 LAKE MICHIGAN 1978

On 18 October 1978, the ERIM X- and L-band SAR system collected two passes of data over Lake Michigan near Pentwater, Michigan. During the SAR data collection flight, surface wind and wave measurements by an array of wave probes were performed by the Physical Oceanography Laboratory of the University of Michigan.

The ERIM X- and L-band SAR operating parameters and environmental conditions for 18 October 1978 are presented in Table 18. Waves were detected in both X-band passes but in only one of the 2 L-band cases. More detailed comparisons between the SAR-derived and surface-measured wave spectra from this data set are given by Shuchman and Meadows (1980) and Meadows, et al. (1982). Reprints of these papers are included in the Appendix.

### 3.1.6 MARSEN

The Maritime Remote Sensing Experiment (MARSEN) was conducted in the southern part of the North Sea during August and September 1979. Seven APD-10 SAR data collection missions were flown by the United States Air Force of Europe (USAFE) RF-4s. In total, 39 passes of data were collected. These flights were concentrated over two instrumented towers in the North Sea where surface wind and wave measurements were performed. A collection of articles describing the scientific results from MARSEN have been published in a special issue of the Journal of Geophysical Research. Two papers from this issue are included in the Appendix (Shuchman, et al., 1983; Lyzenga and Shuchman, 1983).

TABLE 18  
SUMMARY OF ERIM X-L SAR OPERATING PARAMETERS AND  
ENVIRONMENTAL CONDITIONS FOR 18 OCTOBER 1978

1	2	3	4	5	6	7	8	9	10	11	12	13	14	15	16	17	18
4	270.	109.	22000.	6705.	1	1	1	0.95	54.	57.	8.70	230.	1	3	3	0	0
5	180.	156.	22000.	6705.	1	1	1	0.95	54.	57.	8.70	230.	1	2	2	0	0
4	270.	109.	22000.	6705.	2	1	1	0.95	54.	57.	8.70	230.	1	1	2	0	0
5	180.	156.	22000.	6705.	2	1	1	0.95	54.	57.	8.70	230.	2	1	1	0	0

1. AIRCRAFT PASS OR SATELLITE REVOLUTION
2. AIRCRAFT OR SATELLITE HEADING (°TRUE)
3. AIRCRAFT OR SATELLITE VELOCITY (M/S)
4. AIRCRAFT OR SATELLITE ALTITUDE (FT ABOVE SEA LEVEL)
5. RANGE DISTANCE TO NEAR EDGE OF RADAR COVERAGE (M)
6. RADAR WAVELENGTH (1=X-BAND; 2=L-BAND)
7. TRANSMITTED POLARIZATION (1=HORIZONTAL; 2=VERTICAL)
8. RECEIVED POLARIZATION (1=HORIZONTAL; 2=VERTICAL)
9. SIGNIFICANT WAVE HEIGHT (M)
10. DOMINANT WAVELENGTH (M)
11. DOMINANT WAVE DIRECTION (°TRUE)
12. WIND SPEED (M/S)
13. WIND DIRECTION (°TRUE)
14. WAVES PRESENT IN IMAGERY? (0=NO DATA; 1=YES; 2=NO)
15. WAVE DETECTABILITY AT 20° INCIDENCE ANGLE (0=NO DATA; 1=NOT DETECTED; 2=CLEARLY DETECTED)
16. WAVE DETECTABILITY AT 40° INCIDENCE ANGLE (0=NO DATA; 1=NOT DETECTED; 2=CLEARLY DETECTED)
17. WAVE DETECTABILITY AT 60° INCIDENCE ANGLE (0=NO DATA; 1=NOT DETECTED; 2=CLEARLY DETECTED)
18. WAVE DETECTABILITY AT 80° INCIDENCE ANGLE (0=NO DATA; 1=NOT DETECTED; 2=CLEARLY DETECTED)



Presented in Table 19 is a summary of the APD-10 SAR operating parameters and environmental conditions for Line 8 data collected on 25 September 1979. Again, some of the imagery was not available, but signal films exist so that it can be processed in the future. Of the 5 passes where imagery was available, waves were clearly detected. The clarity of the wave images fall off rapidly with increasing range (incidence angle). This is probably due to the effect of scatterer motions in the imaged scene caused by the relatively high wind speed (11.8 m/s). This effect is discussed in greater detail by Lyzenga and Shuchman (1983). A reprint of this article is included in the Appendix.

A summary of the APD-10 SAR operating parameters and environmental conditions is presented in Table 20 for Line 12 data collected on 27 September 1979. Waves were imaged in each pass. Again, wave detectability falls off with increasing range. No waves were visible at 80° incidence angle.

The APD-10 SAR operating parameters and environmental conditions for Line 13 data collected on 27 September 1979 are summarized in Table 21. Waves were again imaged in each pass but none were visible at 80° incidence angle.

The data presented in Table 22 summarize the APD-10 SAR operating parameters and environmental conditions for Line 10 data collected on 28 September 1979. Waves were clearly visible in each pass and in one pass were detected at 80° incidence angle.

Presented in Table 23 is a summary of the APD-10 SAR operating parameters and environmental conditions for Line 7 data collected on 28 September 1979. These data were collected using the same flight pattern as Line 10, but by a different aircraft at a slightly later time. The visibility of waves for this data set are the same as Line 10. This implies that the environmental conditions remained relatively constant between the two flights.

TABLE 19  
SUMMARY OF APD-10 SAR OPERATING PARAMETERS AND  
ENVIRONMENTAL CONDITIONS FOR 25 SEPTEMBER 1979 (LINE 8)

1	2	3	4	5	6	7	8	9	10	11	12	13	14	15	16	17	18
1	212	215	11000	4630	1	1	1	-0.0	-0	-0	-0.0	-0	0	0	0	0	0
2	70	215	11000	4630	1	1	1	-0.0	-0	-0	-0.0	-0	0	0	0	0	0
3	300	215	11000	4630	1	1	1	-0.0	-0	-0	-0.0	-0	0	0	0	0	0
4	168	215	11000	4630	1	1	1	-0.0	-0	-0	-0.0	-0	0	0	0	0	0
5	30	215	11000	4630	1	1	1	-0.0	-0	-0	-0.0	-0	0	0	0	0	0
1	212	215	11000	4630	1	1	1	1.00	35	130	11.80	200	0	0	0	0	0
2	70	215	11000	4630	1	1	1	1.00	35	130	11.80	200	1	0	3	3	1
3	300	215	11000	4630	1	1	1	1.00	35	130	11.80	200	1	0	3	2	1
4	168	215	11000	4630	1	1	1	1.00	35	130	11.80	200	1	0	3	2	1
5	30	215	11000	4630	1	1	1	1.00	35	130	11.80	200	1	0	3	2	1
E-4	75	215	11000	4630	1	1	1	1.00	35	130	11.80	200	1	0	3	2	1

- 1 AIRCRAFT PASS OR SATELLITE REVOLUTION
- 2 AIRCRAFT OR SATELLITE HEADING (°TRUE)
- 3 AIRCRAFT OR SATELLITE VELOCITY (M/S)
- 4 AIRCRAFT OR SATELLITE ALTITUDE (FT ABOVE SEA LEVEL)
- 5 RANGE DISTANCE TO NEAR EDGE OF RADAR COVERAGE (M)
- 6 RADAR WAVELENGTH (1=X-BAND; 2=L-BAND)
- 7 TRANSMITTED POLARIZATION (1=HORIZONTAL; 2=VERTICAL)
- 8 RECEIVED POLARIZATION (1=HORIZONTAL; 2=VERTICAL)
- 9 SIGNIFICANT WAVE HEIGHT (M)
- 10 DOMINANT WAVELENGTH (M)
- 11 DOMINANT WAVE DIRECTION (°TRUE)
- 12 WIND SPEED (M/S)
- 13 WIND DIRECTION (°TRUE)
- 14 WAVES PRESENT IN IMAGERY? (0=NO DATA; 1=YES; 2=NO)
- 15 WAVE DETECTABILITY AT 20° INCIDENCE ANGLE (0=NO DATA; 1=NOT DETECTED; 2=DETECTED; 3=CLEARLY DETECTED)
- 16 WAVE DETECTABILITY AT 40° INCIDENCE ANGLE (0=NO DATA; 1=NOT DETECTED; 2=DETECTED; 3=CLEARLY DETECTED)
- 17 WAVE DETECTABILITY AT 60° INCIDENCE ANGLE (0=NO DATA; 1=NOT DETECTED; 2=DETECTED; 3=CLEARLY DETECTED)
- 18 WAVE DETECTABILITY AT 80° INCIDENCE ANGLE (0=NO DATA; 1=NOT DETECTED; 2=DETECTED; 3=CLEARLY DETECTED)

TABLE 20  
SUMMARY OF APD-10 SAR OPERATING PARAMETERS AND  
ENVIRONMENTAL CONDITIONS FOR 27 SEPTEMBER 1979 (LINE 12)

	1	2	3	4	5	6	7	8	9	10	11	12	13	14	15	16	17	18		
SVLT		297	185	11000	4630	1	1	1	1	00	79	77	10	30	290	1	0	3	2	1
1		283	185	11000	4630	1	1	1	1	00	79	77	10	30	290	1	0	3	3	1
2		56	185	11000	4630	1	1	1	1	00	79	77	10	30	290	1	0	3	3	1
3		191	185	11000	4630	1	1	1	1	00	79	77	10	30	290	1	0	3	3	1

- 1 AIRCRAFT PASS OR SATELLITE REVOLUTION
- 2 AIRCRAFT OR SATELLITE HEADING (°TRUE)
- 3 AIRCRAFT OR SATELLITE VELOCITY (M/S)
- 4 AIRCRAFT OR SATELLITE ALTITUDE (FT ABOVE SEA LEVEL)
- 5 RANGE DISTANCE TO NEAR EDGE OF RADAR COVERAGE (M)
- 6 RADAR WAVELENGTH (1=X BAND; 2=L BAND)
- 7 TRANSMITTED POLARIZATION (1=HORIZONTAL; 2=VERTICAL)
- 8 RECEIVED POLARIZATION (1=HORIZONTAL; 2=VERTICAL)
- 9 SIGNIFICANT WAVE HEIGHT (M)
- 10 DOMINANT WAVELENGTH (M)
- 11 DOMINANT WAVE DIRECTION (°TRUE)
- 12 WIND SPEED (M/S)
- 13 WIND DIRECTION (°TRUE)
- 14 WAVES PRESENT IN IMAGERY? (0=NO DATA; 1=YES; 2=NO)
- 15 WAVE DETECTABILITY AT 20° INCIDENCE ANGLE (0=NO DATA; 1=NOT DETECTED; 2=DETECTED; 3=CLEARLY DETECTED)
- 16 WAVE DETECTABILITY AT 40° INCIDENCE ANGLE (0=NO DATA; 1=NOT DETECTED; 2=DETECTED; 3=CLEARLY DETECTED)
- 17 WAVE DETECTABILITY AT 60° INCIDENCE ANGLE (0=NO DATA; 1=NOT DETECTED; 2=DETECTED; 3=CLEARLY DETECTED)
- 18 WAVE DETECTABILITY AT 80° INCIDENCE ANGLE (0=NO DATA; 1=NOT DETECTED; 2=DETECTED; 3=CLEARLY DETECTED)

TABLE 21  
SUMMARY OF APD-10 SAR OPERATING PARAMETERS AND  
ENVIRONMENTAL CONDITIONS FOR 27 SEPTEMBER 1979 (LINE 13)

1	2	3	4	5	6	7	8	9	10	11	12	13	14	15	16	17	18
1.	212.	215.	11300.	4630.	1	1	1	1.00	47.	150.	8.20	330.	1	0	3	3	1
2.	70.	215.	11300.	4630.	1	1	1	1.00	47.	150.	8.20	330.	1	0	3	3	1
3.	300.	215.	11300.	4630.	1	1	1	1.00	47.	150.	8.20	330.	1	0	3	2	1
4.	168.	215.	11300.	4630.	1	1	1	1.00	47.	150.	8.20	330.	1	0	3	2	1
5.	30.	215.	11300.	4630.	1	1	1	1.00	47.	150.	8.20	330.	1	0	2	2	1
E-4.	75.	215.	11300.	4630.	1	1	1	1.00	47.	150.	8.20	330.	1	0	3	3	1

- 1 AIRCRAFT PASS OR SATELLITE REVOLUTION
- 2 AIRCRAFT OR SATELLITE HEADING (°TRUE)
- 3 AIRCRAFT OR SATELLITE VELOCITY (M/S)
- 4 AIRCRAFT OR SATELLITE ALTITUDE (FT ABOVE SEA LEVEL)
- 5 RANGE DISTANCE TO NEAR EDGE OF RADAR COVERAGE (M)
- 6 RADAR WAVELENGTH (1=X-BAND; 2=L-BAND)
- 7 TRANSMITTED POLARIZATION (1=HORIZONTAL; 2=VERTICAL)
- 8 RECEIVED POLARIZATION (1=HORIZONTAL; 2=VERTICAL)
- 9 SIGNIFICANT WAVE HEIGHT (M)
- 10 DOMINANT WAVELENGTH (M)
- 11 DOMINANT WAVE DIRECTION (°TRUE)
- 12 WIND SPEED (M/S)
- 13 WIND DIRECTION (°TRUE)
- 14 WAVES PRESENT IN IMAGERY? (0=NO DATA; 1=YES; 2=NO)
- 15 WAVE DETECTABILITY AT 20° INCIDENCE ANGLE (0=NO DATA; 1=NOT DETECTED; 2=DETECTED; 3=CLEARLY DETECTED)
- 16 WAVE DETECTABILITY AT 40° INCIDENCE ANGLE (0=NO DATA; 1=NOT DETECTED; 2=DETECTED; 3=CLEARLY DETECTED)
- 17 WAVE DETECTABILITY AT 60° INCIDENCE ANGLE (0=NO DATA; 1=NOT DETECTED; 2=DETECTED; 3=CLEARLY DETECTED)
- 18 WAVE DETECTABILITY AT 80° INCIDENCE ANGLE (0=NO DATA; 1=NOT DETECTED; 2=DETECTED; 3=CLEARLY DETECTED)

TABLE 22  
SUMMARY OF APD-10 SAR OPERATING PARAMETERS AND  
ENVIRONMENTAL CONDITIONS FOR 28 SEPTEMBER 1979 (LINE 10)

	1	2	3	4	5	6	7	8	9	10	11	12	13	14	15	16	17	18	
SYLT		297	215	11500	4630	1	1	1	1	20	88	133	7	50	270	1	0	3	1
1		283	215	11500	4630	1	1	1	1	20	88	133	7	50	270	1	0	3	1
2		56	215	11500	4630	1	1	1	1	20	88	133	7	50	270	1	0	3	1
3		191	215	11500	4630	1	1	1	1	20	88	133	7	50	270	1	0	3	2
4		327	215	11500	4630	1	1	1	1	20	88	133	7	50	270	1	0	3	1
5		102	215	11500	4630	1	1	1	1	20	88	133	7	50	270	1	0	3	1

1. AIRCRAFT PASS OR SATELLITE REVOLUTION
2. AIRCRAFT OR SATELLITE HEADING (°TRUE)
3. AIRCRAFT OR SATELLITE VELOCITY (M/S)
4. AIRCRAFT OR SATELLITE ALTITUDE (FT ABOVE SEA LEVEL)
5. RANGE DISTANCE TO NEAR EDGE OF RADAR COVERAGE (M)
6. RADAR WAVELENGTH (1=X-BAND; 2=L-BAND)
7. TRANSMITTED POLARIZATION (1=HORIZONTAL; 2=VERTICAL)
8. RECEIVED POLARIZATION (1=HORIZONTAL; 2=VERTICAL)
9. SIGNIFICANT WAVE HEIGHT (M)
10. DOMINANT WAVELENGTH (M)
11. DOMINANT WAVE DIRECTION (°TRUE)
12. WIND SPEED (M/S)
13. WIND DIRECTION (°TRUE)
14. WAVES PRESENT IN IMAGERY? (0=NO DATA; 1=YES; 2=NO)
15. WAVE DETECTABILITY AT 20° INCIDENCE ANGLE (0=NO DATA; 1=NOT DETECTED; 2=DETECTED; 3=CLEARLY DETECTED)
16. WAVE DETECTABILITY AT 40° INCIDENCE ANGLE (0=NO DATA; 1=NOT DETECTED; 2=DETECTED; 3=CLEARLY DETECTED)
17. WAVE DETECTABILITY AT 60° INCIDENCE ANGLE (0=NO DATA; 1=NOT DETECTED; 2=DETECTED; 3=CLEARLY DETECTED)
18. WAVE DETECTABILITY AT 80° INCIDENCE ANGLE (0=NO DATA; 1=NOT DETECTED; 2=DETECTED; 3=CLEARLY DETECTED)

TABLE 23  
SUMMARY OF APD-10 SAR OPERATING PARAMETERS AND  
ENVIRONMENTAL CONDITIONS FOR 28 SEPTEMBER 1979 (LINE 7)

1	2	3	4	5	6	7	8	9	10	11	12	13	14	15	16	17	18
SYLT	297	215	11000	4630	1	1	1	1	20	88	133	7 50 270	1	0	3	3	1
1	283	215	11000	4630	1	1	1	1	20	88	133	7 50 270	1	0	3	3	1
2	56	215	11000	4630	1	1	1	1	20	88	133	7 50 270	1	0	3	3	1
3	191	215	11000	4630	1	1	1	1	20	88	133	7 50 270	1	0	3	3	2
4	327	215	11000	4630	1	1	1	1	20	88	133	7 50 270	1	0	3	3	1
5	102	215	11000	4630	1	1	1	1	20	88	133	7 50 270	1	0	3	3	1

- 1 AIRCRAFT PASS OR SATELLITE REVOLUTION
- 2 AIRCRAFT OR SATELLITE HEADING (°TRUE)
- 3 AIRCRAFT OR SATELLITE VELOCITY (M/S)
- 4 AIRCRAFT OR SATELLITE ALTITUDE (FT ABOVE SEA LEVEL)
- 5 RANGE DISTANCE TO NEAR EDGE OF RADAR COVERAGE (M)
- 6 RADAR WAVELENGTH (1=X-BAND; 2=L-BAND)
- 7 TRANSMITTED POLARIZATION (1=HORIZONTAL; 2=VERTICAL)
- 8 RECEIVED POLARIZATION (1=HORIZONTAL; 2=VERTICAL)
- 9 SIGNIFICANT WAVE HEIGHT (M)
- 10 DOMINANT WAVELENGTH (M)
- 11 DOMINANT WAVE DIRECTION (°TRUE)
- 12 WIND SPEED (M/S)
- 13 WIND DIRECTION (°TRUE)
- 14 WAVES PRESENT IN IMAGERY? (0=NO DATA; 1=YES; 2=NO)
- 15 WAVE DETECTABILITY AT 20° INCIDENCE ANGLE (0=NO DATA; 1=NOT DETECTED; 2=DETECTED; 3=CLEARLY DETECTED)
- 16 WAVE DETECTABILITY AT 40° INCIDENCE ANGLE (0=NO DATA; 1=NOT DETECTED; 2=DETECTED; 3=CLEARLY DETECTED)
- 17 WAVE DETECTABILITY AT 60° INCIDENCE ANGLE (0=NO DATA; 1=NOT DETECTED; 2=DETECTED; 3=CLEARLY DETECTED)
- 18 WAVE DETECTABILITY AT 80° INCIDENCE ANGLE (0=NO DATA; 1=NOT DETECTED; 2=DETECTED; 3=CLEARLY DETECTED)

The APD-10 SAR operating parameters and environmental conditions are presented in Table 24 for Line 6 data collected on 28 September 1979. These data were collected approximately 250 km south of Lines 7 and 10, and therefore under a different set of environmental conditions. The wind speeds in this area were only 3.5 m/s. Waves were only visible in 3 of the 6 passes. It is interesting to note that waves were visible at 80° incidence angle in pass E-3. This could be due to the reduced effect of scatterer velocities because of the lower wind speed. The fact that waves were not imaged in 3 of the passes could be due to the low wind speed not causing enough small scale surface roughness to be modulated by the longer waves. For a more detailed analysis of the MARSEN data set, the reader is referred to Shuchman, et al. (1983). A reprint of this article is included in the Appendix.

### 3.1.7 OTHER EXPERIMENTS

In addition to the data described above, SAR experiments have recently been conducted or are planned which will add to the above data set. The Torrey Pines Experiment was held in December 1983 off the coast of Southern California. United States Marine Corps (USMC) RF-4 jets collected APD-10 imagery over an instrumented test site. The surface measurements included a linear pressure sensor array which yields high resolution directional wave spectra. Comparisons between these surface measurements and spectra derived from simultaneously collected SAR imagery are currently being performed.

A SAR experiment is planned to coincide with the SIR-B Experiment this summer (1984) off the coast of Long Island in the New York Bight region. The SAR 580 system will collect X-, L-, and C-band SAR data over an instrumented area. This experiment will provide additional data with which to test various imaging theories.

TABLE 24  
SUMMARY OF APD-10 SAR OPERATING PARAMETERS AND  
ENVIRONMENTAL CONDITIONS FOR 28 SEPTEMBER 1979 (LINE 6)

1	2	3	4	5	6	7	8	9	10	11	12	13	14	15	16	17	18
E-3.	254.	220.	11500.	4630.	1	1	1	1.00	100.	150.	3.50	330.	1	0	3	3	2
1	206.	215.	11600.	4630.	1	1	1	1.00	100.	150.	3.50	330.	2	0	1	1	1
2.	75.	215.	11600.	4630.	1	1	1	1.00	100.	150.	3.50	330.	1	0	2	2	1
3.	300.	215.	11600.	4630.	1	1	1	1.00	100.	150.	3.50	330.	2	0	1	1	1
4.	165.	215.	11600.	4630.	1	1	1	1.00	100.	150.	3.50	330.	2	0	1	1	1
5.	30.	215.	11600.	4630.	1	1	1	1.00	100.	150.	3.50	330.	1	0	3	3	1

1 AIRCRAFT PASS OR SATELLITE REVOLUTION  
2 AIRCRAFT OR SATELLITE HEADING (°TRUE)  
3 AIRCRAFT OR SATELLITE VELOCITY (M/S)  
4 AIRCRAFT OR SATELLITE ALTITUDE (FT ABOVE SEA LEVEL)  
5 RANGE DISTANCE TO NEAR EDGE OF RADAR COVERAGE (M)  
6 RADAR WAVELENGTH (1=X BAND; 2=L BAND)  
7 TRANSMITTED POLARIZATION (1=HORIZONTAL; 2=VERTICAL)  
8 RECEIVED POLARIZATION (1=HORIZONTAL; 2=VERTICAL)  
9 SIGNIFICANT WAVE HEIGHT (M)  
10 DOMINANT WAVELENGTH (M)  
11 DOMINANT WAVE DIRECTION (°TRUE)  
12 WIND SPEED (M/S)  
13 WIND DIRECTION (°TRUE)  
14 WAVES PRESENT IN IMAGERY? (0=NO DATA; 1=YES; 2=NO)  
15 WAVE DETECTABILITY AT 20° INCIDENCE ANGLE (0=NO DATA; 1=NOT DETECTED; 2=DETECTED; 3=CLEARLY DETECTED)  
16 WAVE DETECTABILITY AT 40° INCIDENCE ANGLE (0=NO DATA; 1=NOT DETECTED; 2=DETECTED; 3=CLEARLY DETECTED)  
17 WAVE DETECTABILITY AT 60° INCIDENCE ANGLE (0=NO DATA; 1=NOT DETECTED; 2=DETECTED; 3=CLEARLY DETECTED)  
18 WAVE DETECTABILITY AT 80° INCIDENCE ANGLE (0=NO DATA; 1=NOT DETECTED; 2=DETECTED; 3=CLEARLY DETECTED)



### 3.2 STATISTICAL SUMMARY

A basic question when using synthetic aperture radar (SAR) as a wave measuring device is under what conditions can a SAR detect waves and how accurately? This study has only addressed the detectability question and not the accuracy of the SAR-derived wave spectra. This latter question would require a much larger effort.

Summarizing the above data set with regard to detectability finds: the Seasat SAR detected waves in 17 of 23 overpasses or 74 percent of the time, the APD-10 X-band SAR detected waves in 30 of 33 passes or 91 percent of the time, the X-band channel of the ERIM X-L system detected waves in all 98 passes studied (100 percent), while the L-band channel detected waves in 62 of 86 passes or 78 percent of the time. It should be strongly noted that these results are only valid for the environmental conditions encountered during the various data collection flights. For example, aircraft flights were rarely conducted on days when wind and wave conditions were not conducive for imaging waves. Similarly, the JASIN and GOASEX data were collected in regions where reasonably high wave energy was expected.

#### 4 CONCLUSIONS AND RECOMMENDATIONS

The purpose of this study has been to summarize the synthetic aperture radar (SAR) ocean wave data which is archived at ERIM. This has included documenting the SAR operating parameters and environmental conditions during each pass or overflight when SAR wave data was collected. In addition, the processed imagery from these passes was manually interpreted to determine if waves were detected, and if so, how clearly.

Of the 210 passes of imagery studied, waves were imaged in 183, or 87 percent of the time. This number should not be thought of as the expected performance of a SAR in general. Typically, SAR data collection flights were only conducted on days when wind and wave conditions were suitable for producing wave imagery. More data collected over a wider range of environmental conditions is required to better define the capabilities and limitations of using SAR for ocean wave detection. Also, a wider range of SAR operating configurations over the same set of wind and wave conditions is required for system optimization.

A basic objective of documenting this data set is to provide a basis by which SAR ocean wave imaging theories can be evaluated. Wave detectability is a function of the environmental conditions and SAR system parameters. Imaging theories can suggest which are the most critical parameters or combination of parameters, and these suggestions can be tested using data such as that presented here.

Recommendations for future work in this area would be to digitize the existing wave imagery and produce digital spectral estimates. Quantitative interpretation of these estimates would remove the objectiveness of the manual interpretation used in this study.

## REFERENCES

Allan, T.D. and T.H. Guymer, Seasat and JASIN, Int. J. Remote Sensing, 1, pp. 261-267, 1980.

Allan, T.D. and T.H. Guymer, SEASAT Measurements of Wind and Waves in Selected Passed Over JASIN, Int. J. Remote Sensing, 5, pp. 379-408, 1984.

Alpers, W.R., D.B. Ross, and C.L. Rufenach, On the Detectability of Ocean Surface Waves by Real and Synthetic Aperture Radar, J. Geophys. Res., 86, 6481-6498, 1981.

Alpers, W.R. and C.L. Rufenach, The Effect of Orbit Motions on Synthetic Aperture Radar Imagery of Ocean Waves, IEEE Trans. Antennas Propagat., AP-27, pp. 685-690, 1979.

Ausherman, D.A., Digital Versus Optical Techniques in Synthetic Aperture Radar (SAR) Data Processing, Optical Eng., 19, pp. 157-167, 1980.

Brown, W.M. and L. Porcello, An Introduction to Synthetic Aperture Radar, IEEE Spectrum, 6, pp. 52-66, 1969.

Gonzalez, F.I., R.C. Beal, W.E. Brown, P.S. DeLeonibus, J.W. Sherman, J.F.R. Gower, D. Lichy, D.B. Ross, C.L. Rufenach, and R.A. Shuchman, Seasat Synthetic Aperture Radar: Ocean Wave Detection Capabilities, Science, 204, pp. 1418-1421, 1979.

Gonzalez, F.I., R.A. Shuchman, D.B. Ross, C.L. Rufenach, and J.F.R. Gower, Synthetic Aperture Radar Wave Observations During GOASEX, Oceanography from Space, ed. by J.F.R. Gower, Plenum Press, New York, pp. 459-467, 1981.

Harger, R.O., Synthetic Aperture Radar Systems, Academic Press, New York, NY, 240 pp., 1970.

Hasselmann, K., R.K. Raney, W.J. Plant, W. Alpers, R.A. Shuchman, D.R. Lyzenga, C.L. Rufenach, and M.J. Tucker, Theory of SAR Ocean Wave Imaging: A MARSEN View, submitted to J. Geophys. Res., 1983.

Jordan, R.L., The Seasat-A Synthetic Aperture Radar System, IEEE J. Oceanic Eng., OE-5, pp. 154-164, 1980.

Kasischke, E.S., Extraction of Gravity Wave Information from Synthetic Aperture Radar Data, Univ. of Mich. M.S. Thesis, 108 pp., 1980.

Kozma, A., E.N. Leith, and N.G. Massey, Tilted Plane Optical Processor, Applied Optics, 11, pp. 1766-1777, 1972.

Lyzenga, D.R. and R.A. Shuchman, Analysis of Scatterer Motion Effects in MARSEN X-Band SAR Imagery, J. Geophys. Res., 88, pp. 9769-9775, 1983.

## REFERENCES (Continued)

McLeish, W., D.B. Ross, R.A. Shuchman, P.G. Teleki, S.V. Hsiao, O.H. Shemdin, and W.E. Brown, Synthetic Aperture Radar Imaging of Ocean Waves: Comparison with Wave Measurements, J. Geophys. Res., 85, pp. 5003-5011, 1980.

Meadows, G.A., R.A. Shuchman, and J.D. Lyden, Analysis of Remotely Sensed Long-Period Wave Motions, J. Geophys. Res., 87, pp. 5731-5740, 1982.

Plant, W.J. and W.C. Keller, The Two-Scale Radar Wave Probe and SAR Imagery of the Ocean, J. Geophys. Res., 88, pp. 9776-9784, 1983.

Raney, R.K., Synthetic Aperture Imaging Radar and Moving Targets, IEEE Trans. Aerospace Elect. Syst., AES-7, pp. 499-505, 1971.

Rawson, R., F. Smith, and R. Larson, The ERIM X- and L-Band Dual Polarized Radar, IEEE 1975 International Radar Conference, New York, p. 505, 1975.

Schwab, D.J., R.A. Shuchman, and P.L. Liu, Wind Wave Directions Determined from Synthetic Aperture Radar Imagery and from a Tower in Lake Michigan, J. Geophys. Res., 86, pp. 2059-2064, 1981.

Shemdin, O.H., The Marineland Experiment: An Overview, Trans. Amer. Geophys. Union, 61, No. 38, pp. 625-626, 1980.

Shemdin, O.H., W.E. Brown, Jr., F.G. Staudhammer, R.A. Shuchman, R. Rawson, J. Zelenka, D.B. Ross, W. McLeish, and R.A. Beres, Comparison of In-Situ and Remotely Sensed Ocean Waves Off Marineland, Florida, Boundary Layer Meteorol., 13, pp. 225-234, 1978.

Shuchman, R.A., R.F. Lawson, and E.S. Kasischke, Analysis of Synthetic Aperture Radar Ocean Wave Data Collected at Marineland and Georges Banks, ERIM Report No. 123000-11-F, 129 pp., 1977.

Shuchman, R.A. and O.H. Shemdin, Synthetic Aperture Radar Imaging of Ocean Waves During the Marineland Experiment, IEEE J. Oceanic Eng., OE-8, pp. 83-90, 1983.

Shuchman, R.A., W. Rosenthal, J.D. Lyden, D.R. Lyzenga, E.S. Kasischke, H. Gunther, and H. Linne, Analysis of MARSEN X-Band SAR Ocean Wave Data, J. Geophys. Res., 88, pp. 9757-9768, 1983.

Shuchman, R.A., J.D. Lyden, and D.R. Lyzenga, Estimates of Ocean Wavelength and Direction from X- and L-band Synthetic Aperture Radar Data Collected During the Marineland Experiment, IEEE J. Oceanic Eng., OE-8, pp. 90-96, 1983.

Shuchman, R.A. and G.A. Meadows, Airborne Synthetic Aperture Radar Observations of Surf Zone Conditions, Geophys. Res. Lett., 7, pp. 857-860, 1980.

## REFERENCES (Concluded)

Vesecky, J.F., H.M. Assal, R.H. Stewart, R.A. Shuchman, E.S. Kasischke, and J.D. Lyden, Seasat-SAR Observations of Surface Waves, Large Scale Surface Features and Ships During the JASIN Experiment, 1982 Int. Geoscience and Remote Sensing Symposium Digest, Munich, Germany, pp. WP-3, 1.1-1.6, 1982.

Wu, C., B. Barkan, B. Huneycutt, C. Leang, and S. Pang, An Introduction to the Interim Digital SAR Processor and the Associated Seasat SAR Imagery, JPL Publication 81-26, Pasadena, CA, 1981.

## APPENDIX

Contained in this Appendix are a series of reprints which describe in more detail the experiments during which the SAR ocean wave imagery summarized in this report were collected. These articles are presented in alphabetical order according to first author, as summarized in Table A1. The figures contained in this Appendix are xerox copies, not half-tone prints.

TABLE A1  
PAPERS IN APPENDIX

- A. Gonzalez, F.I., R.A. Shuchman, D.B. Ross, C.L. Rufenach, and J.F.R. Gower, Synthetic Aperture Radar Wave Observations During GOASEX, Oceanography from Space, ed. by J.F.R. Gower, Plenum Press, New York, pp. 459-467, 1981.
- B. Lyzenga, D.R. and R.A. Shuchman, Analysis of Scatterer Motion Effects in MARSEN X-Band SAR Imagery, J. Geophys. Res., 88, pp. 9769-9775, 1983.
- C. Meadows, G.A., R.A. Shuchman, and J.D. Lyden, Analysis of Remotely Sensed Long-Period Wave Motions, J. Geophys. Res., 87, pp. 5731-5740, 1982.
- D. Schwab, D.J., R.A. Shuchman, and P.L. Liu, Wind Wave Directions Determined from Synthetic Aperture Radar Imagery and from a Tower in Lake Michigan, J. Geophys. Res., 86, pp. 2059-2064, 1981.
- E. Shuchman, R.A., J.D. Lyden, and D.R. Lyzenga, Estimates of Ocean Wavelength and Direction from X- and L-band Synthetic Aperture Radar Data Collected During the Marineland Experiment, IEEE J. Oceanic Eng., OE-8, pp. 90-96, 1983.
- F. Shuchman, R.A. and O.H. Shemdin, Synthetic Aperture Radar Imaging of Ocean Waves During the Marineland Experiment, IEEE J. Oceanic Eng., OE-8, pp. 83-90, 1983.
- G. Shuchman, R.A. and G.A. Meadows, Airborne Synthetic Aperture Radar Observations of Surf Zone Conditions, Geophys. Res. Lett., 7, pp. 857-860, 1980.
- H. Shuchman, R.A., W. Rosenthal, J.D. Lyden, D.R. Lyzenga, E.S. Kasischke, H. Gunther, and H. Linne, Analysis of MARSEN X-Band SAR Ocean Wave Data, J. Geophys. Res., 88, pp. 9757- 9768, 1983.
- I. Vesecky, J.F., H.M. Assal, R.H. Stewart, R.A. Shuchman, E.S. Kasischke, and J.D. Lyden, Seasat-SAR Observations of Surface Waves, Large Scale Surface Features and Ships During the JASIN Experiment, 1982 Int. Geoscience and Remote Sensing Symposium Digest, Munich, Germany, pp. WP-3, 1.1-1.6, 1982.

From: OCEANOGRAPHY FROM SPACE  
Edited by J.F.R. Gower  
(Plenum Publishing Corporation, 1981)

SYNTHETIC APERTURE RADAR WAVE OBSERVATIONS DURING GOASEX

F.I. Gonzalez  
National Oceanic and Atmospheric Administration  
Pacific Marine Environmental Laboratory  
Seattle, Washington 98105  
U.S.A.

R.A. Shuchman  
Environmental Research Institute of Michigan  
Radar and Optics Division  
Ann Arbor, Michigan 48107  
U.S.A.

D.B. Ross  
National Oceanic and Atmospheric Administration  
Sea Air Interaction Laboratory  
Miami, Florida 33149  
U.S.A.

C.L. Rufenach  
National Oceanic and Atmospheric Administration  
Wave Propagation Laboratory  
Boulder, Colorado 80303  
U.S.A.

J.F.R. Gower  
Institute of Ocean Sciences  
Sidney, British Columbia V8L4B2  
CANADA

1. ABSTRACT

A comparison of airborne and satellite synthetic aperture radar wave imagery and coincident surface wave observations indicates that for the range of environmental conditions encountered, the radar estimates of dominant wavelength and direction are of equal or better accuracy than the corresponding in-situ estimates.



## 2. INTRODUCTION

This short paper concerns itself with the ocean wave detection capabilities of synthetic aperture radar (SAR). A more detailed report of this work is in preparation. A major field experiment, the September 1978 Gulf of Alaska SEASAT Experiment (GOASEX), provided surface wave measurements coincident with aircraft and satellite SAR imagery. A preliminary assessment of this data was primarily qualitative (Gonzalez et al, 1979). The present work quantifies the correlation among surface and radar estimates for those ocean waves successfully detected by SAR. This report also qualitatively discusses a separate but related issue, that of the dependence of SAR wave image quality on viewing geometry and environmental conditions.

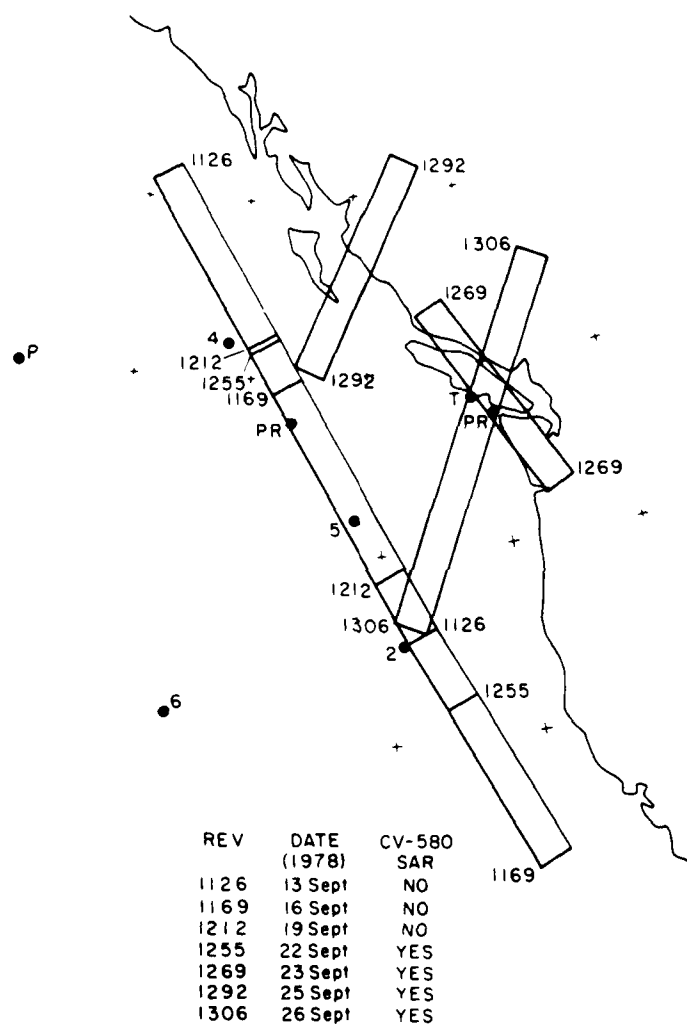
## 3. EXPERIMENTAL RESULTS AND DISCUSSION

Satellite L-band SAR imagery was acquired in the Northeast Pacific during seven Seasat revolutions (Revs); on four of these Revs, coincident airborne SAR images were obtained by the ERIM dual polarized X- and L-band SAR (Rawson et al, 1975) on the Canadian CV-580 aircraft. Coincident surface observations were also made: estimates of directional wave energy spectra were computed from measurements collected by a pitch-roll (PR) buoy; similarly, estimates of one-dimensional wave energy spectra were obtained by NOAA data buoys; surface windspeed and direction measurements were made at all buoy sites. This coverage is summarized in Figure 1. Surface wind speeds encountered in this data set ranged from 2 to 14 m/s; multiple wave systems were common, with a range of significant wave heights from 1 to 3.5 m and wavelengths of from 100 to 500 m.

In what follows, the in-situ estimates of dominant wavelength and direction correspond to peaks in the wave energy spectra computed from buoy measurements; similarly, SAR estimates correspond to peaks in the image intensity spectra obtained by two dimensional Fourier transforms of the SAR scenes.

### 3.1 Aircraft data

Each aircraft mission over the PR buoy included a multi-sided box pattern designed to image the dominant waves from various directions. Figure 2 presents the results obtained as a function of viewing angle for the pattern flown coincident with Seasat Rev 1269. Only parallel polarized imagery has been examined. On this occasion, a dominant wave system of length 150 m and significant height of 2.5 m was present, with wind speeds averaging about 5 m/s. We see that SAR estimates obtained for all viewing angles are in reasonable agreement with surface observations; in particular, we note agreement on flight lines (1) and (4), for which the waves were propagating within a few degrees of azimuth.



## SURFACE OBSERVATIONS

- N NOAA data buoy 4600N
- PR Pitch-roll buoy aboard R/V Oceanographer
- T Waverider buoy at Tofino, B.C.

Fig. 1: SAR and surface observation coverage during GOASEX.

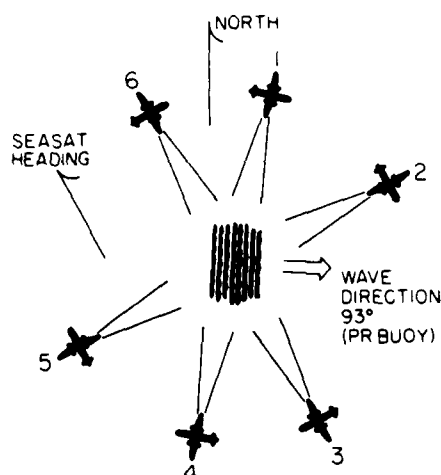
This is significant, because the dependence of SAR ocean wave detectability on viewing geometry and environmental conditions is of some concern; specifically, it appears that wave image quality deteriorates as the wave becomes more nearly azimuthal (Shuchman et al, 1978; Vesecky et al, this volume). It is unclear, however, under what range of environmental conditions a SAR will or will not detect a purely azimuthal wave, and instances of both failed and successful azimuth wave detection have been reported for airborne radar (Elachi, 1978; Shemdin et al, 1978).

The environmental effects on image quality for waves propagating in range (the cross-track coordinate) is somewhat better understood; the primary imaging mechanisms appear to be modulation of radar cross section through tilting and hydrodynamic straining of the relatively short wavelength Bragg scatterers by the longer dominant waves (Elachi and Brown, 1977). Higher and shorter dominant long waves should cause greater tilting and hydrodynamic straining due to larger mean slopes and velocities, though it should be noted that the effects of these two mechanisms could act in concert or opposition.

With this last caveat in mind, a possible interpretation can be made of the data presented in Table 1 for primarily range propagating waves. This table summarizes the satellite and aircraft results processed so far for the particular box pattern flight line which was oriented parallel to the Seasat track for each of three different aircraft missions.

Of special interest is the data collected during Rev 1306. The PR buoy and Tofino Waverider data indicate the presence of a low energy wave system ( $H_s$  about 1 m) composed of three identifiable dominant waves (256, 130, and 19 m), and closer examination of the wave energy spectra indicates roughly equal partition of the total energy among the three systems (individual values of  $H_s$  about .6 m). It is significant that there was a complete failure by all SAR systems employed in this experiment to detect the relatively longer dominant wave, in contrast to the successful detection of the intermediate and short waves of this trio, and the intermediate but more energetic waves present on Revs 1255 and 1269. Furthermore, a visual examination shows that the more energetic wave in Rev 1269 is more clearly imaged than its less energetic counterpart of comparable length in Rev 1306.

These results are consistent with the previous discussion of backscatter modulation through tilting and straining, and suggest that, at least for range waves, some measure of root mean square slope and/or orbital velocity should be used to characterize the lower limits of SAR ocean wave detectability, rather than simply the significant wave height of the entire system, as has been suggested previously (Gonzalez et al, 1979).



PLATFORM HEADING (DEGREES TRUE)	SAR SYSTEM	*SEASAT			**ERIM CV-580			**ERIM CV-580			RELATIVE WAVE HEADING
		(L-BAND)			(L-BAND)			(X-BAND)			
		$\lambda$ (m)	$\theta_t$ Deg	$\theta_A$ Deg	$\lambda$ (m)	$\theta_t$ Deg	$\theta_A$ Deg	$\lambda$ (m)	$\theta_t$ Deg	$\theta_A$ Deg	
102				159	98	356	158	97	355	CROSSWAVE (1)	
152				152	110	318	142	115	323	UPWAVE (2)	
242				162	103	221	168	96	214	UPWAVE (3)	
283				177	108	185	177	108	185	CROSSWAVE (4)	
333		165	94	121	138	109	136	167	109	136	DOWNWAVE (5)
62					141	101	39	153	113	51	DOWNWAVE (6)

From P/R Buoy:  $\lambda = 151$  m

$\theta_e = 093$  deg.

\* Optical Fourier Transform Data

\*\* Digital Fourier Transform Data

Fig. 2: CV-580 and SEASAT SAR wave observations during Rev 1269 September 28, 1978. Airborne observations were made with 6 different viewing angles as illustrated.

Table 1. Coincident SEASAT, CV-580,  
and Pitch-Roll buoy observations

Rev		SEASAT SAR	CV-580 SAR		PR Buoy
			X-Band	L-Band	
1255	$\lambda$ $\theta_T$ $\theta_A$	187 m 96° 135°	193 m 87° 124°	210 m 96° 135°	177 m $H_s = 2.7$ m 93° 121° Wind 8.3 m/s from 243°
1269	$\lambda$ $\theta_T$ $\theta_A$	165 m 93° 121°	167 m 109° 136°	138 m 109° 136°	151 m $H_s = 2.5$ m 93° 121° Wind 5.1 m/s from 90°
1306	$\lambda$ $\theta_T$ $\theta_A$	Undet.	Undet.	Undet.	256 m <sup>c</sup> $H_s = 1.1$ m 336° 128° Wind 11.8 m/s from 100°
1306	$\lambda$ $\theta_T$ $\theta_A$	130 m <sup>b</sup> 95° <sup>b</sup> 248° <sup>b</sup>	128 m 95° 248°	Det. <sup>d</sup>	130 m <sup>c</sup> $H_s = 1.1$ m 105° 258° Wind 11.8 m/s from 100°
1306	$\lambda$ $\theta_T$ $\theta_A$	Undet.	22 m 293° 84°	Det. <sup>d</sup>	19 m <sup>c</sup> $H_s = 1.1$ m 274° 66° Wind 11.8 m/s from 100°

The notation used is  $\lambda$  for wavelength,  $\theta_T$  for wave direction referred to true North,  $\theta_A$  for wave direction referred to azimuth (the along-track coordinate of SEASAT),  $H_s$  for significant wave height.

<sup>b</sup> Undetected in optically processed imagery of 40 m resolution, and detected only with difficulty in contrast-enhanced, digitally processed imagery of 20 m resolution.

<sup>c</sup> Corresponding peaks were found in wave energy spectra obtained by a Waverider buoy at a site 75 km away, near Tofino, British Columbia.

<sup>d</sup> Detected by visual examination only. No transforms available.

### 3.2 Satellite data

A sufficient number of SEASAT SAR/surface observation pairs exist to justify an estimate of their correlation by linear regression analysis. Sixteen pairs were obtained for wavelength, only seven (from the PR buoy) for direction. The results are presented in Figure 3. Error bars for buoy wavelength measurements are determined by the finite frequency intervals for which the spectral estimates are computed; error bars for the PR estimates of mean direction correspond to the half-width of the directional peak. Error bars for the satellite observations reflect the conservative, albeit subjective judgement that individual peaks in image intensity spectra can generally be located with confidence in a circle of 1 mm diameter on the scale of the original data. (An exception is the larger set of error bars assigned to the extremely weak and diffuse maximum for Rev 1306. See note for Table 1.) We see that a high degree of correlation exists for both wavelength and direction. No statistical significance can be attached to the deviation of the slopes from unity and the relatively small biases indicated.

It is probable that SAR estimates of dominant wave direction are superior to those of in-situ buoys. In at least one case the radar evidently detected two dominant waves, similar in length and propagating within 30 degrees of one another, which the PR buoy failed to resolve. The relatively small error bars for the SAR directional estimates should be noted.

With regard to azimuth wave detection, the SEASAT SAR indicated propagation directions within 45 degrees of azimuth for 5 of the sixteen wavelength data pairs of Figure 3. Only one pair included a PR buoy estimate of direction, however, and in that case the associated error bar was so large that the data point was edited (Figure 3); nonetheless, the agreement in wavelength for all 5 data pairs is strong indirect evidence of successful azimuth wave detection.

A separate case of azimuth wave detection, not considered in detail here, should also be mentioned. On a Rev which imaged the region offshore of Baja, California, waves were clearly detected traveling within a few degrees of azimuth (NASA, 1980). These waves were apparently generated some 58 hours earlier by hurricane Gilma; using hurricane parameters estimated from satellite imagery, a parametric model (Ross, 1976) has been used to hindcast a wavelength of about 250 m, in good agreement with the SAR estimates.

### 4. CONCLUSIONS

The data presented here suggest that, for the limited environmental conditions encountered: (1) dominant wavelength estimates by SAR are at least as accurate as the standard surface observations by buoy; (2) the SAR directional estimates are probably superior;

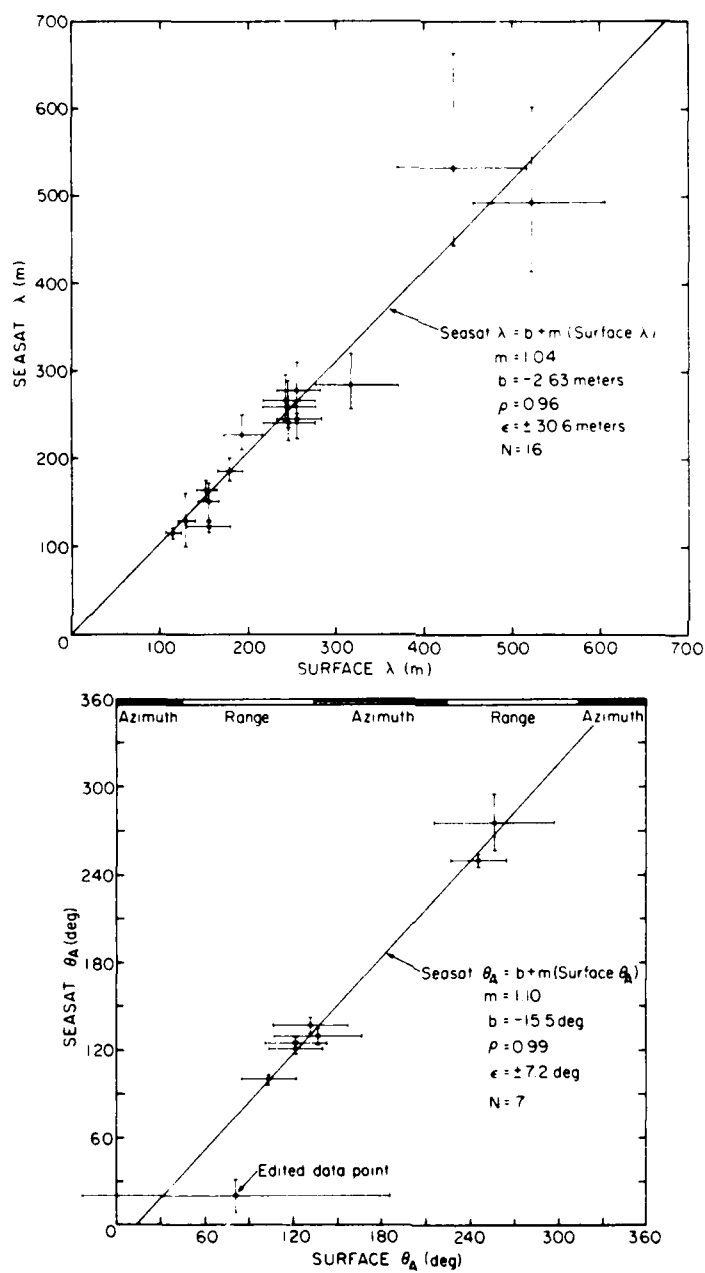


Fig. 3: Results of a regression analysis for SEASAT SAR and surface buoy estimates of dominant wavelength and direction.

(3) both SEASAT and CV-580 SAR successfully detected waves with significant azimuth components; (4) for range waves, a measure of rms slope and/or orbital velocity may be more appropriate than significant wave height for the characterization of sea state in studies of SAR ocean wave image quality.

#### 5. ACKNOWLEDGEMENTS

The NOAA portion of this research was supported by the NOAA SEASAT Project, under the management of Mr. John W. Sherman III.

The ERIM portion of this research was supported by NOAA/NESS-NASA AO Contract No. MO A01-78-00-4322.

The IOS portion of this research was supported by the Canadian Surveillance Satellite (SURSAT) Project.

The authors benefitted from numerous discussions with members of the SEASAT SAR experiment team. Thanks are especially due to W.E. Brown, Jr. and B. Holt of JPL for providing much of the satellite imagery used in this study. W. Stromberg of JPL and A. Klooster of ERIM generated the Fourier transforms used in the analysis.

#### REFERENCES

- Elachi, C. and Brown Jr., W.E., 1977, "Models of Radar Imaging of the Ocean Surface Waves," IEEE Trans., AP-25, 84-95.
- Elachi, C., 1978, "Radar Imaging of the Ocean Surface," Boundary-Layer Met., 13, 165-179.
- Gonzalez, F.I., Beal, R.C., Brown Jr., W.E., DeLeonibus, D.S., Gower, J.F.R., Lichy, D., Ross, D.B., Rufenach, C.L., Sherman III, J.W., and Shuchman, R.A., 1979, "SEASAT Synthetic Aperture Radar: Ocean Wave Detection Capabilities," Science, 204, 1418-1421.
- NASA, 1980, "SEASAT Gulf of Alaska Workshop II Report," Jet Propulsion Laboratory Report No. 622-107, January.
- Rawson, R., Smith, F. and Larson, R., 1975, "The ERIM Simultaneous X- and L-Band Dual Polarized Radar," Proceedings of the IEEE 1975 International Radar Conference, New York, 505.
- Ross, D.B., 1976, "A Simplified Model for Forecasting Hurricane Generated Waves," (Abstract), Bull. Am. Meteorological Soc.
- Shemdin, O.H., Brown Jr., W.E., Staudthammer, F.G., Shuchman, R., Rawson, R., Zelenka, J., Ross, D.B., McLeish, W. and Berles, R.A., 1978, "Comparison of In-Situ and Remotely Sensed Ocean Waves off Marineland, Florida," Boundary-Layer Met., 13, 193-203
- Shuchman, R.A., Kasischke, E.S. and Klooster, A., 1978, "Synthetic Aperture Radar Ocean Wave Studies," Environmental Research Institute of Michigan, Report No. 131700-3-F.



## Analysis of Scatterer Motion Effects in Marsen X Band SAR Imagery

D. R. LYZENGA AND R. A. SHUCHMAN

*Radar and Optics Division, Environmental Research Institute of Michigan, Ann Arbor, Michigan 48107*

Synthetic aperture radar X band images collected over the North Sea during the 1979 MARSEN experiment show numerous apparent point scatterers imaged with a degraded resolution in the along-track direction. The observed resolution of these features is consistent with a scatterer coherence time of the order of  $10^{-2}$  s or a vertical acceleration of the order of  $5 \text{ m/s}^2$ . Observations of the resolution as a function of the processor integration time tend to support the coherence time explanation. Similar coherence times have been measured for breaking waves by conventional high-resolution radars, suggesting that the same phenomena may be responsible for the features observed on the synthetic aperture radar imagery.

## 1. INTRODUCTION

Synthetic aperture radar (SAR) data were collected over the North Sea during the Maritime Remote Sensing (MARSEN) experiment in the fall of 1979. X band (3-cm wavelength) SAR images obtained at higher wind speeds during this experiment are dominated by bright features which change in appearance from essentially pointlike objects at near range to elongated streaks at far range. The streaks are always aligned in the along-track or azimuth direction, indicating that they are the result of localized scatterers which are imaged at reduced resolution in azimuth because of the motion or finite coherence time of the scatterers.

In this paper, measurements of the streak lengths as a function of range are compared with calculations of the azimuth resolution assuming various motion parameters, and conclusions are drawn as to the probable cause of the observed image features. Comparisons are also made with conventional radar observations of breaking waves, and the properties of these radar returns are shown to be consistent with the properties of the observed SAR image features.

## 2. DATA DESCRIPTION

The data sets studied during the present investigation consist of six passes of X band SAR imagery collected by the APD-10 system over the North Sea. The AN/UPD-4 SLAR system is an X band synthetic aperture radar developed by Goodyear for the military and mounted in an F-4 jet aircraft. The APD-10 is the radar system portion of the UPD-4 system which includes a ground data processing unit. The data presented in this study was processed at ERIM, using its precision optical processor.

The APD-10 sensor was one among several remote sensing instruments used to collect data as part of the 1979 MARSEN experiment. APD-10 data were collected over a 2-day period (September 27 and 28, 1979) during which the wind speed varied from 3.5 m/s to 10.3 m/s while the wave conditions remained fairly constant. The wind and wave conditions during the overflights considered in this paper are presented in Table 1.

The data collected by the APD-10 system are recorded separately in four slant range intervals, referred to as sub-

swaths A-D. The slant range varies from 4.6 km at the near edge of subswath A to 23.2 km of the far edge of subswath D, corresponding to a range of incidence angles from approximately  $40^\circ$  to  $80^\circ$  for the altitude (3.5 km) at which the aircraft was flown. Additional APD-10 SAR system parameters relevant to this study are as follows:

- A altitude, = 3.5 km;
- V platform velocity, = 200 m/s;
- R range, = 4.6-23.2 km;
- $\theta$  incidence angle, =  $40^\circ$  to  $80^\circ$ ;
- $\lambda$  wavelength, = 3.1 cm;
- $\beta$  azimuth antenna beamwidth, = 0.0252 rad;
- PRF pulse repetition frequency, = 1300 Hz;
- nominal processed resolution = 3 m.

The data sets analyzed in this paper include four segments collected during the highest wind speed (10.3 m/s) on September 27 and two segments collected during an intermediate wind condition (7.5 m/s) on September 28. The significant wave height was approximately 1.0 m on the first day and 1.2 m on the second day, with a period of 7.5 s in both cases. The radar look directions relative to the wind direction and wave propagation direction are shown in Table 2 for each of the data segments considered. Examples of the imagery obtained on September 27 and 28 are shown in the companion paper by Shuchman *et al.* [this issue]. All of the data considered in this paper were collected in relatively deep water (30 m) near the Nordsee tower in the German Bight.

## 3. MEASUREMENTS

Extensive image streaking occurred in all of the SAR data over the North Sea except that collected at the lowest wind speed. Land features were imaged with good resolution, indicating that the streaking over water was not due to a system malfunction. During the lowest wind speed (3.5 m/s), very few of these features were observed except near the coastline, where wave shoaling occurred. An enlargement of subswath C of the September 27 data is presented in Figure 1. Note that the streaks are always parallel with the flight path, indicating they are localized scatterers which are imaged with a degraded resolution in the azimuth direction.

The observed streak lengths are smaller than the synthetic aperture length (i.e., the antenna beamwidth multiplied by the range distance), indicating that some azimuth compression of the signals is occurring. Thus the observed lengths

Copyright 1983 by the American Geophysical Union.

Paper number 201861.  
0148-0227/83/0020-1861\$05.00

TABLE 1. Wind and Wave conditions at Time of Data Collection Over MARSEN Test Site on September 27 and 28, 1979

	September 27	September 28
Wind speed	10.3 m/s	7.5 m/s
Wind direction	110°	90°
Significant wave height	1.0 m	1.2 m
Dominant wave period	7.5 s	7.5 s
Dominant wave direction	77°	133°

are apparently determined by the characteristics of the scatterers and are not limited by the SAR system itself. The signals were observed to persist over essentially the entire SAR integration time by reducing the processor integration time and noting the appearance of the image features. Figure 2 shows a set of enlarged images obtained by processing data from pass 10-3, swath B with three different integration time settings. The antenna-limited integration time is approximately 1.5 s for swath B, while the normal processor setting for the data presented elsewhere in this report corresponds to an integration time of 0.9 s for swath B. Note that although there is a slight change in the signal-to-noise ratio, the streaked image features persist and their appearance is essentially the same in each of these images. The lengths of the features were also observed to be relatively unaffected by changes in the processor focus settings.

The lengths of the image streaks increase dramatically from subswath A to subswath D. In order to quantify this range dependence, image subsets were selected from the center of each subswath and were digitized for further analysis. The range and incidence angle at the center of each subswath is shown in Table 3. The method of measuring the effective azimuth resolution for the streaks was to compute the autocorrelation function for the images using fast Fourier transforms (FFT) of the digitized data. A typical set of FFT's for all four subswaths of one of the data segments (pass 12-4) is shown in Figure 14 of the companion paper [Shuchman *et al.*, this issue]. The squared amplitude of the image FFT was inverse-transformed to yield the image autocorrelation function. One-dimensional plots of the autocorrelation in the azimuth direction for pass 12-4 are shown in Figure 3. These plots apparently contain a component due to random noise and speckle, which is manifested as a narrow spike at zero shift. This component was ignored and the 3-dB width of the wider part of each curve was measured.

The results of the correlation length measurements for all six passes are summarized in Figure 4. This figure shows an approximately linear dependence of the streak lengths on

range. Although there is some variability in the lengths at a given range, this variability does not appear to be correlated with either the wind or the wave direction (see Table 2). The lengths for the September 28 data are smaller than for September 27, indicating a possible dependence on the wind speed. The kinds of scatterer motions which are consistent with these observations are discussed in the following section.

#### 4. THEORETICAL CONSIDERATIONS

The image features described in the previous section represent the SAR response to a set of point scatterers which are smeared in the azimuth direction due to the motion of the finite lifetimes of the scatterers. In this section, we review the theory which describes the degradation in the azimuthal resolution for such scatterers and calculate the dependence of the resolution on the range and incidence angle.

For a stationary point scatterer, the nominal azimuthal resolution ( $\rho_a$ ) of a SAR image processed at full bandwidth is

$$\rho_a = \frac{\lambda}{2\beta} \frac{D}{2} \quad (1)$$

where  $\lambda$  is the radar wavelength,  $\beta$  is the antenna beamwidth, and  $D$  is the physical length of the antenna in the azimuth direction. The radar wavelength, antenna beamwidth and other system parameters for the APD-10 system have been presented above. The resolution indicated by (1) is a theoretical limit and is not attained in practice because of uncorrected platform motions as well as target motions. The resolution is also limited by the bandwidth or integration time of the processor. This effect can be taken into account by replacing the actual antenna beamwidth  $\beta$  by an effective value which is determined by the processor characteristics and settings. For the data discussed in this paper, the processor was set to yield an effective antenna beamwidth of 0.0155 radians, and subsequent multi-looking was done to achieve a nominal azimuth resolution of 3 for stationary scatterers. This effective beamwidth was used in all of the calculations involving  $\beta$  in this paper.

The resolution indicated by (1) is realized only if the scatterers are stationary and the scattering cross section remains constant over the integration time interval

$$T = \frac{\beta R}{V} \quad (2)$$

during which the scatterer is within the antenna beam, where  $R$  is the range distance to the target and  $V$  is the platform

TABLE 2. Radar Look Directions for Six Data Segments Studied

Pass	Date	Time, UT	Aircraft Heading, °	Look Direction With Respect to Wind, °	Look Direction With Respect to Waves, °
12-1	Sept. 27, 1979	0840-0850	297	83	50
12-2	Sept. 27, 1979	0854-0900	283	97	64
12-3	Sept. 27, 1979	0902-0908	056	36	69
12-4	Sept. 27, 1979	0912-0917	191	171	156
10-1	Sept. 28, 1979	0954-0958	283	77	120
10-3	Sept. 28, 1979	1012-1017	191	169	148

\*Radar look direction measured clockwise from wind direction (0° would be looking downwind).

†Radar look direction measured clockwise from wave propagation direction (0° would be looking downwave).

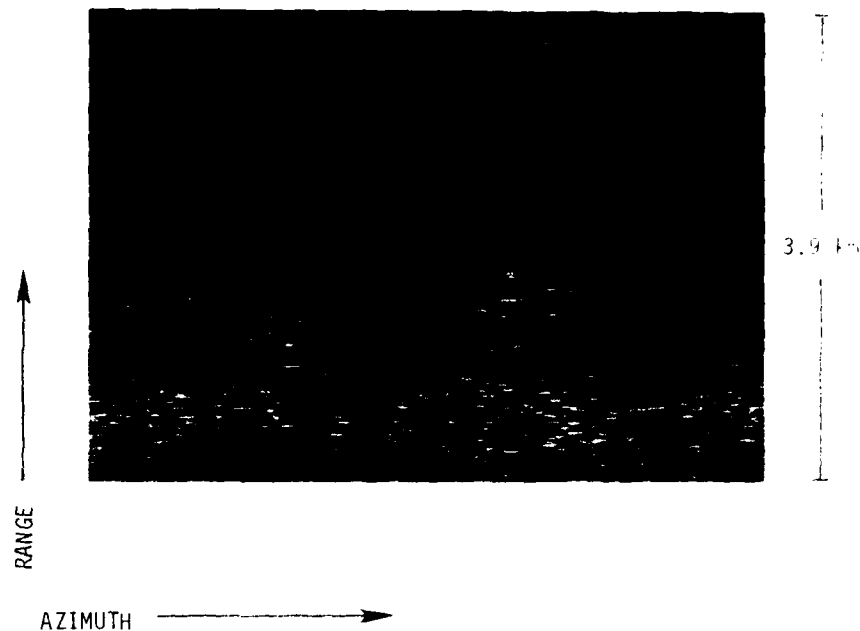


Fig. 1. Enlargement of a portion of swath C image for pass 12-4 (September 27, 1979) showing image streaks aligned in azimuth direction.

velocity. If the radar cross section fluctuates during this time interval, such that the temporal autocorrelation function of the scattering cross section has a width  $\tau$ , the resolution is reduced [Raney, 1980] to

$$\rho_{az} = \frac{\lambda}{2\beta} \left[ 1 + \left( \frac{BR}{V\tau} \right)^2 \right]^{1/2} \quad (3)$$

The coherence time  $\tau$  which enters this expression corresponds to the decorrelation time which might be measured, for example, by a scatterometer mounted on the SAR platform if the scatterometer were able to track the object's position continuously during the time  $T$ . It does not describe the gross motion of the scatterer (which is accounted for below) but may be due to random particle motions within the resolution cell. In fact, a completely equivalent expression for the azimuthal smearing can be obtained by assuming that the feature contains a distribution of radial velocities of width  $\delta V$ , and equating  $\delta V$  with  $\lambda/2\tau$ . This expression follows directly from the azimuthal displacement formula

$$\Delta x = V_r \frac{R}{V} \quad (4)$$

given by Raney [1971]. Such a model would also predict a fluctuation in the power received from the resolution cell due to interference of the returns from each scattering center within the cell. Note that this model implies that for a given physical distribution of scatterer velocities the coherence time would be proportional to  $\lambda$ . In fact, however, the scattering elements are likely to be different for widely different radar wavelengths, so this proportionality is probably only approximate at best.

If the coherence time is much smaller than the integration time  $T$ , the azimuth resolution is approximately

$$\rho_{az} = \frac{\lambda R}{2V\tau} \quad (5)$$

Thus if the coherence time were proportional to  $\lambda$  as suggested above, the resolution of rapidly fading scatterers would be independent of the wavelength. The resolution is also independent of the antenna beamwidth or processor integration time. Note that the effect of scatterer coherence time depends on the ratio  $R/V$ . Typical values for  $R/V$  are 25–100 s for the UPD-4, 50–100 s for the ERIM CCRS A and L band SAR, and 120 s for SEASAT. A plot of  $\rho_{az}$  versus range for the APD-10 system is shown in Figure 5a for coherence times of 0.01 and 0.10 s. It is important to note that the loss of resolution due to coherence time is a true smearing and not a defocusing and is therefore not recoverable by a change in the processor focus or integration time settings.

In addition to coherence time effects, the SAR azimuthal resolution is influenced by gross scatterer motions. The motion parameters which primarily influence the azimuthal resolution are the azimuth component of the velocity and the range component of the acceleration. Both of these types of motion cause a defocusing effect which is correctible by a change in the focus settings of the processor. For a coherent scatterer with a range acceleration  $a_r$ , the azimuthal resolution [Raney, 1971] is

$$\rho_{az} = \frac{\lambda}{2\beta} \left[ 1 + \left( \frac{2\beta^2 R^2 a_r}{\lambda V^2} \right)^2 \right]^{1/2} \quad (6)$$

The asymptotic expression for  $a_r \rightarrow \lambda/2T^2$  is

$$\rho_{az} = \frac{BR^2 a_r}{V} \quad (7)$$

which has a stronger range dependence than the coherence time effect described above and is also dependent on the antenna beamwidth or, equivalently, the processor integration time. The factor  $BR^2/V^2$  varies from about 10 to 150 s across the swath for the APD-10. For the ERIM CCRS A

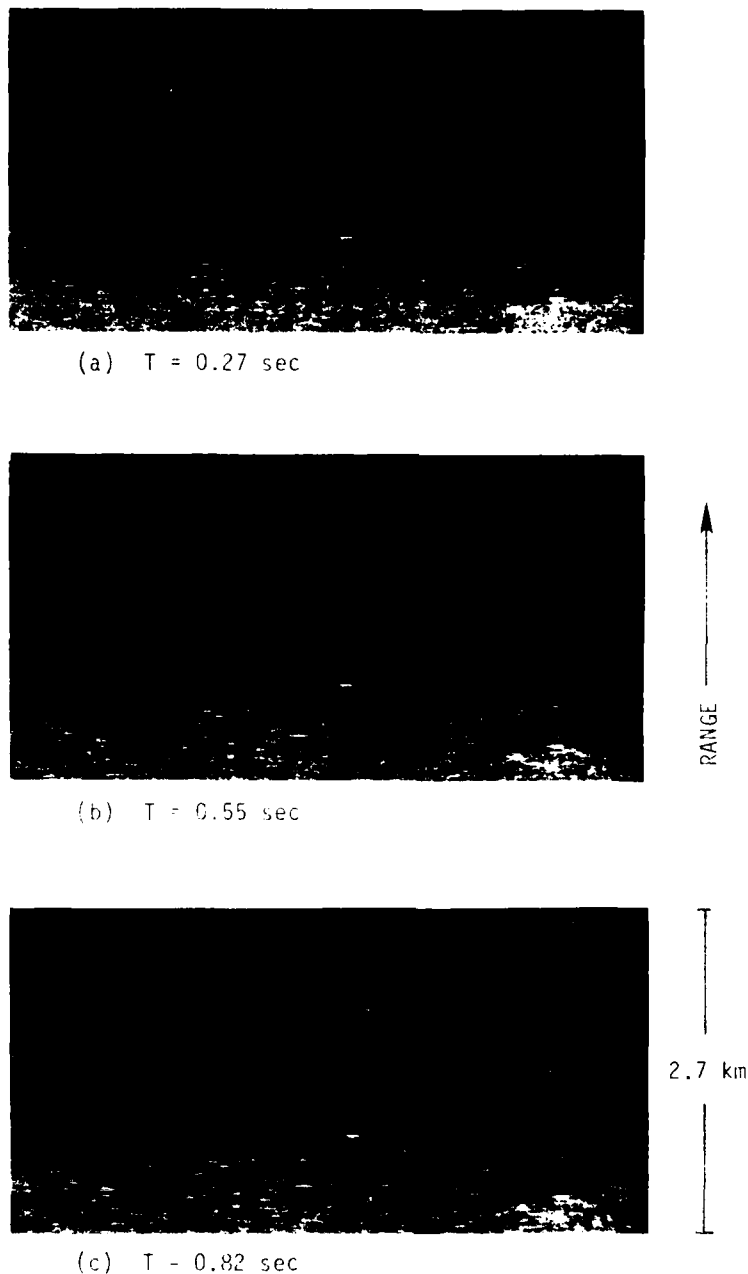


Fig. 2. Images generated from pass 10-3 (September 28, 1979) swath B data using three different processor integration time settings: (a) 0.27 s; (b) 0.55 s; (c) 0.82 s.

and  $L$  band SAR, this factor typically ranges from about 50 to  $200 \text{ s}^2$  at  $X$  band and from 300 to  $1200 \text{ s}^2$  at  $L$  band, while for SEASAT it is approximately  $300 \text{ s}^2$ . SAR system parameters for the SEASAT and ERIMCCRS system are as follows:

#### SEASAT SAR:

- $R$  range, 840 km,
- $V$  platform velocity, 7 km/s,
- $\beta$  antenna beamwidth, 0.02 rad.

#### ERIMCCRS $X/L$ band SAR:

- $R$  range, 6–12 km;
- $V$  platform velocity, 120 m/s;
- $\beta$   $X$  band antenna beamwidth, 0.019 rad;
- $\beta$   $L$  band antenna beamwidth, 0.122 rad.

It is instructive to consider the effects of horizontal and vertical accelerations separately. The range component of a horizontal acceleration  $a_x$  is given by

$$a_r = a_x \sin \theta \cos \phi \quad (8)$$

TABLE 3. Range and Incidence Angle for Each Image Area Selected for Analysis

Subswath	Range, km	Incidence Angle
A	7.0	60
B	11.6	72
C	16.2	78
D	20.8	80

where  $\theta$  is the incidence angle and  $\phi$  is the angle between the acceleration vector and the cross-track direction. Substituting this into (6) results in the effective azimuthal resolution shown in Figure 5b for the APD-10 system. The results plotted in Figure 5b are for three look directions relative to the wave propagation direction, assuming a horizontal acceleration of  $1 \text{ m/s}^2$  in the direction of wave propagation. This value for  $a_h$  is a liberal estimate based on the wave conditions of the time of the overflights.

For vertical accelerations, the range component of the acceleration  $a_r$  is given by

$$a_r = a_v \cos \theta = a_v \frac{A}{R} \quad (9)$$

where  $A$  is the platform altitude. Thus the asymptotic expression for the azimuthal resolution is

$$\rho_{a2} \approx \beta A \frac{R}{v^2} a_v \quad (10)$$

which, like the coherence time effect, varies linearly with range and is independent of the look direction. Unlike the coherence time effect, however, the effect of a vertical acceleration depends on the processor integration time. This

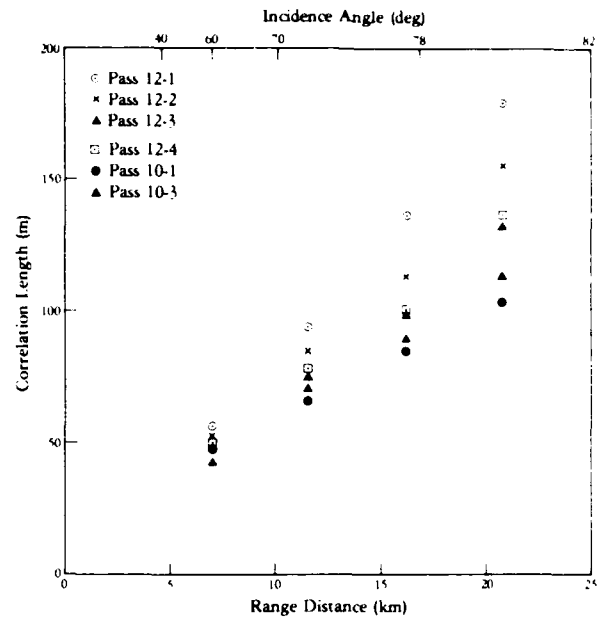


Fig. 4. Average streak lengths as determined from width of autocorrelation function in azimuth direction.

can be understood by considering that the longer the object is observed, the greater the range of velocities (and azimuthal displacements) is during this integration time. The degraded azimuthal resolution due to a vertical acceleration is plotted versus range in Figure 5c, assuming vertical accelerations of  $1 \text{ m/s}^2$  and  $9.8 \text{ m/s}^2$  (i.e., freely falling particles).

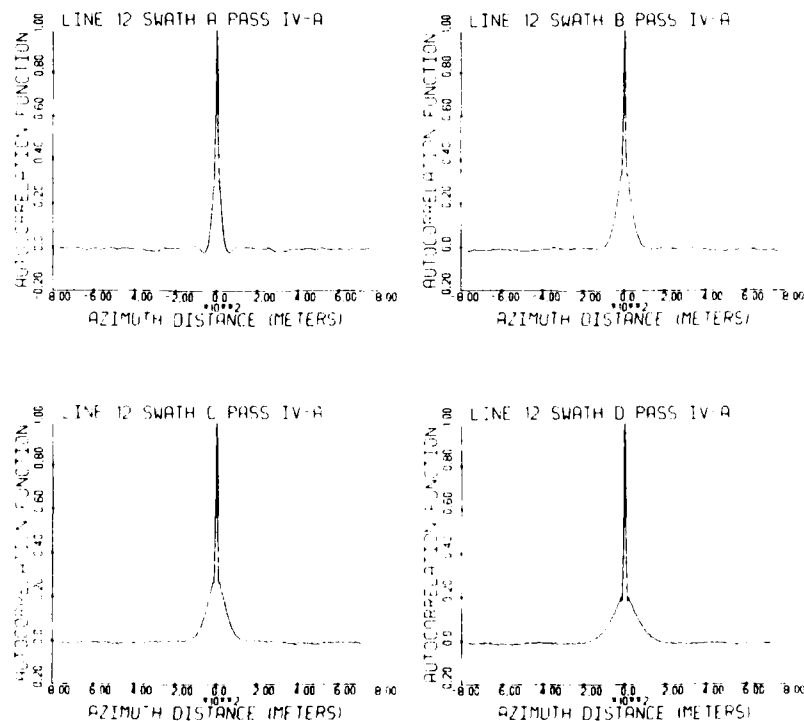


Fig. 3. One-dimensional image autocorrelation functions in azimuth direction for pass 12-4 (September 27, 1979), subswaths A-D.

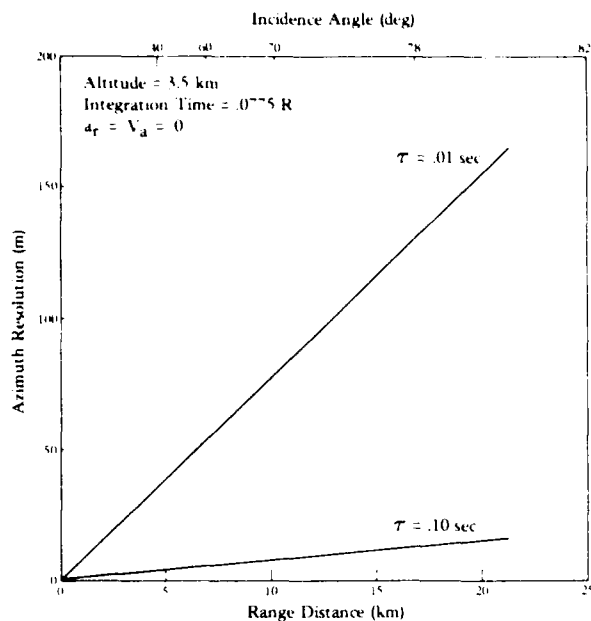


Fig. 5a

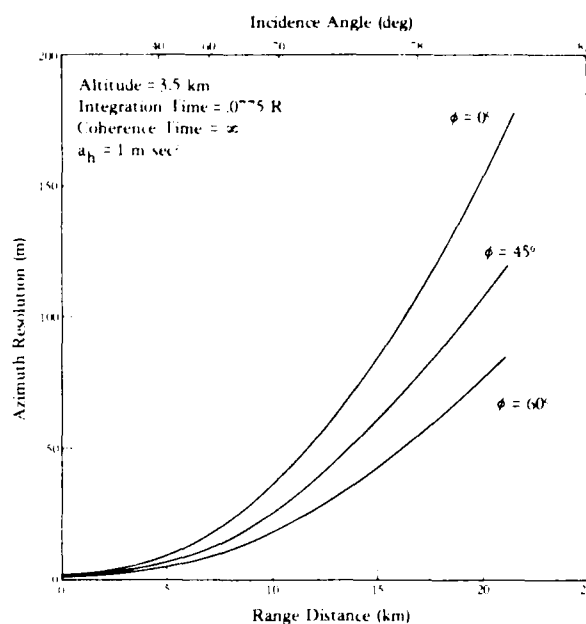


Fig. 5b

Fig. 5. Azimuth resolution for the APD-10 system versus range as calculated using equations given by *Raney* [1971, 1980], for (a) stationary scatterers with coherence times of 0.01 and 0.10 s; (b) coherent scatterers with a horizontal acceleration of  $1 \text{ m/s}^2$  and three look directions, and (c) coherent scatterers with a vertical acceleration of  $1 \text{ m/s}^2$  and  $9.8 \text{ m/s}^2$ .

An additional type of scatterer motion which produces a degradation in azimuthal resolution is a velocity in the azimuth direction. For an azimuthal velocity  $V_a$ , the azimuthal resolution is given [Raney, 1971] by

$$\rho_{az} = \frac{\lambda}{2\beta} \left[ 1 + \left( \frac{4\beta^2 R V_a}{\lambda V} \right)^2 \right]^{1/2} \quad (11)$$

which for  $V_a \ll \lambda \beta I$  reduces to

$$\rho_{az} = 2\beta R V_a / V \quad (12)$$

In breaking waves, particle velocities can approach the phase speed of the wave, which was of the order of  $10 \text{ m/s}$  for the dominant waves occurring during the time the MARSEN data was collected. The azimuth smear in swath D of the APD-10 data for an azimuth velocity of  $10 \text{ m/s}$  would be approximately  $30 \text{ m}$ , which is much smaller than the observed smearing. Thus azimuthal velocity effects do not appear to play a major role in the formation of the observed artifacts in the MARSEN APD-10 data.

### 5. Discussion

The lengths of the observed image streaks in the MARSEN APD-10 data appear to increase linearly with range and to have a maximum length of about  $180 \text{ m}$  in swath D. No clear dependence on the look direction has been observed, although the streak length does appear to depend slightly on the wind speed as indicated in Figure 4 and Table 1.

These observations are consistent with a scatterer coherence time of the order of  $10^{-2} \text{ s}$  or to a vertical acceleration of the order of  $5 \text{ m/s}^2$ . The coherence time explanation appears to be supported by the observation that the streak

lengths do not change significantly when the processor integration time is reduced (Figure 2) or the focus settings are altered. The possibility that horizontal accelerations are the primary cause of the streaking seems to be ruled out by the lack of sensitivity to integration time and focus adjustments, by the linear rather than quadratic range dependence, and by the fact that no clear dependence on the look angle is observed in the streak lengths. Azimuthal velocity effects do not appear to be capable of producing features as long as those observed, and would also cause a more pronounced look angle dependence. Gross scatterer motions (velocities and accelerations) may, however, cause secondary effects

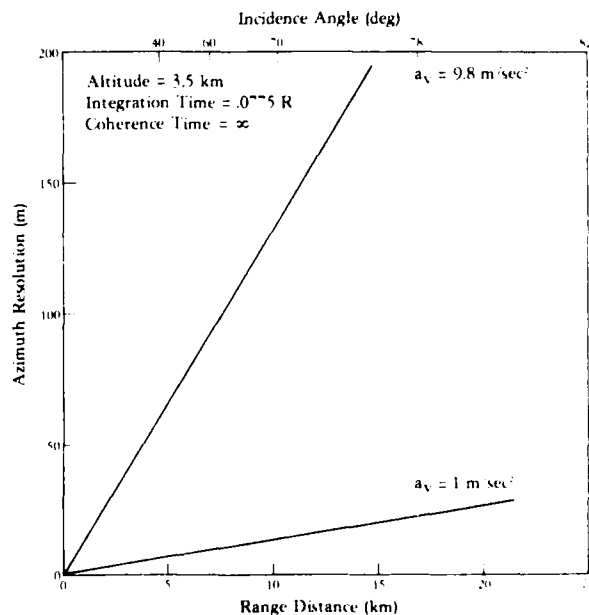


Fig. 5c

which are measurable in the SAR processor by virtue of their dependence on focus and integration time.

The scatterer characteristics which explain the SAR image features described here have been observed by other investigators in connection with breaking or near-breaking waves. Breaking waves are manifested in conventional radar observations of the ocean surface as a burst of very high radar return lasting for about a second but with very rapid fluctuations in amplitude during this period [Long, 1974]. High-resolution  $X$  band measurements have indicated the size of these features to be of the order of a few meters and the radar cross section per unit area  $\sigma_0$  to be about 1.5 at near-grazing incidence [Lewis and Olin, 1980]. These measurements have also indicated the decorrelation time for the radar return from breaking waves to be of the order of  $10^{-2}$  s at  $X$  band. Other investigators have measured similar decorrelation times at incidence angles between  $0^\circ$  and  $70^\circ$  in the North Sea under a variety of conditions [Rufenach and Alpers, 1981; DeLoor and Hoogetboom, 1982]. Finally, measurements of the Doppler spectra of breaking waves, using a coherent  $X$  band radar at incidence angles of  $55^\circ$  and  $70^\circ$  [Keller et al., 1981] have indicated bandwidths of the order of 100 Hz which also imply decorrelation or coherence times of the order of  $10^{-2}$  s.

Using the coherence time model discussed in section 4, the above measurements appear to imply a spread of radial velocities of the order of a few meters per second due to the turbulence associated with breaking waves. A model explaining the rapid fluctuations in the backscattered signal from breaking waves has also been proposed by Lewis and Olin [1980]. This model, as well as their experimental data, shows similar fluctuations in the radar return from steep but unbroken waves, although the amplitude of these returns is much lower. Therefore we may expect that not all of the observed image features are due to actively breaking waves, but the brighter features are very likely to correspond with such waves. Although the percent of the images covered by streaks appears to be larger than most observations of whitecap formation, it must be remembered that the area of the streaks is 10–100 times the actual area of the features, due to the smearing effect discussed in this paper. Preliminary estimates of the actual number density of streaks yield results comparable to the frequency of the events observed by Longuet-Higgins and Smith [this issue]. A final determination of the geophysical source for these features will await more detailed comparisons with in situ measurements such as those of Longuet-Higgins and Smith.

## 6. SUMMARY

It is concluded that the streaked image features which appear at higher wind speeds in the APD-10 SAR data collected during the MARSEN experiment are due to scat-

terers which have  $X$  band coherence times of the order of  $10^{-2}$  s. These coherence times are consistent with conventional radar observations of breaking waves. It is therefore also provisionally concluded that these features are due to the phenomenon of wave breaking.

Additional evidence for or against this conclusion could be obtained by comparisons with in situ observations of the frequency of wave breaking and with simultaneous scatterometer data. Such comparisons, as well as examination of simultaneous  $X$ - $L$  band SAR data, are planned as a sequel to this study. Additional optical processor measurements are also planned to determine the magnitudes of the secondary effects due to gross scatterer motions.

**Acknowledgments.** This study was supported by the Office of Naval Research (ONR) under contract N00014-81-C-0692. The ONR technical monitor was Hans Dolezalek. We would like to acknowledge the help of the following individuals: A. Klooster and J. Losce of ERIM for optically processing the APD-10 data and generating the digital data; Chris Wackerman of ERIM for generating the autocorrelation functions; Eric Kasischke and James Lyden of ERIM and Wolfgang Rosenthal of the Max Planck Institute of Meteorology in Hamburg, Germany, for providing the MARSEN sea truth; and Omar Shemdin of JPL and Klaus Hasselmann of the Max Planck Institute of Meteorology for coordinating this research activity in their capacity as coprincipal investigators.

## REFERENCES

- DeLoor, G. P., and P. Hoogetboom, Radar backscatter measurements from platform Noordwijk in the North Sea, *IEEE J. Oceanic Eng., OE* 7, 15–20, 1982.
- Keller, W. C., W. S. Plant, and G. R. Valenzuela, Observation of breaking ocean waves with coherent microwave radar, paper presented at Symposium on Wave Dynamics and Radio Probing of the Ocean Surface, Inter-Union Comm. on Radio Meteorol., Miami Beach, Fla., May 13–20, 1981.
- Lewis, B. L., and I. D. Olin, Experimental study and theoretical model of high resolution backscatter from the sea, *Radio Sci.* 15, 815–828, 1980.
- Long, M. W., On a two-scatter theory of sea echo, *IEEE Trans. Antennas Propag.*, AP 22, 667–672, 1974.
- Longuet-Higgins, M. S., and N. D. Smith, Measurement of breaking waves by a surface jump meter, *J. Geophys. Res.*, this issue.
- Raney, R. K., Synthetic aperture imaging radar and moving targets, *IEEE Trans. Acoust. Electron. Syst.*, AES 7, 499–505, 1971.
- Raney, R. K., SAR response to partially coherent phenomena, *IEEE Trans. Antennas Propag.*, AP 28, 777–787, 1980.
- Rufenach, C. L., and W. Alpers, Imaging ocean waves by synthetic aperture radars with long integration times, *IEEE Trans. Antennas Propag.*, AP 29, 422–428, 1981.
- Shuchman, R. A., W. Rosenthal, J. D. Lyden, D. R. Lizenka, E. S. Kasischke, M. Gunther, and H. Linne, Analysis of MARSEN  $X$  band SAR ocean wave data, *J. Geophys. Res.*, this issue.

(Received July 30, 1982;  
revised November 29, 1982;  
accepted November 29, 1982.)

# Analysis of Remotely Sensed Long-Period Wave Motions

G. A. MEADOWS<sup>1</sup>

*Department of Atmospheric and Oceanic Science, University of Michigan, Ann Arbor, Michigan 48109*

R. A. SHUCHMAN AND J. D. LYDEN

*Radar and Optics Division, Environmental Research Institute of Michigan, Ann Arbor, Michigan 48107*

Synthetic aperture radar has been used to image long-period (15–200 s) gravity waves in the nearshore region of Lake Michigan. These long-period waves are a response of the sea surface to forcing by a nonmonochromatic, wind-generated surface wave field. The synthetic aperture radar data were successfully compared with an in situ wave gauge record. Both one- and two-dimensional fast Fourier transforms were generated from near and offshore regions of synthetic aperture radar data. The synthetic aperture radar-derived near and offshore spectral estimates exhibited both low- and high-frequency wave components. Classical bathymetrically controlled wave refraction was observed for both the short as well as long wave components of the sea surface. This paper demonstrates the ability of X band synthetic aperture radar to detect low-amplitude, long-period signals. The signals appear to correspond to a 'surf beat' generated by the incident wind wave field.

## INTRODUCTION

Since the initial observations of long-period (30–300 s) wave motions by *Munk* [1949] and *Tucker* [1950], several conjectures concerning the generation and propagation of 'surf beats' have been proposed. The theoretical development of *Longuet-Higgins and Stewart* [1962] employed interactions of a nonmonochromatic sea to generate an amplitude-modulated sea surface. Through the use of the calculated increased radiation stress beneath groups of large waves and a corresponding decrease in the stress associated with lower waves, a forced long-period wave is generated at the beat frequency. *Meadows* [1977] showed that this long-period forced wave propagated at the short wave group velocity and was observable in the nearshore zone. Similarly, *Larsen* [1979] has observed long-period forced waves in the North Pacific which appeared to have been generated by, and propagated with, the modulated sea surface.

All inferences, as well as previous attempts at field verification of the physical characteristics of these long-period waves, have been based on single point time series measurements. The studies of *Meadows* [1977] represented the first two-dimensional, synchronous time series observations of nearshore, long-period wave motions. These studies, however, were still conducted over an offshore spatial interval which was small (of the order of half the wavelength) compared to the wavelengths of the forced surf beat.

Investigation of the backscatter of microwave energy from the sea surface provides a unique way to view large spatial regions of the sea surface nearly simultaneously. Synoptic coverage of wave characteristics, as available from synthetic aperture radar (SAR), has provided a three-dimensional (two spatial dimensions and radar backscatter modulation) representation of the propagation and physical characteristics of

long-period wave motions across the sea surface. Since the intensity of radar backscatter can be related to the characteristics of ocean wave propagation [*Gonzales et al.*, 1979; *Gower and Hughes*, 1979; *Shuchman and Meadows*, 1980; *Schwab et al.*, 1981], definitive information is now available concerning the generation and propagation of these wave motions.

SAR sea surface information was collected over a region of Lake Michigan by the Environmental Research Institute of Michigan (ERIM). At the time of the SAR overflight, the University of Michigan Department of Atmospheric and Oceanic Science was operating its mobile nearshore wave and current monitoring array [*Meadows*, 1979; *Meadows et al.*, 1980; *Shuchman and Meadows*, 1980]. The concurrent acquisition of airborne SAR sea surface data with in situ sea truth has provided a valuable opportunity to investigate the three-dimensional characteristics of a complex nearshore wave field. A previous paper, utilizing this coincident SAR and in situ wave gauge data [*Shuchman and Meadows*, 1980], has shown SAR can successfully image the incident wind-generated gravity wave field. This paper will concentrate on the long-period (15–200 s) response of the sea surface to forcing by a nonmonochromatic, wind-generated surface wave field and the ability of SAR to image successfully these subtle surface wave motions.

## THEORY OF LONG-PERIOD WAVE GENERATION

Employing the classic formulation for the linear interaction of two sinusoidal waves of differing radian wave numbers  $k_1$  and  $k_2$  and radian wave frequencies  $\sigma_1$  and  $\sigma_2$ , a solution for the resultant sea surface is possible by simple superposition of these wave components. The resultant sea surface  $\eta$  is a function of both space  $x$  and time  $t$  and is given by

$$\eta(x, t) = a \cos(k_1 x - \sigma_1 t) + a \cos(k_2 x - \sigma_2 t) \quad (1)$$

where  $a$  is the wave amplitude. As suggested by *Kinsman* [1965] for the condition when the two component waves are very nearly the same length and period, such that

$$\Delta k \ll k_1 \quad \Delta \sigma \ll \sigma_1$$

<sup>1</sup> Also a consultant at Environmental Research Institute of Michigan, Ann Arbor, Michigan 48107



where  $\Delta k = k_1 - k_2$  and  $\Delta\sigma = \sigma_1 - \sigma_2$ , then

$$k_1 \approx k_2 \quad \sigma_1 \approx \sigma_2$$

Hence the amplitude-modulated sea surface, as a function of distance in the propagation direction, may be expressed as

$$\eta(x) \approx 2a \cos\left(\frac{\Delta k}{2}x\right) \cos(kx) \quad (2)$$

and as a function of time as

$$\eta(t) \approx 2a \cos\left(\frac{\Delta\sigma}{2}t\right) \cos(\sigma t) \quad (3)$$

Since  $\Delta k \ll k$  and  $\Delta\sigma \ll \sigma$ , the spatial and temporal scales of the modulation are very long compared to the individual wave components which comprise the group. This interference pattern results in the generation of groups of large waves separated by groups of small waves (see Figure 1 from *Longuet-Higgins and Stewart [1962]*). The length of the long-period modulation is given by *Kinsman [1965]* as

$$L_{\text{mod}} = \frac{4\pi}{\Delta k} \quad (4)$$

while the period of the modulation is

$$T_{\text{mod}} = \frac{4\pi}{\Delta\sigma} \quad (5)$$

The distance between successive groups of high waves is therefore  $\frac{1}{2}L_{\text{mod}}$ , and the corresponding time interval is  $\frac{1}{2}T_{\text{mod}}$ .

Consider a conventional right-handed rectangular coordinate system with the  $x$  axis horizontal and in the direction of wave propagation and the  $z$  axis vertical and upward. Let  $u$ ,  $v$ , and  $w$  be the velocity components in the  $x$ ,  $y$ , and  $z$  directions, respectively, and let  $p$ ,  $\rho$ , and  $g$  denote the pressure, density, and gravitational acceleration, respectively. Also, let the free surface be given by the equation  $z = \eta(x, y, t)$ , where  $t$  is time, and the rigid horizontal bottom by the equation  $z = -h$ .

When the length of the modulated wave groups are long compared to the local water depth, changes in the mean sea level and the wave mass-transport correspond to those that would result from an applied horizontal force, in this case the radiation stress [*Whitham, 1962; Longuet-Higgins and Stewart, 1962*]. For this condition, the flux of momentum across an  $x = \text{constant}$  vertical plane is given by *Longuet-Higgins and Stewart [1962]* as

$$S = \int_{-h}^{\eta} (p + \rho u^2) dz \quad (6)$$

where the radiation stress  $S_x$  is the difference between  $S$  and the contribution due to the hydrostatic pressure:

$$\begin{aligned} S_x &= \int_{-h}^{\eta} (p + \rho u^2) dz - \int_{-h}^{\eta} \rho g(\eta - z) dz \\ &= S - \frac{1}{2}\rho g(h + \eta)^2 \end{aligned}$$

which is approximately equal to

$$\approx S - \rho g\left(\frac{1}{2}h^2 + h\bar{\eta}\right) \quad (7)$$

where the overbars denote time averages. For the condition of long waves in shallow water, the vertical accelerations are

assumed negligible, hence, correct to second order

$$S_x = E \left[ \frac{2C_g}{C} - \frac{1}{2} \right] \quad (8)$$

where  $E$  is the wave energy per unit horizontal area and is defined as

$$E = \frac{1}{2} \rho g a^2$$

$C_g$  in (8) denotes the deep water group velocity of the waves, and  $C$  is the phase speed of the individual waves.

Conservation of mass and momentum may be expressed as

$$\frac{\partial(\rho\bar{\eta})}{\partial t} + \frac{\partial M}{\partial x} = 0 \quad (9)$$

and

$$\frac{\partial M}{\partial t} + \frac{\partial S}{\partial x} = 0 \quad (10)$$

where  $M$  is the mean, vertically integrated horizontal momentum given by

$$M = \int_{-h}^{\eta} \rho u dz \quad (11)$$

Substituting for  $S_x$  from (7), the momentum equation may be written as

$$\frac{\partial M}{\partial t} + gh \frac{\partial}{\partial x} (\rho\bar{\eta}) = - \frac{\partial S_x}{\partial x} \quad (12)$$

Since the applied force  $-\partial S_x/\partial x$  travels with the group velocity,  $\partial/\partial t$  may be replaced with  $-C_g \partial/\partial x$ , which upon substitution into (9) and (12) gives

$$-\rho C_g \frac{\partial \bar{\eta}}{\partial x} + \frac{\partial M}{\partial x} = 0 \quad (13)$$

and

$$\rho gh \frac{\partial \bar{\eta}}{\partial x} - C_g \frac{\partial M}{\partial x} = - \frac{\partial S_x}{\partial x} \quad (14)$$

The solution to this set of equations is given by *Longuet-Higgins and Stewart [1962]* as

$$\rho \frac{\partial \bar{\eta}}{\partial x} = - \left( \frac{1}{gh - C_g^2} \right) \frac{\partial S_x}{\partial x} \quad (15)$$

and

$$\frac{\partial M}{\partial x} = - \left( \frac{C_g}{gh - C_g^2} \right) \frac{\partial S_x}{\partial x} \quad (16)$$

Upon integration, the free surface elevation and mean horizontal momentum become

$$\bar{\eta} = - \frac{S_x}{\rho(gh - C_g^2)} \quad (17)$$

and

$$M = - \frac{C_g S_x}{(gh - C_g^2)} \quad (18)$$

respectively.

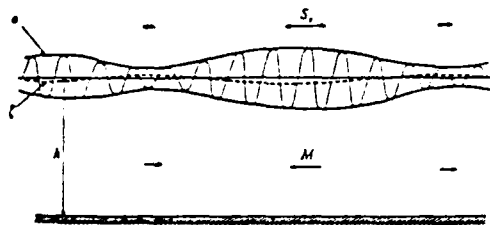


Fig. 1. Schematic representation of the forced long-period modulation of the surface resulting from short wind-generated wave component interactions [from Longuet-Higgins and Stewart, 1962].

The interpretation suggested by Longuet-Higgins and Stewart [1962] is as follows:

It will be noticed that beneath a group of high waves, where  $S$ , and  $E$  are both large,  $\eta$  and  $\bar{u}$  are more negative, that is to say there is a relative depression in the mean surface level, coupled with a mean flow opposite to the direction of wave propagation. Beneath a group of low waves, on the other hand, the mean surface level is raised and the flow is positive.

(See Figure 1.)

#### SEA SURFACE-SAR INTERACTIONS

It is generally accepted that the scattering of microwave energy from the sea surface is a Bragg-Rice resonance phenomenon [Wright, 1968], thus making the received radar image particularly sensitive to capillary and short ultragravity ocean surface waves. Nonlinear interaction of these short waves with longer period wave motions is the subject of much research [Phillips, 1981; Longuet-Higgins and Stewart, 1964; McGoldrick, 1970, 1972]. It is generally agreed, however, that the short wavelengths are increased in the troughs of the long waves and that the correspondingly short wave height is decreased. Conversely, on the wave crest of the long waves, the short wave height is increased and the short wavelength is decreased. Both effects act to increase the sea surface roughness in the crest regions of long waves and correspondingly decrease the roughness in the trough region [Phillips, 1981]. The radar backscatter increases as a function of increasing sea surface roughness, thus producing regions of intense radar backscatter from modulated long wave crests and diminished radar return from modulated long wave troughs. Furthermore, it also appears that the existence of a surface capillary or ultragravity wave field is a necessary condition to provide radar images of long-period ocean internal wave motions.

The proposed physical mechanism for the indirect imaging of 'surf beats' by radar backscatter is as follows. A modulated, wind-driven, capillary/ultragravity wave field exists in conjunction with a shoreward propagating, nonmonochromatic, gravity wave field. Nonlinear capillary-gravity wave interactions occur which produce increased surface roughness on the crests of the gravity waves and decreased surface roughness in the troughs. Concurrently, similar but slightly different gravity wave components of the nonmonochromatic wave field are interacting to form surf beats consisting of groups of high waves separated by groups of low waves. These wave groups produce corresponding depressions and relaxations of the mean water level in response to fluctuations of the applied radiation stress. Hence a forced, long-period wave, traveling at the group velocity of

the wind wave packet, is generated. Bright radar returns, therefore, should correspond to groups of high-gravity waves and corresponding troughs of the forced long-period waves.

#### DATA DESCRIPTION

The synthetic aperture radar (SAR) used to collect the data is the ERIM X and L band dual polarized radar described by Rawson *et al.* [1975]. The ERIM SAR system records four channels of radar return, but we will focus our attention here on the X band horizontal-transmit-horizontal-receive (HH) channel, as this data provided the clearest wave images. The SAR was flown at an altitude of 6100 m and operated with a center incident angle from the vertical of 20°, yielding a swath width of 5.6 km. The cross-track or range resolution of SAR is limited by radar bandwidth and is about 2 m for X band. The along-track or azimuth resolution is obtained from the synthetic aperture technique described by Brown and Porcello [1968]. For the X band, the azimuthal resolution is about 2.5 m. This SAR data was processed on the ERIM tilted-plane precision optical processor described by Kozma *et al.* [1972].

The SAR data was collected on October 1<sup>st</sup>, 1978, at approximately 1635 EST. The airborne data was collected along the shoreline of Lake Michigan centered at latitude 43°50' N. The site for this field experiment as shown in Figure 2 was the eastern shore of Lake Michigan, between the cities of Ludington and Pentwater, Michigan. This thirteen kilometer section of shoreline, extending approximately north-south, is characterized by a multiple-barred bathymetry with nearly straight and parallel contours.

At the same time as the ERIM flight, the University of Michigan Department of Atmospheric and Oceanic Science was operating its mobile surf zone, wave, and current sensing array [Meadows, 1979]. Monitoring of incident wave characteristics and longshore current velocities was conducted through the growth of a major storm on Lake Michigan. A detailed discussion of the experimental design is presented by Wood and Meadows [1975] and Meadows [1977]. Surface-piercing, step-resistance wave probes and bidirectional ducted impeller flow meters were used to make simultaneous measurements of wave and current conditions. These sensors were oriented on a line perpendicular to

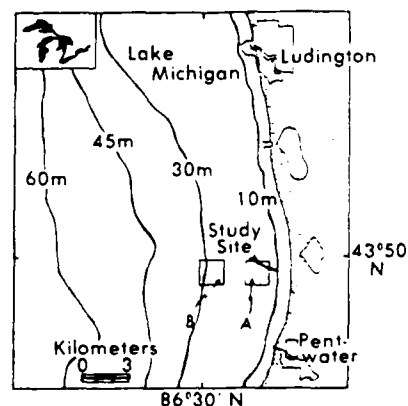


Fig. 2. General study area showing nearshore bathymetry and location of fast Fourier transformed SAR data

shore, extending from the beach to the outer surf zone. Other coastal sensing equipment included a directionally mounted motion picture camera and Lagrangian drifters. Unfortunately, high wind and wave action on October 17 and 18 destroyed much of the array; however, sufficient sensors survived to make this comparative study possible.

#### METHODS

The SAR collected data were digitized with an approximate resolution of 6 m (3-m pixels) by using the ERIM hybrid image dissector [Ausherman, 1975]. The range coordinates of the digitized data were analytically corrected for slant-to-ground range geometry [Feldkamp, 1978]. Two  $1.5 \times 1.5$  km subsections (see Figure 2) with 6-m resolution were extracted from the digitized data. The two sections are labeled A and B, where A is closest to shore.

The 3.0-m pixel digitized SAR images were converted to 6-m samples by 4 pixel into 2 pixel averaging in order to decrease the speckle in the image. The average value of each azimuthal line was subtracted from the line to remove the trend of intensity falloff with increasing range distance. Two-dimensional fast Fourier transforms (FFT's) were performed on each  $256 \times 256$  cell subsection to yield raw directional wave number spectra with a Nyquist wave number of  $0.5 \text{ m}^{-1}$ . The raw spectra were smoothed by replacing each value with the average of the surrounding  $5 \times 5$  cell. The approximate number of degrees of freedom for the resulting spectrum is 142 [Kinsman, 1965]. The 99% confidence limits are then  $\pm 1.5 \text{ dB}$  [Jenkins and Watts, 1968].

In addition to the two-dimensional FFT analysis, five isorange SAR backscatter records 1.5 km long were analyzed by using both a one-dimensional spectral analysis and a band pass filtering program. This one-dimensional analysis was performed on the SAR data to better quantify the long-period components of the prevalent wave field. To perform this analysis, five adjacent isorange lines of data were extracted from the digital image corresponding to the center of both study areas A and B. These lines were then averaged or, in effect, smoothed in the range direction; this was done to reduce the speckled nature of the SAR data. The averaged lines were then plotted in order to characterize the relative backscatter across these study areas. These data were then selectively filtered for wavelengths between 177 and 1180 m for study area A and from 249 to 1660 m for study area B. This wavelength filtering corresponds to the temporal region of interest, 15–200 s.

To calculate the directional wave spectrum at the instrumented surf zone site, a 16-min analog record was digitized at 0.25-s intervals and analyzed by using conventional one-dimensional fast Fourier transform techniques. The directional information was obtained from the directionally mounted camera. One-dimensional spectral analysis using a FFT routine was performed on the total 16-min, outer surf zone water level elevation time history. The smoothed spectrum resulting from this analysis is presented in Figure 3. This spectrum exhibits a well-defined broad peak in the wind wave range (2–8 s), composed of multiple components. This spectrum is characteristic of locally generated seas. In addition, this spectral analysis has also identified significant long-period wave motion at specific periods of 17.2 and 32.3 s and a less significant peak at approximately 59 s. These nearshore spectral estimates were obtained from a continuous digital record consisting of 3840 equally spaced values at

0.25-s intervals. The 80% confidence band lies between 1.42 and 0.62 times the spectral estimate and is indicated on Figure 3 [Kinsman, 1965].

Based upon these results, this total water level elevation record was band pass filtered to retain only surface wave motions with periods between 15 and 200 s. A representative portion of the original and band pass filtered, long-period records is presented in Figure 4. It, therefore, appears that significant long-period wave motions are present in the nearshore region with a mean amplitude of approximately 10% of that of the incident wind waves. These results agree favorably with the finding of Meadows and Wood [1982] where both progressive as well as standing long-period wave motions were observed in the nearshore region. The question arises, however, as to the generation mechanism of these waves. It is the hypothesis of the authors that these long-period waves are formed as a result of nonlinear interactions between the dominant wind-wave components and that they propagate as forced waves at the group velocity of wind-generated waves. Hence it should be anticipated that these wave motions should exist somewhat homogeneously across the sea surface provided that wind waves of sufficient amplitude and prescribed frequency exist.

#### ANALYSIS

Synthetic aperture radar provides a unique perspective from which to investigate this hypothesis, namely, that long-period surf beats are generated by and propagate with the wind wave field. The nearly simultaneous view of a relatively large spatial region of the sea surface provided by either an airborne or spaceborne SAR affords an ideal measurement tool for these wave motions. To examine this capability, the results of both the SAR two-dimensional and the nearshore in situ wave gauge data series will be evaluated.

Results of the nearshore step resistance wave gauge spectral analysis have indicated several well-defined peaks in the wind wave range. In addition, two long-period peaks at 17.2 and 32.3 s, respectively, were also well resolved. A poorly resolved spectral peak is also apparent at approximately 59 s. Linear combinations of the dominant wind wave components are formed in Table 1 to produce their respective beat periods. It may be noted that the dominant wind wave components of 5.6, 4.8, and 4.2 s combine, theoretically, to form beats of 16.8 and 33.6 s, respectively. These calculated beat periods are very close to those periods resolved by the spectral analysis of the total 16-min water

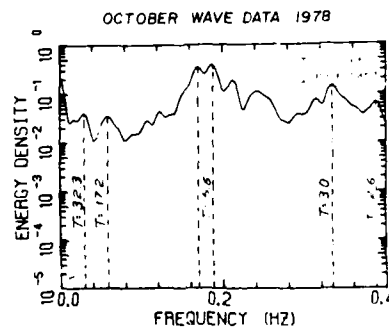


Fig. 3. One-dimensional wave height spectrum of water surface elevation time history from resistance wave gauge. Dominant wave periods are identified.

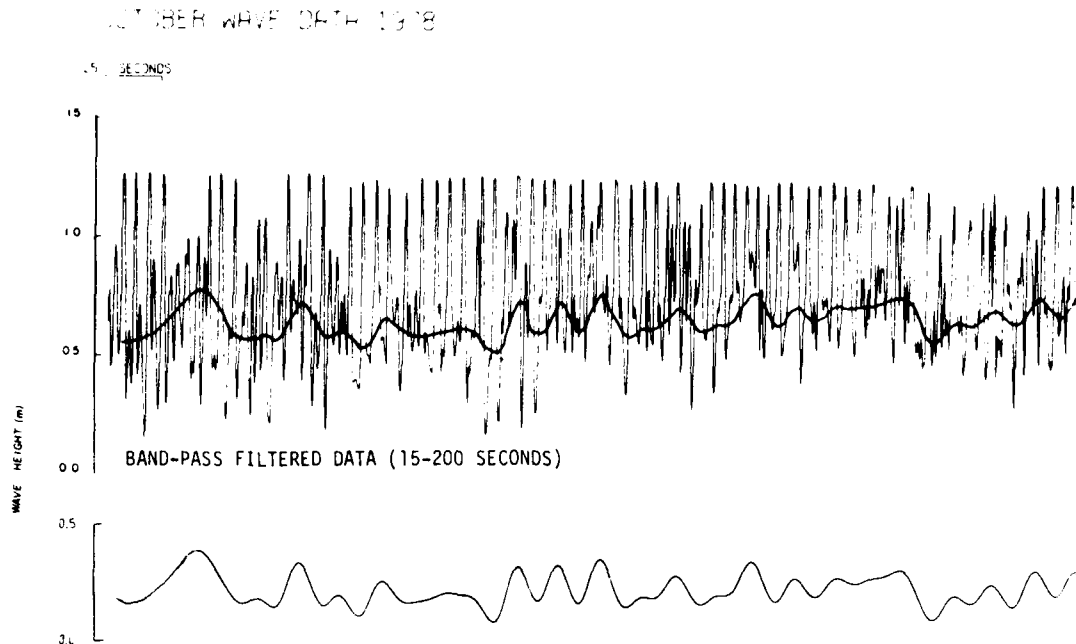


Fig. 4. Representative section of 16-min time history of water elevation data from resistance wave gauge. Also shown is the corresponding 15–200 s band pass filtered data. (Note the negative correlation [180° phase shift] between the wind wave amplitudes and the mean surface level.)

surface elevation recorded from the nearshore wave gauge. It therefore appears that forced long-period wave motions were present in the nearshore region resulting from the nonlinear interaction of the dominant wind wave components.

The energy associated with these long-period forced waves is an order of magnitude below that of the peak in the wind wave spectra. Theoretical calculations of the maximum mean surface deformation from (17) suggest a forced wave height of approximately 0.38 m. The energy associated with the forced wave would be approximately a factor of 8.4 less than that associated with the peak wind wave component. It appears that long-period wave motion in the nearshore region is present with both a period and an amplitude close to theoretical predictions.

To further identify these long-period wave motions, the total 16-min water surface elevation record from the nearshore wave gauge was band pass filtered for periods between 15 and 200 s. A representative portion of the original water surface elevation record and its associated long-period component are presented in Figure 4. This series, as well as the data of Meadows [1977], suggests that the mean surface level

is 180° out of phase with the wind wave amplitudes. As theoretically suggested, this implies that depressions in the water surface are associated with groups of large waves and long-period elevations of the water surface correspond to groups of low waves.

Based upon these considerations, SAR imagery of a relatively large region of the sea surface should also exhibit these long-wave features. In an effort to investigate this potential of SAR, a manual photo-interpretation of the radar image film was performed. A portion of the X band (HH) SAR data collected over the Lake Michigan test site is presented in Figure 5. The image extends 7.9 km offshore and is 5.6 km wide. Alternating groups of large and small wind wave packets can be readily seen across this image. At three representative locations across this nearshore imagery, the long-wave lengths are indicated on the figure. As these long waves, forced by short-wave groups, propagate shoreward, both wavelength compression and refraction are plainly observable. The long wavelengths decrease from approximately 510 m (area B) to approximately 410 m (area A). These radar observations of the long wave components of surface elevation are in excellent agreement with sea truth measurements made at the outer surf zone.

To further document the existence and propagation characteristics of these SAR-sensed long wave components, a conventional two-dimensional FFT of the radar backscattered energy was performed. One FFT analysis was performed in both the offshore and nearshore regions of the aircraft swath. The SAR FFT's were generated by the algorithm described by Shuchman *et al.* [1979]. However, in this application, only the long-wave portion of the spectrum is of interest. For a detailed discussion of the total SAR-sensed wave spectra and associated sea truth see Shuchman and Meadows [1980]. A summary of the general sea state

TABLE 1. Calculated Beat Periods

Input Components, s	Input Components, s				
	5.6	4.8	4.2	3.0	2.6
5.6	...	33.6	16.8	6.5	4.9
4.8	...	...	33.6	8.0	5.7
4.2	...	...	...	10.5	6.8
3.0	...	...	...	...	19.5
2.6	...	...	...	...	...

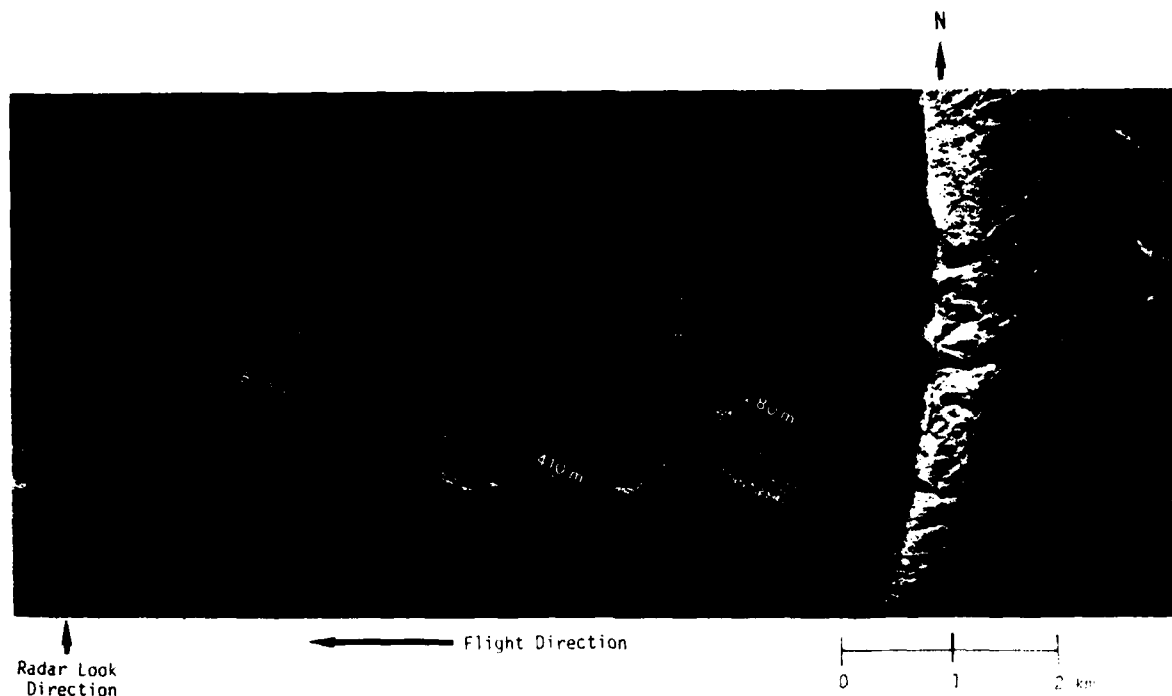


Fig. 5. X band (HH) SAR image of test site showing long-period wave components.

conditions during this experiment as well as a comparison of the SAR-derived, wind-generated sea spectral estimates to sea truth are presented in Table 2.

In the offshore region, the SAR-derived spectral analysis resolved a long-wave component with energy concentrated at a wavelength of approximately 511 m, traveling in a direction of  $025 \pm 3^\circ T$ . Similarly, in the nearshore region, a long-wave component of 408 m wavelength traveling at  $035 \pm 3^\circ T$  was resolved. The nearshore and offshore two-dimensional FFT's are shown in Figures 6 and 7, respectively. Also shown on each of the figures is the one-dimensional plot of the low-frequency components versus relative energy. These estimates of long-wave characteristics exhibit two

important properties. First, the long wavelengths are in excellent agreement with the representative offshore wave group dimensions derived from the SAR image film. Second, the degree of observed refraction from the offshore to the nearshore region of these forced long-period wave motions is also in close agreement with the sea truth as well as with the calculated wave refraction for the dominant wind wave components. A comparison of SAR-derived and sea truth wave characteristics is presented in Table 3.

Furthermore, the two directly observed quantities which determine the propagation of these SAR and sea truth sensed long-period wave motions are the length and period of the modulated wave group. The lengths of the dominant long-

TABLE 2. Comparison Between the SAR-Derived Surf Zone Conditions and the in Situ Sea Truth

Distance From Shore, m	Depth, m	SAR-Derived Estimates		Sea Truth*	
		Dominant Short-Period Wavelengths, m	Direction, $T^\circ$	Dominant Short-Period Wavelengths, m	Direction, $T^\circ$
900	10.5	48	$35 \pm 3$	48	$34 \pm 2$
		43		44	
2200	14.0	55	$30 \pm 3$	54	$30 \pm 2$
		43		44	
4600	27.0	55	$25 \pm 3$	55	$28 \pm 2$
		48		46	
6900	31.0	55	$25 \pm 3$	55	$28 \pm 2$
		48		46	

\* Actual measurements made at surf zone; values for test areas are depth-corrected [Shuchman and Meadows, 1980].

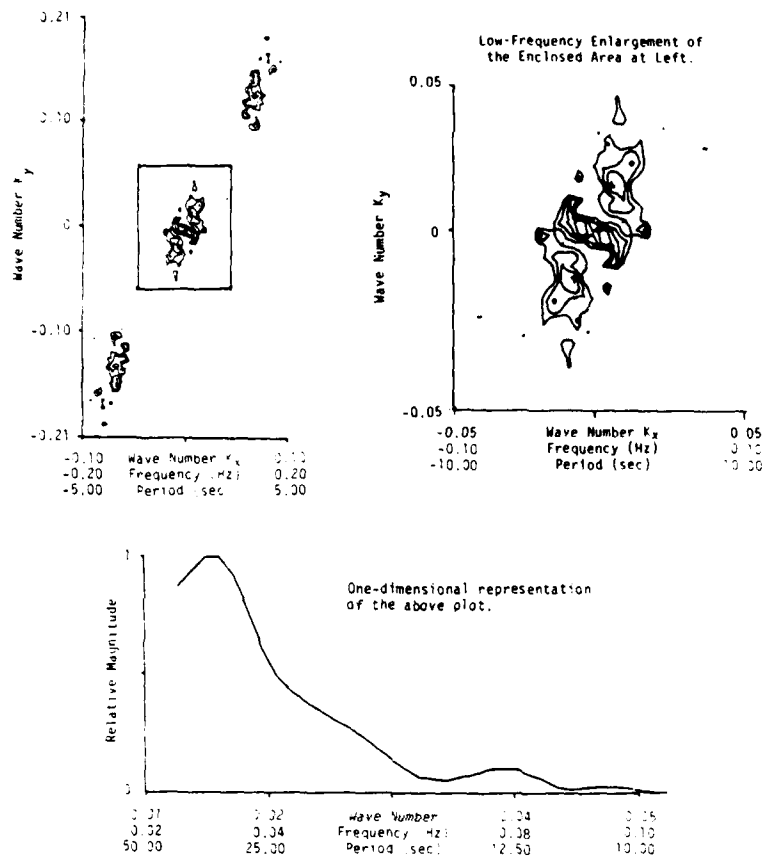


Fig. 6. SAR-derived two-dimensional spectral estimate (nearshore). (Note: Negative wave numbers, frequencies, and periods are included due to the symmetric nature of a two-dimensional FFT. The frequency and period axes assume shallow water waves; see text for further explanation.)

period waves were obtained from the SAR-derived, two-dimensional FFT. Similarly, the periods of the dominant long-wave components were obtained from a one-dimensional spectral analysis of the nearshore wave gauge data. By combining equations (4) and (5), the celerity of these modulated long-period waves may be expressed as

$$C_{\text{mod}} = \frac{L_{\text{mod}}}{T_{\text{mod}}} \quad (19)$$

The calculated long-period wave celerity utilizing both the

SAR and wave gauge measured dominant long-period wave parameters, results in values of  $12.6 \text{ ms}^{-1}$  and  $15.8 \text{ ms}^{-1}$  for areas A and B, respectively. It is interesting to note that assuming these long-period waves are propagating as shallow water waves with celerity given by

$$C = \sqrt{gd} \quad (20)$$

long-period wave celerities of  $12.6 \text{ ms}^{-1}$  and  $16.8 \text{ ms}^{-1}$  are calculated for areas A and B, respectively. On the basis of this close agreement, it appears that these observed long-

TABLE 3. Comparison Between the Long-Period SAR-Derived Spectral Estimates and the in Situ Sea Truth

Test Area	Distance From Shore, m	Depth, m	SAR-Derived Estimates		Sea Truth*	
			Dominant Long-Period Wavelengths, m	Direction, $T^\circ$	Dominant Long-Period Wavelengths, m	Direction, $T^\circ$
A (Nearshore)	2650	16.2	157-167	$35 \pm 3$	216	$34 \pm 2$
			393-423		406	
B (Offshore)	5800	28.7	498-523	$25 \pm 3$	288	$28 \pm 2$
					541	

\*Actual measurements made at the surf zone; values for test areas A and B are depth-corrected

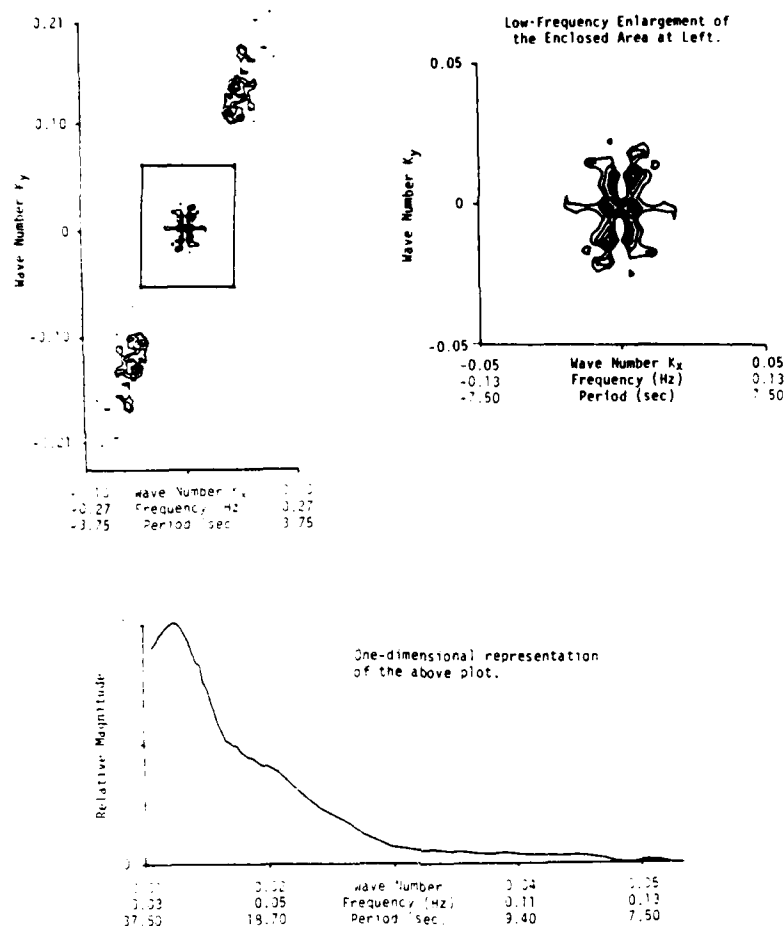


Fig. 7. SAR-derived two-dimensional spectral estimate (offshore). (Note: Negative wave numbers, frequencies, and periods are included due to the symmetric nature of a two-dimensional FFT. The frequency and period axes assume shallow water waves; see text for further explanation.)

period wave motions are propagating as shallow water waves and not as forced waves as suggested from theory. This apparent discrepancy arises from a complex interaction between the relatively short, steep, locally generated waves and the shallow bathymetry of this region. The theoretical formulation employed in this study is based upon the assumption that the character of the SAR-sensed modulated sea surface is a function of  $\Delta K$  of the wind wave components, and that  $\Delta K \ll K_1$ . Hence, for limited fetch situations such as the conditions of this study, the two wind wave components separated by  $\Delta K$  do not explicitly satisfy the mathematical constraint of  $\Delta K \ll K_1$ . This produces a modulated long-period wave which is not completely 'phase locked' with the short wave components and, in fact, appears to propagate as a shallow water wave.

The close agreement between the long-period celerity derived above and that predicted for a shallow water wave prompted the inclusion of frequency and period axes on the various plots in Figures 6 and 7. Recall that the SAR only provides a spatial measure of waves, therefore, the only 'true' axes in Figures 6 and 7 is that for wave number. The frequency and period axes are both based on the shallow water wave assumption for a given wave number. They are not derived from any physical measurements.

To document further the existence and character of the

SAR-sensed long-period wave motions, one-dimensional scans of the raw radar backscatter were obtained. One spatial series, consisting of 512 digital values sampled at 3 m, was obtained from each of the two regions where the two-dimensional FFT analysis was performed. Area A was centered 2650 m offshore and area B was centered at 5800 m offshore. The total series of radar backscatter as well as their associated band pass filtered (177–1180 m, area A and 249–1660 m, area B) long-period components are presented in Figure 8. Once again, long-period oscillations of the radar backscatter intensity are clearly visible, with maximum radar return occurring in phase with peaks of the long-period oscillations (i.e., groups of large wind waves). These SAR-sensed, long-period oscillations represent approximately a 1.5-dB change in radar backscatter intensity from crest to trough. The dynamic range of the total, unfiltered radar backscatter intensity is approximately 5.2 dB. Hence the energy associated with these radar-sensed long-period oscillations is approximately a factor of 2.3 less than the energy of the radar backscatter associated with the wind wave components of the sea surface structure.

#### SUMMARY

It appears that a direct correlation exists between the amplitude of these long-period wave motions, as sensed in

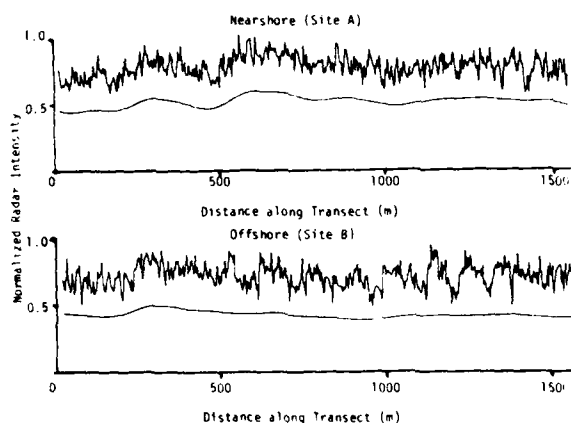


Fig. 8. Filtered and unfiltered radar transects for both near and offshore study sites.

situ, and the long-period component of the radar backscatter. From the sea truth measurements, the ratio of short-period wave to long-period wave mean amplitude is 5.4. Similarly, for the radar-sensed long-period oscillation this ratio is approximately 6.0. Kasischke [1980] has reported a linear relationship between SEASAT SAR modulation depth (crest-to-trough intensity) and wave height.

Investigation of the information contained in the backscatter of microwave energy from the sea surface can provide detailed and nearly synoptic coverage of relatively large portions of the ocean surface. To illustrate this unique capability, a three-dimensional representation of a portion of a SAR-sensed sea surface is presented in Figure 9, which depicts the long-period undulations present in study area B. This plot was produced from the SAR digital data by extracting six isorange lines of 5 pixels each, averaging these 5 pixels, in effect, to smooth in the range direction. These lines were then band pass filtered for wavelengths between 249 and 1660 m (15–200 s), and this filtered output was used as input to a perspective view-plotting program.

It is clear from this plot that long-period waves are present

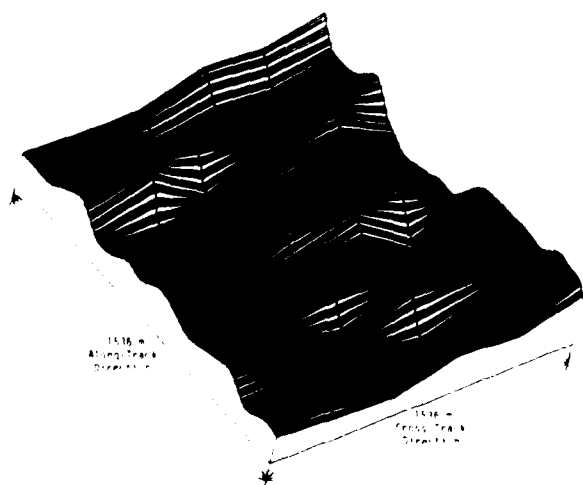


Fig. 9. Perspective plot of offshore area B showing filtered long-period components.

in this area. However, care should be exercised in interpreting what information this plot contains. This is merely a convenient graphical technique that shows the long-period components, not a detailed analysis technique.

This paper has demonstrated that a synoptic remote sensing device such as SAR has the ability to successfully image low-amplitude, long-period signals (surf beats). The analysis techniques utilized to extract this information from the SAR data, include (1) a manual photographic interpretation, (2) one- and two-dimensional spectral analyses employing FFT techniques, and (3) extraction of band-pass filtered long-period components from radar backscatter plots. It should be mentioned when utilizing SAR data such as presented in this paper that the spectral estimates presented are wave number, directional spectra of the radar return intensity. The data do not represent wave height information in a direct sense. SAR intensities (i.e., crest-to-trough modulation) have been successfully correlated to wave height, but the exact mathematical modulation transfer function (i.e., SAR gravity wave imaging mechanism) is not totally understood at the present time.

**Acknowledgments.** The ERIM analysis of the SAR gravity wave data was supported by the Office of Naval Research (ONR) contract N00014-76-C-1048. The technical monitor for this ONR contract is Hans Dolezalek. The field installation of the mobile wave and current monitoring system, as well as the reduction of the in situ sea truth data, was supported by The University of Michigan Rackham grant 387349.

#### REFERENCES

- Ausherman, D. A., W. D. Hall, J. N. Latta, and J. S. Zelenka. Radar data processing and exploitation facility, paper presented at International Radar Conference, IEEE, Washington, D. C., 1975.
- Brown, W. J., and L. Porcello. An introduction to synthetic aperture radar, *IEEE Spectrum*, 6, 52–66, 1968.
- Feldkamp, G. B., Correction of SAR-induced distortions in SEASAT imagery, paper presented at Conference on Applications of Digital Image Processing, Soc. of Photo-Opt. Instrum. Eng., San Diego, Calif., August 1978.
- Gonzalez, F. L., R. C. Beal, W. F. Brown, P. S. DeLeonibus, J. S. Sherman, J. F. R. Gower, D. Lichy, D. B. Ross, C. L. Rufenach, and R. A. Shuchman. SEASAT synthetic aperture radar: Ocean wave detection capabilities, *Science*, 204, 1418–1421, 1979.
- Gower, J. F. R., and B. A. Hughes. Radar and ship observations of coastal sea surface roughness patterns in the Gulf of Georgia, paper presented at Thirteenth International Symposium on Remote Sensing of Environment, Environ. Res. Lab. of Mich., Ann Arbor, Mich., 1979.
- Jenkins, A. M., and D. G. Watts. Spectral analysis and its applications, 525 pp., Holden-Day, San Francisco, Calif., 1968.
- Kasischke, E. S., Extraction of gravity wave information from space-borne synthetic aperture radar data, Master's thesis, Univ. of Mich., Ann Arbor, 1980.
- Kinsman, B., *Wind Waves—Their Generation and Propagation on the Ocean Surface*, 676 pp., Prentice-Hall, Englewood Cliffs, N. J., 1965.
- Kozma, A., E. N. Leith, and N. G. Massey. Tilted plane optical processor, *Appl. Opt.*, 11, 1766, 1972.
- Larsen, L. H., An instability of packets of short gravity waves in waters of finite depth, *J. Phys. Oceanogr.*, 99, 1139–1143, 1979.
- Longuet-Higgins, M. S., and R. W. Stewart. Radiation stress and mass transport in gravity waves, *J. Fluid Mech.*, 13, 481–504, 1962.
- Longuet-Higgins, M. S., and R. W. Stewart. Radiation stresses in water waves in a physical discussion, with applications, *Deep Sea Res.*, 11, 529–562, 1964.
- McGoldrick, L. F., On Wilton's ripples: A special case of resonant interactions, *J. Fluid Mech.*, 42, 193–200, 1970.
- McGoldrick, L. F., On the rippling of small waves: A harmonic nonlinear nearly resonant interaction, *J. Fluid Mech.*, 52, 725–751, 1972.
- Meadows, G. A., A field investigation of the spatial and temporal



- structure of longshore currents, Ph.D. dissertation, Purdue Univ., West Lafayette, Ind., 1977.
- Meadows, G. A., The wind-driven component of surf zone circulation (abstract), *Eos Trans. AGU*, 60(46), 848, 1979.
- Meadows, G. A., and W. L. Wood, Long-period surf zone motions, submitted to *J. Geophys. Res.*, 1982.
- Meadows, G. A., E. S. Kasischke, and R. A. Shuchman, SAR observations of coastal zone conditions, paper presented at Fourteenth International Symposium on Remote Sensing of Environment, Environ. Res. Lab. of Mich., San José, Costa Rica, 1980.
- Munk, W. H., Surf beats, *Eos Trans. AGU*, 30, 849-854, 1949.
- Phillips, O. M., The structure of short gravity waves on the ocean surface, in *A Symposium to Explore the Potential of Spaceborne Synthetic Aperture Radar for Radio Oceanography*, Johns Hopkins Press, Baltimore, Md., 1981.
- Rawson, R., F. Smith, and R. Larson, The ERIM simultaneous X- and L-band dual polarized radar, paper presented at International Radar Conference, IEEE, Washington, D. C., 1975.
- Schwab, D., R. A. Shuchman, and D. Liu, Wind wave directions determined from synthetic aperture radar imagery and from a tower in Lake Michigan, *J. Geophys. Res.*, 86(C3), 2059-2064, 1981.
- Shuchman, R. A., and G. A. Meadows, Airborne synthetic aperture radar observations of surf zone conditions, *Geophys. Res. Lett.*, 7(11), 857-860, 1980.
- Shuchman, R. A., K. Knorr, J. C. Dwyer, A. Klooster, and A. I. Maffett, Imaging ocean waves with SAR, *ERIM Rep. 124300-2-T*, 130 pp., Environ. Res. Inst. of Mich., Ann Arbor, Mich., 1979.
- Tucker, M. J., Surf beats: Sea waves of 1 to 5 minutes period, *Proc. R. Soc. London Ser. A*, 207, 565-573, 1950.
- Whitham, G. B., Mass momentum and energy flux in water waves, *J. Fluid Mech.*, 12, 135-147, 1962.
- Wood, W. L., and G. A. Meadows, Unsteadiness in longshore currents, *Geophys. Res. Lett.*, 2(11), 503-505, 1975.
- Wright, J. W., A new model for sea clutter, *IEEE Trans. Antennas Propag.*, AP-16, 195-223, 1968.

(Received April 21, 1981;  
revised January 29, 1982;  
accepted February 1, 1982.)

## Wind Wave Directions Determined From Synthetic Aperture Radar Imagery and From a Tower in Lake Michigan

DAVID J. SCHWAB,<sup>1</sup> ROBERT A. SHUCHMAN,<sup>2</sup> AND PAUL C. LIU<sup>1</sup>

Directional wave spectra calculated from digitized synthetic aperture radar (SAR) images of waves on Lake Michigan are compared to a wave directional spectrum determined from measurements taken at a tower and to a one-dimensional spectrum determined from a Waverider buoy. The comparison is within one frequency band for peak energy frequency and within 20° for direction, but the SAR image intensity spectrum does not have the same shape as a wave height spectrum. Wave refraction directions observed in the SAR spectra are within 10° of classical wave refraction calculations.

### INTRODUCTION

Directional wave spectra have been measured by a variety of techniques and instruments since the pioneering work of Barber [1954, 1963], Cote *et al.* [1960], and Longuet-Higgins *et al.* [1963]. Early measurements were made with pitch and roll buoys or wave staff arrays. More recently, remote sensing techniques have been used. The principles behind in situ and remote sensing techniques are so different that the two methods have rarely been carefully compared. This paper intends to meet that need.

Synthetic aperture radar (SAR) has been used to image ocean waves over large areas from both conventional aircraft [Elachi, 1976; Shuchman and Zelenka, 1978; Shemdin *et al.*, 1978] and from satellites [Gonzalez *et al.*, 1979]. Image resolution does not depend on antenna aperture size or altitude, as with real aperture radar, or external illumination, as with photography. SAR images have then been used to determine wave direction and wavelength. Although the imaging mechanism has not been explained completely, the forward face and rear face of sufficiently large waves exhibit different scattering characteristics at SAR wavelengths and can be distinguished in SAR imagery.

The Environmental Research Institute of Michigan (ERIM) has been acquiring and processing SAR data from aircraft for several years [Cindrich *et al.*, 1977]. In October 1977 ERIM acquired SAR data on a flight across Lake Michigan between Muskegon, Michigan, and Milwaukee, Wisconsin. At this time the Great Lakes Environmental Research Laboratory (GLERL) was operating a solar-powered research tower 1.8 km off Muskegon capable of measuring and recording wind, temperature, and directional wave information [Schwab *et al.*, 1980]. A sample of the SAR imagery showing the location of the GLERL tower is presented in Figure 1. In addition, a Waverider buoy was deployed 12 km offshore of Muskegon. The purpose of this paper is to compare SAR wave directional measurements to in situ wave directional spectra at the GLERL research tower and one-dimensional spectra at the Waverider buoy and to examine the variability of the directional wave spectrum across the lake. In so doing, we hope to show that the combination of in situ and remotely sensed

wave information is a powerful tool in gaining a better understanding of wave processes.

### DATA

On October 6, 1977, at approximately 1130 h EST ERIM's C46 aircraft carrying the X-L band dual polarization imaging radar [Rawson *et al.*, 1975] flew west over Muskegon across Lake Michigan to Milwaukee along a latitude of 43°10'N and then from Milwaukee back to Muskegon. The ground track corresponds to the tails of the numbered arrows in Figure 2. The ERIM SAR system records four channels of radar return, but we will focus our attention here on the X band horizontal-transmit horizontal-receive channel, as these data provided the clearest wave images. L band SAR has been used to image ocean waves from aircraft and the Seasat satellite, but in the present case the wave images from the L band system were not clear enough to warrant further processing. The aircraft flew at 3500 m and operated the radar with an average angle of depression from the horizontal of 30°, yielding a swath width of 5.6 km. The cross-track or range resolution of SAR is limited by radar frequency and is about 2 m for the X band. The along-track or azimuth resolution is obtained from the synthetic aperture technique described by Brown and Porcello [1968] during subsequent processing on the ERIM optical processor. For the X band, the azimuthal resolution is about 2.5 m.

At the same time as the ERIM flight, GLERL was operating a solar powered research tower 1.8 km offshore of Muskegon in 15 m of water [Schwab *et al.*, 1980]. The location is shown in Figure 1 and corresponds to the arrow labeled 1 in Figure 2. The tower operated from July 19, 1977, to October 11, 1977. Sensors on the tower measured wind speed at two levels, wind direction, air and water temperature, and directional wave information from an array of four Zwarts water level gages [Zwarts, 1974]. Data were transmitted to a shore-based recording station at half-second intervals for 30 min out of each hour. The water level gages were deployed at the vertices and center of an equilateral triangle with 3 m sides. The wave gage at the eastern vertex failed on September 2, 1977, so that at the time of the ERIM flight only three gages were operating. The three-gage array can unambiguously determine wave direction for wavelengths greater than about 6 m.

In addition, a Waverider buoy continuously recording wave fluctuations was deployed by GLERL 12 km offshore of Muskegon in 75 m of water. Its location corresponds to the arrow labeled 3 in Figure 2. No directional information is available

<sup>1</sup> National Oceanic and Atmospheric Administration, Great Lakes Environmental Research Laboratory, Ann Arbor, Michigan.

<sup>2</sup> Radar and Optics Division, Environmental Research Institute of Michigan, Ann Arbor, Michigan.

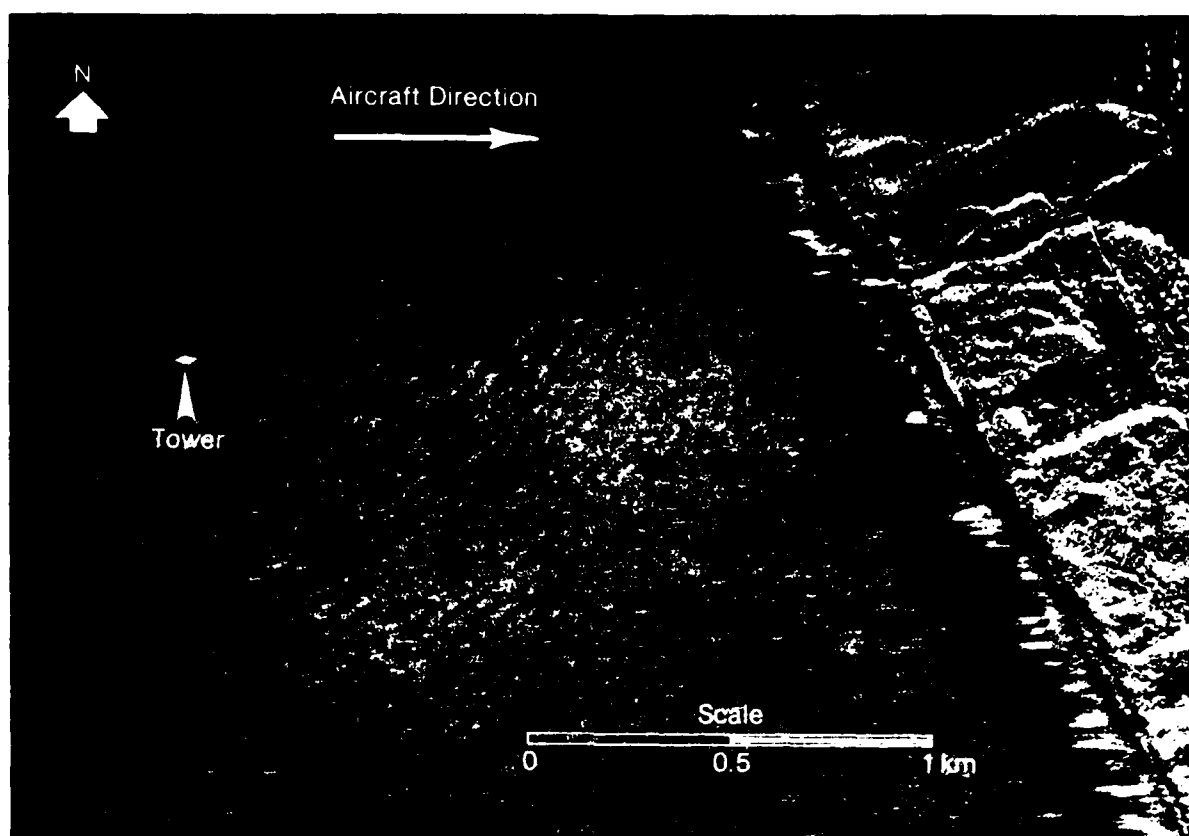


Fig. 1. Synthetic aperture radar imagery of wind waves in Lake Michigan on October 6, 1977, offshore of Muskegon, Michigan.

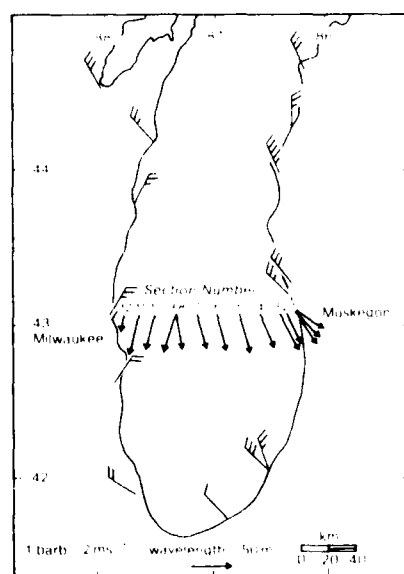


Fig. 2. Wind and wave observations on October 6, 1977, 1200 h EST. Wind speed and direction are from Coast Guard and National Weather Service stations. Wavelength and direction are from directional spectra of the digitized sections of synthetic aperture radar imagery indicated in Tables 1 and 2.

from the buoy, but the one-dimensional wave spectrum can be determined from the recorded water level fluctuations.

#### METHODS

Twelve sections of SAR images were digitized with an approximate resolution of 3 m (1.5-m pixels). Four sections were from the westbound flight and eight from the eastbound, as indicated in Table 1. The sections are numbered east to west, with sections 8 and 9 overlapping. (See Figure 2). The range coordinate of each section was corrected in a computer program for slant-to-ground range radar geometry [Feldkamp, 1978]. Then 768-m square subsections, with a resolution of 3

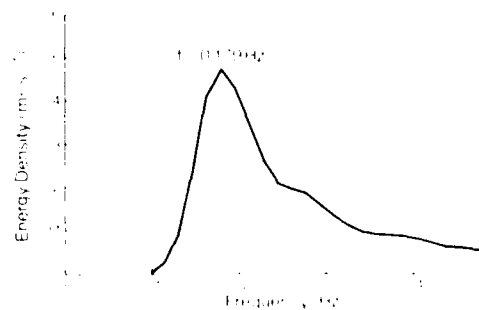


Fig. 3. Wind wave spectrum determined from Waverider buoy data on October 6, 1977, 1200 h EST.

m centered on the coordinates shown in Table 1, were extracted from the digitized sections. Section 1 corresponded to the location of the GLERL tower and section 3 to the location of the Waverider buoy. In section 1, one subsection east of the tower (1a) and one subsection west of the tower (1c) were taken in addition to one centered on the tower (1b) to examine refraction effects.

The 1.5-m pixel digitized SAR images were converted to 3 m resolution by 4 pixel averaging to increase coherence in the image. The average value of each azimuthal line was subtracted from the line to remove the trend of intensity falloff with increasing range distance. Two-dimensional fast Fourier transforms were performed on each  $256 \times 256$  cell subsection to yield raw directional wave number spectra each with a Nyquist wave number of  $1.04 \text{ m}^{-1}$ . The raw spectra were smoothed by replacing each value with the average of the surrounding  $5 \times 5$  cell. The approximate number of degrees of freedom for the resulting spectrum is 142 [Kinsman, 1965, p. 464]. The 99% confidence limits are then  $\pm 1.5 \text{ dB}$  [Jenkins and Watts, 1968].

To calculate a directional wave spectrum at the GLERL research tower, wave slopes were determined for 10 min of data as the slopes of the plane passing through the measured locations of the water surface at the three operating gages. Wave height was taken as the average of the measurements of the three gages. Since wave measurements were at  $\frac{1}{2}$ -s intervals, the Nyquist frequency for tower spectra was 1 Hz. The first five Fourier coefficients of the angular distribution of energy in 20 frequency bands between 0 and 1 Hz were calculated from the wave height and wave slope records by the method described in Longuet-Higgins *et al.* [1963]. The calculated wave directional spectrum has approximately 120 degrees of freedom with 99% confidence limits of  $\pm 1.5 \text{ dB}$ .

It is important to remember that the energy spectrum derived from SAR imagery is an image intensity spectrum and not a wave height spectrum. The relationship between SAR image intensity and wave height is still being investigated [Jain, 1977; Shuchman *et al.*, 1979]. The directional spectrum determined from wave staff data, although it may not have the directional resolving power of the SAR spectrum, is a true wave height spectrum.

## RESULTS

The wave number and direction corresponding to the peak energy point in each of the 14 SAR spectra are presented in

TABLE 1. Location of SAR Directional Spectra

Section	Flight Leg	Sub-section	Distance From Muskegon Shore, km	Average Water Depth, m	Time, h, EST
1	E	1a	1.01	8	1235
		1b	1.78	15	
		1c	2.55	18	
2	E	2	7.05	35	1233
3	E	3	12.32	66	1232
4	E	4	26.10	110	1230
5	E	5	39.87	103	1227
6	E	6	53.65	96	1224
7	E	7	67.43	83	1221
8	E	8	81.21	75	1218
9	W	9	81.21	75	1146
10	W	10	94.98	82	1149
11	W	11	108.76	96	1152
12	W	12	118.45	75	1154

TABLE 2. Peak Energy Wave Number and Direction from SAR Directional Spectra

Subsection	Wave number, $\text{m}^{-1}$		Direction, True	
	Uncorrected	Corrected	Uncorrected	Corrected
1a	0.130	0.141	306	303
1b	0.133	0.142	321	317
1c	0.120	0.127	328	321
2	0.147	0.151	342	336
3	0.117	0.123	333	328
4	0.123	0.129	344	339
5	0.117	0.111	350	345
6	0.123	0.126	348	343
7	0.140	0.143	349	344
8	0.150	0.152	354	349
9	0.133	0.136	9	15
10	0.137	0.140	11	16
11	0.123	0.126	8	14
12	0.294	0.296	5	9

Table 2. The SAR process distorts the apparent wavelength of waves moving in the azimuthal direction and distorts the apparent direction of waves with a velocity component in the range direction. A detailed description of these effects and the appropriate corrections can be found in Shuchman *et al.* [1977]. Corrected values of wave number and direction based on the perceived values are also shown in Table 2. Wavelengths range from 21 m at section 12 to 53 m at section 5. There is a  $180^\circ$  ambiguity in wave direction measured by SAR, which was resolved by assuming the waves were coming from the same quadrant as the wind.

A graphical illustration of the results shown in Table 2 is presented in Figure 2, along with wind speed and direction observations from Coast Guard and National Weather Service stations around the lake. Wavelengths in Figure 2 correspond to corrected wave numbers in Table 2, and directions correspond to corrected directions. Wave directions determined from SAR imagery are consistent with observed wind directions. Waves and wind are north-northeast on the western side of the lake and north-northwest on the eastern side. However, the wave direction for section 8 on the eastbound leg of the flight is  $26^\circ$  different from the wave direction determined for the same location (section 9) on the westbound leg. Note, however, that section 8 was imaged 32 min later than section 9.

Wind at the GLERL tower was  $288^\circ$  and 6.5 m/s at 10 m and 5.7 m/s at 5 m. Air temperature was  $5.8^\circ\text{C}$  and water temperature  $7.1^\circ\text{C}$ , indicating a slightly unstable atmospheric boundary layer over the lake. Significant wave height was 0.99 m. The one-dimensional wind wave spectrum (Figure 3) calculated from Waverider buoy data near section 3 showed an energy peak at 0.179 Hz and a significant wave height of 1.03 m.

The directional frequency spectrum obtained from the GLERL research tower data and the directional wave number spectrum obtained from ERIM SAR imagery are compared in Figure 4. The frequency spectrum shows an energy peak at 0.211 Hz and  $300^\circ$ . As indicated in Table 2, the wave number spectrum has a peak at  $0.142 \text{ m}^{-1}$  and  $317^\circ$ . Because of the  $180^\circ$  directional ambiguity in analyzing images of waves, the wave number spectrum is symmetric about the origin. The wave number spectrum in Figure 4 is uncorrected for wave motion effects discussed above, but as shown in Table 2, these corrections are small. There is still a large amount of energy at zero wave number owing to imperfect removal of the intensity

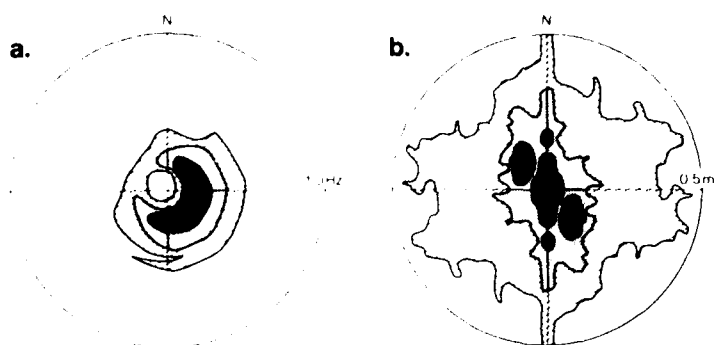


Fig. 4. (a) Directional frequency spectrum of wave height determined from wave research tower measurements, and (b) directional wave number spectrum of image intensity determined from synthetic aperture radar image. Contour levels of the logarithm of spectral density are shown in 5-dB increments relative to the maximum density.

falloff in the range direction. There is also an increase in energy at all wave numbers as the direction approaches the range direction (north-south). The energy lobes in the wave number spectrum are more elongated in the north-south direction than those in the frequency spectrum and show less directional spreading. The reasons for these differences will be discussed in the next section.

#### DISCUSSION

The peak energy wave number calculated from SAR data at subsection 1b corresponds to a wave frequency of 0.196 Hz. This is within the frequency band of peak energy calculated from the wave gages, 0.185–0.238 Hz. Empirical formulas for the peak energy frequency of fetch limited equilibrium spectra with a fetch of 125 km (appropriate for the wind direction measured at the tower) and 10-m wind speed of 6.5 m/s give 0.178 Hz according to Hasselmann *et al.* [1973] and 0.198 Hz according to Liu [1971]. Measurements from SAR and from tower wave gages are both consistent with these estimates of peak energy frequency. At section 3, the average peak energy wave number determined from the three SAR spectra is 0.124  $m^{-1}$ . The corresponding wave frequency of 0.175 Hz also agrees very well with the peak energy frequency of 0.179 Hz determined from the Waverider spectrum (Figure 3). From these comparisons it is apparent that the frequency of peak energy waves determined from SAR imagery is consistent with both types of in situ measurements.

The discrepancy in peak energy wave direction between SAR and tower systems, 317° versus 300°, is within acceptable directional resolution limits for both the three-gage tower system and the SAR system. The directional spreading of energy in the tower spectrum in Figure 4, which conforms in general to previously published directional wave spectra [e.g., Mitsuyasu *et al.*, 1975], differs somewhat from the spreading in the SAR spectrum. In this case the directional resolution of the SAR system is probably better than a three-gage array, and therefore the SAR spectrum shows less directional spreading. In the SAR spectrum the energy lobes corresponding to waves are elongated in the north-south direction and not spread azimuthally as in the tower spectrum. We believe that this feature is due to range traveling artifacts introduced into the SAR image by multiple-velocity range traveling scatterers. The artifacts appear in the SAR image as bright, east-west (azimuthal) streaks 6–60 m long and rather randomly distributed in space. The effect of this type of noise on a directional spectrum calculated from a digitized image is to introduce energy at all wavelengths and at directions near the range direction, north-south in this case. We speculate that each artifact is due to radar return from a whitecap that appears to the radar as a scatterer with a range of velocities. In the SAR imaging process, a scatterer with a component of velocity in the range direction is displaced on the image in the azimuthal direction by an amount proportional to its range component of velocity [Raney, 1971]. If the scatterer appears to have a vari-

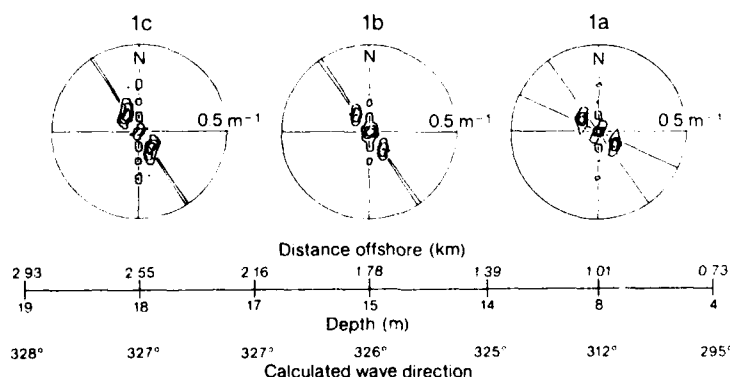


Fig. 5. Contour plots of SAR spectra in 3-dB increments relative to the maximum density for subsections 1a, 1b, and 1c, showing effects of wave refraction. The radial lines on each spectrum correspond to wave directions calculated for the depths at the edges of each subsection.

ety of velocities, its image will be displaced various proportional amounts and will appear as a streak in the azimuthal direction. This is a common feature of SAR images of the breaker zone. The recorded wind speed of 6.5 m/s in an unstable atmosphere is approximately the critical speed for initiation of whitecapping in the Great Lakes according to Monahan [1969]. It appears that the whitecaps are responsible for the resulting range traveling image artifacts and resultant contamination of the wave number spectrum.

If we take  $328^\circ$  true as the mean direction of waves incident on the Muskegon shore (the average direction of section 3) and 0.211 Hz (as measured at the tower) as the wave frequency, wave refraction can be observed in the SAR directional spectra. Contour plots (given in 3 dB levels) of the directional spectra for subsection 1a, 1b, and 1c are shown in Figure 5. Also drawn on the figure are classical refraction directions calculated for depths corresponding to the edges of each subsection. (Kinsman [1965] gives a typical example of refraction calculations on pages 156–167.) For example, the two lines drawn on the contour plot of subsection 1a represent angles of  $295^\circ$  and  $325^\circ$ , the wave directions predicted by classical methods assuming depths of 4 and 14 m, respectively. The entire wave spectrum should be corrected for refraction for a proper comparison, but the spectra in Figure 5 are so peaked that the single component refraction calculations are a good approximation.

Figure 5 indicates that the SAR spectra are sensitive to refraction effects. Also given on the figure is the wave refraction angle assuming the average depth of each of the subsections. When these directions are compared to the Table 2 results, the SAR data have a tendency to show more refraction than was predicted, but the tendency is in the right direction, and  $10^\circ$  can still be considered good agreement.

The SAR wave number spectra shown in Figures 3 and 5 are typical of all 14 SAR spectra. Spectra from the middle of the lake (sections 5–9) have wave energy lobes of somewhat greater magnitude relative to the background noise and show more of the features that appear in the tower wave frequency spectrum, such as a steep forward face and more directional energy spread. The SAR spectrum is of course a wave number spectrum of radar return intensity and is not expected to have the same appearance as the directional frequency spectrum determined from wave heights. Even if the wave number spectrum is converted to a frequency spectrum or vice versa, it is clear that the SAR spectra examined here cannot be easily transformed to or interpreted as wave height spectra. However, the peak energy wave number and direction determined from SAR spectra agree very well with in situ measurements, and the synoptic availability of even these parameters is prohibitively expensive by ground-based measurements.

### CONCLUSIONS

Directional spectra calculated from synthetic aperture radar (SAR) data of Lake Michigan have been compared to an in situ directional spectrum from the GLERL research tower and to a one-dimensional spectrum from a Waverider buoy. The comparisons were favorable, indicating SAR's ability to image accurately wind-generated water waves. In addition to data collected over the tower and Waverider buoy, data were continually collected across Lake Michigan in both directions. These data represent a synoptic view of wind waves across the

entire width of Lake Michigan and should prove very useful to those modeling waves on the Great Lakes.

The major caveat about using directional spectra from SAR data is that the SAR spectral estimates are proportional to radar return intensity and not wave energy. The data do not represent wave height information, at least not in a recognizable form. The modulation transfer function (i.e., SAR gravity wave imaging mechanism) is not totally understood at the present time. The determination of the transfer function, as well as determination of wave height, using SAR data will be a major scientific advance, for at that time SAR gravity wave data can be used to obtain power density estimates of the sea surface. Until this is accomplished, SAR wave directional measurements must be accompanied by either in situ (wave staff or Waverider) or remotely sensed (laser altimeter) measurements to give an estimate of wave height.

**Acknowledgments.** The ERIM contribution to this study was supported by GLERL contract NA79RHA00107. The algorithms used by ERIM to reduce the SAR data and generate spectral estimates were developed under Office of Naval Research support (contract N000-14-1048). The authors thank K. Knorr and K. Amble of ERIM for reducing the SAR data. GLERL contribution 205.

### REFERENCES

- Barber, N. F., Finding the direction of travel of sea waves, *Nature*, **174**, 1048–1050, 1954.
- Barber, N. F., The directional resolving power of an array of wave detectors, in *Ocean Wave Spectra*, Prentice-Hall, Englewood Cliffs, N. J., 1963.
- Brown, W. J., and L. Porcello, An introduction to synthetic aperture radar, *IEEE Spectrum*, **6**, 52–66, 1968.
- Cindrich, I., J. Marks and A. Klooster, Coherent optical processing of synthetic aperture radar data, *Proc. Soc. Photo-Opt. Instrum. Eng.*, **128**, 1977.
- Cote, L. J., J. O. Davis, W. Marks, R. J. McGough, E. Mehr, W. J. Pierson, Jr., J. F. Ropek, G. Stephenson, and R. C. Vetter, The directional spectrum of a wind generated sea as determined by the Stereo Wave Observation Project, *Meteorol. Pap.*, **2**, N. Y. Univ. Coll. of Eng., New York, 1960.
- Elachi, C., Wave patterns across the North Atlantic on September 28, 1974, from airborne radar imagery, *J. Geophys. Res.*, **81**, 2655–2656, 1976.
- Feldkamp, G. B., Correction of SAR-induced distortion in SEASAT imagery, paper presented at the SPIE Conference on Applications of Digital Image Processing, San Diego, Calif., August 1978.
- Gonzalez, F. I., R. C. Beal, W. E. Brown, P. S. DeLeonibus, J. S. Sherman, J. F. R. Gowere, D. Lichy, D. B. Ross, C. L. Rufenach, and R. A. Shuchman, Seasat synthetic aperture radar: Ocean wave detection capabilities, *Science*, **204**, 1418–1421, 1979.
- Hasselmann, K., T. P. Barnett, E. Bouws, H. Carlson, D. E. Cartwright, K. Enke, J. A. Ewing, H. Gienapp, D. E. Hasselmann, P. Kruseman, A. Meerburg, P. Muller, D. J. Olbers, K. Richter, W. Sell, and H. Walden, Measurements of wind-wave growth and swell decay during the Joint North Sea Wave Project (JONSWAP), *Deut. Hydrogr. Z., Suppl. A*, **8**, 1973.
- Jain, A., Determination of ocean wave heights from synthetic aperture radar imagery, *Appl. Phys.*, **13**, 371–382, 1977.
- Jenkins, A. M., and D. G. Watts, *Spectral Analysis and Its Applications*, Holden-Day, San Francisco, Calif., 1968.
- Kinsman, B., *Wind Waves—Their Generation and Propagation on the Ocean Surface*, Prentice-Hall, Englewood Cliffs, N. J., 1965.
- Liu, P. C., Normalized and equilibrium spectra of wind waves in Lake Michigan, *J. Phys. Oceanogr.*, **1**, 249–257, 1971.
- Longuet-Higgins, M. S., D. E. Cartwright, and N. D. Smith, Observations of the directional spectrum of sea waves using the motions of a floating buoy, in *Ocean Wave Spectra*, Prentice-Hall, Englewood Cliffs, N. J., 1963.
- Mitsuyasu, H. F. Tasai, T. Suhara, S. Mizuno, M. Ohkusu, T. Honda, and K. Rikishi, Observations of the directional spectrum of ocean waves using a cloverleaf buoy, *J. Phys. Oceanogr.*, **5**, 750–760, 1975.

- Monahan, E. C., Fresh water whitecaps, *J. Atmos. Sci.*, 26, 1026-1029, 1969.
- Raney, R. K., Synthetic aperture imaging radar and moving targets, *IEEE Trans. Aerosp. Electron. Syst.*, AES-7, 1971.
- Rawson, R., F. Smith and R. Larson, The ERIM simultaneous X- and L-band dual polarized radar, *IEEE 1975 Int. Radar Conf.*, 505, 1975.
- Schwab, D. J., P. C. Liu, H. K. Soo, R. D. Kistler, H. L. Booker, and J. D. Boyd, Wind and wave measurements taken from a tower in Lake Michigan, *J. Great Lakes Res.*, 6, 76-82, 1980.
- Shemdin, O. H., W. E. Brown, F. G. Standhammer, R. Shuchman, R. Rawson, J. Zelenka, D. B. Ross, W. McLeish, and R. A. Berles, Comparison of in situ and remotely sensed ocean waves off Marine-land, Florida, *Boundary Layer Meteorol.*, 13, 193-202, 1978.
- Shuchman, R. A., and J. S. Zelenka, Processing of ocean wave data from a synthetic aperture radar, *Boundary Layer Meteorol.*, 13, 181-191, 1978.
- Shuchman, R. A., P. L. Jackson, and G. B. Feldkamp, Problems of imaging ocean waves with synthetic aperture radar, *Rep. 124300-1-T*, Environ. Res. Inst. of Mich., Ann Arbor, 1977.
- Shuchman, R. A., K. Knorr, J. C. Dwyer, A. Klooster, and A. L. Maffett, Imaging ocean waves with SAR, *Rep. 124300-2-T*, Environ. Res. Inst. of Mich., Ann Arbor, 1979.
- Zwarts, C. M. G., Transmission line wave height transducer, *Proc. Int. Sym. Ocean Wave Meas. Anal.*, 1, 605-620, 1974.

(Received February 13, 1980;  
revised September 19, 1980;  
accepted September 29, 1980.)

## Estimates of Ocean Wavelength and Direction From X- and L-Band Synthetic Aperture Radar Data Collected During the Marineland Experiment

ROBERT A. SHUCHMAN, JAMES D. LYDEN, AND DAVID R. LYZENGA

**Abstract**—Simultaneously obtained X- and L-band synthetic aperture radar (SAR) data collected during the Marineland Experiment were spectrally analyzed by fast Fourier transform (FFT) techniques to estimate ocean wavelength and direction. An eight-sided flight pattern was flown over the same ocean area in order to study the sensitivity of the spectral estimate on radar look direction. These spectral estimates were compared with *in situ* wave measurements made by a pitch-and-roll buoy. The comparison revealed that the

X-band SAR detected all gravity waves independent of radar look direction, while the L-band SAR detected all range-traveling gravity waves but failed to detect waves in three of four cases in which the waves were traveling within 25° of the azimuth direction. The analysis also indicates that azimuth-traveling waves appear longer and more range-traveling in the SAR imagery than observed by *in situ* instrumentation. It is postulated that degraded azimuth resolution due to scatterer motion is responsible for these observations.

Manuscript received November 4, 1982; revised February 9, 1983. This work was supported by the Office of Naval Research under Contract N00014-76-C-1048 and NOAA/NES Grant 04-6-158-44078.

The authors are with the Radar Division, Environmental Research Institute of Michigan (ERIM), Ann Arbor, MI 48107.

### I. INTRODUCTION

A PREVIOUS study [1] of the Marineland synthetic aperture radar (SAR) data set showed close agreement between SAR-derived wave spectra and *in situ* measurements made by a



pitch-and-roll buoy which operated coincidentally with the SAR overflights. This previous study utilized only a single pass of *X*-band data collected on Dec. 14, 1975. This particular pass imaged waves traveling in the range direction (towards the radar line-of-sight), which is the most favorable imaging geometry for the SAR [2], [3]. The present study considers data collected at both *X*- and *L*-band for eight different look directions relative to the wave propagation direction.

As discussed in the companion paper of this issue [3], the SAR imaging mechanism for ocean waves is highly dependent on radar look direction. Tilt and hydrodynamic modulation are the dominant mechanisms for SAR imaging range-traveling waves [2], [3], while azimuth-traveling waves are believed to be imaged primarily because of velocity bunching [4]. However, controversy still exists regarding the effects of moving ocean wave scatterers on the SAR image formation process. The Marineland simultaneous *X*- and *L*-band data set provides needed information on the SAR imaging mechanism for ocean waves, as well as a direct indication of the ability of SAR to accurately image ocean gravity waves as a function of radar wavelength and look direction.

Past studies utilizing the Marineland data set have concentrated on the conditions under which ocean waves are imaged rather than the accuracy of the spectral estimates [1]–[3], [5]. This paper presents a comparison of the SAR-derived wave spectral estimates with *in situ* measurements (pitch-and-roll buoy data) using the entire SAR *X*- and *L*-band data set collected from an eight-sided flight pattern flown on Dec. 14, 1975.

## II. DATA SET

The SAR data used in this study were collected by the Environmental Research Institute of Michigan (ERIM) four-channel system which was flown in a C-46 aircraft during the Marineland Experiment. For a complete description of this SAR, the reader is referred to [6]. It consists of a dual-wavelength and dual-polarization SAR that simultaneously images at *X*-band (3.2-cm wavelength) and *L*-band (23.5-cm wavelength). Recently a C-band (5.3-cm wavelength) capability has been added to this system. The data presented in this paper were obtained from the horizontal-transmit/horizontal-receive channel (HH) of both *X*- and *L*-band receivers. Presented in Table I are radar system and imaging geometry parameters for the Marineland flights.

The data used in this study were collected on Dec. 14, 1975, using an eight-sided flight pattern shown in Fig. 1. This multisided flight pattern allowed SAR and surface-measured wave estimates to be compared as a function of wave orientation with respect to radar look direction. During the flight, a wave train identified as swell with an 8-s dominant period and 1.5- to 1.8-m significant wave height ( $H_{1/3}$ ) was propagating due west (270 degrees true). The winds on this day were 10 m/s offshore and 3 m/s near-shore, both from due east (90 degrees true).

## III. ANALYSIS

Simultaneously obtained *X*- and *L*-band SAR ocean wave data collected during passes 1–8 (see Fig. 1) were spectrally analyzed using fast Fourier transform (FFT) techniques and the results compared to *in situ* measurements. The SAR signal

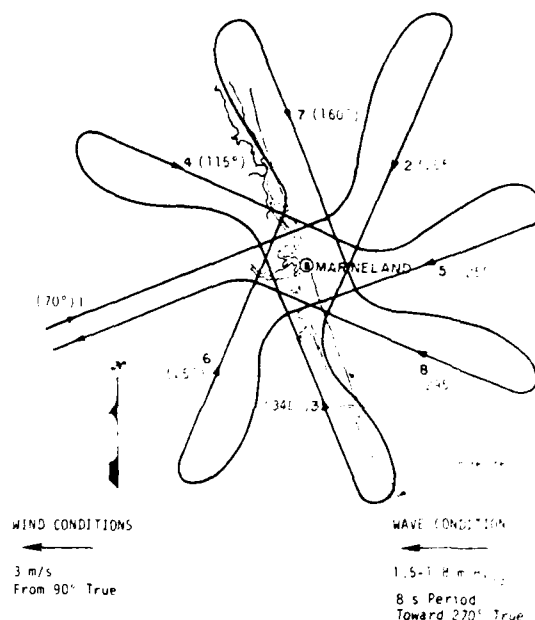


Fig. 1. ERIM flight patterns flown over Marineland test site on Dec. 14, 1975. The aircraft heading with respect to true north is given in parentheses next to the pass number. The surface wind and wave conditions during the data collection flight are also shown.

TABLE I  
RADAR SYSTEM AND IMAGING GEOMETRY PARAMETERS  
USED DURING THE MARINELAND EXPERIMENT

Parameter	<i>X</i> -band	<i>L</i> -band
Frequency	9.375 GHz	1.25 GHz
wavelength	3.2 cm	23.5 cm
Pulse length	2.5 μs	2.5 μs
Along Track Beamwidth	1.2°	1.2°
Swath width	4 km	4 km
Nominal Resolution	10 m slant range 10 m azimuth	10 m slant range 10 m azimuth
Altitude	4,700 m	4,700 m
Range to Target, R*	10 km	10 km
Platform Velocity, V	70 m/s	70 m/s
θ*	4.5°	4.5°
Incidence Angle	90°	90°
Integration Time*	100 μs	100 μs

\*value at 0° incidence angle.

histories for the above data were optically processed into image film using the ERIM precision optical processor (POP) as described in [7]. These image films were then digitized using a pixel size corresponding to 3 m in slant range and azimuth. The digitization was performed on the ERIM hybrid image processing facility (HIPF) described in [8]. Digital spectral estimates were produced for passes 1–8, both *X*- and *L*-band data following the method described in [9]. These spectral estimates each have approximately 144 degrees of freedom [9].

Presented in Figs. 2 and 3 are two-dimensional contour plots of the FFT's produced in passes 1–8, *X*- and *L*-band, respectively. Each contour on these plots represents a 3 dB (50 percent) decrease in spectral intensity from the previous contour. The SAR-derived dominant wave is represented by the center of the highest contour (−3 dB) on these plots. For each E-2

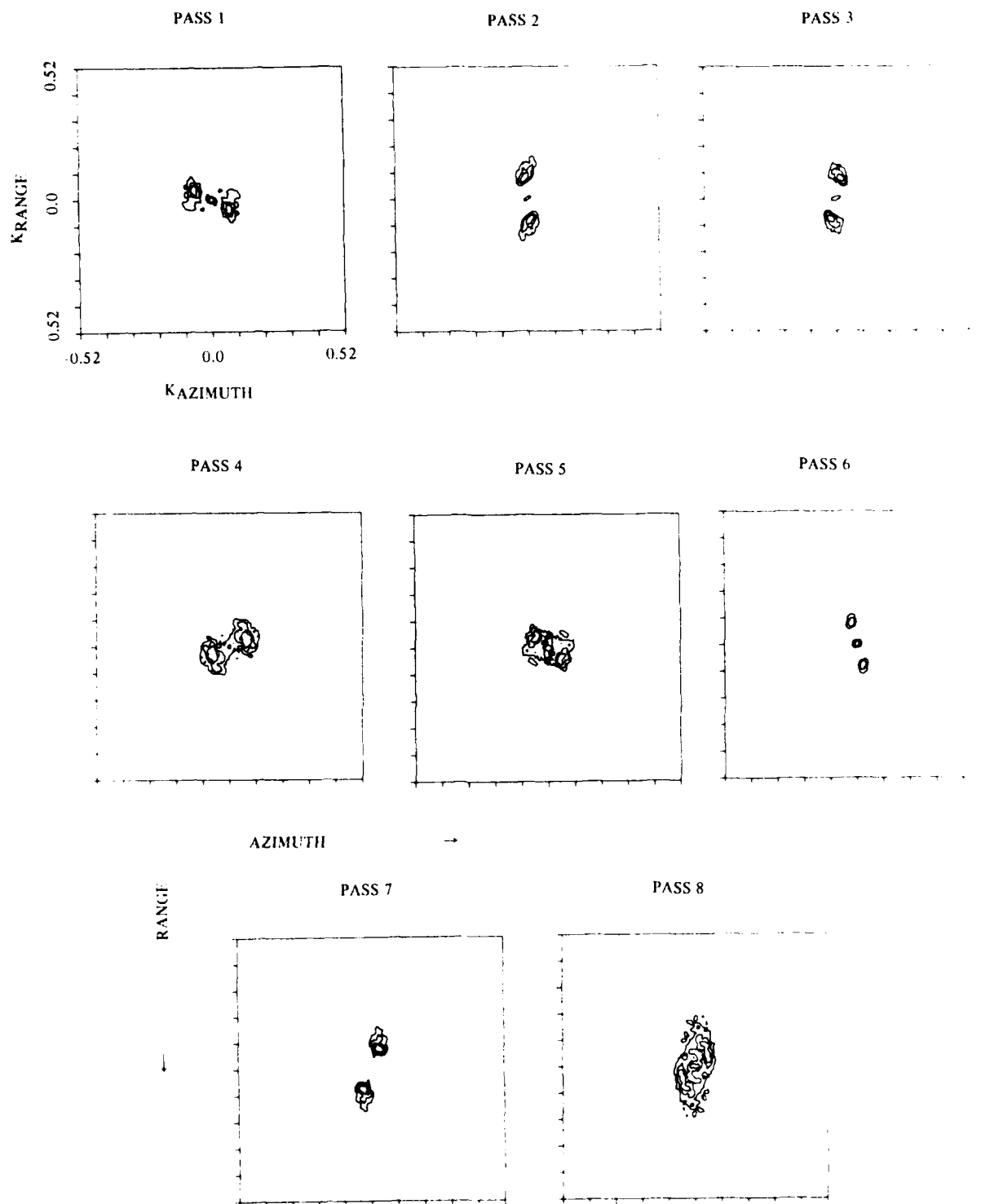


Fig. 2 Contour plots of the two-dimensional FFT's produced from digitized X-band (HH) imagery from Dec. 14, 1975 passes 1 through 8. The aircraft flight direction was to the right for each of the transforms. The axes for each plot are consistent with those shown for pass 1.

of the contour plots presented, the horizontal axis represents the along-track or azimuth direction, while the vertical dimension represents the SAR range component. Note from Fig. 3 that on three of the L-band contour plots (passes 1, 4, and 8), there is no clearly defined top contour (e.g., pass 8). In these cases, the SAR failed to image the gravity wave field. These re-

sults will be discussed in detail in the following paragraphs. It should be emphasized that the spectral estimates presented here are simply the directional wavenumber spectra of the radar return intensity. Although several possible methods have been proposed [10]-[12], there is still no reliable technique to obtain estimates of wave height using SAR data.

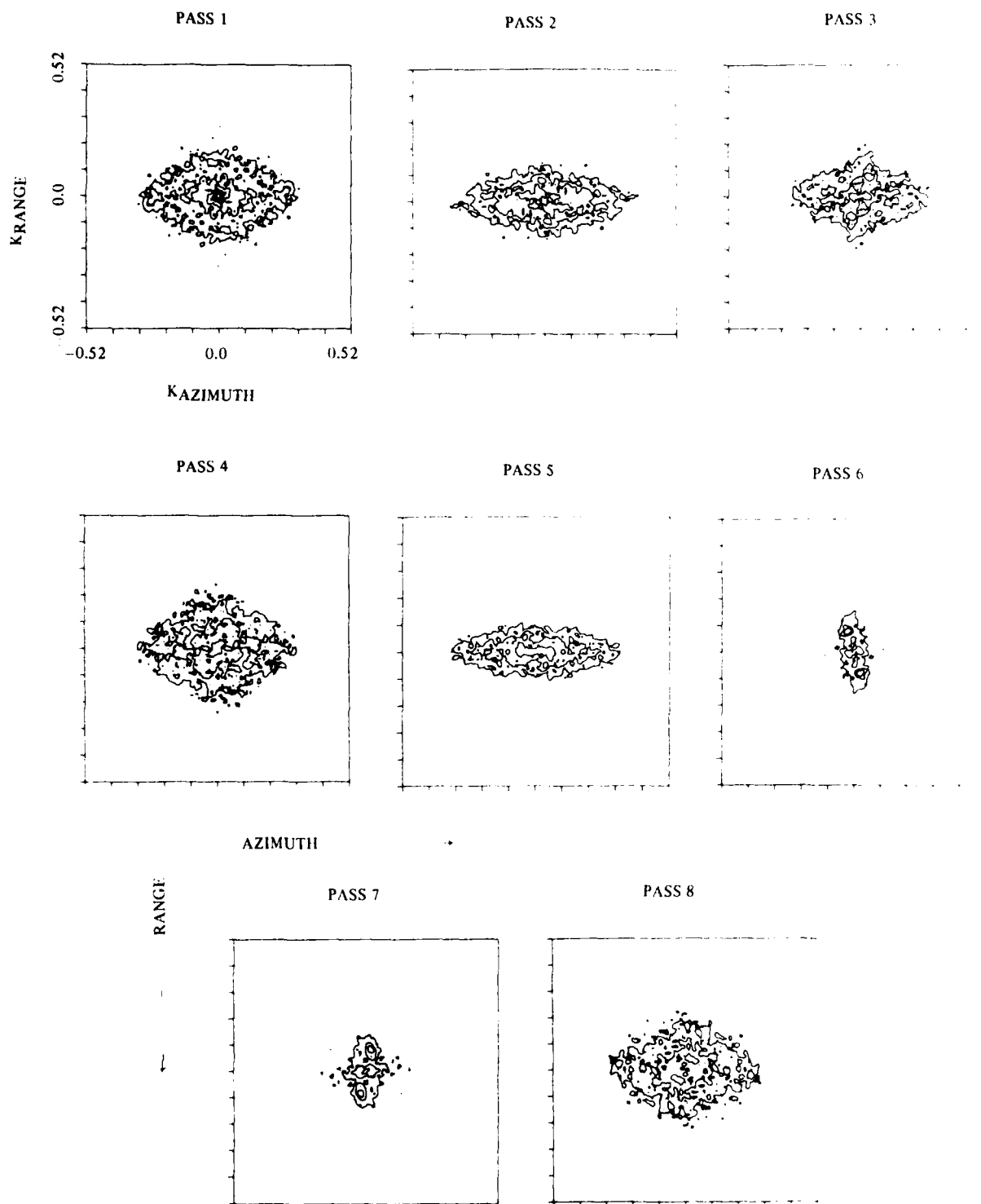


Fig. 3. Contour plots of the two-dimensional FFT's produced from digitized L-band (HH) imagery from Dec. 14, 1975, passes 1 through 8. The aircraft flight direction was to the right for each of the transforms. The axes for each plot are consistent with those shown for pass 1.

The coincident surface wave measurements used for comparison with the SAR data were obtained by a surface pitch-and-roll buoy operating in the test area during the SAR data collection flights. This buoy operated in approximately 10-m water depth. A series of nine consecutive 34-min records were processed. During the 5 h of measurement, no significant

changes in the wave properties were found, hence the data were combined in one calculation. Estimates at groups of adjacent frequencies were averaged to produce a spectrum with more than 500 degrees of freedom [1].

Table II is a comparison of the dominant SAR-derived and surface-measured wave spectral estimates for the Manneland

TABLE II  
SUMMARY OF SURFACE MEASURED AND SAR-DERIVED  
WAVE ESTIMATES

Pass	Aircraft Heading (° True)	Surface Measured				SAR Derived				Observed Differences			
		$\lambda$ (True) (m)	$f$ (Hz)	Water Depth (m)	$\lambda$ (m)	X-band		L-band		X-band		L-band	
						$\lambda$ (True) (m)	$\lambda$ (m)	$\lambda$ (True) (m)	$\lambda$ (m)	$\lambda$ (True) (m)	$\lambda$ (m)	$\lambda$ (True) (m)	$\lambda$ (m)
1	070	270	0.125	13	76	276	86	N/D	N/D	+6	+10		
2	095	270	0.125	14	78	275	82	274	89	+5	+4	+4	+11
3	340	270	0.125	13	76	266	77	265	67	4	+1	5	9
4	115	270	0.125	16.5	95	265	95	N/D	N/D	5	+10		
5	250	270	0.125	13	76	284	90	302	87	+14	+14	+32	+11
6	025	270	0.125	12	75	282	80	283	76	+12	+5	+13	+1
7	160	270	0.125	13	76	260	77	260	80	10	+1	10	+4
8	295	270	0.125	13	76	255	84	N/D	N/D	-15	+8		
R.M.S. Errors										9.8	2.9	16.3	6.1

<sup>1</sup> These wavelengths were calculated assuming a linear dispersion relation.

N/D indicates spectral estimate was unobtainable from data.

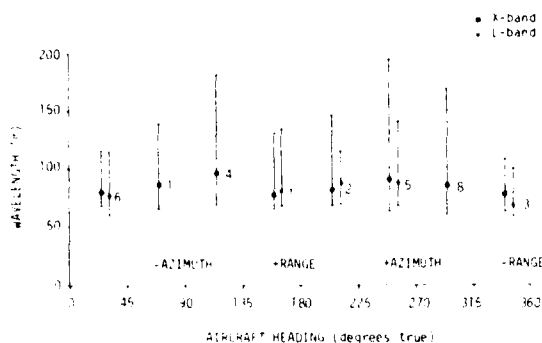


Fig. 4. SAR-derived wavelength estimates plotted against aircraft heading for both X- and L-band data simultaneously collected on Dec. 14, 1975. The wave propagation direction relative to the aircraft heading is also presented.

data. The SAR-derived estimates were obtained from the plots in Figs. 2 and 3 and have been corrected for motion of the waves while being imaged following the method described in [1]. The surface-measured values came from the pitch-and-roll buoy. Since the buoy measures in the temporal or frequency domain, the estimated peak frequency of 0.125 Hz (8-s period) was converted to a wavelength using the linear dispersion relation. The depth values used in the dispersion calculation were chosen to be at the center of the SAR subimage used to produce the 2-D Fourier transform.

Examination of Table II reveals that the L-band channel detected waves in only five of the eight passes. The absence of waves in passes 1, 4, and 8 of the L-band data appears to represent a limitation in the capability of SAR to detect these gravity waves. In contrast, the X-band channel detected waves in every pass. The rms errors for the dominant wavelength and directional estimates are also larger at L-band than at X-band, 8.3 to 7.9 m for wavelength, and 16.3° to 9.8° for direction.

To address the question of the dependence or the quality of wave estimates on the radar viewing angle, the SAR-derived wavelength and direction estimates summarized in Table I were plotted against aircraft heading in Figs. 4 and 5, respectively. The sharpness of the SAR-derived wavelength and direction estimate can be characterized by the width of the 3 dB contour level of the two-dimensional FFT's shown in Figs. 2 and 3. The width of the 3 dB contour in the direction of

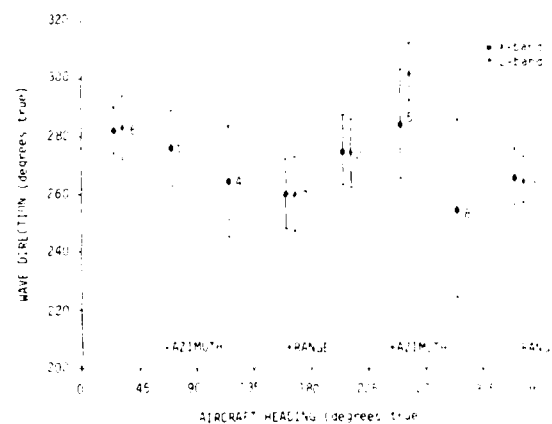


Fig. 5. SAR-derived wave direction estimates plotted against aircraft flight direction for both X- and L-band data simultaneously collected on Dec. 14, 1975. The wave propagation direction relative to aircraft heading is also presented.

wave propagation provides an estimate of the wavelength variability, while the width of the contour orthogonal to wave propagation provides an estimate of the directional variability. These contour widths are indicated on Fig. 4 and 5. Fig. 4 indicates that the SAR-derived wavelength estimates at X-band both increase and are more variable as the waves become azimuth-traveling. Similarly, Fig. 5 indicates an increase in the variability of the SAR-derived directional estimates at X-band as the waves become more azimuth-traveling. An alternative method of plotting the accuracy of the SAR-derived directional estimates is shown in Fig. 6. Here the angle of the SAR-derived spectral estimate off range is shown plotted against the angle off range predicted by surface measurements. This plot shows an interesting result: the SAR-imaged waves show a definite bias in direction toward range, particularly as the waves become more azimuth-traveling. Thus the graph suggests that waves would be imaged as propagating more in the range direction than is actually the case.

A possible explanation of the observation presented in Fig. 6 is the degradation of the azimuth resolution due to scatterer motions. This is caused by the orbital velocity of the dominant gravity waves and is discussed in detail in [4]. Recall that the SAR image intensity is the convolution of the effective inten-

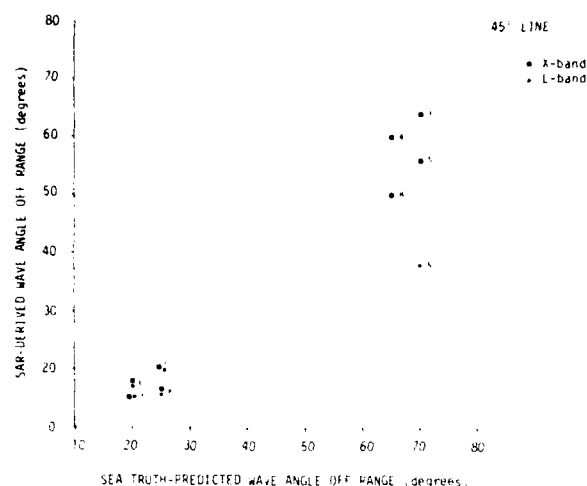


Fig. 6. SAR-derived wave angle off range plotted against the wave angle off range predicted by surface measurements.

sity distribution  $\sigma_0(a, r)$ , with the system impulse response function  $I(a, r)$ , where  $a$  and  $r$  are the azimuth and range coordinates, respectively. The impulse response function can be modeled by a Gaussian function. The Fourier transform or spectrum of a SAR-imaged wave field is the product of the Fourier transforms of  $\sigma_0$  and  $I$  or

$$\tilde{S}(k_a, k_r) = \tilde{I}(k_a, k_r) \tilde{\sigma}_0(k_a, k_r) \quad (1)$$

where the  $k_a$  and  $k_r$  are the azimuth and range wavenumbers, respectively. Thus the spectrum of  $\sigma_0$  is weighted by a Gaussian function whose width is inversely proportional to the azimuth resolution. This is shown schematically in Fig. 7. As the azimuth resolution (impulse response) widens, its Fourier transform becomes narrower and the resultant spectrum is more distorted. The result of this is to make the SAR-derived waves appear longer and more range-traveling than they actually are. This degraded resolution may be the reason that waves were not imaged at L-band for three of the azimuth-traveling cases, although they were imaged at X-band. This effect also decreases the contrast of waves traveling in the azimuth direction.

The degradation in azimuth resolution can be caused by either gross scatterer motions (azimuth velocities or range accelerations), or by a range of scatterer velocities within each resolution element, which is equivalent to the coherence time effect discussed in [13]. The effects of gross scatterer motions are proportional to integration time, and, therefore, are larger at L-band than at X-band, as illustrated in Fig. 8 for the acceleration effect. These effects are at least partially reducible by changing the processor focus settings, and, as expected, a greater sensitivity to these focus adjustments is found at L-band than at X-band [3].

The degradation in azimuth resolution due to a given coherence time is proportional to radar wavelength and is not reducible by changing the processor focus. Thus if the coherence time is substantially the same at L-band and X-band, a greater loss of resolution is expected at L-band. This may be the reason for the failure of the L-band system to image waves for those azimuth-traveling cases when waves were visible on the X-band images. The assumption that the coherence time is the

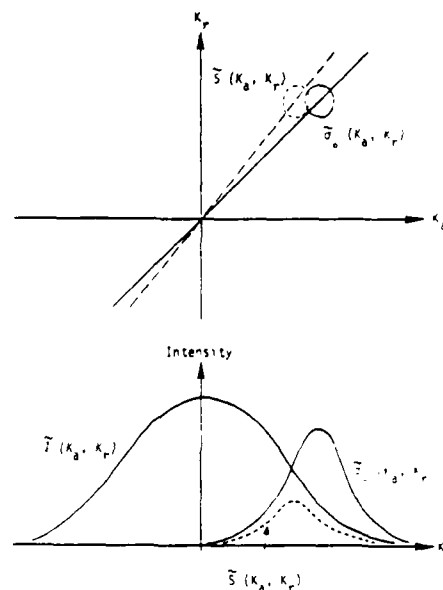


Fig. 7. Schematic diagram showing the effect of degraded azimuth resolution on SAR-derived spectra.

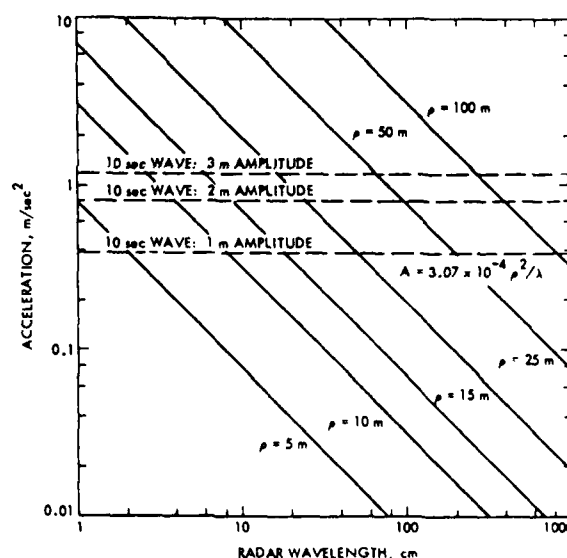


Fig. 8. SAR azimuth resolution as a function of radar wavelength and target acceleration.

same at L-band and X-band may not be correct, however. More measurements of the coherence time are needed to test this hypothesis. In addition to these SAR effects, it is also possible that the inherent modulation of the radar cross section is greater at X-band than at L-band due to hydrodynamic considerations or electromagnetic scattering effects.

#### IV. CONCLUSIONS

The comparison of SAR-derived and *in situ* measured wave data from the Marineland Experiment indicates several results. The X-band data was able to image ocean waves in each of the 8 passes flown over the test site with a variety of headings. The L-band data on the other hand, failed to image waves in 3 of the 4 passes in which nearly azimuth-traveling waves occurred

The accuracy of the SAR-derived wave estimates when compared to *in situ* measurements appears to be better at  $X$ - than at  $L$ -band for the limited cases in this data set.

The SAR-derived wavelength and directional estimates appear to change as a function of radar look direction with respect to wave propagation direction. As waves become more azimuth-traveling, SAR estimates of their wavelength increase and become more variable. This appears to hold for both  $X$ -band and the limited number of  $L$ -band cases. Also, it was observed that as waves become more azimuth-traveling their directions become more variable and are imaged as propagating more in the range direction than indicated by surface measurements. Again these observations appear independent of radar wavelength. One possible explanation for the above observations is the degraded azimuth resolution caused by surface scatterer motion. When transformed, this degraded resolution would cause wave spectral estimates to be longer and more range-traveling than the true surface waves. This degraded azimuth resolution is also a possible reason why waves were not imaged in 3 of the 4 nearly azimuth-traveling  $L$ -band passes.

The environmental conditions encountered during the Marineland Experiment corresponded to low wind speeds, low wave heights, and relatively short wavelengths. Additionally, the waves are being influenced by the relatively shallow water. Thus shoaling of the waves could contribute to the degraded  $L$ -band wave data. The results presented in this study are considered valid only for such conditions. It should also be noted that only the dominant wave estimates from the SAR and pitch-and-roll buoy were compared.

#### ACKNOWLEDGMENT

The technical monitor for the ONR Contract is H. Dolezalek. The technical monitor for the NOAA Contract was J. Sherman, III. The authors would like to thank all the members of the Marineland Experiment Team, particularly the efforts of D. Ross and W. McLeish in providing the pitch-and-roll buoy data.

#### REFERENCES

- [1] W. McLeish, D. Ross, R. A. Shuchman, P. G. Teleki, S. V. Hsiao, O. H. Shemdin, and W. E. Brown, Jr., "Synthetic aperture radar imaging of ocean waves—Comparison with wave measurements," *J. Geophys. Res.*, vol. 85, pp. 5003-5011, 1980.
- [2] W. R. Alpers, D. B. Ross, and C. L. Rufenach, "On the detectability of ocean surface waves by real and synthetic aperture radar," *J. Geophys. Res.*, vol. 86, pp. 6481-6498, 1981.
- [3] R. A. Shuchman and O. H. Shemdin, "Synthetic aperture radar imaging of ocean waves during the marineland experiment," *IEEE J. Oceanic Eng.*, pp. 83-90, this issue.
- [4] W. R. Alpers and C. L. Rufenach, "The effect of orbital motions on synthetic aperture radar imagery of ocean waves," *IEEE Trans. Antennas Propagat.*, vol. AP-27, pp. 685-690, 1979.
- [5] R. A. Shuchman and J. S. Zelenka, "Processing of ocean wave data from a synthetic aperture radar," *Boundary-Layer Meteorol.*, vol. 13, pp. 181-191, 1978.
- [6] R. Rawson, F. Smith, and R. Larson, "The ERIM  $X$ - and  $L$ -band dual polarized radar," in *Proc. IEEE Int. Radar Conf.* (Arlington, VA), pp. 505-510, 1975.
- [7] A. Kozma, E. N. Leith, and N. G. Massey, "Tilted-plane optical processor," *Appl. Opt.*, vol. 11, pp. 1766-1777, 1972.
- [8] D. A. Ausherman, W. D. Hall, J. N. Latta, and J. S. Zelenka, "Radar data processing and exploitation facility," in *Proc. IEEE Int. Radar Conf.* (Arlington, VA), pp. 493-498, 1975.
- [9] D. J. Schwab, R. A. Shuchman, and P. I. Liu, "Wind wave directions determined from synthetic aperture radar imagery and from a tower in Lake Michigan," *J. Geophys. Res.*, vol. 86, pp. 2059-2064, 1981.
- [10] R. O. Harger, "A sea surface height estimator using SAR complex imagery," *IEEE J. Oceanic Eng.*, this issue, pp. 71-78.
- [11] A. Jain, G. Medlin, and C. Wu, "Ocean wave height measurement with Seasat SAR using speckle diversity," *IEEE J. Oceanic Eng.*, vol. OE-7, pp. 103-107, 1982.
- [12] M. H. B. Thomas, "The estimation of wave height from digitally processed SAR imagery," *Int. J. Remote Sensing*, vol. 3, pp. 63-68, 1982.
- [13] R. K. Raney, "SAR response to partially coherent phenomena," *IEEE Trans. Antennas Propagat.*, vol. AP-28, pp. 777-787, 1980.



**Robert A. Shuchman** received the B.S.E. and B.S. degrees in environmental engineering and geological oceanography, respectively, in 1974, the M.S. degree in remote sensing in 1976, and the Ph.D. degree in natural resources and oceanic science—all from the University of Michigan, Ann Arbor, MI.

He has been employed at the Environmental Research Institute of Michigan (ERIM) since 1974, where he has worked extensively on analysis of synthetic aperture radar (SAR) systems and the quantification of SAR signatures of the ocean surface. His work includes the development of spectral analysis techniques to study SAR wave data, as well as exploring the use of SAR-Doppler signal histories to measure ocean surface currents and wave heights. He presently is Director of the Radar Science Laboratory in the Radar Division at ERIM. As a member of the Seasat Experiment Team, he has been involved in a variety of programs helping to validate the Seasat SAR instrument.

Dr. Shuchman is a member of the American Geophysical Union.



**James D. Lyden** received the B.S. and M.S. degrees in physical oceanography from the University of Michigan, Ann Arbor, MI in 1979 and 1983, respectively.

He has been employed by the Environmental Research Institute of Michigan (ERIM) since 1980, where he has worked on active and passive remote sensing with application to oceanography. The emphasis of his work has been in the development of processing and analysis techniques for the extraction of oceanographic information from synthetic aperture radar (SAR) data.



**David R. Lyzenga** received the B.S.E. in physics from the University of Michigan in 1967 and an M.S. degree in physics from Yale University in 1968. After teaching mathematics and physics at Calvin College in 1968-1969, he received the Ph.D. degree in electrical engineering from the University of Michigan in 1973.

He worked at the Space Physics Research Laboratory of the University of Michigan from 1970-1972, and joined the Environmental Research Institute of Michigan (ERIM) in 1973. At ERIM, he has been involved in a variety of remote sensing projects involving both visible and microwave sensors. Since 1981, his primary research interest has been in the extraction of oceanographic information from synthetic aperture radar data. He is presently a Research Engineer in the Radar Science Laboratory at ERIM.

Dr. Lyzenga is a member of the Optical Society of America, Sigma Xi, Tau Beta Pi, and Phi Kappa Phi.

# Synthetic Aperture Radar Imaging of Ocean Waves During the Marineland Experiment

ROBERT A. SHUCHMAN AND OMAR H. SHEMDIN

**Abstract**—X- and L-band simultaneously obtained synthetic aperture radar (SAR) data of ocean gravity waves collected during the Marineland Experiment were analyzed using wave contrast measurements. The Marineland data collected in 1975 represents a unique historical data set for testing still-evolving theoretical models of the SAR ocean wave imaging process. The wave contrast measurements referred to are direct measurements of the backscatter variation between wave crests and troughs. These modulation depth measurements, which are indicators of wave detectability, were made as a function of: a) the settings used in processing the SAR signal histories to partially account for wave motion; b) wave propagation direction with respect to radar look direction for both X- and L-band SAR data; c) SAR resolution; and d) number of coherent looks. The contrast measurements indicated that ocean waves imaged by a SAR are most discernible when X-band frequency is used (as compared to L-band), and when the ocean waves are traveling in the range direction. Ocean waves can be detected by both X- and L-band SAR, provided that the radar surface resolution is small compared to the ocean wavelength (at least 1/4 of the ocean wavelength is indicated by this work). Finally, wave detection with L-band SAR can be improved by adjusting the focal distance and rotation of the cylindrical telescope in the SAR optical processor to account for wave motion. The latter adjustments are found to be proportional to a value that is near the wave phase velocity.

## I. INTRODUCTION

THIS PAPER discusses a specialized form of side-looking airborne radar (SLAR) called synthetic aperture radar (SAR). SAR is an imaging radar which utilizes the Doppler history (change of phase) associated with the motion of the aircraft, recording both the phase and the amplitude of the backscattered energy, thus improving the along-track or azimuth resolution [1], [2].

The principle in imaging any surface with radar is that the backscatter of microwave energy (echo) sensed by the radar receiver contains information on the roughness characteristics (shape, dimension, and orientation) of the reflecting area. Factors that influence the echo received from ocean waves include the motion of the scattering surfaces, the so-called "speckle" effect, system resolution, and integration time, as well as contributions attributable to wind, waves, surface currents, and surface tension. The effect of orientation of ocean waves to the radar line-of-sight must also be considered. When attempting to understand the SAR ocean wave imaging

mechanism, one must consider factors pertaining to wave orbital velocity, Bragg scatterer velocity, and long gravity (or resolvable) wave phase velocity [3].

This paper presents a series of backscatter measurements of SAR imaged gravity waves. Analysis of these measurements indicates that the ability of SAR to image gravity waves is dependent upon: a) wave motion; b) radar look direction with respect to ocean wave propagation direction; and c) resolution and noncoherent averaging. The backscatter measurements performed in this study measure the contrast ratios between wave crests and troughs as observed on the SAR imagery, and are referred to as wave modulation depth scans.

A summary is first presented of radar concepts pertinent to understanding SAR operation as it images an ocean surface. This is followed by a description of the wave modulation scan measurements. The results of these scans are then presented and discussed.

## II. RADAR CONCEPTS

Several models [4]–[10] have been postulated that attempt to explain wave image formation with SAR. The final output of a SAR system is usually in the form of a two-dimensional intensity display of relative black and white shades. The fundamental backscatter mechanism is believed to be Bragg scattering when the incidence angle is greater than  $20^\circ$  [11]. That is, transmitted radar energy with wavenumber  $k$  interacts in a resonant or constructive interference fashion with ocean surface waves of wavenumber  $k_w$  such that

$$k_w = 2k \sin \theta \quad (1)$$

where  $k_w = 2\pi/L$  and  $k = 2\pi/\lambda$  are the wavenumbers,  $L$  and  $\lambda$  are the wavelengths of the surface waves in the range direction and that of the radar, respectively, and  $\theta$  is the incidence angle.

For the Environmental Research Institute of Michigan (ERIM) X- and L-band aircraft system discussed in this paper which operated with a nominal incidence angle ( $\theta$ ) of  $45^\circ$ , the use of (1) leads to a Bragg wavelength of approximately 2 cm for X-band ( $\lambda = 3.2$  cm) and 17 cm for L-band ( $\lambda = 23.5$  cm). In contrast, the Seasat L-band system with an incidence angle of  $20^\circ$ , has approximately a 34-cm wavelength Bragg wave. These waves represent the capillary and short gravity wave portion of the ocean wave spectrum.

In general, the mechanisms that contribute to wave patterns observed on SAR imagery are: a) tilt modulation, b) hydrodynamic modulation, and c) velocity bunching effects. Shadowing effects also play an important role at large incidence angles.

Manuscript received May 1, 1980; revised February 9, 1983. The ERIM contribution of this work was performed under ONR Contract N00014-76-C-1048 and NOAA/NFSS Grant 04-6-158-44078. The JPL contribution of this work was performed under NASA Contract 7-100 and ONR Contract N00014-76-MP60029.

R. A. Shuchman is with the Radar Division, Environmental Research Institute of Michigan (ERIM), Ann Arbor, MI 48107.

O. H. Shemdin is with the Jet Propulsion Laboratory (JPL), California Institute of Technology, Pasadena, CA 91103.

Tilt modulation refers to periodic variation in the local incidence angle caused by the long gravity waves. As the incidence angle changes, it modulates the radar cross section of the surface that backscatters the microwave energy.

Hydrodynamic modulation as reported in [5], [12] refers to the change in short wave amplitude which is partially due to the straining of the small ocean Bragg waves due to divergence of the surface orbital velocity field of the long gravity waves. The modulation in wind stress induced by the long waves is another contributor to such hydrodynamic modulation.

The velocity bunching effect refers to a periodic azimuth target displacement on the imagery. This displacement is described at length in [13].

Tilt and hydrodynamic modulation are maximum for range-traveling waves and minimum for azimuth-traveling waves. The velocity bunching effect is maximum for waves traveling in the azimuth direction [5].

Other effects of wave motions in SAR imagery may include: a) image displacement, smearing, and loss of focus in the azimuth direction; and b) loss of focus in the range direction [14]. Some of these effects can be removed during processing of the SAR signal histories by making appropriate adjustments to the processor [15]. The effects which cannot be removed during processing may reduce the detectability of gravity waves, and can also influence the wave spectral estimates obtained from SAR wave data.

Loss of focus in the range direction is due to a rotation of the phase history of the target (i.e., migration through range cells). This loss of focus is proportional to the range velocity and the integration time, and can be corrected by a rotation of the cylindrical lenses in the optical processor, assuming the range velocity is constant during the integration time.

Loss of focus in the azimuth direction can be caused by a constant velocity in the azimuth direction or a changing velocity (i.e., an acceleration) in the range direction. These effects can be corrected by a change in the azimuth focus setting of the processor, assuming that the azimuth velocity and radial acceleration are constant. Since they are both inversely proportional to the platform velocity, these effects are expected to be important for the X- and L-band ERIM SAR aircraft system that operated during Marineland with a typical platform velocity of only 75 m/s.

The intent of this paper is to provide experimental evidence which can be used as a basis for evaluating the concepts discussed above, and also to provide an empirical basis for achieving optimal detection of ocean waves with SAR.

### III. RADAR SYSTEM AND FLIGHT PATTERNS

The experimental observations presented here were obtained from analysis of data collected by the ERIM dual-frequency and dual-polarization SAR system. The ERIM X-band and L-band system, which is presently jointly owned by ERIM and the Canada Centre for Remote Sensing (CCRS), is described in detail by [16]. It consists of a dual-wavelength and dual-polarization SAR that simultaneously images at X-band (3.2 cm) and L-band (23.3 cm). Recently, a C-band (5.3 cm) wavelength capability has been added to this system. The Marineland data presented in this paper were obtained

from the horizontal-transmit horizontal-receive channel (HH) of both X- and L-band receivers.

The along-track or azimuth resolution of the ERIM system is obtained from the synthetic aperture techniques given by [1] and the cross-track or range resolution from compression of the frequency modulated pulse. During flight the radar signals are recorded in their frequency-dispersed form and are later optically compressed in a ground-based processor. The latter has been extensively described in [17].

Typically in a SAR, the phase history of a scattering point in the scene is recorded on photographic film as an anamorphic (astigmatic) Fresnel zone plate. The parameters of the zone plate are set in the azimuth direction by the Doppler frequencies produced by the relative motion between the sensor and the point scatterer, and in the range direction by the structure of the transmitted pulses. The film image is a collection of superimposed zone plates representing the collection of point scatterers in the scene. This film is used by a coherent optical processor to focus the anamorphic zone plates into points, which, when coherently combined and detected (imaged), recreate the microwave scatter of the scene.

Fig. 1 is a schematic of a typical SAR optical processor. Shown on the figure are the spherical and cylindrical telescopes used to control image focus.

The SAR ocean wave data set used in this study was collected at Marineland, FL, during mid-December 1975. This historical data base is unique because of the quality of this high resolution SAR data and the surface truth data collected. The Marineland Experiment was conducted to obtain SAR ocean wave data in support of the Seasat L-band SAR [18]. Wave height and direction of long waves and slope intensity of capillary and short gravity waves were measured by an array of *in situ* instruments, including a capillary sensor mounted on a wave follower, pitch-and-roll buoy, and paired orthogonal current meters.

The SAR system was flown over the Marineland test area using the flight pattern shown in Fig. 2. This enabled the authors to study the sensitivity of the SAR to wave orientation with respect to radar look direction.

The data used in this study were collected on Dec. 15, 1975. The surface environmental conditions on this day consisted of a wave train identified as swell with an 8-s dominant period and 1.5- to 1.8-m significant wave height ( $H_{1/3}$ ) propagating toward 275 degrees true. The winds were 5-7 m/s from due east (90° true).

### IV. DATA ANALYSIS AND RESULTS

A series of backscatter measurements were performed on the data collected on Dec. 15, 1975. The backscatter measurements are referred to as wave modulation depth scans. The wave modulation depth scans measure the variation in image intensity associated with backscatter from different points along the profiles of long waves. These measurements were obtained by scanning in the direction of wave propagation with an aperture corresponding to 436 m along the wave crest and 2.18 m in the propagation direction. This aperture provided sufficient signal-to-noise ratio for the individual



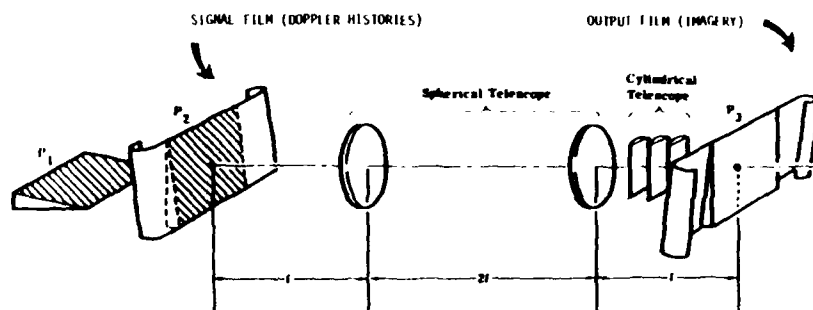


Fig. 1. Schematic diagram of a typical SAR optical processor. The spherical telescope controls the range focus while the cylindrical telescope is responsible for azimuth focus.

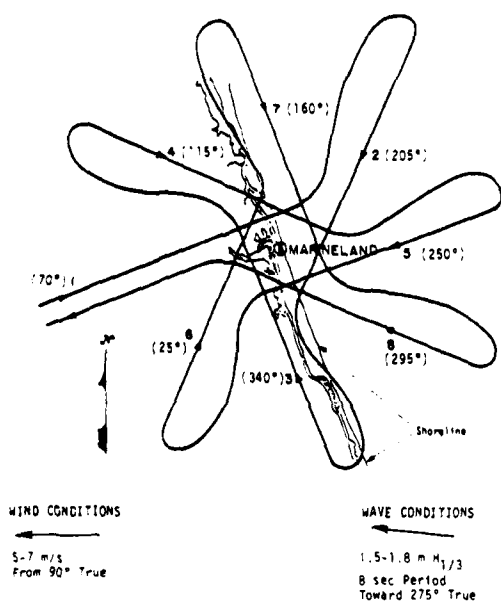


Fig. 2. FRIM flight patterns flown over Marineland test site on Dec 15, 1975. Both land and water are imaged on passes 3, 4, and 6. The aircraft heading with respect to true north is given in parentheses next to the pass number. The surface wind and wave conditions during the data collection flight are also shown.

scans to insure repeatable measurements. Additionally, it was experimentally determined that the optical probe could be misaligned as much as  $\pm 7^\circ$  with respect to the wave propagation direction without adversely affecting the modulation measurement. These modulation depth measurements, which are indicators of wave detectability, were made as a function of: a) azimuth focus and rotation adjustments for both azimuth- and range-traveling waves; b) wave direction with respect to radar look direction; c) SAR resolution; and d) number of coherent looks (amount of noncoherent integration).

Fig. 3 is an example of a wave modulation depth scan of the type produced by using the Marineland signal film and placing a recording photomultiplier in the output plane of the optical processor. By placing a recording photomultiplier in place of the SAR image film, a wave modulation results where the waves themselves modulate the scan. The position

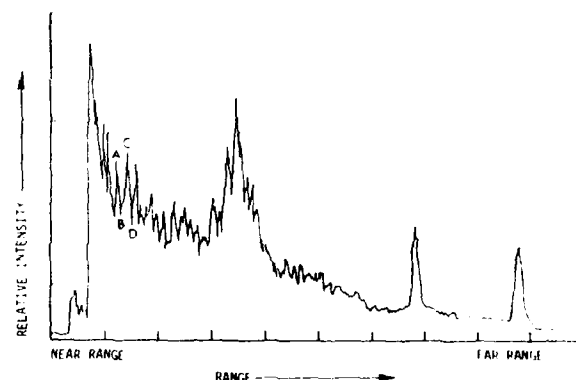


Fig. 3. Typical wave modulation depth scan for L-band data collected on Dec. 15, 1975.

and orientation of the modulation depth measurement was held constant for each individual azimuth and range focus test, thus the scans were made using the same portion of the signal film and only the focus was varied for each scan. As evident on Fig. 3, an overall change in mean backscatter with radar range occurs across the scan. Wave patterns in the image are superimposed on this mean variation. Therefore, detrending of the backscatter signal obtained in the modulation scans is necessary to accurately specify the modulation depth. This is accomplished by two procedures. For a maximum A (see Fig. 3) followed by a minimum B, followed by a maximum C, the following equation can be used:

$$M_d' = \frac{2B - A - C}{2B + A + C} \quad (2)$$

For a minimum B, followed by a maximum C, followed by a minimum D, the following equation can be used:

$$M_d'' = \frac{B + D - 2C}{B + D + 2C} \quad (3)$$

Finally, to obtain a single modulation depth measurement for a given wave, we average  $M_d'$  and  $M_d''$

$$M_d^* = \frac{M_d' + M_d''}{2} \quad (4)$$

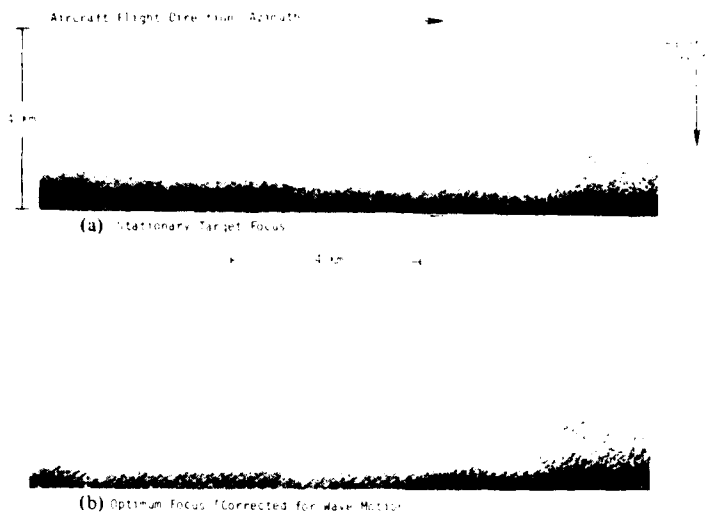


Fig. 4. *L*-band (HH) SAR wave data optically processed: (a) Assuming a stationary target. (b) Accounting for wave motion.

By using many different focusing adjustments, numerous wave modulation scans similar to Fig. 3 were produced for a given area of wave imagery. The 25 to 30 modulation depths produced for each of the different focus setting scans were then analyzed with respect to their variances using techniques outlined in [19] to test if focusing adjustments increased contrast in wave imagery (contrast being defined as the highest average modulation depth). In addition to modulation depths made as a function of focus adjustment, modulation depths were also made as functions of radar look direction, resolution, and amount of mixed integration.

#### A. Wave Detectability Versus SAR Processing Settings

Azimuth- and range-traveling wave enhancement tests were performed on the SAR data collected during the Marine-land Experiment. As reported in [19], a higher modulation (crest-to-trough) depth resulted when the SAR imaged gravity waves were processed assuming a motion that is in the near proximity of the phase velocity of the dominant gravity waves.

As discussed earlier, the velocity and acceleration components of wave motion modify the radar backscatter so that conventional data processing results in defocused and displaced images. If the defocusing effect is caused by the azimuth velocity component, then this effect can be compensated in part by changing the azimuth focus control in the processor in proportion to the azimuth velocity or radial acceleration component. A sample of an *L*-band wave image processed assuming stationary and moving surfaces is shown in Fig. 4. The waves are more clearly discernible in the image corrected for wave motion. In this case, the corrected image was processed to account for an azimuthal target velocity of approximately 12 m/s. The wave phase velocity was approximately 12.5 m/s. It should be noted that the waves in Fig. 4 are traveling at almost  $60^\circ$  from the azimuth direction. Thus the wave pattern is effectively moving almost twice as fast in the azimuth direction as in the wave propagation direction, and the correction applied would correspond to half of this

effective translation velocity. The focus adjustment for orbital accelerations is also of the same order of magnitude [5], so it is not possible to determine which is the dominant effect based upon this observation alone.

Figs. 5 and 6 show wave enhancement tests performed on azimuth- and range-traveling waves for *L*- and *X*-band SAR data, respectively. Dec. 15th Marineland data from pass 1 (see Fig. 2) at six different locations (six values averaged) and from pass 2 at one location were used in this azimuth focusing test. The waves in pass 1 are traveling in a direction ranging from  $20^\circ$  to  $60^\circ$  from the azimuth direction and should be sensitive to azimuth focusing enhancements. The waves in pass 2 travel in nearly the range direction and should be relatively insensitive to azimuthal focusing enhancements.

Six shifts of the cylindrical telescope were used on the *L*-band data in the processor, as indicated in Fig. 5. Four focus shifts corresponding to five azimuth target velocities were used on the *X*-band data (see Fig. 6). The 0.0-mm focus shift indicated on the figures reflects a stationary target setting while the ( ) and (+) values indicate movement of the cylindrical telescope toward and away from the signal plane of the optical processor, with respect to the 0.0-mm focus setting. A  $3 \times 3$ -m resolution setting was used in processing the signal film in the optical processor. The  $3 \times 3$ -m resolution determines the depth of focus of the measurement and is indicated on the graphs. Note the depth of focus is larger for the *X*-band, thus a larger range of velocities can be represented with one focus setting in the *X*-band processor. Also indicated on the figures are the phase velocities for the waves present in pass 1. These velocities were calculated assuming deep water waves. The orbital velocity (an order of magnitude lower than the phase velocity) is adequately represented by the 0.0-mm or stationary focus, since the azimuthal focus shift for orbital velocity is nearly zero and within the depth of focus of both the *X*- and *L*-band processors [20].

Fig. 5 typifies the results obtained using azimuth focus shift corrections to refocus *L*-band SAR wave imagery. As

SUMMARY OF SAR (SYNTHETIC APERTURE RADAR) OCEAN WAVE  
DATA ARCHIVED AT ERI... (U) ENVIRONMENTAL RESEARCH INST  
OF MICHIGAN ANN ARBOR RADAR DIV J D LYDEN MAY 84  
ERIM-155900-17-T N00014-81-C-0692 F/G 20/4

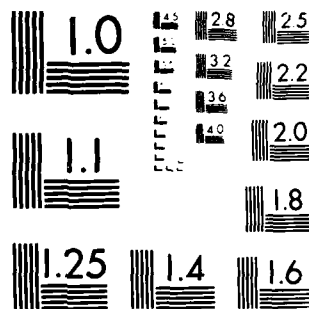
UNCLASSIFIED

ERIM-155900-17-T N00014-81-C-0692

F/G 20/4

NI

END  
DATE  
FILMED  
8-84  
DTIC



MICROCOPY RESOLUTION TEST CHART  
NATIONAL BUREAU OF STANDARDS-1963-A

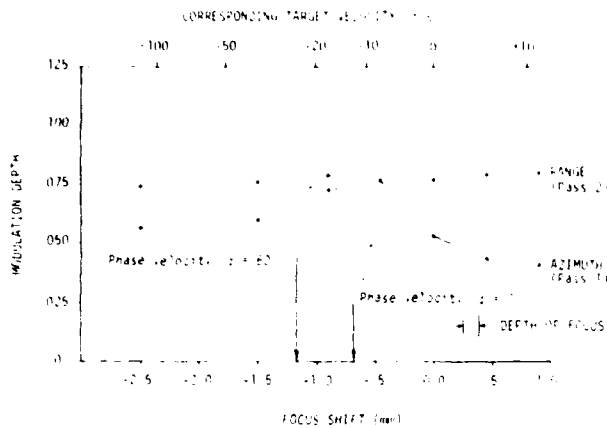


Fig. 5. Graph of modulation depth versus azimuth focus setting for azimuth- and range-traveling gravity waves for *L*-band passes 1 and 2. Arrows indicate effective phase velocity in azimuth direction for two wave propagation directions ( $\phi$ ) with respect to azimuth. For example,  $\phi = 0^\circ$  for azimuth-traveling waves.

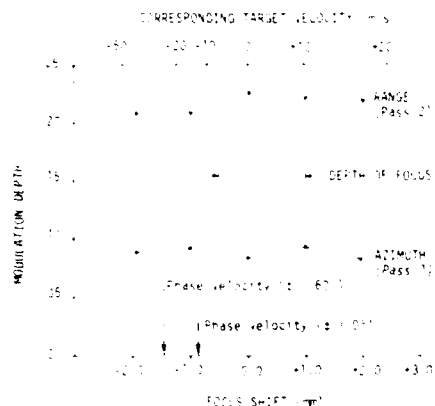


Fig. 6. Graph of modulation depth versus azimuth focus setting for azimuth- and range-traveling gravity waves for *X*-band passes 1 and 2. Arrows indicate effective phase velocity in azimuth direction for two wave propagation directions ( $\phi$ ) with respect to azimuth. For example,  $\phi = 0^\circ$  for azimuth-traveling waves.

observed on the graph for azimuth-traveling waves imaged by an *L*-band SAR, a greater wave contrast (modulation depth) occurs when the SAR data is adjusted for a target velocity that lies in the proximity of the phase velocity of the dominant gravity wave. Note the range-traveling wave (pass 2) data is insensitive to the azimuthal focus settings. The *X*-band data in Fig. 6 does not appear to be motion sensitive. This is most likely due to the large depth of focus and short integration times for the *X*-band [20], [21]. The analysis of the focusing experiments for the *X*-band data indicated there was no appreciable change in modulation depth for *X*-band unless extreme focus shifts of  $\pm 15$  mm were reached. Thus for *X*-band data, it appears that azimuth-traveling waves are relatively insensitive to wave motion effects, and it takes shifts of many depths of focus ( $\pm 15$  mm) to defocus ocean wave imagery. The modulation depths for pass 2 showed no dependence on focus shifts, indicating that range-traveling waves imaged with an *X*-band SAR are relatively insensitive to all azimuth velocity effects resulting from gravity waves. Note in

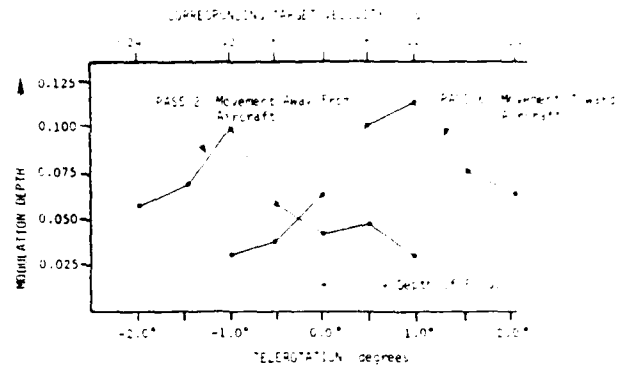


Fig. 7. Graph of modulation depth versus telerotation for *L*-band passes 2 and 6. The waves for these passes are primarily range-traveling.

comparing the modulation depths in Figs. 5 and 6 that range-traveling waves imaged at *X*-band have significantly higher modulation depths when compared to the range-traveling *L*-band data.

A series of measurements similar to those made for azimuth-traveling waves were made for range-traveling waves. Radial (range) velocity effects can also cause blurring in the resulting SAR imagery. Similar to azimuthal motion, range-velocity effects can be partially corrected for in the optical processor. The adjustment requires rotation of the cylindrical lenses of the optical processor (hereafter referred to as telerotation). The correction is necessary because the motion in range causes an apparent tilt to the SAR signal histories [14], [15].

The *L*-band data from passes 2 and 6 (see Fig. 2) were used in this experiment. Both passes have essentially range-traveling waves in them with the aircraft heading varying  $180^\circ$  between the two passes. In pass 6, the waves are traveling toward the radar (the radar look direction is upwave), and in pass 2, the radar was looking nearly downwave.

Imaging waves moving away from the aircraft (a downwave radar look direction) requires a negative telerotation, while imaging waves moving toward the aircraft (an upwave radar look direction) requires a positive telerotation. If two sets of waves are imaged, with the only difference being opposite look directions (i.e.,  $180^\circ$  apart), the telerotation magnitude needed to correct for image distortion due to radial velocity should be the same for each, one being a negative correction (downwave) and the other being a positive adjustment (upwave).

To study this radial velocity phenomenon, wave-frequency scans of pass 2 with seven telerotations from  $-2.0$  to  $+1.0$  degrees, and of pass 6 with seven telerotations from  $-1.0$  to  $+2.0$  degrees were made on the optical processor. The  $-1.0$  degree setting for pass 2 corresponds to approximately the phase velocity of the waves. For pass 6,  $+1.0$  degrees corresponds to the phase velocity correction. The correction for wave orbital velocity for both passes 2 and 6 is best represented by the  $0^\circ$  setting.

Results of the radial velocity scans are graphically shown in Fig. 7. The graph indicates that rotation of the cylindrical optics of the SAR processor is effective in improving wave

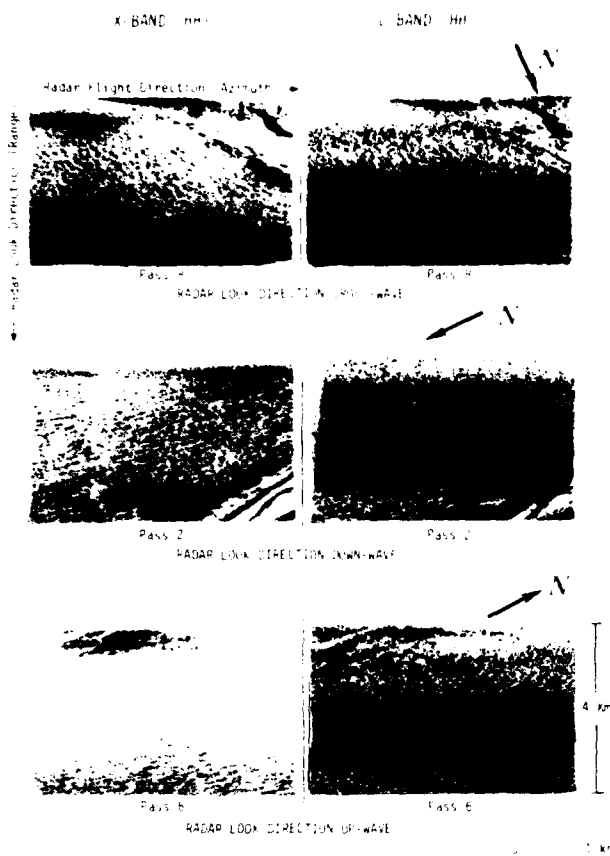


Fig. 8. The same ocean wave area imaged simultaneously with *X*- and *L*-band. These data were processed to  $3 \times 3$ -m resolution.

image contrast for range-traveling waves in the Marineland *L*-band radar data. This velocity correction corresponds closely to the phase velocity of the waves and cannot, to our knowledge, be explained by any alternative hypothesis.

The improvement in wave contrast by rotation of the processor cylindrical telescope was achieved without offsetting the azimuth frequency bandpass. The moving waves seem to be able to produce rotated signal histories without the expected azimuth Doppler spectrum shift. One possible explanation for this observation is that the azimuth Doppler spectrum is influenced by the actual scatterer motions, which are related to the orbital velocity, while the phase history rotation is due to the change in the brightest scatterers, which is related to the phase velocity [15].

#### B. Wave Detectability Versus Radar Look Direction

The eight-sided flight pattern at Marineland was used to quantify the dependency of radar look direction on wave detectability. Fig. 8 shows an identical ocean area simultaneously imaged with *X*- and *L*-band SAR on Dec. 15, 1975. Shown on the figure are three cases consisting of the radar looking cross-wave (upper figures), down-wave (middle), and up-wave (lower figures). Qualitative evaluation of the figure indicates that range-traveling waves are more discernible than azimuth-traveling waves.

Wave modulation depth scans for the eight-sided pattern

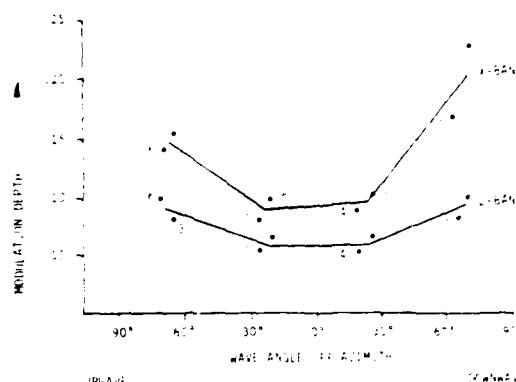


Fig. 9. Graph of modulation depth versus wave angle off azimuth for both *X*- and *L*-band passes 1 thru 8.

from Dec. 15 were examined to better quantify the wave detectability as a function of look angle. For the *L*-band data, three distinct focus settings were used to generate wave scans at the optimum focus setting for a given pass; thus a total of four separate scans were produced for each pass (three *L*-band and one *X*-band). For the *L*-band data, the scan producing the highest average modulation depth was assumed to be the one in focus; the other two were discarded.

Fig. 9 is a graph of modulation depth versus radar look direction. For *X*-band, it is evident that azimuth-traveling waves are significantly less detectable than range-traveling waves. A similar drop in modulation depth for  $60^\circ$  is present in the *L*-band data, but the decrease is less dramatic. Nevertheless, Fig. 9 indicates that waves are more detectable at *X*-band compared to *L*-band at all radar look angles (see [12]). It is useful to note that once the focusing adjustment is made for *L*-band data, the waves become nearly equally detectable regardless of look angle.

#### C. Wave Detectability as a Function of SAR Resolution and Mixed Integration

A section of *L*-band (HH) data from pass 1 obtained in deep water on Dec. 15 was used to test the effects of resolution cell size on modulation depths. The SAR data were optically processed to resolutions of  $3 \times 3$  m;  $5 \times 5$  m;  $6.25 \times 8$  m;  $25 \times 8$  m; and  $25 \times 25$  m in azimuth and range, respectively. Since the resolution of a SAR image is a function of the bandwidth used in the optical processor, reducing the bandwidth achieves a proportional reduction in resolution. Also, it is noted that a reduction in bandwidth is proportional to a reduction in synthetic aperture length, the time necessary to image a given object. Thus synthetic aperture length is important because of the motion of the ocean scatterers during imaging.

Fig. 10 shows the SAR wave imagery processed to the five resolutions discussed above. By inspection of the figure, the  $3 \times 3$ -m resolution wave image appears most discernible from the standpoint of wave detectability. Waves are also clearly discernible in the  $5 \times 5$ - and  $6.25 \times 8$ -m resolution images. No waves are visible in the  $25 \times 8$ - or  $25 \times 25$ -m resolution images.

The effects of mixed integration techniques on the modulation depth was also investigated. Mixed integration is an optical processing technique which allows, for a specific band-

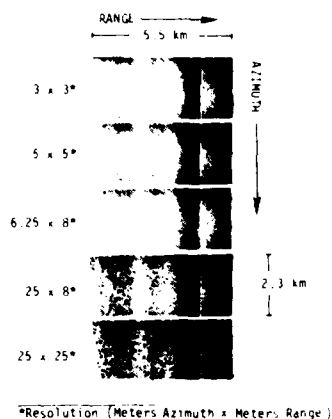


Fig. 10. L-band (HH) SAR wave data from pass 1 optically processed to five different resolutions.

width in the processor, a reduction in the speckle effect at the cost of spatial resolution (see [22] for an in-depth discussion of mixed integration theory). The question arises, given a bandwidth in the optical processor, will the modulation depth be affected by taking a single-look full-resolution scan as compared to a multiple-look reduced-resolution scan, using the equivalent bandwidth.

For this investigation, the pass and location of L-band data used previously was reprocessed. Scans were made using three separate resolutions:  $3 \times 3$  m;  $6.25 \times 8$  m; and  $25 \times 8$  m in azimuth and range, respectively. The  $25 \times 8$ -m resolution scan was processed using four looks, while the other two used only one look. The modulation depth was then calculated in the standard manner.

The result of this investigation which utilized a one-way analysis of variance indicated significant differences exist between the  $3 \times 3$ -m resolution scan modulation depth and those for both the  $6.25 \times 8$ - and  $25 \times 8$ -m resolution scans. No significant differences were detected between modulation depths from the  $6.25 \times 8$ - and the  $25 \times 8$ -m resolution scans [19]. The lack of a noticeable difference between the  $6.25 \times 8$ -m resolution one-look scan and  $25 \times 8$ -m resolution four-look scan suggests that wave detectability is not strongly dependent on the use of one-look full resolution versus multiple-looks reduced resolution processing. The noticeable difference between the  $3 \times 3$ -m resolution modulation depths and the  $6.25 \times 8$ -m resolution modulation depths is produced by decreased resolution as noted earlier. Noting that the waves being imaged are approximately 100 m long, it is qualitatively suggested, based on these results, that waves can only be detected if their wavelength exceeds four resolution cells.

## V. CONCLUSIONS

The environmental conditions encountered during the Marineland experiment corresponded to low wind speeds, low wave heights, and relatively short wavelengths. The results presented in this study are considered valid only for such conditions.

The analysis of modulation depth as a function of wave velocity indicates that maximum modulation depth occurs when a motion correction is utilized corresponding to a veloc-

ity that is in the near proximity of the phase velocity of the dominant gravity wave. This occurs for both azimuth- and range-traveling waves. These results may be consistent with either the phase velocity [19], [23] or the acceleration [5] explanations of this effect. L-band data is more sensitive to wave motion associated with the dominant gravity waves than X-band. In summary, the detectability of azimuth- and range-traveling waves can be improved by adjusting the focal distance and rotation of the cylindrical telescope in the SAR processor. These wave detectability enhancement techniques are inversely proportional to the SAR platform velocity, thus this may be less important for SAR systems that utilize faster moving platforms.

The modulation depth results derived from the Marineland data indicated that optimum wave detectability is achieved when X-band frequency is used and when the radar is essentially looking in the range direction. It is of interest to note that L-band range- and azimuth-traveling waves have about the same modulation depth when the waves are visible provided that focusing adjustments are made for azimuth-traveling waves.

The greater modulation depths produced by the X-band SAR may be explained in part by considering SAR system effects. X-band data has a larger depth of focus than L-band, and, therefore, the azimuth-traveling waves are not appreciably defocused as commonly occurs on L-band images of comparable resolution. The X-band also incorporates a shorter synthetic aperture length or integration time than L-band. By using a shorter integration time, there are more limited motion effects (azimuth velocities or range acceleration) which directly affect the azimuth or Doppler resolution. The integration time for the ERIM X- and L-band SAR system flown at Marineland was 0.34 and 2.47 s, respectively. Accelerations due to wave motion during the integration time causes degradation of azimuth resolution. The longer integration time required for L-band also makes it more sensitive to wave acceleration compared to the X-band SAR.

The resolution tests performed on the L-band data indicates that the 100-m waves could not be discerned when the radar surface resolution was coarser than  $20 \times 20$  m. This observation is consistent with the low level of ocean wave detectability reported by the JPL L-band SAR system which also collected data at Marineland. The resolution for the JPL L-band SAR was  $25 \times 25$  m. It is qualitatively deduced that ocean waves need to be at least four times longer than the SAR resolution to be detected. The Marineland data set was not sufficient to define minimum wave height and wind speed levels for detecting waves.

## ACKNOWLEDGMENT

The insight gained in this paper could not have been achieved without the critical reviews and open discussions by members of the Marineland Experiment Team. Here, the incisive contributions of the late J. W. Wright are especially recognized.

The modulation measurements were made on the ERIM SAR processor by A. Klooster and J. Losee. E. S. Kasishchke carried out the computer reduction and statistical analysis on the radar modulation backscatter data. D. Ross and B.

McLeish of NOAA/SAIL are acknowledged for providing the pitch and roll buoy sea truth.

# REFERENCES

- [1] W. M. Brown and L. J. Porcello, "An introduction to synthetic aperture radar," *IEEE Spectrum*, vol. 6, pp. 57-62, 1969.
- [2] R. O. Harger, *Synthetic Aperture Radar Systems*. New York: Academic, 1970.
- [3] P. G. Teleki, R. A. Shuchman, W. E. Brown, Jr., W. McLeish, D. Ross, and M. Mattie, "Ocean wave detection and direction measurements with microwave radars," in *Oceans '78*, IEEE/MTS, pp. 639-648, 1978.
- [4] G. R. Valenzuela, "An asymptotic formulation for SAR images of the dynamical ocean surface," *Radio Sci.*, vol. 15, pp. 104-114, 1980.
- [5] W. E. Alpers, D. B. Ross, and C. L. Rufenach, "On the detectability of ocean surface waves by real and synthetic aperture radar," *J. Geophys. Res.*, vol. 86, pp. 6481-6498, 1981.
- [6] R. A. Shuchman, A. L. Maffett, and A. Klooster, "Static and dynamic modeling of a SAR imaged ocean scene," *IEEE J. Oceanic Eng.*, vol. OE-6, pp. 41-49, 1981.
- [7] J. F. Vesecky and R. H. Stewart, "The observation of ocean surface phenomena using imagery from the seasat synthetic aperture radar—An assessment," *J. Geophys. Res.*, vol. 87, pp. 3397-3430, 1982.
- [8] R. K. Raney, "SAR response to partially coherent phenomena," *IEEE Trans. Antennas Propagat.*, vol. AP-28, pp. 777-787, 1980.
- [9] R. O. Harger, "SAR ocean imaging mechanisms," in *Spaceborne Synthetic Aperture Radar for Oceanography*, R. C. Beal, P. S. DeLeonibus, and I. Katz, Eds., Baltimore, MD: Johns Hopkins Univ. Press, 1982, pp. 41-52.
- [10] A. Jain, "SAR imaging of ocean waves: Theory," *IEEE J. Oceanic Eng.*, vol. OE-6, pp. 130-139, 1981.
- [11] J. W. Wright, "Backscattering from capillary waves with application to sea clutter," *IEEE Trans. Antennas Propagat.*, vol. AP-14, pp. 749-754, 1966.
- [12] W. Alpers and K. Hasselmann, "The two-frequency technique for measuring ocean wave spectra from an airplane or satellite," *Boundary-Layer Meteorol.*, vol. 13, pp. 215-230, 1978.
- [13] W. R. Alpers and C. L. Rufenach, "The effect of orbital motions on synthetic aperture radar imaging of ocean waves," *IEEE Trans. Antennas Propagat.*, vol. AP-27, pp. 685-690, 1979.
- [14] R. K. Raney, "Synthetic aperture imaging radar and moving targets," *IEEE Trans. Aerospace Electron. Syst.*, vol. AES-7, pp. 499-505, 1971.
- [15] R. A. Shuchman, "Processing synthetic aperture radar data of ocean waves," in *Oceanography from Space*, J. F. R. Gower, Ed., New York: Plenum, pp. 477-496, 1981.
- [16] R. Rawson, F. Smith, and R. Larson, "The ERIM X- and U-band dual polarized radar," in *Proc. IEEE Int. Radar Conf.* (Arlington, VA), pp. 505-510, 1975.
- [17] A. Kozma, E. N. Leith, and N. G. Massey, "Tilted plane optical processor," *Applied Opt.*, vol. 11, pp. 1766-1777, 1972.
- [18] R. L. Jordan, "The Seasat-A synthetic aperture radar system," *IEEE J. of Oceanic Eng.*, vol. OE-5, pp. 154-164, 1980.
- [19] E. S. Kasischke and R. A. Shuchman, "The use of wave contrast measurements in the evaluation of SAR/gravity wave models," in *Proc. 15th Int. Symp. Remote Sens. Environ.* (Ann Arbor, MI), pp. 1187-1206, 1981.
- [20] R. A. Shuchman and J. S. Zelenka, "Processing of ocean wave data from a synthetic aperture radar," *Boundary-Layer Meteorol.*, vol. 13, pp. 181-191, 1978.
- [21] O. H. Shemdin, W. E. Brown, Jr., F. H. Staudhammer, R. A. Shuchman, R. Rawson, J. Zelenka, D. B. Ross, W. McLeish, and R. A. Berles, "Comparison of *in-situ* and remotely sensed ocean waves off Marineland, Florida," *Boundary Layer Meteorol.*, vol. 13, pp. 225-234, 1978.
- [22] L. J. Porcello, N. G. Massey, R. B. Innes, and J. M. Marks, "Speckle reduction in synthetic aperture radar imagery," *J. Opt. Soc. Amer.*, vol. 66, pp. 1305-1311, 1976.
- [23] A. V. Ivanov, "On the synthetic aperture radar imaging of ocean surface waves," *IEEE J. Oceanic Eng.*, vol. OE-7, pp. 96-103, 1982.

★

Robert A. Shuchman, for photograph and biography see page 96 of this issue

★

Omar H. Shemdin, photograph and biography not available at time of publication



## AIRBORNE SYNTHETIC APERTURE RADAR OBSERVATION OF SURF ZONE CONDITIONS

R. A. Shuchman

Radar and Optics Division, Environmental Research Institute of Michigan, P.O. Box 8618, Ann Arbor, Michigan 48107

G. A. Meadows

Department of Atmospheric and Oceanic Science/ERIM Consultant, University of Michigan, Ann Arbor, Michigan 48109

## INTRODUCTION

Synthetic aperture radar (SAR) has been used to image ocean waves over large areas from both conventional aircraft (Elachi, 1976; Shemdin, et al., 1978) and from satellites (Gonzalez, et al., 1979). Imaging is not restricted by platform size or altitude as with real aperture radar, or by external illumination, as with photography. SAR images have then been used to determine surface wave direction and wavelength. Although the imaging mechanism has not been explained completely, the forward face and rear face of sufficiently large waves exhibit different scattering characteristics at SAR wavelengths and can be distinguished in SAR imagery (Shuchman, et al., 1978).

The Environmental Research Institute of Michigan (ERIM) has been acquiring and processing SAR data from aircraft for several years (Cindrich, et al., 1977). In October 1978, ERIM acquired SAR data on a flight along the coast of Lake Michigan approximately halfway between Pentwater and Ludington, Michigan (latitude 43° 50' N).

At this time, the University of Michigan's Department of Atmospheric and Oceanic Science was operating a series of resistance wave gauges and ducted impeller current meters in the nearshore zone (Meadows, 1979). This paper compares SAR wave directional spectra measurements to *in situ* wave spectra obtained in the surf zone. Additionally, the SAR Doppler history is exploited to obtain an estimate of surface current magnitude and direction. This SAR derived information is also compared to the *in situ* nearshore surface current sea truth.

The following sections describe the *in situ* sea truth and the ERIM SAR system. Methods of computing wave direction, wavelength, and current information from the SAR are discussed. The comparisons of the SAR derived information with the sea truth are good, indicating remotely sensed surf zone information is a useful tool to oceanographers and coastal engineers. In addition, directions of wave travel, as obtained from the SAR coastal imagery, are shown to be consistent with classical wave refraction calculations.

## DATA COLLECTION

On 18 October, 1978 at approximately 16:35 EST, SAR data was collected along the shoreline of Lake Michigan centered at latitude 43° 50' N. The site for this field experiment was the eastern shore of Lake Michigan, between the cities of Ludington and Pentwater, Michigan. This thirteen-kilometer section of shoreline, extending approximately north-south, is characterized by a multiple-barred bathymetry with nearly straight and parallel contours. The SAR system used to collect the data was the ERIM X- and L-band dual-polarized imaging radar described by Rawson, et al. (1975). The ERIM SAR system records four channels of radar return but we will focus our attention here on the X-band horizontal-transmit-horizontal-receive channel as this data provided the clearest wave images. The SAR was flown at an altitude of 6100 m and operated with a center incident angle from the vertical of 20°, yielding a swath width of 5.6 km. The cross-track or range resolution of SAR is limited by radar frequency bandwidth and is about 2 m for X-band. The along track or azimuth resolution is obtained from the synthetic aperture technique described by Brown and Porcello (1968). For the X-band, the azimuthal resolution is about 2.5 m. A sample of the X-band imagery showing the location of the coastal array (letter A) is shown in Figure 1. This SAR data was processed on the ERIM processor described by Kozma (1972).

At the same time as the ERIM flight, the University of Michigan, Department of Atmospheric and Oceanic Science was operating its

mobile surf zone, wave and current sensing array (Meadows, 1979). Monitoring of incident wave characteristics and longshore current velocities was conducted through the growth of a significant storm on Lake Michigan. A detailed discussion of the experimental design is presented in Wood and Meadows (1975) and Meadows (1977). Surface-piercing, step resistance wave probes and bi-directional ducted impeller flow meters were employed to make simultaneous measurements of wave and current conditions. These sensors were oriented on a line perpendicular to shore, extending from the beach through the outer surf zone. Other coastal sensing equipment included a directionally mounted motion picture camera and Lagrangian drifters. Unfortunately, increasing wind and wave action on 17 and 18 October, destroyed much of the array, however, sufficient sensors survived to make this comparative study possible. A representative portion of the 18 minute record from the outer surf zone resistance wave gauge is shown in Figure 2.

## METHODS

The SAR data shown in Figure 1 was digitized using the ERIM hybrid image digitizer (Ausherman, et al. 1975). The data was digitized with an approximate resolution of 6 meters (3 m pixels). The range coordinates of the digitized data were analytically corrected for slant-to-range geometry (Feldkamp, 1978). Four 1.5 x 1.5 km subsections (see Figure 3) with 6 meter resolution were extracted from the digitized data. The four sections are labeled A-D where A is closest to shore.

The 3.0 m pixel digitized SAR images were converted to 6 m resolution by 4 pixel averaging in order to increase coherence in the image. The average value of each azimuthal line was subtracted from the line to remove the trend of intensity falloff with increasing range distance. Two-dimensional fast Fourier transforms were performed on each 256 x 256 cell subsection to yield raw directional wave number spectra with a Nyquist wave number of 0.52 m<sup>-1</sup>. The raw spectra were smoothed by replacing each value with the average of the surrounding 5 x 5 cell. The approximate number of degrees of freedom for the resulting spectrum is 142 (Kinsman, 1965). The 99% confidence limits are then  $\pm 1.5$  dB (Jenkins and Watts, 1968).

The longshore current magnitude and directional information was extracted from the SAR data by exploitation of the SAR Doppler history (Shuchman, et al., 1979). This technique takes advantage of the fact that the SAR instrument responds primarily to backscatter from

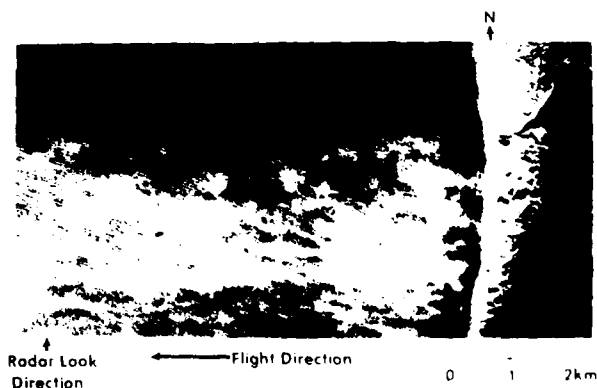


FIGURE 1. X-Band (HH) SAR data used in study. (The letter A indicates approximate location of surf zone array. Image represents 3 x 3-meter resolution.)

Copyright 1980 by the American Geophysical Union.

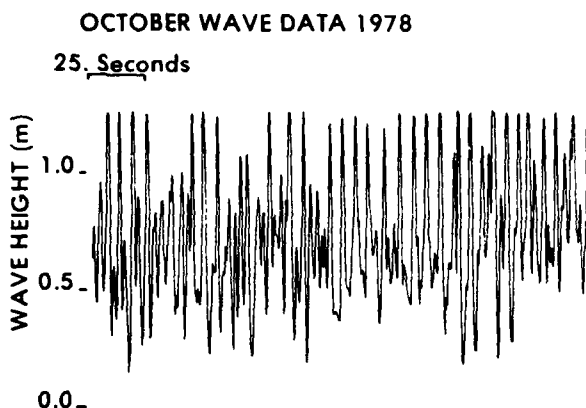


FIGURE 2. Representative Section of 18 minute time history of water level elevation data from nearshore resistance wave gauge

capillary waves, which, in conventional SAR processing, are assumed stationary with respect to other time scales of the radar system. However, these scatterers are not stationary; they move with a characteristic phase velocity as well as with a velocity due to the presence of currents and longer gravity waves. The radial (line of sight) component of this resultant velocity produces a Doppler shift in the temporal frequency of the return signal, which translates to a spatial frequency shift recorded on SAR signal film.

The Doppler frequency shift ( $\Delta f_D$ ) for a moving target relative to a stationary target in a SAR system is

$$\Delta f_D = -\frac{2V_r}{\lambda} \quad (1)$$

where  $V_r$  = radial component of target velocity, and  
 $\lambda$  = transmitted radar wavelength.

This temporal frequency shift will produce an azimuth spatial frequency shift of

$$\Delta f' = -\frac{\Delta f_D P}{V_{AC}} \quad (2)$$

on the SAR signal film, where  $P$  = azimuth packing factor, and  $V_{AC}$  = aircraft velocity.

Equations 2 and 3 can be combined to relate radial target velocity to Doppler spectrum shift:

$$V_r = \frac{\Delta f' \lambda V_{AC}}{2P} \quad (3)$$

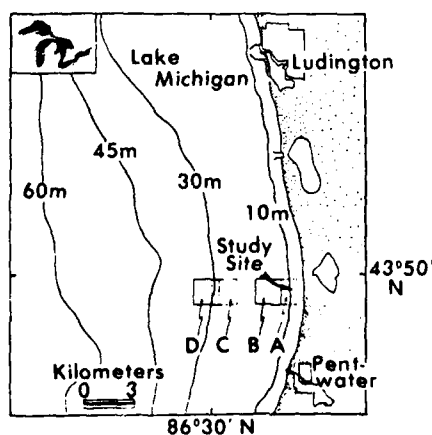


FIGURE 3. General study area showing nearshore bathymetry and locations of fast Fourier transforms performed on SAR data

Typical values for  $\lambda$ ,  $V_{AC}$ , and  $P$  for the imaging of the Lake Michigan data are 0.032 m, 109 m/s, and 15,000 respectively. This relationship can be used to measure the average radial velocity component of an ocean-wave scattering field relative to a fixed-land scattering field. A shift in the azimuth spatial frequency spectrum between fixed-land and moving-ocean surfaces yields an estimate for  $\Delta f'$ . Variations in spectrum location due to antenna pointing may be eliminated by choosing imagery having land and ocean imaged near simultaneously. An assumption was made that the antenna pointing angle did not change between the land and water measurements. If, however, the antenna angle did change, a slightly higher radial velocity would be calculated.

To calculate the wave spectrum at the instrumented surf zone site, the total 18-minute analog record shown in Figure 2 was digitized at 0.25 s intervals and analyzed using conventional one-dimensional fast Fourier transform techniques. The directional information was obtained by utilizing data from the directionally-mounted camera and the surveyed positions of the array stations. The current information was obtained by again using the directionally-mounted camera but this time photographing the Lagrangian drifters since, by the time of the aerial overflight, the last current meter station had been destroyed.

## RESULTS

Figure 4 consists of contour plots of energy density for two test areas (A & D) extracted from the digitized SAR data. Six contour levels are given in 3 dB increments. The data is normalized to the highest value found within the transform. The average depth for each of 1.5 x 1.5 km<sup>2</sup> areas are indicated on Figure 4. Note the large amount of low frequency energy on the contours even though the data was extensively corrected to reduce the DC bias. The reason for these low frequency components will be discussed later. These contour plots have not been corrected for distortions caused by wave motion. The SAR process distorts the apparent wavelength of waves moving in the azimuthal direction and distorts the apparent direction of waves with a velocity component in the range direction. A detailed description of these effects and the appropriate corrections can be found in Raney and Lowry (1977) and Shuchman, et al. (1979a). The contour data presented was motion corrected and those results will be presented in table form. There is a 180° ambiguity in wave direction measured by SAR which was resolved by assuming the waves were coming from the west and therefore propagating towards the shore.

Close inspection of the contour plots indicates dominant wavelengths of 43, 48, and 55 meters have been resolved by the spectral analysis. Although, spectral energy was resolved at wavelengths as short as 26 m, only the dominant wavelengths have been utilized in the analysis. The general direction of wave travel in the nearshore region is approximately 30°. Note that wave refraction can be observed when comparing the direction obtained in area D with the shallow water area, A.

Figure 5 is a scan of Doppler history for stationary land and the surf zone. Both scans used a 1 x 1 km<sup>2</sup> aperture. The surf zone scan was centered approximately 650 meters offshore. Note on Figure 5 how the coastal zone (water) scan is displaced to the left of the stationary

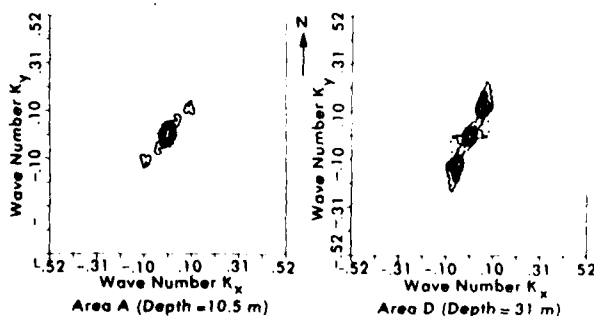


FIGURE 4. Contour plots of fast Fourier transforms (FFT's) of SAR X-Band Lake Michigan wave data

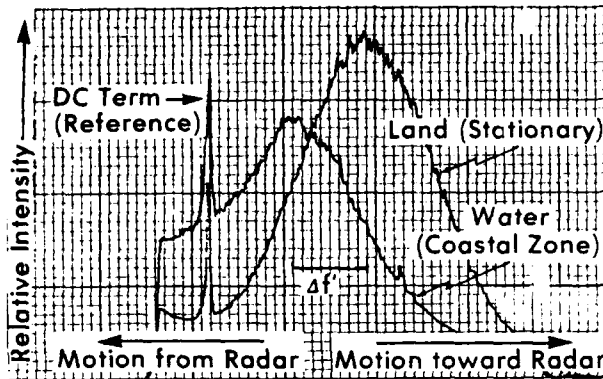


FIGURE 5. Plot of Doppler displacement caused by radial velocity component of longshore current averaged over 1 km<sup>2</sup> area

(land) target. This indicates a radial motion away from the radar. Recall from Figure 1 that the radar was traveling with a heading of 270° T, thus, the longshore current sensed by the radar was in the northward direction. The  $\Delta f$  frequency which is used in Equation 3 is indicated on the figure. This  $\Delta f$  is corrected for a bias caused by the laser illumination in the SAR optical processor. A  $\Delta f$  of 0.55 lp/mm was detected, which indicates a current velocity of approximately 0.5 m/sec.

A summary of the incident surf zone conditions during the SAR overflight is presented in Table 1. They were obtained by statistical analysis of the 18-minute continuous sea surface elevation record. A representative portion of this surface piercing wave staff record is presented in Figure 2. A one-dimensional spectrum of this wave height data, incident at the outer surf zone, is shown in Figure 6. The dominant frequencies resolved by the spectral analysis are indicated on the figure. In addition, the calculated wave periods and deep water wavelengths are also shown on the figure for each of the major spectral peaks. These correspond to deep water wavelengths of 13, 26, 36, 44 and 54 m, respectively. This analysis indicates the presence of a multi-component incident gravity wave group with dominant periods in the range of 3-6 s. Significant long-period wave components have also been identified with the wave group. The periods of these low frequency components are 17, 40 and a less significant peak at 59 seconds, respectively and appear to resemble surfbeats (Munk, 1949; Tucker, 1950). These results are consistent with measurements of near-shore

Table 1  
Incident Surf Zone Conditions at the Time of the SAR Overflight

Significant Wave Height	0.95 (m)
Dominant Wave Periods	5.9, 5.3, 4.8, 4.0, 2.9 (s)
Deep Water Wavelength	54, 44, 36, 25, 13 (m)
Incident Wave Direction	57 ± 5°
Longshore Current Velocity	0.26 (m/s)
Longshore Current Direction	North (360° T)
Wind Speed	7.5-10 m/s
Wind Direction	230° T

multi-component wave trains reported by Meadows and Wood (1980).

Incident wave direction and longshore current velocity were determined by a frame-by-frame analysis of synchronous motion picture sequence from the shore based directionally-mounted camera. The mean wave angle of attack to the beach was determined to be 57 ± 5° (T) and the mean longshore current velocity midway across the active surf zone was 0.26 m/sec flowing toward the north.

#### COMPARISON BETWEEN THE SAR AND SURF ZONE MEASUREMENTS

Table 2 provides a comparison between the SAR derived surf zone conditions and the sea truth provided by the surf zone array. The values presented in Table 1 represent surf zone conditions actually measured at the shoreward edge of test area A. The wave directions and wavelengths were then corrected for depth effects using classical linear wave theory. The depths used for the corrections are also indicated on the table. The SAR derived results presented in Table 2 are also corrected for the previously discussed motion distortions. The excellent agreement between SAR observations and the surf zone sea truth shown in the table indicates the following:

1. The dominant surface gravity wave wavelengths and direction are obtainable from the SAR.
2. These observations are in excellent agreement with sea truth, even within the active surf zone.
3. Wave refraction can be observed with SAR and favorably compares to the calculated refraction using classical linear wave theory.

The SAR derived radial current velocity measurement of 0.5 m/sec was higher than reported in Table 1 (0.26 m/sec). However, recall that the current measurement derived from the SAR was not taken in the surf zone but was centered 650 m from the shore (Meadows

#### OCTOBER WAVE DATA 1978

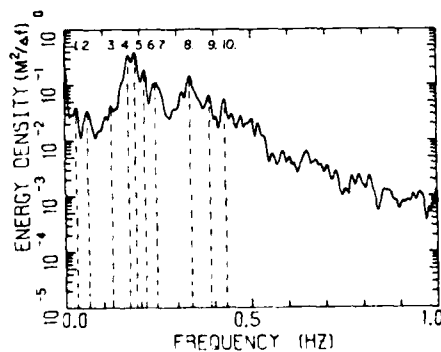


FIGURE 6. One-dimensional wave height spectrum of water surface elevation time history from resistance wave gauge. Dominant wave periods and wavelengths are as follows: (1) T = 40.0 s, L = 685.9 m; (2) T = 17.2 s, L = 294.9 m; (3) T = 8.1 s, L = 138.9 m; (4) T = 5.9 s, L = 54.3 m; (5) T = 5.3 s, L = 43.8 m; (6) T = 4.8 s, L = 35.9 m; (7) T = 4.0 s, L = 25.0 m; (8) T = 2.9 s, L = 13.1 m; (9) T = 2.6 s, L = 10.5 m; (10) T = 2.3 s, L = 8.25 m.

Table 2. Comparison Between the SAR Derived Surf Zone Condition and the In Situ Sea Truth

Test Area	SAR Derived				Sea Truth*	
	Distance from Shore (M)	Depth (M)	Dominant Wavelength (M)	Direction (T°)	Wavelength (M)	Direction (T°)
A	900	10.5	48	35 ± 3	47.72	34 ± 2
			43		43.7	
					53.8	
B	2200	14	55	30 ± 3	43.7	30 ± 2
			55		55.3	
			43		45.7	
C	4600	27	48	25 ± 3	45.7	28 ± 2
			55		55.3	
			48		45.7	
D	6900	31	55	25 ± 3	45.7	28 ± 2
			48		45.7	
			48		45.7	

\* Actual measurements made at surf zone, values for test areas a-d are depth corrected.

(1977 and 1979), reports that under certain conditions, an increase in longshore current velocity as one moves from the surf zone into deeper water may be expected. As presented earlier, the SAR Doppler measurement is a radial velocity and is denoted by a line of sight. Thus, only rather coarse directional information is obtainable; in this case, a current velocity away from the radar look direction (northward flowing current). Two orthogonal flight headings and resulting current measurements could greatly enhance the directional sensing capability.

#### DISCUSSION

The SAR spectrum data presented in Figure 4 are wave number spectrum of the radar intensity and as such are not expected to have the same appearance as the one-dimensional spectrum from the resistance wave gauge (Figure 6) which was determined from wave height and period data. Even if the wave number spectrum is converted to a frequency spectrum or vice-versa, it is clear that the SAR spectra examined here cannot be easily transformed to, or interpreted as, wave height spectra. However, the wave number and direction of the peak energy, determined from SAR spectra, agree very well with *in situ* measurements. Synoptic availability of even these parameters is currently unobtainable by conventional ground-based measurements. This addition represents a significant advance in large scale wave data acquisition.

Both of the SAR derived wave spectra presented in Figure 4 exhibit significant low frequency components. These components were observed even after the digital SAR data was extensively smoothed and the intensity falloff in the range direction was digitally corrected. The low frequency (near zero wave number) components could in fact be real components of the sea surface and will be further evaluated in a follow-on study.

#### SUMMARY

Synthetic aperture radar (SAR) surface gravity wave data of the coastal zone of a portion of Lake Michigan has been compared to *in situ* surf zone wavelength, period, direction, and surface current information. The comparisons were favorable, indicating SAR's utility as a tool to remotely sense coastal zone conditions. This could in turn enable oceanographers to synoptically study the entire coastline of large water bodies. This data could then prove useful in mapping not only surface wave climates and currents, but also provide a mechanism for rapid and large scale assessment of changes in coastal conditions.

Specifically, this study has shown:

1. SAR derived wavelengths and directions are in good agreement with sea truth,
2. SAR spectra taken in various water depths do correlate with predicted wave refraction,
3. Longshore current direction and relative magnitude as obtainable from SAR Doppler history are in reasonable agreement with sea truth, and
4. Low-frequency components observed on SAR spectra seem to correlate with low frequency "surf beat" found in sea truth spectral estimates.

It should be mentioned when utilizing SAR data such as presented in this paper, that the SAR spectral estimates presented are wave number-directional spectra of the radar return intensity. The data does not represent wave height information, at least not in a recognizable form. The modulation transfer function (i.e., SAR gravity wave imaging mechanism) is not totally understood at the present time. The determination of the transfer function as well as determination of wave height using SAR data will be a major scientific advance. At that time, it would then be possible to use SAR gravity wave data to obtain power density estimates of the sea surface.

**Acknowledgements.** The ERIM analysis of the SAR gravity wave data was supported by the Office of Naval Research (ONR) Contract N00014-76-C-1048. The technical monitor for this ONR contract is Mr. Hans Dolezalek. The field installation of the mobile wave and

current monitoring system, as well as the reduction of the *in situ* sea truth data, was supported under the University of Michigan research grant no. 387349.

#### REFERENCES

- Ausherman, D. A., W. D. Hall, J. N. Latta, and J. S. Zelenka, Radar Data Processing and Exploitation Facility, Proceedings IEEE International Radar Conference, Washington, D.C., 1975.
- Brown, W. J. and L. Porcello, An Introduction to Synthetic Aperture Radar, *IEEE Spectrum*, 6, pp. 52-66, 1968.
- Cindrich, I., J. Marks, and A. Klooster, Coherent Optical Processing of Synthetic Aperture Radar Data, *Proceedings of the Society of Photo. Optical Instrumentation Engineers*, p. 128, 1977.
- Elachi, C., Wave Patterns Across the North Atlantic on September 28, 1974, from Airborne Radar Imagery, *J. Geophys. Res.*, 81, pp. 2655-2656, 1976.
- Feldkamp, G. B., Correction of SAR-Induced Distortion in Seasat Imagery, Paper Presented at the SPIE Conference on Applications of Digital Image Processing, San Diego, Calif., August 1978.
- Gonzalez, F. I., R. C. Beal, W. E. Brown, P. S. DeLeonibus, J. S. Sherman, J. F. R. Gower, D. B. Ross, C. L. Rufenach, and R. A. Shuchman, Seasat Synthetic Aperture Radar: Ocean Wave Detection Capabilities, *Science*, 204, pp. 1418-1421, 1979.
- Jenkins, A. M. and D. G. Watts, *Spectral Analysis and Its Applications*, Holden-Day, San Francisco, Calif., 525 pp., 1968.
- Kinsman, B., *Wind Waves—Their Generation and Propagation on the Ocean Surface*, Prentice-Hall, Englewood Cliffs, N.J., 676 pp., 1965.
- Kozma, A., E. N. Leith, and N. G. Massey, Tilted Plane Optical Processor, *Applied Optics*, 11, p. 1766, 1972.
- Meadows, G. A., The Wind Driven Component of Surf Zone Circulation (Abstract), *Trans. Amer. Geophys. Union*, Vol. 60, No. 46, 1979.
- Meadows, G. A., A Field Investigation of the Spatial and Temporal Structure of Longshore Currents, Ph.D. Dissertation, Purdue Univ., West Lafayette, Indiana, 1977.
- Meadows, G. A. and W. L. Wood, Long-Period Surf Zone Motions (In Review), 1980.
- Munk, W. H., Surf Beats, *Trans. Amer. Geophys. Union*, Vol. 30, 1949.
- Raney, R. K. and R. T. Lowry, Oceanic Wave Imagery and Wave Spectra Distortions by Synthetic Aperture Radar, Twelfth International Symposium on Remote Sensing of Environment, Manila, Philippines, 20-29 April 1978.
- Rawson, R., F. Smith, and R. Larson, The ERIM Simultaneous X- and L-Band Dual Polarized Radar, *IEEE 1975 International Radar Coherence*, 505, 1975.
- Shemdin, O. H., W. E. Brown, F. G. Standhammer, R. Shuchman, R. Rawson, J. Zelenka, D. B. Ross, W. McLeish, and R. A. Berles, Comparison of In Situ and Remotely Sensed Ocean Waves Off Marineland, Florida, *Boundary-Layer Meteorol.*, 13, pp. 193-202, 1978.
- Shuchman, R. A., C. L. Rufenach, and F. I. Gonzalez, The Feasibility of Measurement of Ocean Surface Currents Using Synthetic Aperture Radar, Published in the Proceedings of the Thirteenth International Symposium on Remote Sensing of Environment, Ann Arbor, Mich., April 1979.
- Shuchman, R. A., K. Knorr, J. C. Dwyer, A. Klooster, and A. L. Maffett, Imaging Ocean Waves with SAR, *ERIM Report No. 124300-2-T*, Environmental Research Institute of Michigan, Ann Arbor, Mich., 130 pp., 1979a.
- Shuchman, R. A., E. S. Kasischke, and A. Klooster, Synthetic Aperture Radar Ocean Wave Studies, *ERIM Final Report No. 131700-3-F*, Ann Arbor, Michigan, 1978.
- Tucker, M. J., Surf Beats: Sea Waves of 1 to 5 Minutes Period, *Proc. Roy. Soc. A* 207, pp. 565-573, 1950.
- Wood, W. L. and G. A. Meadows, Unsteadiness in Longshore Currents, *Geophys. Res. Lett.*, Vol. 2, No. 11, 1975.

(Received February 2, 1980;  
accepted March 10, 1980.)

## Analysis of MARSEN X Band SAR Ocean Wave Data

R. A. SHUCHMAN,<sup>1</sup> W. ROSENTHAL,<sup>2</sup> J. D. LYDEN,<sup>1</sup> D. R. LYZENGA,<sup>1</sup> E. S. KASISCHKE,<sup>1</sup>  
H. GUNTHER,<sup>2</sup> AND H. LINNE<sup>2</sup>

Analysis of X band SAR imagery collected during the MARSEN experiment indicates that the APD-10 SAR system imaged both range- and azimuth-traveling gravity waves. However, only the near-edge portion of the APD-10 imagery provided reliable spectral wave estimates. Numerous motion artifacts, which manifest themselves as azimuth-oriented streaks, are visible on the data and are believed to be caused by breaking waves. Because of the large platform velocity, the APD-10 SAR data are relatively insensitive to wave enhancement adjustments performed during the processing of SAR signal histories. A modulation transfer function to relate SAR-derived spectra to in situ measurements has been developed. The transfer function is smaller and falls off more rapidly with wave number for azimuth-traveling waves than for range-traveling waves. This is a consequence of the smaller inherent modulation for azimuth-traveling waves and the degraded resolution in the azimuth direction as a result of motion effects and agrees, at least qualitatively, with theoretical predictions.

## 1. INTRODUCTION

The Maritime Remote Sensing Experiment (MARSEN) was held in the southern part of the North Sea during August and September of 1979, with the primary goal of further developing remote sensing techniques for the retrieval of oceanographic information. The data collected during this experiment included both remotely sensed and in situ measurements. Among the remote sensing instruments used at MARSEN were synthetic aperture radars (SAR's). Both X band (3.2 cm) and L band (25 cm) SAR data were collected. In this paper we analyze only the data taken with the X band SAR.

The purpose of the SAR participation during MARSEN was to better understand the SAR imaging mechanism for ocean waves. This paper presents an analysis of the data collected by APD-10 SAR systems mounted in RF-4 aircraft operated by the United States Air Force of Europe (USAFE). The analysis consisted of (1) examining the effects of scatterer motion on both the wave imagery and the resulting spectra, (2) studying the effect of aircraft heading on the SAR-derived spectral estimates, and (3) performing a comparison between the SAR-derived and surface-measured spectral estimates, including the development of a modulation transfer function (MTF) to relate the two measurements.

Previous experiments with aircraft SAR's have shown that it is possible to detect the dominant wavelength and direction of a surface wave field [Shemdin *et al.*, 1978; Gonzalez *et al.*, 1979; McLeish *et al.*, 1980; Pawka *et al.*, 1980]. The shape of in situ and SAR-derived surface wave spectra, however, show large differences. It is therefore worthwhile to look for a functional relationship between in situ and SAR spectra and to determine the dependence of that relationship on the relevant environmental parameters. This paper presents first results of such investigations. It does not derive

them from theoretical assumptions about the mapping mechanism but uses available sea truth to establish quantitative empirical relationships with the SAR image.

In this paper we present first a description of the MARSEN test site and APD-10 system. This is followed by a discussion of the effects of ocean scatterer motion on the resultant SAR images. Next, spectral comparisons between the SAR and in situ measurements are presented. Finally, the development of a modulation transfer function is discussed.

## 2. DATA DESCRIPTION

The APD-10 is a high-resolution, airborne, side-looking reconnaissance SAR operating at X band (3.2 cm). The APD-10 is the radar portion of the UPD-4 system, which includes a ground-based SAR processor. The APD-10 SAR data were recorded on 24-cm film in four subswaths. Each subswath is nominally 4.6 km in width, with an additional 0.46 km overlap between adjacent channels. The nominal operating parameters for the APD-10 at MARSEN are listed in the following table.

APD-10 Radar Parameters for MARSEN Flights

Wavelength	0.032 m
Frequency	9.4 GHz
Polarization	HH (horizontal transmit horizontal receiver)
Pulse width	0.95 $\mu$ s
FM rate	105 MHz $\mu$ s
Average power	70 W
Swath width	18.5 km
Nominal processed resolution	3-m slant range 3-m azimuth
Platform altitude	3.35 km
Near-edge slant range	4.6 km
Far-edge slant range	23.2 km
Near-edge incidence angle	43°
Far-edge incidence angle	82°
Platform velocity	210 m/s

Synthetic aperture radar is a coherent imaging device that uses the motion of a moderately broad physical antenna beam to synthesize a very narrow beam, thus providing fine azimuthal (along-track) resolution [Harger, 1970; Brown and Porcello, 1969]. Fine range (cross-track) resolution is achieved by transmitting either very short pulses or longer

<sup>1</sup> Radar and Optics Division, Environmental Research Institute of Michigan (ERIM), P.O. Box 8618, Ann Arbor, Michigan 48107.

<sup>2</sup> Max Planck Institute of Meteorology, Institute of Geophysics, University of Hamburg, Hamburg, West Germany.

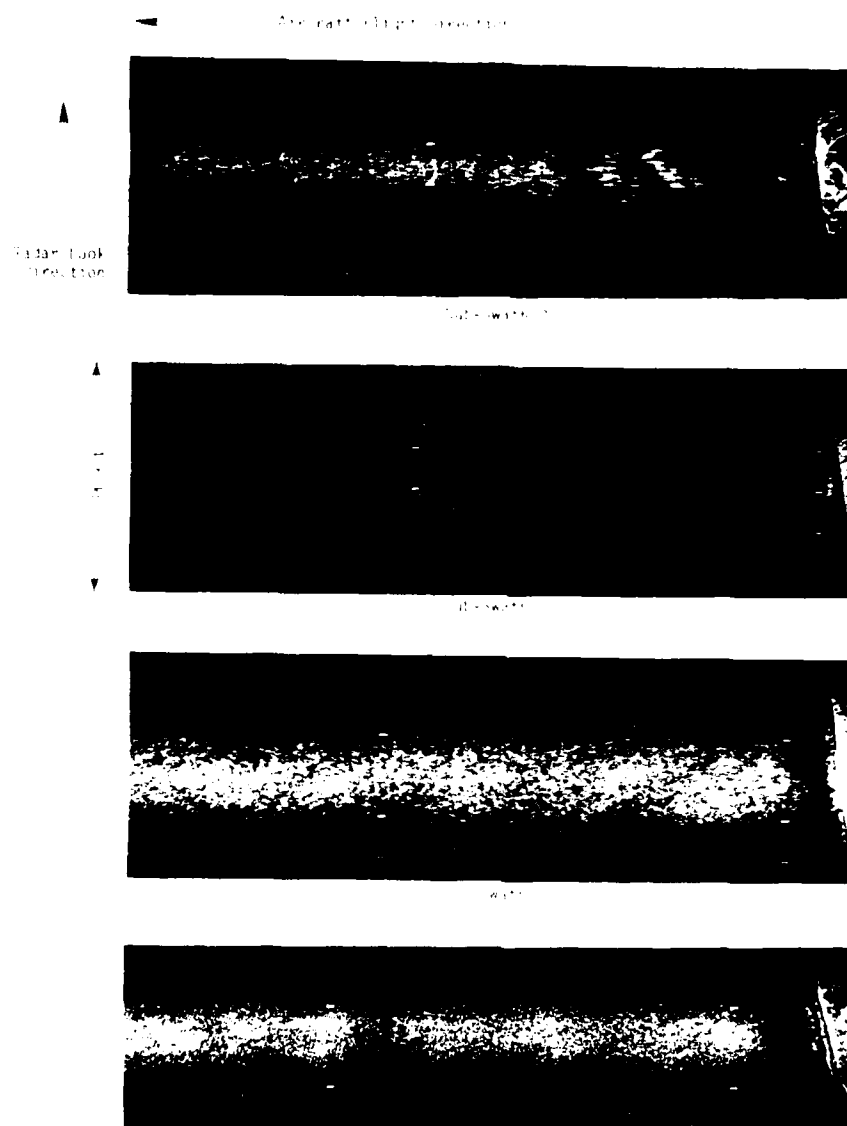


Fig. 1. Example of optically processed APD-10 imagery collected on September 28, 1979, off the coastline of Sylt.

coded pulses that are compressed by matched filtering techniques into equivalent short pulses.

The APD-10 system is a typical SAR in the sense that the amplitude and phase history information of the returned backscatter is recorded onto photographic film (signal film) aboard the aircraft. These recorded data are utilized by processing the SAR signal film into image film by using standard optical processing techniques [Kozma *et al.*, 1972] and digitizing the SAR image data by using the ERIM Hybrid Image Processing Facility [Ansherman *et al.*, 1975].

Typically, the RF-4 aircraft on which the APD-10 was mounted flew a mission (or line) consisting of a four- or five-sided box or star pattern over the test site. This was done to determine the sensitivity of the SAR look direction for detecting gravity waves. Each individual change of aircraft direction is referred to as a pass of data within a line. The 18.5-km swath of data consists of four subswaths, designated

A, B, C, and D (the near edge subswath being A and the far edge being subswath D). During the MARSEN experiment, the APD-10 imaged over incidence angles ranging from approximately 40° to 80°. Figure 1 gives an example of the APD-10 data collected off the island of Sylt.

SAR imagery collected during seven separate missions over two test sites were processed at ERIM. These test sites were two instrumented towers in the German Bight in the North Sea. One tower (Nordsee) was located approximately 80 km west of the German island of Sylt; the other tower (Noordwijk) was situated approximately 10 km west of the Dutch coast. A chart showing the general test site area is shown in Figure 2. Presented in Table 1 are the environmental conditions during the seven SAR data collection flights. Note from the table that during the experiment the waves ranged in period from 5.5 to 8.0 and in significant wave height from 1.0 to 1.2 m. The range of winds present varied

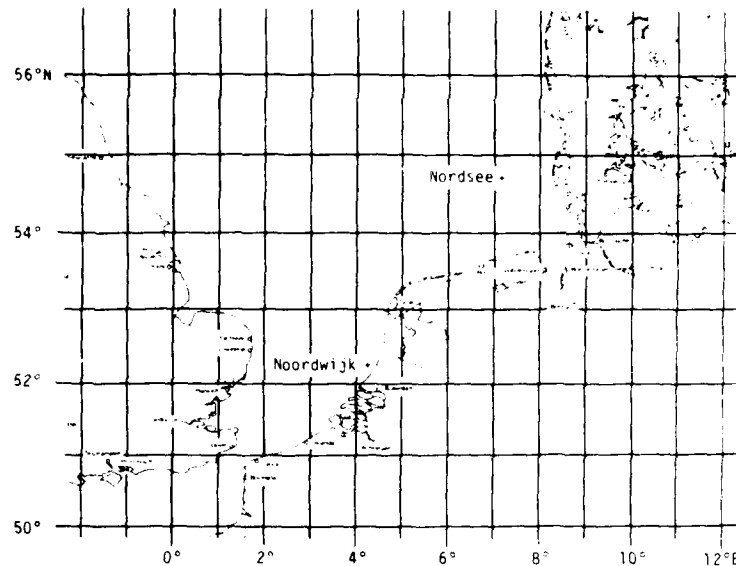


Fig. 2. Chart of the southern portion of the North Sea, showing the location of the Nordsee and Noordwijk research towers.

from 3.5 to 10.3 m/s. Data collected at the Nordsee research tower during lines 7, 10, and 12 are presented in this paper.

The environmental data came from ships and buoys operating near the Nordsee tower. Located at the tower was a wave gauge combined with an electromagnetic current meter (mounted 4 m below the surface) so that the surface elevation and the orbital velocity would be measured at the same time. These data time series were collected by S. Stolte from the 'Forschungsanstalt für Wasserschall und Geophysik der Bundeswehr,' who made them available to us. These time series were then used to calculate the variance spectrum of the surface waves together with the mean direction for a variety of frequencies. This in situ data was extensively compared to the SAR-derived spectral estimates.

### 3. EFFECTS OF SCATTERER MOTIONS

Synthetic aperture radars are sensitive to velocity components present in the imaged scene [Raney, 1971]. Effects of wave motions present in SAR imagery may include (1) image displacement, smearing and loss of focus in the azimuth direction, and (2) loss of focus in the range direction. Some of these effects can be removed during processing of the SAR signal histories by making appropriate adjustments to the processor [Shuchman, 1981]. The effects that cannot be

removed during processing may reduce the detectability of gravity waves and can also influence the wave spectral estimates from the SAR, as discussed in section 4.

Loss of focus in the range direction is due to migration of the phase history of the target (i.e., migration through range cells). This loss of focus is proportional to the range velocity and the integration time and can be corrected by a rotation of the lenses in the optical processor, assuming the range velocity of the target is constant during the integration time.

Loss of focus in the azimuth direction can be caused by a constant velocity in the azimuth direction or a changing velocity (i.e., an acceleration) in the range direction. These effects can be corrected by a change in the azimuth focus setting of the processor, assuming that the azimuth velocity and radial acceleration are constant. Since they are both inversely proportional to the platform velocity, these effects are expected to be less important for the APD-10 than for lower-speed aircraft SAR systems.

The effects of image displacement and smearing are not correctable during processing. An image displacement in the azimuth direction occurs as a result of the range velocity of the target. Since the range velocities of the scatterers on the ocean surface vary with position, the resulting differential displacement (velocity bunching) can cause the wave image

TABLE 1. Summary of Environmental Conditions During MARSEN APD-10 Data Collection Flights

Line	Date	Area	Period, s	Frequency, Hz	Wave Parameters		Wind Conditions	
					Propagation Direction*, true	Height, m	Speed, m/s	Direction†, true
6	September 28	Noordwijk	8.0	0.125	150	1.0	3.5	330
7	September 28	Nordsee	7.5	0.133	135	1.2	7.2	280
8	September 25	Noordwijk	4.7	0.211	130	1.0	11.8	200
10	September 28	Nordsee	7.5	0.133	133	1.2	7.5	270
11	September 27	Noordwijk	5.5	0.182	150	1.0	8.2	290
12	September 27	Nordsee	7.1	0.141	77	1.0	10.3	290
13	September 27	Noordwijk	5.5	0.182	150	1.0	8.2	330

\*Direction waves are propagating towards

†Direction wind is coming from

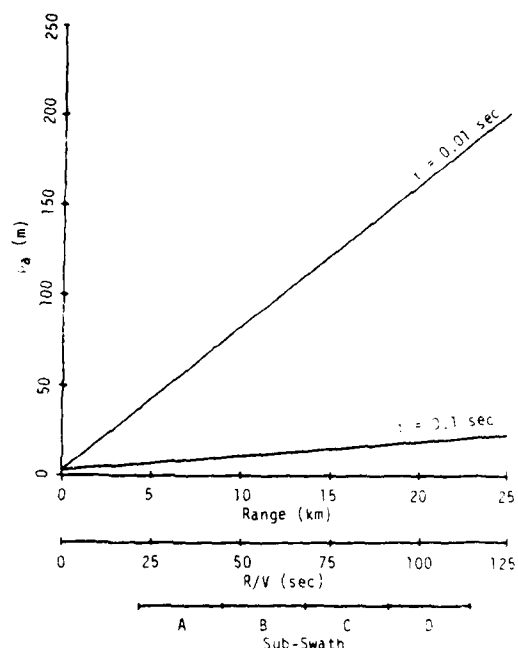


Fig. 3. Azimuth resolution as a function of radar range for the APD-10 system, assuming two values of the coherence time ( $\tau$ ).

to be either enhanced or degraded, depending on the viewing geometry and the SAR system parameters [Alpers *et al.*, 1981]. This effect is probably not extremely important for the APD-10 data collected at MARSEN because of the relatively large incidence angles and the high velocity of the platform.

When a given resolution cell contains scatterers moving at different range velocities, each scatterer is displaced in azimuth by a different amount, resulting in a smearing or loss of resolution in the azimuth direction. This effect is particularly important in breaking seas and is illustrated by the streaked image features appearing prominently in the MAR-

SEN SAR imagery. These observed streaks will be discussed in detail later in this section. This loss of resolution is not recoverable during processing and appears to be the primary limiting factor in the ability of the APD-10 to image ocean waves at MARSEN.

The effect of a range of velocities  $\delta V$ , within a resolution cell is equivalent to the coherence time effect discussed by Raney [1980], with a coherence time ( $\tau$ ) given by

$$\tau = \frac{\lambda}{2\delta V} \quad (1)$$

X band coherence times on the order of  $10^{-2}$  to  $10^{-1}$  s have been measured for conditions similar to those encountered at MARSEN [DeLoor and Hoogchoom, 1982]. The effective azimuthal resolution is given by

$$\delta\lambda = \left[ \left( \frac{\lambda}{2\beta} \right)^2 + \left( \frac{\lambda R}{2V\tau} \right)^2 \right]^{1/2} \quad (2)$$

where  $\lambda$  is the radar wavelength,  $\beta$  is the antenna beamwidth,  $R$  is the range, and  $V$  is the platform velocity. The resolution is plotted versus range for the APD-10 system for both  $\tau = 10^{-2}$  s and  $\tau = 10^{-1}$  s in Figure 3. Note that for  $\tau = 10^{-2}$  s, the resolution becomes equal to the wavelength of the dominant waves at MARSEN (i.e., 90 m) at about the middle of swath B. Thus azimuth-traveling waves of this length would not be imaged in swath B under these conditions. Range-traveling waves are not influenced by this loss of azimuth resolution and are therefore imaged at larger ranges. This effect is in fact observed in the APD-10 imagery, as shown in Figure 4.

#### A. Processor Adjustments

Previous studies using aircraft SAR data have shown that the visibility or detectability of gravity waves is often sensitive to motion compensation adjustments made during the processing of SAR signal histories [Shuchman, 1981; Kasischke and Shuchman, 1981]. An aspect of this study

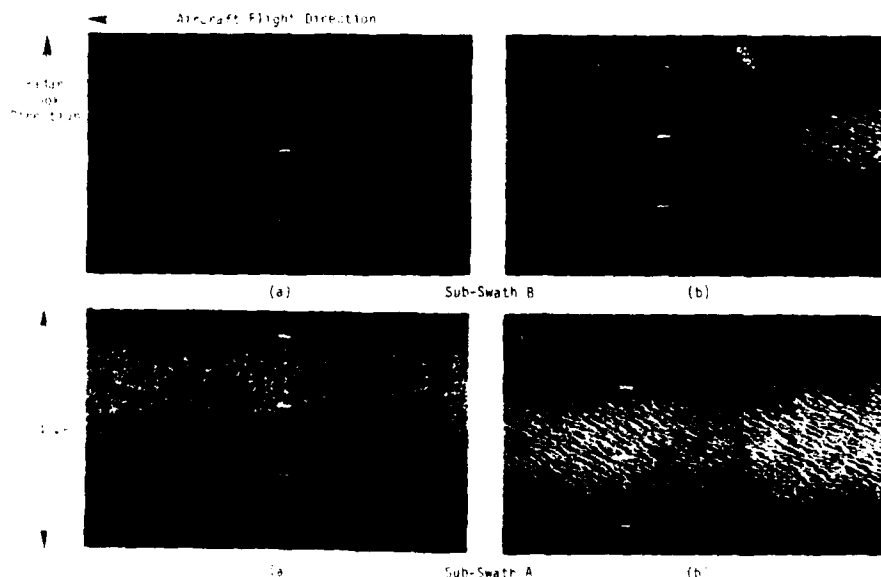


Fig. 4. Examples of APD-10 wave imagery from line 7, subswaths A and B for azimuth-traveling (a), and range-traveling waves (b).



was to determine if SAR data collected by the APD-10 system are also sensitive to these motion compensation adjustments.

Two SAR processor adjustments were evaluated by using the MARSEN APD-10 data set to determine if the SAR wave imagery could be improved. These processor adjustments include (1) an azimuth focus shift to correct for azimuth velocities and range accelerations and (2) a telerotation adjustment to correct for range walk. These two processing adjustments were varied during the optical processing so as to determine the sensitivity of SAR data collected by the APD-10 system to focus adjustment techniques. These focus adjustments are inversely proportional to the velocity of the SAR platform. Since the RF-4 has a high platform velocity ( $\sim 210$  m/s), the adjustments, if necessary, are probably quite small and the effect on SAR imagery quite subtle.

Azimuth focus shifts were used on SAR data for waves traveling perpendicular to the radar line of sight, and range telerotation adjustments were used for waves traveling parallel to the radar line of sight. For intermediate cases a combination azimuth focus shift and range telerotation adjustment was used. For calculation of the azimuth focus shifts, the range walk corrections, and the combination azimuth and range corrections, a family of velocities was used that ranged from a stationary target to twice the phase velocity of the gravity waves present. The direction of wave propagation was not assumed, thus positive and negative velocity corrections were tested. This resulted in nine velocity values being used for each of the enhancement tests. In all, a total of seven passes of imagery from three lines were evaluated.

To measure wave visibility, a crest-to-trough contrast measurement called a peak-to-background ratio (PBR) was used. A PBR is obtained by measuring the peak intensity of the two-dimensional Fourier transform of the SAR wave image and dividing that peak by the lowest intensity at the same wave number [Kavichke and Shuchman, 1981].

Five separate PBR measurements were obtained for each telerotation, focus shift, or combination setting. By running a statistical analysis of variance test [Shuffle, 1959] on the PBR's from a set of focus adjustments, a determination was made as to whether the adjustments resulted in significantly higher PBR's, hence improved wave visibility on the SAR imagery.

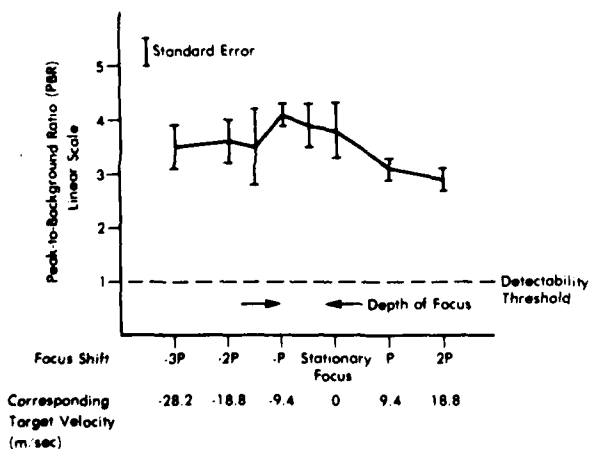


Fig. 5. Wave peak-to-background ratio as a function of azimuth focus shifts for line 7, pass 4 data.

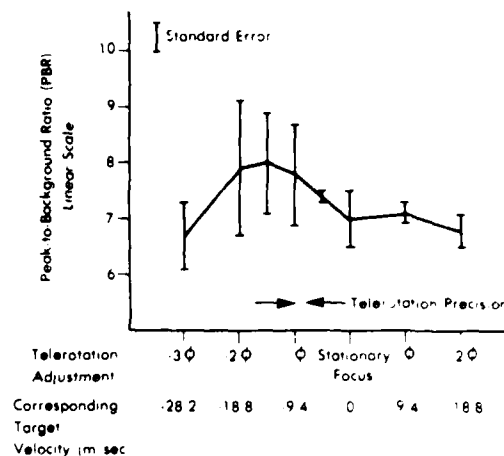


Fig. 6. Wave peak-to-background ratio as a function of range telerotation adjustments for line 7, pass 2 data.

Figure 5 represents a graph of the PBR versus azimuth focus setting for line 7, pass 4 data. Figure 6 is a similar graph, which shows the relationship of PBR to range focus adjustment. The data utilized in this example is from line 7, pass 2. The results of the azimuth focus shift and range telerotation adjustments indicated the APD-10 A-band SAR imagery was relatively insensitive to azimuth focus shifts and somewhat sensitive to range telerotation adjustments. This result is due to the high platform velocity of the F-4 aircraft (210 m/s). In most cases the distribution of the nine velocity settings versus PBR (on each of the three types of enhancement) gave an indication as to which direction the waves were traveling because the curve was skewed in that direction.

### B. Azimuth Streaking

The APD-10 SAR data collected over both shallow and deep water shows numerous bright streaks in the along-track or azimuth direction. These streaks become longer and more apparent as the range or incidence angle increases, as shown in Figure 7, and frequently obliterate the wave images in the further subswaths. They are apparently related to the 'sea spike' phenomenon noted in conventional radar observations of the ocean at large incidence angles [Long, 1974; Lewis and Olin, 1980]. These features appear more prominently at far range because the Bragg scattering background falls rapidly with increasing incidence angle while the return from the streaks remains nearly constant. An analysis of this phenomenon is presented in the companion paper [L'Ecuyer and Shuchman, 1983], and the implications of this streaking for the wave imaging process are described in this section and section 4B.

The effects of these features on the SAR image spectrum is to add a background component that has a spectral shape determined by the length, or resolution, of the streaks. If the streaking is not so severe as to completely obliterate the wave image, this background component can be removed by the methods discussed in the following section. However, when the streak lengths become comparable to the azimuth component of the wavelength, the wave information is effectively lost. This streaking, along with the loss of azimuth resolution of the wave component itself, limits the range of incidence angles over which wave imagery can be

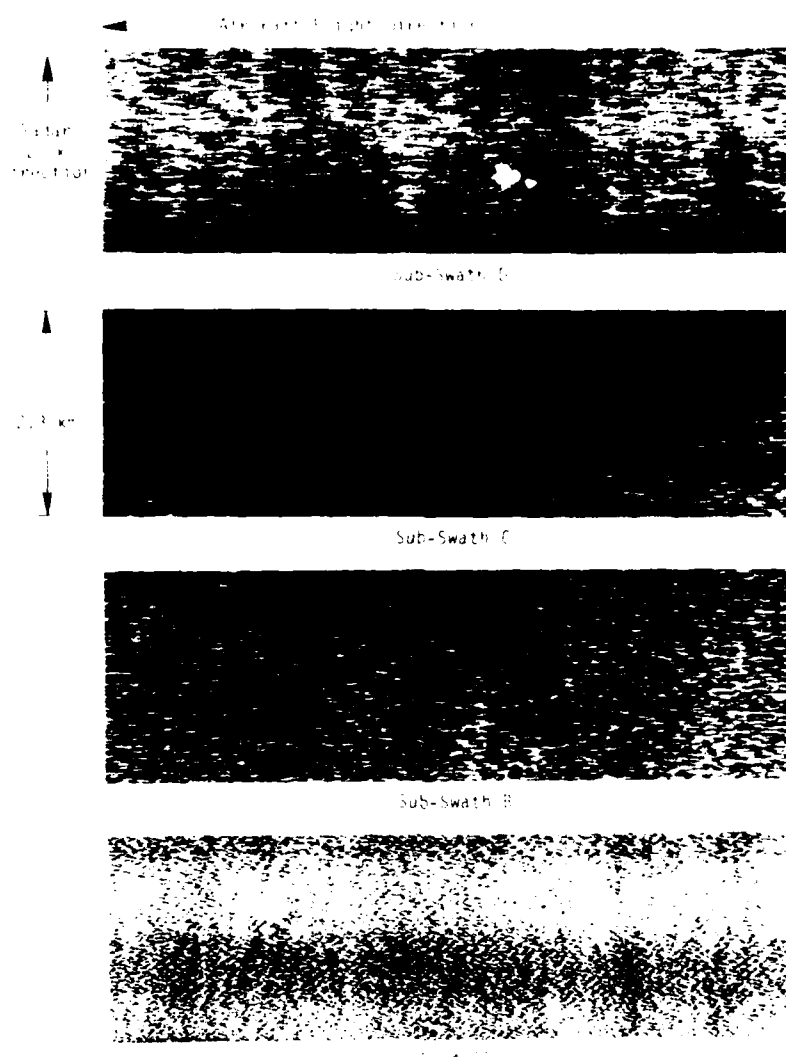


Fig. 7. Optically processed APD-10 imagery for a portion of all four subswaths for line 12, pass 3. Note the streak length increases with range.

obtained, as discussed in section 4B, below. The relationship between the characteristics of the streaks and the SAR modulation transfer function for ocean waves is currently under investigation.

In addition to their negative impact on the wave imaging process, these features may be useful indicators of the sea state. A comparison of the frequency or number density of the streaks with in situ measurements of wave breaking [Longuet-Higgins and Smith, 1983] is under way and will be reported in the near future.

#### 4. SAR VS. IN SITU SPECTRAL COMPARISONS

This section of the paper compares the SAR-derived spectral estimates with in situ oceanographic measurements. The surface-based spectra were obtained by processing data collected by a wave gauge and current meter which were operating during the SAR overflights at the Nordsee Tower. Recall that the SAR-derived spectra are in wave number space, while the surface-based spectra are given in frequency. Prior to making any comparisons between the two, one

estimate has to be converted to the other's domain. For this study the surface-measured spectral estimates were converted to wave number space assuming a dispersion relationship of the form

$$\omega = \left( \frac{g}{\lambda} \tanh kd \right)^{1/2} \quad (3)$$

appropriate for intermediate water depths where  $\omega$  is the wave frequency,  $g$  is the acceleration of gravity,  $\lambda$  is the wavelength,  $k$  is the wave number ( $2\pi/\lambda$ ), and  $d$  is the water depth (assumed to be 30 m).

The SAR data used in this study were collected during lines 7, 10, and 12. These SAR signal films were optically processed into image film by using the ERIM Precision Optical Processor (POP). These image films were digitized with 3-m samples by the ERIM Hybrid Image Processing Facility (HIPI), described by Ausherman *et al.* [1975]. Digital spectral estimates are produced from 512 × 512 pixel (1.5 × 1.5 km) subsets of these digital data. Prior to spectra

TABLE 2. SAR Versus Sea Truth Comparisons

Line	Pass	Aircraft Heading, °true	Surface Measured*			SAR Derived		Observed Differences	
			f, Hz	$\lambda$ , m	$\theta$ , true	$\lambda$ , m	$\theta$ , true	$\lambda$ , m	$\theta$ , true
7	Syll	297	0.133	86	135	86	133	0	2
	1	283				92	131	-6	4
	2	056				60	109	26	26
	3	191				86	131	0	4
	4	327				86	130	0	5
10	5	102			109	147	-23	-12	
	1	283	0.133	86	133	99	148	-13	-15
	2	056				91	129	-5	4
	3	191				103	129	-17	4
	4	327				109	152	-23	-19
5	102	130				152	-44	-19	
12	Syll	297	0.141	78	77	75	52	3	25
	1	283				75	43	3	34
	2	056				75	78	3	-1
	3	191				89	61	-11	16
Mean								7.6	4.1
Standard Deviation								16.6	16.8

\*The surface-measured wavelengths were derived assuming a water depth of 30 m.

generation, these subsets undergo corrections for slant range distortion and to remove long-period variations of intensity in both range and azimuth. The data is also smoothed by using a  $4 \times 4$  pixel weighted filter, which reduces the coherent speckle found in the imagery and also reduces the number of samples by a factor of 2 in each dimension. Two-dimensional fast Fourier transforms (FFT's) were performed on each  $256 \times 256$  cell subsection to yield raw directional wave number spectra with a Nyquist wave number of  $0.52 \text{ m}^{-1}$ . The raw spectra were smoothed by replacing each value with the average of the surrounding  $5 \times 5$  cell. The approximate number of degrees of freedom for the resulting spectrum is 142 [Kinsman, 1965], and the 99% confidence limits are  $\pm 1.5 \text{ dB}$  [Jenkins and Watts, 1968].

The surface measurements used for comparison with the SAR were obtained at the Nordsee tower, coincident with the SAR flights. These measurements were made by a wave gauge coupled with an electromagnetic current meter so that simultaneous measurement of surface elevation and orbital velocity could be made with a sampling rate of 2 Hz. From these time series we were able to calculate the variance spectrum of the surface waves as well as the mean direction for 128 intervals equally spaced from 0 to 1 Hz, following the method of Forristall *et al.* [1978]. Ten of these spectra were averaged to increase the degrees of freedom to about 30.

Presented in Table 2 is a comparison of the dominant SAR-derived (subswath A) and surface-measured spectral estimates for lines 7, 10, and 12. Line 12 was flown on September 27 from 0840 to 0917 GMT. The surface wind speed during this flight was approximately 10 m/s, from a direction of  $290^\circ$ . The surface-measured wave spectrum had a peak frequency of 0.141 Hz propagating at  $77^\circ$ , which corresponded to a fully developed wind-generated sea. Because of the recent passage of a storm, the difference between surface wind and wave directions during the flight was  $33^\circ$ , which results in a change of wave direction with frequency so that the higher frequencies become more aligned with the wind [Hasselmann *et al.*, 1980; Günther *et al.*, 1981]. Lines 10 and 7 were flown on September 28 from 0938 to 1035 and 1121 to 1222 GMT, respectively. The

surface conditions during lines 10 and 7 were very similar, with surface wind speeds and directions of 7.5 and 7.2 m/s and  $270^\circ$  and  $280^\circ$ , respectively. The surface wave conditions were also almost identical, with each having a peak frequency of 0.133 Hz and directions of  $133^\circ$  and  $135^\circ$  for lines 10 and 7, respectively. This wave frequency is well beneath the Pierson-Moskowitz frequency for the prevailing wind speed. Upon examination of the surface-measured spectrum and the wind conditions prior to the flights, it was concluded that these conditions represent the typical situation of a wave spectrum after a recent decrease of the local wind speed.

From Table 2 it appears that the APD-10 SAR operating at MARSEN was able to detect ocean gravity waves with an accuracy of 16.6 m in length and 16.8° in direction once the mean biases were removed. Consistent with past studies the SAR-derived waves were slightly longer than the in situ measurements. The question of SAR-derived spectral estimate accuracy as a function of radar look direction will be discussed in more detail below.

#### A. Wave Detectability vs. Radar Look Direction

As previously mentioned, multisided SAR flight patterns were flown during MARSEN. An example of this pattern is shown in Figure 8 for line 7. This figure is a diagram of the

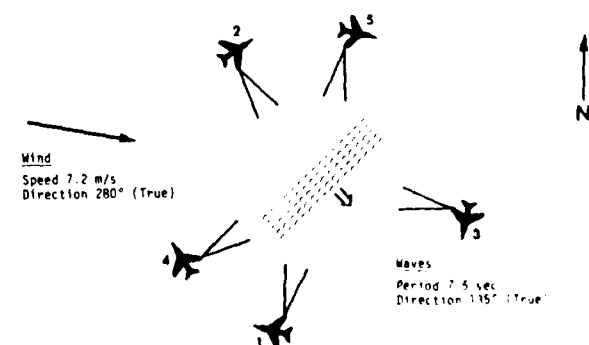


Fig. 8. SAR collection geometry for line 7, passes 1-5. Also shown are the surface environmental conditions during the data collection.

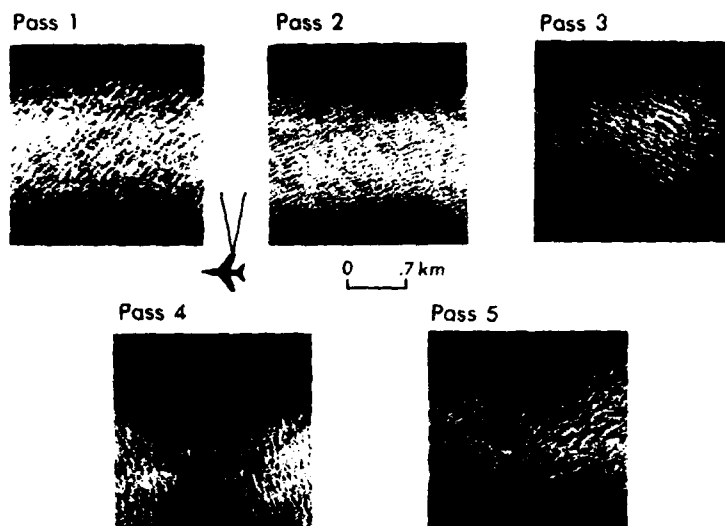


Fig. 9. Optically processed APD-10 gravity wave imagery from subswath A for line 7, passes 1-5.

collection geometry for five passes from line 7. Figure 9 shows imagery for a section from each of these five passes. Figure 10 presents two-dimensional contour plots of the FFT's produced for each of the passes described in the previous section. Each contour on these plots represents a 3-dB (50%) decrease in spectral intensity from the previous one. On the plots the azimuth direction is the horizontal axis,

and the range direction is the vertical axis. The SAR-derived dominant wave is represented by the highest contour on these plots.

Past studies in SAR imaging of ocean waves have shown that range-traveling waves are more clearly imaged than azimuth-traveling waves [Shemdin *et al.*, 1978]. It should be noted that the waves in these past studies consisted of swell,

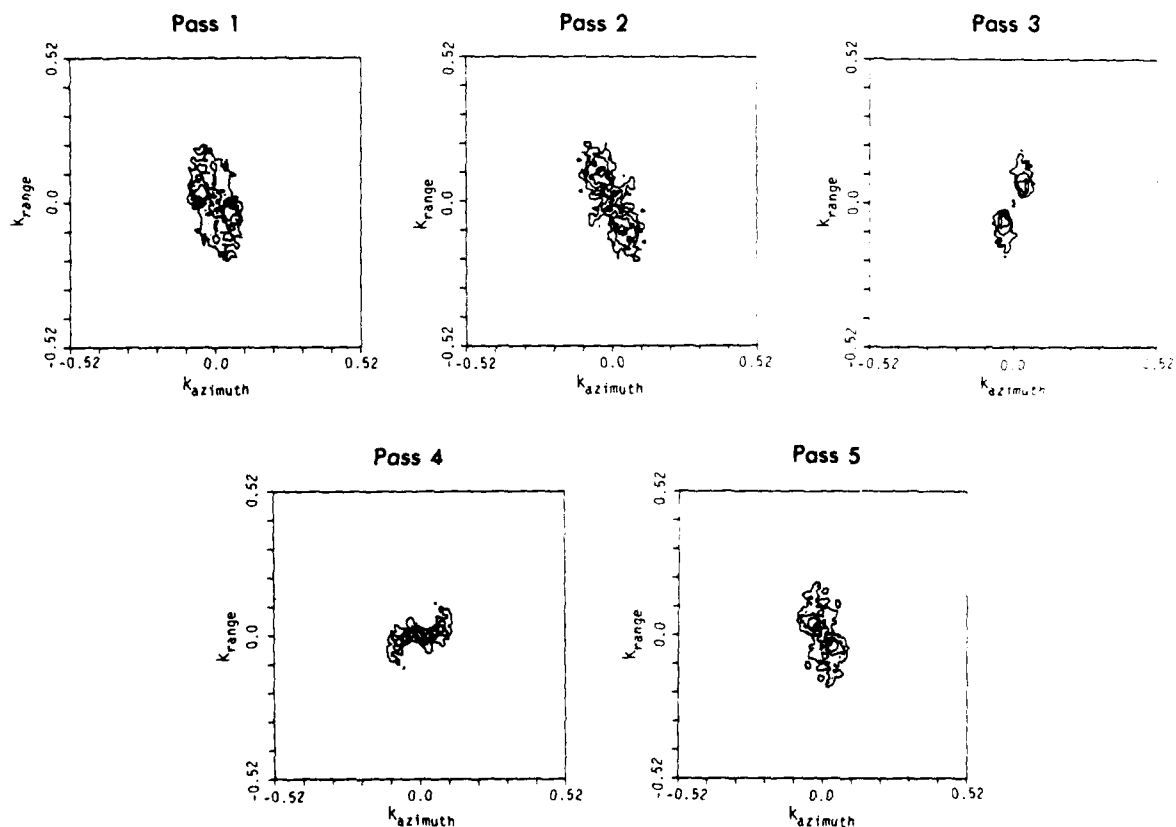


Fig. 10. Two-dimensional contour plots of the fast Fourier transforms (FFT's) produced from the digitized imagery shown in Figure 9.

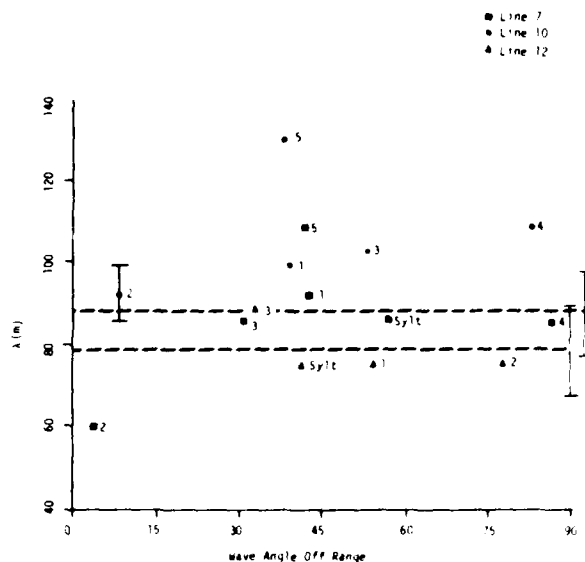


Fig. 11. SAR-derived wavelength estimates ( $\lambda$ ) versus wave angle off range for lines 7, 10, and 12. Included on the plot as dashed lines are the wavelength estimates based on surface measurements. The error bars indicate the accuracy for the surface measurements and a single pass of SAR data. These error bars were based on the resolution of the spectra from both instruments.

not wind-generated waves as were present at MARSEN. The accuracy of SAR-derived spectral estimates as a function of the radar look direction, however, has not been rigorously studied. To address this question, the SAR-derived spectral estimates summarized in Table 2 were plotted versus the relative look angle from purely range-traveling waves, based on surface measurements for both wavelength and direction. These plots are shown in Figures 11 and 12, respectively. Also shown on the figures are the surface-measured waves for each line. Note that these plots

ignore up or downwave differences. By displaying the data in this coordinate system, it was hoped that any systematic or periodic bias in the SAR-derived spectral estimates caused by changing look direction could be ascertained. Examination of Figure 11 shows that the wavelength estimates from the SAR appear to be randomly scattered as a function of radar look direction. With the exception of four points, the wavelength estimates are all within 20 m of the surface-measured values. It is interesting to note the variability between lines 7 and 10, which were flown with nearly identical geometries. This suggests that the variability of the SAR wavelength estimate at a given look direction is on the order of the variability of SAR-derived wavelength estimates as a function of look angle.

Examination of Figure 12 shows similar results to Figure 11, that is, the variability between the SAR-derived wave directions for lines 7 and 10 is on the order of the variability of the directional estimates across the whole range of angles. The line 12 estimates shown on Figure 12 do not appear very accurate. Three more range-traveling passes show a monotonic increase in directional difference to the surface-measured values with increasing angle off range, but the azimuth-traveling pass is very close to the surface-measured value.

Several points should be made about Figures 11 and 12. We have assumed the aircraft headings, as recorded in the flight log, to be correct. Past experience has shown this assumption to be a possible source of error; if that is true in this case, the results of Figure 12 will change. We have also assumed a constant water depth of 30 m; if not valid, this assumption would alter the surface-derived values in Figure 11 as a function of pass location (i.e., water depth). Finally, we have based this analysis on a limited set of passes with somewhat random look angles with respect to wave propagation direction. To adequately perform this sort of analysis, wave imagery should be available with 10° intervals from purely range-traveling to purely azimuth-traveling waves.

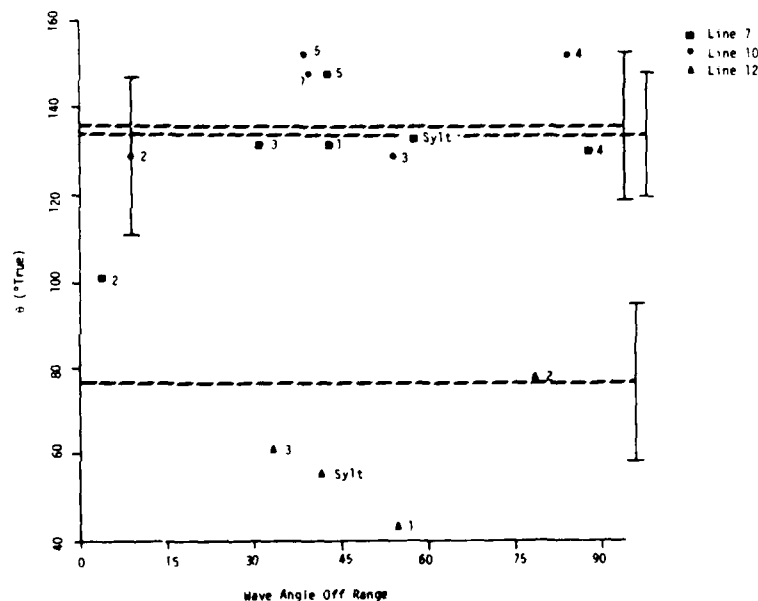


Fig. 12. SAR-derived directional estimates ( $\theta$ ) versus wave angle off range for lines 7, 10, and 12. Included on the plot as dashed lines are the directional estimates based on surface measurements. The error bars indicate the directional spread of the surface measurements and the average 3-dB contour width of the SAR-derived spectra.

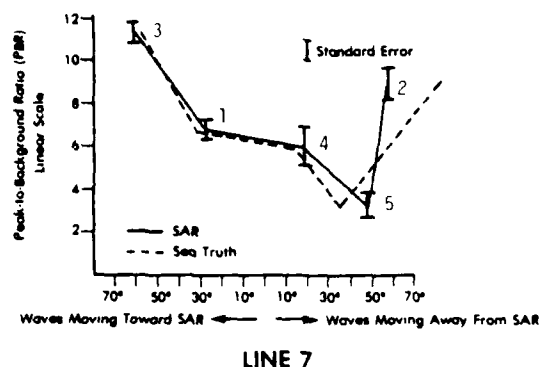


Fig. 13. Wave peak-to-background ratio versus radar look direction for line 7, passes 1-5. Refer to Figure 8 for the collection geometry and Figure 9 for representative imagery from each pass.

Ideally, this data would be gathered over a full 360°. This type of data set would be useful in evaluating and developing SAR wave imaging theories. Recent examination of Marine-land SAR data, where more data points were available than MARSEN, shows that azimuth-traveling waves are consistently imaged as being longer than range-traveling waves [Shuchman et al., 1983].

The sensitivity of wave visibility with respect to radar look direction was evaluated by using the PBR method described in section 3A. The PBR's from the enhancement tests consistently showed highest wave contrast resulting from SAR images of range-traveling waves and lower values resulting from azimuth waves. It has been previously reported [Teleki et al., 1978] that SAR's, particularly when operating at L band, will image range-traveling waves more clearly than azimuth waves. Using line 7 data, PBR measurements were obtained from subswath A in the same general location around the Nordsee Tower for each of the five passes. Figure 13 shows a graph of the PBR value obtained versus the orientation of the waves with respect to the radar look direction (see Figure 8 for the collection geometry). Note that two curves are presented on the graph: one indicates PBR versus the sea truth direction, while the other is PBR versus the radar-derived value. A zero-degree value on the graph indicates azimuth-traveling waves. Analysis of Figure 13 indicates that (1) SAR images range-traveling waves more clearly than azimuth-traveling waves, (2) SAR images waves more clearly when they are moving toward the SAR than when they are moving away from the SAR (i.e., pass 1 versus 5 or 2 versus 3), and (3) the APD-10 X band SAR imaged gravity waves during line 7, regardless of radar look direction.

#### B. Wave Detectability vs. Incidence Angle

The effect of varying incidence angle on the detection of gravity waves was also evaluated by using this APD-10 data set. Recall that the APD-10 system collects an 18.5-km swath in four subswaths where the incidence angle varies from 43° to 82°. Figure 14 shows contour plots of FFT's obtained from each of the four subswaths for pass 3 from line 12. The corresponding imagery was previously shown as Figure 7. It is apparent that an azimuth-oriented artifact becomes more pronounced as the incidence angle or range to the ocean surface increases (i.e., from subswath A to subswath D). In fact the spectra in swaths C and D are

completely dominated by this artifact. Over this same interval, the gravity waves of interest become less visible, and the azimuth-oriented streaks can lead to a perceived range-traveling wave. Thus, because of these streaks on the MARSEN APD-10 imagery and the relative fading (decreased contrast) of imaged gravity waves with range, accurate wave estimates can only be extracted from subswath A.

#### C. Modulation Transfer Function

As part of the MARSEN data analysis an attempt was made to establish an experimental relationship between the variance spectrum of the radar image  $S(k)$  and the wave height spectrum  $W(k)$ . This relationship is most likely nonlinear, in the sense that it is dependent on the total shape of  $W(k)$  instead of the value at one single  $k$  value. However, it may be possible to describe the spectral shape by a small set of characteristic properties (for example, the averaged frequency, direction, and spectral width) and use these as parameters in the mathematical description of the mapping from  $W(k)$  into  $S(k)$  or vice versa.

The spectrum of the SAR image includes both the desired wave information as well as contributions caused by SAR system noise, speckle effects, and imaged point scatterers. Thus, in order to provide a more meaningful comparison with in situ measured wave height spectra, the SAR image spectra were partially corrected by subtracting off the components caused by speckle, system noise, and imaged point scatterers. The sum of these three components was estimated by examining the spectrum in the wave number quadrants not containing the dominant wave and by assuming symmetry in the background spectrum with respect to the  $k_x$  and  $k_y$  axes. That is, the corrected image spectrum is given by

$$S(k_x, k_y) = I_m(k_x, k_y) - I_b(k_x, k_y) \quad (4)$$

where  $I_m(k_x, k_y)$  is the (total) measured spectrum, and  $I_b(k_x, k_y)$  is the background spectrum estimated from  $I_m(-k_x, k_y)$  or

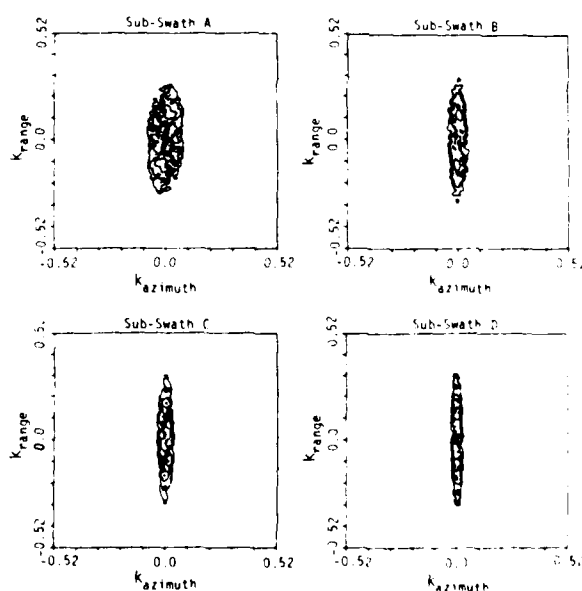


Fig. 14. Two-dimensional contour plots of the fast Fourier transforms (FFT's) produced for all four subswaths from Line 12 Pass 3 data. Refer to Figure 7 for the corresponding optically processed imagery.

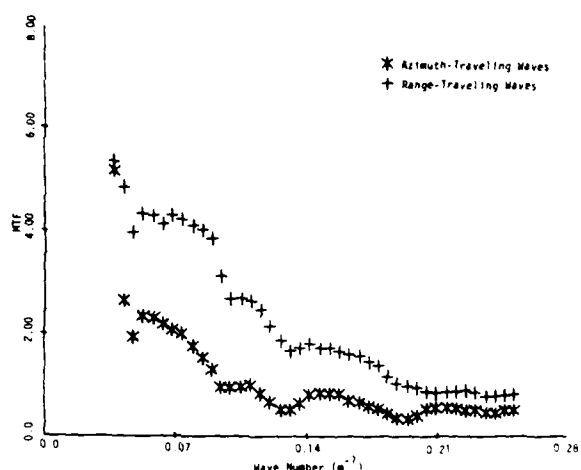


Fig. 15. One-dimensional modulation transfer function ( $m$ ) as a function of wave number for a nearly azimuth-traveling and a nearly range-traveling wave.

$I_m(k_r, -k_r)$ . This corrected spectrum may be written in polar form (i.e.,  $S(k, \theta)$ ) and then converted into a one-dimensional spectrum

$$S(k) = k \int_0^{2\pi} S(k, \theta) d\theta \quad (5)$$

using the coordinate transformation

$$k = (k_r^2 + k_t^2)^{1/2} \quad (6)$$

and

$$\theta = \tan^{-1}(k_t/k_r) \quad (7)$$

and this quantity was then compared with the in situ measured wave height spectrum  $W(k)$  by calculating the modulation transfer function.

The terms 'modulation transfer function,' 'mapping transfer function,' and just 'transfer function' are used somewhat ambiguously in the radio-oceanographic literature to denote the relationship between the ocean wave information measured by a radar and the physical surface descriptions usually measured by conventional in situ instruments.

In the linear modulation theory developed by Keller and Wright [1975] and Alpers and Hasselmann [1978], the radar return for a monochromatic ocean wave is written as

$$P = P_0 \left[ 1 + \frac{mV_0}{C} \cos(\Omega t + \phi) \right] \quad (8)$$

or

$$P = P_0 [1 + R \zeta_0 \cos(\Omega t + \phi)] \quad (9)$$

where  $m$  is the modulation transfer function defined by Keller and Wright,  $R$  is the modulation transfer function defined by Alpers and Hasselmann,  $V_0$  is the maximum orbital velocity of the wave,  $C$  is the phase velocity,  $\Omega$  is the angular frequency, and  $\zeta_0$  is the amplitude of the wave. Thus, these two modulation transfer functions are related by

$$m = (R/k) \quad (10)$$

where  $k$  is the wave number of the wave.

When the sea surface is described in terms of a wave

height spectrum instead of a monochromatic wave, the modulation transfer function describes the relationship between the wave height spectrum and the signal spectrum measured by a radar. According to Alpers *et al.* [1981], the ratio of the SAR image spectrum  $S(k_r, k_t)$  to the wave height spectrum  $W(k_r, k_t)$  is equal to the square of the modulation transfer function, i.e.,

$$R^2 = \frac{S(k_r, k_t)}{W(k_r, k_t)} \quad (11)$$

where  $R$  includes a velocity bunching component that is assumed to be linear. However, in his Monte Carlo modeling work, W. Alpers (personal communication, 1982) appears to use a different definition for the modulation transfer function and refers to the quantity  $R$  defined by (11) as a 'spectral mapping function.'

For the comparisons presented in this paper the definitions represented by (10) and (11) are combined to yield the one-dimensional modulation transfer function

$$m = \frac{1}{kI} \left[ \frac{S(k)}{W(k)} \right]^{1/2} \quad (12)$$

where  $I$  is the mean signal intensity. This function is plotted versus wave number in Figure 15 for two cases, including a nearly azimuth-traveling wave and a nearly range-traveling case. Note that the modulation transfer function is smaller and falls off more rapidly with  $k$  for the azimuth-traveling wave than for the range-traveling wave. This is a direct consequence of the lower inherent modulation for azimuth-traveling waves and the degraded resolution in the azimuth direction as a result of motion effects, and it agrees, at least qualitatively, with theoretical prediction.

## 5. SUMMARY

This analysis has indicated that the APD-10 SAR system imaged the dominant gravity wave component present during the MARSEN experiment, although only the first, or near-range, subswath of the APD-10 system produces reliable wave estimates. Dominant wavelength and directional information was obtainable independent of the radar look direction, although range-traveling waves are more clearly visible on the imagery than azimuth-traveling waves, based on the wave contrast criteria used in this study.

The MARSEN X-band SAR data set, although limited, offers a unique opportunity to study the effect of radar look direction on the detectability of wind-generated waves and the accuracy of the SAR-derived wavelength and direction. Past studies in SAR imaging of ocean waves, such as Marineland [Shemdin *et al.*, 1978], GOASEX [Gonzalez *et al.*, 1979] and JASIN [Vesecky *et al.*, 1982], have generally shown that dominant range-traveling swell is more frequently imaged than azimuth-traveling swell and that the dominant gravity wavelength and direction is more accurately estimated for range-traveling than azimuth-traveling waves. Our MARSEN X-band analysis has indicated that the accuracy of SAR-derived dominant wavelength and directional estimates is independent of radar look direction, although range-traveling waves have higher peak-to-background ratios than azimuth-traveling waves. This is probably because X-band SAR data collected by a higher-velocity aircraft was used at MARSEN than at previous experiments, thus minimizing motion effects. However, the reader is cautioned to note

differences in environmental conditions as well as SAR system parameters used in these experiments.

The analysis has also indicated that the APD-10 system is relatively insensitive to wave image enhancements performed during the SAR processing. The enhancement adjustments, which are inversely proportional to the SAR platform velocity, compensate for motion of the ocean waves during the SAR observation time. Although SAR data from the APD-10 system is insensitive to the wave motion correction algorithms, numerous motion artifacts are visible on the data. These artifacts, which appear as azimuth-oriented streaks on the imagery, are more pronounced in the far subswaths. They appear to be caused by velocity variations (or coherence time) of the ocean scatterers. One possible source for these image artifacts is breaking waves.

The extraction of information on the wave height spectrum from the SAR image has also been investigated. The shape of the SAR-derived spectrum of the wave field is different from the shape of the wave spectrum obtained from surface measurements. A transfer function to relate SAR-derived spectra to in situ measurements has been developed. The transfer function is smaller for azimuth-traveling waves than for range-traveling waves, and it falls off more rapidly with wave number for the azimuth-traveling wave. This is a consequence of the smaller inherent modulation for azimuth-traveling waves and the degraded resolution in the azimuth direction as a result of motion effects, and it agrees, at least qualitatively, with theoretical predictions.

**Acknowledgments.** The ERIM portion of the work presented in this paper was performed under the sponsorship of the Office of Naval Research contracts N00014-76-C-1048 and N00014-81-C-0692. The technical monitor for this program was Hans Dolezalek. We thank Jack Losee and Alex Klooster of ERIM for processing the SAR data and generating the digital tapes. It is a pleasure for us to express our gratitude to a group of people involved in making this work possible, especially the two MARSEN coordinators, K. Hasselmann and O. Shemdin, and the teams from the American Air Force and the German Air Force who very generously cooperated to collect this data set.

#### REFERENCES

- Alpers, W., and K. Hasselmann. The two-frequency technique for measuring ocean wave spectra from an airplane or satellite. *Boundary-Layer Meteorol.*, **13**, 215-230, 1978.
- Alpers, W. E., D. B. Ross, and C. L. Rufenach. On the detectability of ocean surface waves by real and synthetic aperture radar. *J. Geophys. Res.*, **86**, 6481-6498, 1981.
- Ausherman, D. A., W. D. Hall, J. N. Latta, and J. S. Zelenka. Radar data processing and exploitation facility, paper presented at IEEE International Radar Conference, Washington, D.C., April 21-23, 1975.
- Brown, W. M., and L. Porcello. An introduction to synthetic aperture radar. *IEEE Spectrum*, **6**, 52-66, 1969.
- DeLoor, G. P., and P. Hoozeboom. Radar backscatter measurements from platform Noordwijk in the North Sea. *IEEE Oceanic Eng.*, **OE-7**, 15-20, 1982.
- Forristall, G. Z., E. G. Ward, V. J. Cardone, and L. E. Borgmann. The directional spectra and kinematics of surface gravity waves in Tropical Storm Delia. *J. Phys. Oceanogr.*, **8**, 888-909, 1978.
- Gonzalez, F. I., R. C. Beal, W. E. Brown, Jr., D. S. DeLeonibus, J. F. R. Gower, D. Lichen, D. B. Ross, C. L. Rufenach, J. W. Sherman, III, and R. A. Shuchman. Seasat synthetic aperture radar: Ocean wave detection capabilities. *Science*, **204**, 1418-1421, 1979.
- Gunther, H., W. Rosenthal, and M. Dunckel. The response of surface gravity waves to changing wind direction. *J. Phys. Oceanogr.*, **11**, 718-728, 1981.
- Harger, R. O. *Synthetic Aperture Radar Systems*, 240 pp., Academic, N.Y., 1970.
- Hasselmann, D. E., M. Dunckel, and J. A. Ewing. Directional wave spectra observed during JONSWAP 1973. *J. Phys. Oceanogr.*, **10**, 1264-1280, 1980.
- Jenkins, A. M., and D. G. Watts. *Spectral Analysis and Its Applications*, 525 pp., Holden-Day, San Francisco, Calif., 1968.
- Kasischke, E. S., and R. A. Shuchman. The use of wave contrast measurements in the evaluation of SAR gravity wave models. *Proc. 15th Int. Symp. Remote Sensing Environ.*, **3**, 1187-1206, 1981.
- Keller, W. C., and J. W. Wright. Microwave scattering and streaming of wind-generated waves. *Radio Sci.*, **10**, 139-147, 1975.
- Kinsman, B. *Wind Waves—Their Generation and Propagation on the Ocean Surface*, 676 pp., Prentice-Hall, Englewood Cliffs, N.J., 1965.
- Kozma, A., E. N. Leith, and N. G. Massey. Tilted plane optical processor. *Appl. Opt.*, **11**, 1766-1777, 1972.
- Lewis, B. L., and I. D. Olin. Experimental study and theoretical model of high-resolution backscatter from the sea. *Radio Sci.*, **15**, 815-828, 1980.
- Long, M. W. On a two-scatter theory of sea echo. *IEEE Trans. Antennas Propagat.*, **AP-22**, 667-672, 1974.
- Longuet-Higgins, M. S., and M. D. Smith. Measurement of breaking waves by a surface jump meter. *J. Geophys. Res.*, this issue, 1983.
- Lyzenga, D. R., and R. A. Shuchman. Analysis of scatterer motion effects in MARSEN A-band SAR imagery. *J. Geophys. Res.*, this issue, 1983.
- McLeish, W., D. Ross, R. A. Shuchman, P. G. Teleki, S. V. Hsiao, O. H. Shemdin, and W. E. Brown, Jr. Synthetic aperture radar imaging of ocean waves—comparison with wave measurements. *J. Geophys. Res.*, **85(C9)**, 5003-5011, 1980.
- Pawka, S. S., S. V. Hsiao, O. H. Shemdin, and O. T. Inman. Comparison between wave-directional spectra from SAR and pressure sensor arrays. *J. Geophys. Res.*, **85(C9)**, 4987-4995, 1980.
- Raney, R. K. Synthetic aperture imaging radar and moving targets. *IEEE Trans. Aerosp. Electr. Syst.*, **AE-7**, 499-505, 1971.
- Raney, R. K. SAR response to partially coherent phenomena. *IEEE Trans. Antennas Propagat.*, **AP-28**, 777-787, 1980.
- Sheffe, H. *The Analysis of Variance*, 477 pp., John Wiley, N.Y., 1959.
- Shemdin, O. H., W. E. Brown, Jr., F. G. Staudhammer, R. Shuchman, R. Rawson, J. Zelenka, D. B. Ross, W. McLeish, and R. A. Berles. Comparison of in situ and remotely sensed ocean waves off Marineland, Florida. *Boundary-Layer Meteorol.*, **13**, 193-203, 1978.
- Shuchman, R. A. Processing synthetic aperture radar data of ocean waves, in *Oceanography from Space*, edited by J. F. R. Gower, pp. 477-496, Plenum, New York, 1981.
- Shuchman, R. A., J. D. Lyden, and D. R. Lyzenga. Estimates of ocean wavelength and direction from X- and I-band synthetic aperture radar data collected during the Marineland experiment. *IEEE J. Oceanic Eng.*, in press, 1982.
- Teleki, P. G., R. A. Shuchman, W. E. Brown, Jr., W. McLeish, D. Ross, and M. Mattie. Ocean wave detection and direction measurements with microwave radars. *Oceans*, **78**, 639-648, 1978.
- Vesecky, J. F., H. M. Assal, R. H. Stewart, R. A. Shuchman, E. S. Kasischke, and J. D. Lyden. Seasat-SAR observations of surface waves, large scale surface features and ships during the JASIN experiment. *1982 Int. Geosci. Remote Sensing Symp. Dig.*, **1**, 1.1-1.6, 1982.
- Wright, J. W., W. J. Plant, W. C. Keller, and W. I. Jones. Ocean wave radar modulation transfer functions from the West Coast experiment. *J. Geophys. Res.*, **85**, 4957-4966, 1980.

(Received August 2, 1982;  
revised January 12, 1983;  
accepted January 12, 1983.)



GEOSAT-SAR OBSERVATIONS OF SURFACE WAVES, LARGE-SCALE WAVE PATTERNS  
AND SHIPS DURING THE CASIN EXPERIMENT

J. F. Vesecky, and H. M. Issa  
Stanford Center for Radar Astronomy, Stanford, CA 94305

R. W. Stewart  
 Scripps Institution of Oceanography, La Jolla, CA 92037  
 Jet Propulsion Laboratory, Pasadena, CA 91103

R. W. Shuchman, E. S. Kasitskaya and J. C. Yden  
Environmental Research Institute of Michigan, Ann Arbor, MI 48106

the SEASAT satellite system, using an onboard 23 cm wavelength synthetic aperture radar (SAR), collected ~25 to 40 m resolution radar images of land and ocean. We summarize results from 18 SEASAT SAR passes during the Joint Air-Sea Interaction (JASIN) experiment conducted off the west coast of Scotland in summer 1978. Gravity waves of length ~20 to 200 m are often seen in SAR images; however, existing waves are not always seen. We find that wavelength, SAR resolution and wind velocity are important criteria for determining wave visibility. Buoy measurements of  $U_{10}$  correlate with peak signal to noise ratio in Fourier transforms of SAR images. Although there are significant differences, SAR estimates of omnidirectional wavelength spectra are in rough agreement with buoy spectra. Features resampling internal wave patterns are almost always found over seamounts and at the edge of the continental shelf. Ships and their wakes are often, but not always, detectable in SEASAT SAR images.

Keywords: Radio Oceanography, Remote Sensing,  
Gravity Waves, Ships, Waves

reflecting properties of the ocean surface are modified by surface motion effects. Since the dielectric properties of the ocean surface are relatively uniform, variations in surface roughness are primarily responsible for changes in the radar backscatter strength. In particular, resonant ocean waves with  $\lambda \sim 30$  cm interacting with the 30 cm radar waves via a Bragg scatter mechanism produce the dominant radar echo. Because the



Fig. 1. Inter-branch interaction with the  
near and distant branch systems in the  
swaths and sections of main and sub-  
arboresis. A - main branch and part of  
C2, C3, and C4; B - main branch and  
C2, C3, and C4; C - main branch and  
C2, C3, and C4.

## 1. INTRODUCTION

The synthetic aperture radar (SAR) carried aboard the SEASAT satellite collected radar images of the ocean in 100 km wide swaths ranging in length from about 300 to 3000 km. During the JASIN experiment (June-September, 1978) surface observations of many air and sea parameters were made by ships, buoys and aircraft, e.g. the wind and wave conditions which are of most interest here [Ref. 1]. During August and September, 1978, 19 SEASAT passes produced SAR imagery of the JASIN area. Examples of such passes are illustrated in Fig. 1. These multiple SEASAT observations coupled with intensive surface measurements provide a unique opportunity to assess the ocean measurement capabilities of satellite synthetic aperture radar.

SAR imagery is capable (under suitable conditions) of sensing a large variety of ocean surface phenomena including long gravity waves (with wavelengths  $\lambda$  greater than about twice the SAR resolution), winds, surface currents, internal waves, ocean fronts, underwater topography, slicks, and ships and their wakes (Barnes, 1973). The SAR image is basically a high resolution map of the radar

utilizes the phase of the radar wave to achieve high resolution in the direction parallel to the flight path, i.e., to correctly locate the origin of a given echo, motion of the ocean surface can cause echo energy to be misplaced in the image. This misplacement is illustrated in Fig. 4 where a moving ship is displaced from its wake. Spatial modulation of surface roughness and motion (owing rise to Doppler shifts) produces the majority of ocean surface features in SAR imagery. Phillips (4) describes a number of ways in which wind, wave and current variations can modulate decimeter scale surface roughness.

## 2. GRAVITY WAVE OBSERVATIONS

### 2.1 Wave Visibility in SAR Images

Although gravity waves of length 40 to 300 m are often seen in SAR imagery, we find that waves observed by surface buoys are not always visible. In our study we have used only imagery optically processed at Jet Propulsion Laboratory (JPL) and Environmental Research Institute of Michigan (ERIM). Study of JASIN data indicates three criteria are important in determining wave visibility: wave height, SAR resolution and wind velocity. Alpers, Ross and Rufenach (5) point out that the orbital velocities associated with surface waves produce a smearing effect on SAR imagery increasing resolution cell size especially along the azimuth direction (parallel to the SAR flight path). An expression for the degraded resolution cell length  $L_x$  along the azimuth direction is given in Ref. 5. Knowing  $L_x$  and the ocean wavelength along the azimuth direction  $L_y = \lambda / \cos \theta$ , the number of samples per wavelength  $n_y$  along the azimuth direction can be calculated. Here  $\theta$  is the angle between the spacecraft velocity vector  $V$  and the ocean wave vector  $K$ . The Nyquist sampling criterion demands  $n_y \geq 2$  in order that the waves be adequately sampled. Jain (6) and Vesceky et al. (7) have developed wave visibility criteria along these lines. Because of the roles played by waveheight and/or slope in wave imaging mechanisms (Ref. 5) one expects wave visibility to decrease with decreasing significant waveheight  $H_{1/2}$  and indeed we find waves are seldom imaged for  $H_{1/2} \leq 1$  m. Applying these two criteria  $n_y \geq 2$  and  $H_{1/2} \geq 1$  m to the JASIN data set we find only one case out of 15 in which these criteria did not work-nine cases where waves were visible in SAR images and six where waves were not observed in SAR images. All ocean wave data were drawn from buoy measurements.

Since wind raises the 15 m ocean waves which the radar senses, one expects reduced wave visibility at low wind speeds. During the JASIN-JASIN experiment waves were detectable over a range of wind speeds of from 1.5 to 15.2 m/s while for wind speeds of from 6.5 to 12.3 m/s waves were not detected. It is thus apparent that wind speed was not a factor during the JASIN-JASIN experiment mainly because wind speeds were always above 3.5 m/s.

### 2.2 Comparisons of SAR and Buoy Estimates of Wave Characteristics

2.2.1 Wave Measurement Method. The wave measurements from SAR imagery made here are based on a simple assumption, to wit, that fluctuations in SAR image intensity  $I(x,y)$  are proportional to ocean wave height fluctuations. The  $x,y$  plane

is the plane of the radar wavefront. Under this assumption the fluctuating ocean wave height spectrum  $M(x,y)$  is simply proportional to the magnitude squared of the Fourier transform  $F(x,y)$  of the intensity fluctuations, namely  $F(x,y) = \sqrt{M(x,y)}$ . Here  $x$  is directed to the wave wavelength and  $y$  is directed to the wave period.  $y$  is usually degrees clockwise from the  $x$  axis.  $F(x,y)$  will become clear below. The assumption is not precisely correct, however, it is an approximation for wind waves (4,6,7) and provides a convenient working hypothesis. Although this is not strictly correct, it is a good approximation for the implementation. Here we have used only SAR image data produced at the JPL and ERIM JPL Laboratory (JPL) and at the Environmental Research Institute of Michigan (ERIM). From the imagery's Fourier transform, estimates of the dominant wave length and direction can be made on the basis of our assumption by simply finding the peak of  $F(x,y)$  and noting the location in terms of wave number  $x$  and direction  $y$ . The SAR image resolution can be resolved by special processing measurements during the optical imaging process. Vesceky et al. (7) note that the peak signal to noise power ratio (PSNR) in the Fourier transform of a SAR image is correlated with  $H_{1/2}$  with significant waveheight  $H_{1/2}$ . Peak PSNR is estimated in Ref. 7 by noting the level contours in  $F(x,y)$  at  $y = 0$  (K = 0.15 m/s) and very high K (2.0 m/s) wave numbers and averaging the two levels to obtain a background noise level. With this method  $H_{1/2}$  can probably be measured to  $\pm 0.4$  m using this correlation.

2.2.2 SAR and Buoy Estimates of Dominant Wave Length and Direction. Buoy estimates of dominant surface buoys during the JASIN experiment were compared. The average distance between the center of the SAR image and the buoy was 400 m with a range of 0 to 146 km. The average percent difference in wavelength was 15% with a constant bias of SAR estimates toward longer wavelengths by about 10%. Six SAR and buoy estimates of dominant wave direction were compared with an average error of 12°. However, two of these estimates were only approximate due to compass problems. If we exclude these two approximate estimates, the average error was only 3°. There was no bias relative to the range direction, i.e., perpendicular to the subsatellite track.

2.2.3 SAR and Buoy Estimates of Dominant Wave Wavelength Spectrum. During the JASIN experiment estimates of the omnidirectional wave height spectrum  $M_{00}$  from buoys and from SAR images were compared in seven cases. Fig. 2 shows a typical example of these comparisons. The buoy estimates were computed by standard methods with  $M_{00}$  and the SAR estimates are simply  $F(x,y)$  at  $y = 0$  averaged over a 10° angular sector around the dominant wave direction and normalized to the ordinate to the peak of  $M_{00}$  from buoy measurements. No normalization was done about the abscissa. Since in these cases there is only a single dominant wave direction, data from buoys stays away from the dominant wave direction, i.e., stays only background fluctuations. The buoy data would only serve to raise the noise level in the SAR estimate of  $M_{00}$ .

The following information is being furnished to you for your information only. It is not intended to constitute an offer of insurance or any other financial product. The information is being provided to you for your information only and is not intended to constitute an offer of insurance or any other financial product. The information is being provided to you for your information only and is not intended to constitute an offer of insurance or any other financial product.

1. *Chlorophyll a* and *Chlorophyll b* contents were determined by spectrophotometry using the method of Lichtenthaler and Wherry (1987).

[illegible]

Estimates concerning the presence of a  
pattern of "bunching" of estimates for the same  
month were based upon year-to-year and month-to-  
month comparisons of the estimates. The estimates are prob-  
ably primarily dependent on the state of the econ-  
omy. It is possible that patterns of change in the  
labor force may be related to seasonal changes in the  
economy. However, data appear to indicate that the  
economy fell off in 1952 in this region.

[illegible]





